# Boiling Burnout at Low Flow Rate and Low Pressure Conditions( Dissertation_全文 )

AUTHOR(S):

Mishima, Kaichiro

# BOILING BURNOUT AT LOW FLOW RATE AND LOW PRESSURE CONDITIONS

KAICHIRO MISHIMA

# BOILING BURNOUT AT LOW FLOW RATE AND LOW PRESSURE CONDITIONS

KAICHIRO MISHIMA

RESEARCH REACTOR INSTITUTE
KYOTO UNIVERSITY

1984

TABLE OF CONTENT

## Abstract

The occurrence of burnout in natural convection boiling can be very important in relation to the safety of various types of nuclear reactors under a number of different accident conditions. It is noted that accidents which lead to the decay heat removal by natural convection have much higher probability than those of the severe accidents extensively studied recently. However, the breakdown of the natural convection boiling which leads to dryout and burnout of heated surface in these conditions can have very significant consequences.

In view of the above, experimental studies have been conducted for water with three basic channel geometries, i.e. annulus, rectangular channel and round tube in order to investigate the mechanisms of burnout particularly focussed on low-flow-rate and low-pressure conditions. The effects of buoyancy on the flow were also studied by comparing the results between upflow and downflow.

The results evidently indicated that the CHF was strongly affected by the occurrence of flow instabilities. The destabilizing effects of less inlet throttling, upstream compressibility and bypassing have been also observed and the buoyancy effects enlarged those destabilizing effects.

There was a minimum value in the critical heat flux which occurred at the complete bottom blockage or very low downflow conditions. Visual observation indicated that burnout occurred due to countercurrent flow limitation under such conditions.

The critical exit quality at burnout considerably reduced in annulus and rectangular channels because of the existence of unheated

walls. Therefore, observed critical heat fluxes were generally lower than the high-quality CHF at atmospheric pressures. On the other hand, there are some indications that the critical quality is close to unity even in those channel geometries other than round tubes at high pressures. It may be explained by the location of the annular flow boundary which moves toward higher quality with increasing pressure. However, further studies are needed to verify the statement.

As a conclusion, in any case at low mass velocities, burnout appears to occur due to dryout or breakdown of the liquid film on the heated surface. Therefore, if the film flow rate and the criteria for the dryout or breakdown of liquid film are known in detail, the CHF can be predicted theoretically. On the other hand, it is also probable that those criteria are met consequently if such hydrodynamical phenomena as countercurrent flow limitation, flow-regime transition and flow excursion cause the liquid deficiency in the heated channel. Therefore, in such cases, the CHF can be calculated by using the criteria for such hydrodynamical phenomena.

# CHAPTER I.

# INTRODUCTION

## I.1. PURPOSE OF THE STUDY

In a boiling heat transfer system such as a steam generator or a nuclear reactor core, there exists a certain upper limit of heat removal due to the phenomenon of thermal crisis which may result in "burnout" of the heat transfer surface at some "critical heat flux." The burnout phenomenon has been extensively studied particularly in the development of liquid-cooled nuclear reactors, since it is desirable to increase the power as much as possible while keeping the fuel elements under conditions far from burnout.

A large number of investigations have been performed on the burnout phenomenon at light water reactor (LWR) conditions, i.e. high flow rate and high pressure conditions. The burnout phenomenon at high flow rate and relatively low pressure has been also studied in relation to the core cooling of MTR-type research reactors. In spite of all those investigations, information on the burnout phenomenon at such low flow conditions as natural convection boiling is very limited, although it is important particularly in the decay heat removal of nuclear reactors. For this reason, it is aimed in this study to provide a better understanding of burnout mechanisms at low flow rates typical of natural convection conditions.

Natural convection boiling burnout can become important in relation to the safety of various types of liquid cooled nuclear reactors under a

number of different accident conditions such as loss-of-heat-sink, loss-of-flow and loss-of-piping-integrity accidents as well as planned decay heat removal conditions after the shutdown in high power research reactors. In spite of the importance of the cooling due to natural convection boiling and its upper limitation imposed by the occurrence of burnout, the main emphases of reactor safety analyses both for water and liquid-metal cooled reactors have been directed to more drastic accident conditions where the natural convection boiling is of little importance. However, it may be recognized that milder accidents which lead to the decay heat removal by natural convection have much higher probability than those severe accidents extensively studied recently. Furthermore, the breakdown of the natural convection boiling lead to a very significant consequence as exemplified by the accident at Three Mile Island Nuclear Power Plant under small loss-of-coolant accident (LOCA) conditions.

A number of different accidents can lead to cooling of a reactor core by natural convection boiling. These are small LOCA's for light water reactors, loss-of-flow accidents due to pump failure with mismatched decay heat, loss-of-heat-sink accidents both for LWR's and liquid-metal cooled reactors. Regardless of the initial stages of these accidents, a similar condition can develop which is basically the decay heat removal by natural convection boiling. For example, in case of a pump failure, the reactor will be shut down or set back immediately to reduce the heat load. As the resistance of the flow channels forces the coolant to stagnate, a transition of coolant flow to natural convection will follow. During this period, some flow instabilities may initiate which may cause a premature burnout. Eventually, a stable natural convection may be attained. However, a burnout can occur before the

decay heat becomes sufficiently low if the period of the flow coast down is too short. On the other hand, if the flow coast down lasts long enough, a natural convection will allow the core to be cooled safely without any additional cooling devices.

In many MTR-type research reactors, the primary coolant flows downward through the core at rated power while the upflow by natural convection removes the decay heat after the shutdown. During the slow transient from the forced downflow to the natural convection, a flow reversal occurs. At this moment, a very low flow condition may develop. Thus if the coolant flow is mismatched with the decay heat, a burnout condition could be approached even under normal operating conditions.

Moreover, in such engineering equipments as thermosyphon reboilers, the system is often operated under near natural convection conditions. In those systems, too, the maximum heat output is limited by the occurrence of burnout.

In order to design or to allow possible correction of these systems to overcome the occurrence of burnout, critical heat flux (CHF) under such conditions as encountered in these systems must be known. Although the CHF data at low flow rate typical of natural convection are important, they appear to be at present not sufficient so that in the design of these systems either the CHF is extrapolated based on the conventional correlations or conservative design criteria are imposed. There exist some CHF correlations at low flow rates, however they are applicable only to a limited range of parameters and the relationship which may exist among those correlations has not yet been thoroughly understood.

Therefore it is desirable to obtain CHF data at low flow rates and

low pressure conditions and to investigate the relationship among various burnout mechanisms. The investigation is needed not only for engineering safety but also it is expected to make some contribution in interpreting the burnout phenomenon systematically.

## I.2. BACKGROUND

### I.2.1. Definition of Burnout

There have been several synonyms describing "burnout" phenomenon such as "boiling crisis" and "critical heat flux." The term "burnout" is adopted here since it appears to be more widely accepted [1,2].

The term "burnout" is defined here by the sudden drop in boiling heat transfer coefficient due to an inordinate change in heat transfer mechanism. The corresponding heat flux is referred to as "critical heat flux (CHF)" which means that, according to Hewitt [2], the heat flux at which a small increase in heat flux gives rise to an inordinate deterioration in heat transfer.

In a system where the heat flux is controlled (e.g. electrically or nuclear heated systems), burnout is indicated by an excursive temperature rise of the heated wall, while in a system where the wall temperature is controlled (e.g. a steam-heated systems), it is indicated by a sudden drop in heat flux [1,2].

### I.2.2. Basic Mechanisms of Burnout

In rather crude words, it can be said that burnout occurs when sufficient liquid cannot reach onto a part of the heated surface and the vapor covers there permanently. As a consequence, an inordinate reduction in heat transfer is resulted because of very low heat transfer coefficient of the vapor flow compared to that of the liquid flow. Thus local or bulk liquid deficiency on the heated surface is considered as a

necessary condition for burnout. Such liquid deficiency can be caused by various thermal-hydraulic conditions, hence the mechanism of burnout depends on those.

I.2.2.1. Pool boiling burnout

Figure 1 depicts the basic mechanism of pool-boiling burnout. In pool boiling, the heated surface is immersed in a large volume of liquid where the geometrical condition is such that sufficient liquid could be supplied to the heated surface. Boiling occurs at the nucleation sites in the heated wall. Therefore, it is called "nucleate boiling." In pool boiling, the heat flux q depends mainly on the wall superheat $\Delta T_{sat}$. Figure 2 shows diagrammatically the relation between the heat flux and the wall superheat for the boiling of water at atmospheric pressure. At low heat flux, the heat is transferred by single-phase natural convection until point B is reached, where incipient boiling occurs on the heated surface. Point B is called onset of nucleate boiling (ONB). When the boiling has been initiated at point B, the boiling curve goes quickly to point B'. The region from B' to C corresponds to nucleate boiling region depicted in Fig. 1(a). Further increase in heat flux beyond C leads to a larger increase in wall temperature until point D where, if the heat flux is kept constant, the wall temperature rapidly rises up to point E. This is explained as follows. In nucleate boiling region, bubbles rise due to buoyancy and liquid flows downward to compensate the amount of vapor carried away from the heated surface. In the neighborhood of the heated surface, a countercurrent flow arises and a drag force acts between the two phases. When the heat flux is sufficiently high, the drag force becomes large enough to prevent the liquid from approaching the heated surface

(Fig. 1(b)). Thus the liquid defficiency on the heated surface cause a sudden change in boiling regime, i.e. a burnout which manifests itself in the curve D-E. The transition is also called "departure from nucleate boiling (DNB)" when a specific burnout process is interested in. In most cases when this transition occurs, the magnitude of the temperature excursion is such that leads to a "physical burnout" or damage to the heated wall. The region E-F is film boiling region where a stable vapor film covers the heated surface. Conversely, when the heat flux is decreased from point F, film boiling is sustained until point G where, if the heat flux is controlled, the wall temperature decreases to point H. In a system where the wall temperature is controlled, the boiling curve goes through C-D-G-E. The region D-G is "transition boiling" where an unstable vapor blanket covers the heated surface.

I.2.2.2. Flow boiling burnout

Basic burnout mechanisms in flow boiling are shown in Fig. 3. When the bulk liquid is subcooled or the vapor quality is low, burnout occurs due to the formation of a vapor blanket covering the heated surface (Fig. 3(a)). This is called "DNB-type burnout" because the burnout process is similar to DNB in pool boiling. Corresponding critical heat flux is so high in a DNB-type burnout that the wall temperature rises rapidly resulting in a "physical burnout" of the heated wall. For this reason, it is also referred to as "fast burnout". When the vapor quality is high, the vapor flows in the central part of the channel and the liquid film is formed along the channel wall, which flow regime is "annular flow" (Fig.3(b)). In the annular flow regime, the heat transfer is dominated by the evaporation of liquid film, therefore

burnout takes place due to dryout or breakdown of the liquid film. The liquid film dries out by progressive entrainment and evaporation even at low heat fluxes. The mechanisms of burnout due to liquid-film breakdown have been discussed in detail by Hewitt [3]. The following basic processes have been postulated for burnout due to film breakdown;

(1) vapor film formation under the liquid film,

(2) burnout limited by droplet mass transfer rate,

(3) sudden disruption of the liquid film,

(4) dry patch formation, causing a hot spot on the heated surface that cannot be rewetted.

Burnout in a high quality region is called "dryout", which does not always mean a physical burnout of the heated wall. "Slow burnout" is an alternative for "dryout", however the term "high-quality burnout" will be used in this thesis instead of "slow burnout."

Burnout process in flow boiling is diagrammatically depicted by Collier [4] as a function of quality with increasing heat flux as ordinate, which is reproduced in Fig. 4. It is obvious from the figure that, as mentioned above, burnout in subcooled or low quality region, i.e. DNB-type burnout likely causes physical burnout due to rupture or melting of the heated wall whereas the occurrence of burnout in high quality region, i.e. dryout does not always result in physical burnout.

I.2.2.3. Burnout due to flow instability

In a boiling system, various flow instabilities are encountered [5-11] particularly at low pressures. They often cause a sudden reduction of the flow rate with a small increase in the heat flux. Thus, under certain circumstances, the vapor quality increases so high

as to initiate burnout. The CHF due to flow instabilities is often much lower than that corresponding to stable flow [5-7]. The flow instabilities are classified into two categories: excursive instability and oscillatory instabilities. The excursive flow instability is called Ledinegg instability because it was first analyzed by Ledinegg [8]. This instability occurs when the slope of the system-demand pressure-drop versus flow-rate curve is more negative than the supply pressure-drop versus flow-rate curve. When a system with a compressible volume upstream of the heated section is operated in the region where the slope of the system-demand pressure-drop versus flow-rate curve is negative, an oscillatory flow instability occurs. This instability is called pressure-drop oscillation in which the upstream compressible volume serves as an energy storage mechanism. Another important oscillatory instability is known as the density-wave oscillation which occurs in the region where the slope of the system demand pressure-drop versus flow-rate curve is positive. This instability is attributed to the finite transit time of the density wave along the heated section.

## I.3. THESIS OBJECTIVES

In order to meet the above mentioned requirements, this investigation is aimed at the following objectives.

(1) To develop appropriate criteria to describe two-phase flow regimes, which will be usefull in determining the flow regimes at burnout,

(2) to observe the flooding and flow reversal phenomena which are important because they may cause a burnout at a very low heat flux,

(3) to observe flow regimes at burnout and find the relationship between the mechanisms of burnout and the resulting critical heat flux,

(4) to find the lower boundary of CHF in the safety-design point of view of a nuclear reactor,

(5) to find CHF correlations which are relevant to the describe observed burnout mechanisms,

(6) to identify the flow instabilities, if any, observed in burnout phenomenon and to find their effects on the CHF.

In this research, the working fluid is limited to water because it is the most basic, most widely used and easiest-to-handle fluid. The flow is vertical upflow or downflow in three basic single-channel geometries: round tubes, annulus and rectangular channels. The two orientations of flow are tested in order to know the effects of gravity which is expected to become more important at low flow rates. The system pressure is limited to atmospheric because the burnout phenomenon is more complicated at low pressures due to large density ratio of liquid to vapor, and in addition to this, a large number of data are already available for high pressure systems. However, the comparison of CHF will be made between high pressure systems and low pressure systems using existing information.

## I.4. OUTLINE OF THE THESIS

Since it is the most basic concern in describing phenomena associated with two-phase flow to identify the flow regimes, the transition criteria for the flow regimes are first discussed in Chapter II. New transition criteria are developed based on appropriate modeling, and they are compared to the existing experimental data both for air-water flow and steam-water flow.

Secondly, flooding and flow reversal phenomena are discussed in

Chapter III. The basic equations to describe the film flow are derived to discuss the theoretical limit of the countercurrent flow. The theoretical limit are compared with the flooding velocities observed in the experiment for air-water flow in thin rectangular test sections which is similar to the coolant channels of a MTR-type research reactor, and the difference between them are discussed in view of flooding mechanisms

Burnout phenomenon in an annulus is discussed in Chapter IV, where the main concern is to observe the mechanisms of burnout in an annulus at very low flow rate and low pressure conditions. The comparison of CHF is made between natural convection and forced convection. The relation between the CHF due to flooding and the pool-boiling CHF is also discussed.

Chapter V is devoted to studying the significance of two-phase flow instabilities in burnout phenomenon. Several flow instabilities are identified in the experiment conducted with round tubes and their relation to the CHF are discussed. The effects of inlet throttling, upstream compressibility, bypass and the flow orientation on the instabilities are also discussed.

In Chapter VI, the CHF in rectangular channels is discussed particularly in relation to the core cooling of a MTR-type research reactor. The CHF in downflow as well as in upflow is investigated in order to see the effect of buoyancy, which may become important in stagnant flow conditions which may develop during decay-heat-removal.

The results from the above investigations are brought together and compared to the existing data in order to draw more generic conclusions in Chapter VII. The relation to the CHF at higher pressures and higher

flow rates and the difference in burnout mechanisms between three channel geometries are discussed.

Finally, Chapter VIII provides the summary and the conclusions extracted from the present research.

## REFERENCES


[1] A.E. Bergles, "Burnout in boiling heat transfer, Part II: Subcooled and low-quality forced-convection systems," Nucl. Safety, 18[2], p.154 (1977).

[2] G.F. Hewitt, "Mechanisms of burnout," in Two-phase flow and heat transfer, ed. D. Butterworth and G.F. Hewitt, Oxford University Press, p.279 (1978).

[3] G.F. Hewitt, "Burnout," in Handbook of multiphase system, ed. G. Hetsroni, Hemisphere, pp.6-125 (1982).

[4] J.G. Collier, Convective boiling and condensation, McGraw-Hill, p.217 (1972).

[5] J.A. Bouré, A.E. Bergles and L.S. Tong, "Review of two-phase flow instability," Nucl. Eng. Design, 25, p.165 (1973).

[6] D.B. Collins, M. Gacesa and C.B. Parsons, "Study of the onset of premature heat transfer crisis during hydrodynamic instability in a fullscale reactor channel," ASME Paper No.71-HT-11 (1971).

[7] W.H. Lowdermilk, C.D. Lanzo and B.L. Siegel, Investigation of boiling burnout and flow stability for water flowing in tubes, NACA-TN4382 (1958).

[8] M. Ledinegg, "Instability of flow during natural and forced circulation," Die Wärme, 61, p.8 (1938).

[9] J.S. Maulbetsch and P. Griffith, "System-induced instabilities in forced-convection flows with subcooled boiling," Proc. 3rd. Int. Heat Transfer Conf., Chicago, 4, p.247 (1966).

[10] S. Kakaç and T.N. Veziroglu, "A review of two-phase flow

instabilities," in Advances in two-phase flow and heat transfer, Vol. II, ed. S. Kakaç and M. Ishii, Martinus Nijhoff Publ. Co., p.577 (1983).

[11] M. Ishii, Study on flow instabilities in two-phase mixtures, ANL-76-23 (1976).

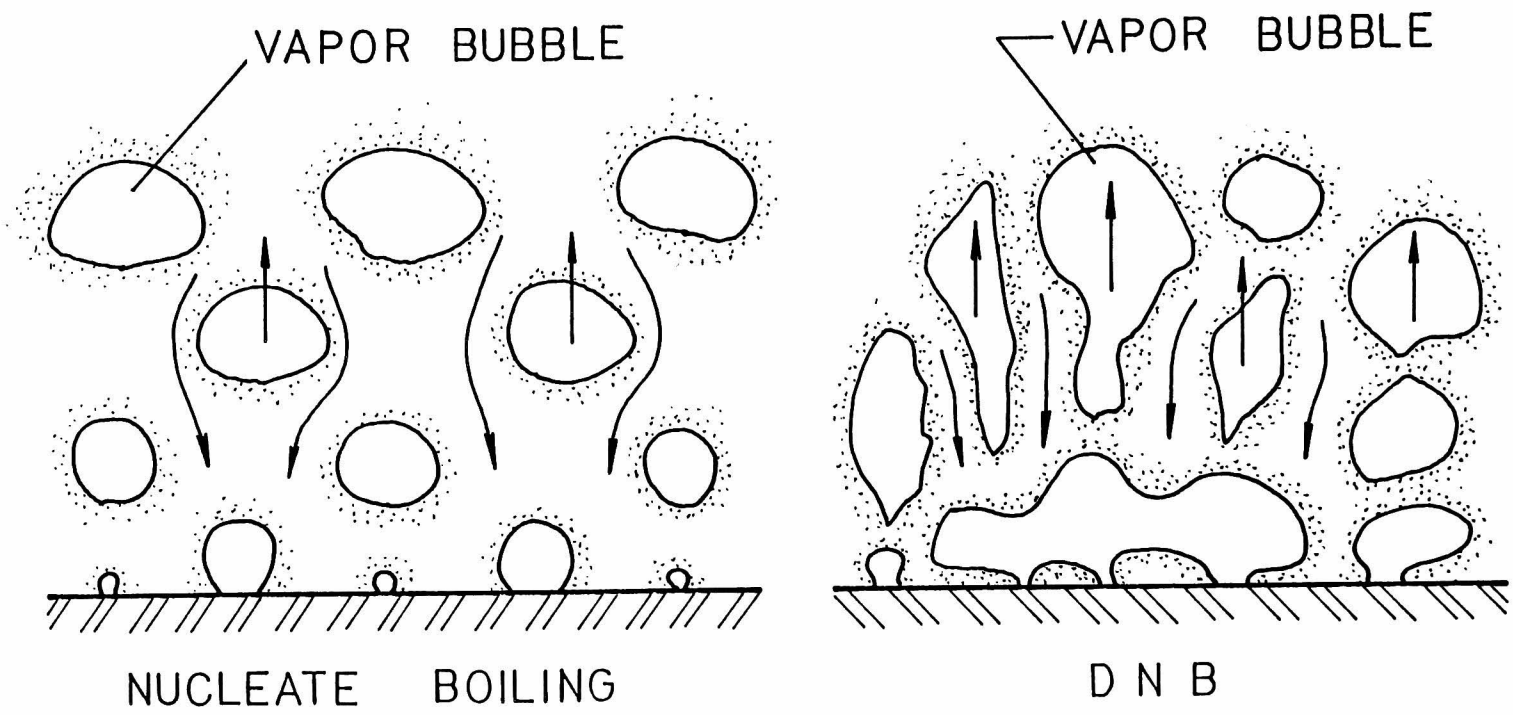


Figure 1 Burnout mechanism in pool boiling.

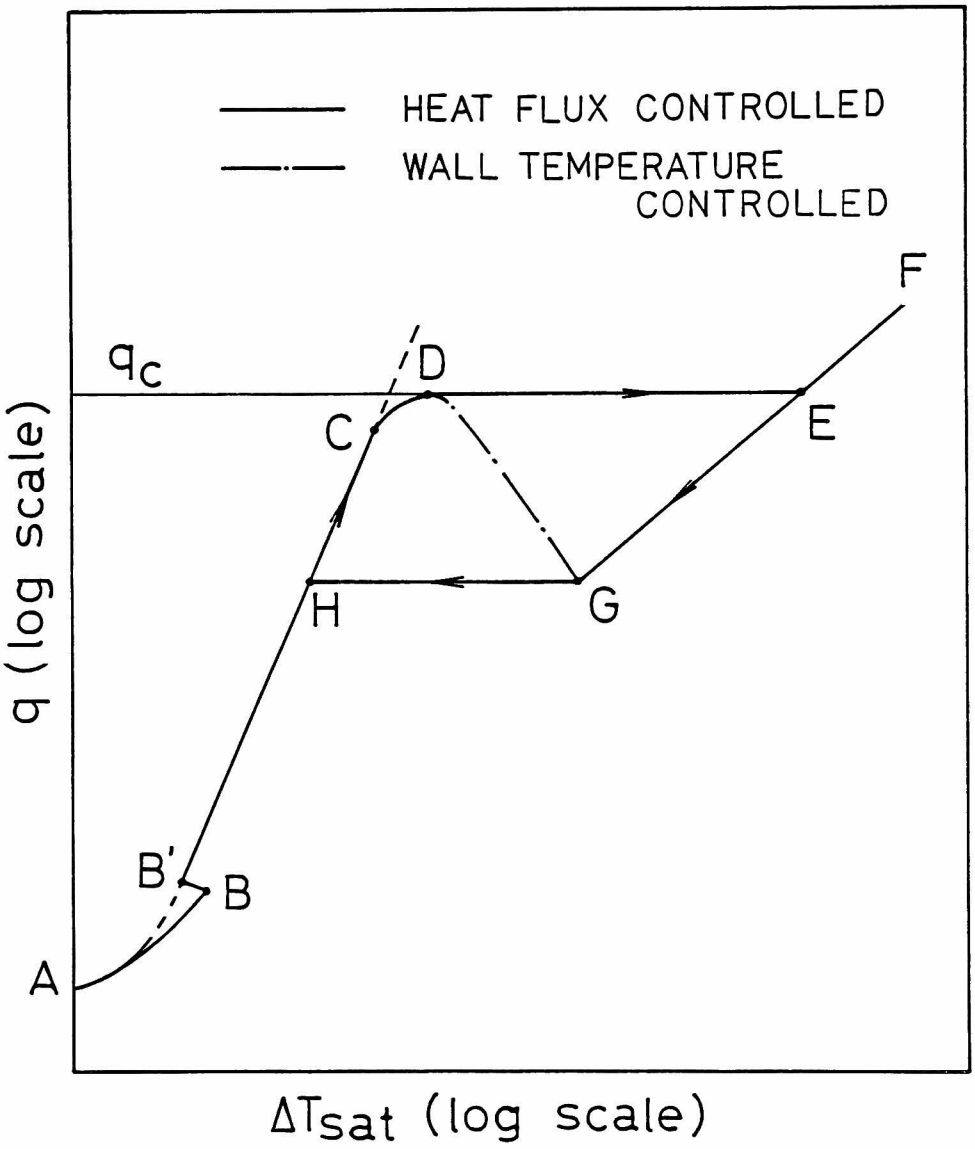


Figure 2 Boiling curve.

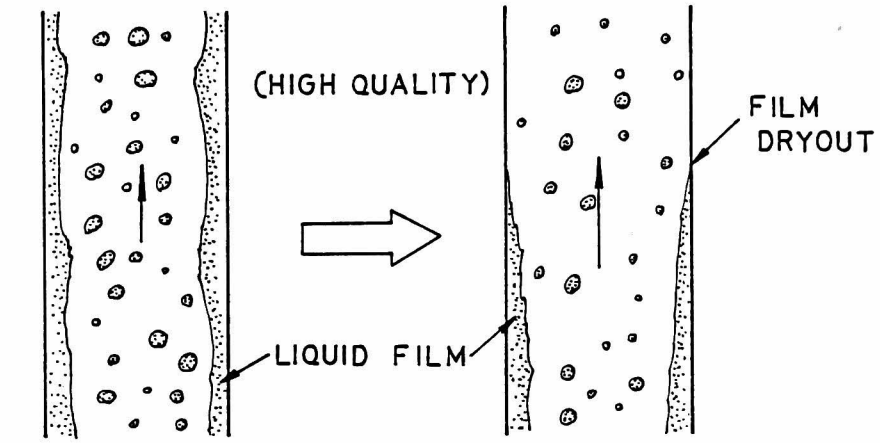


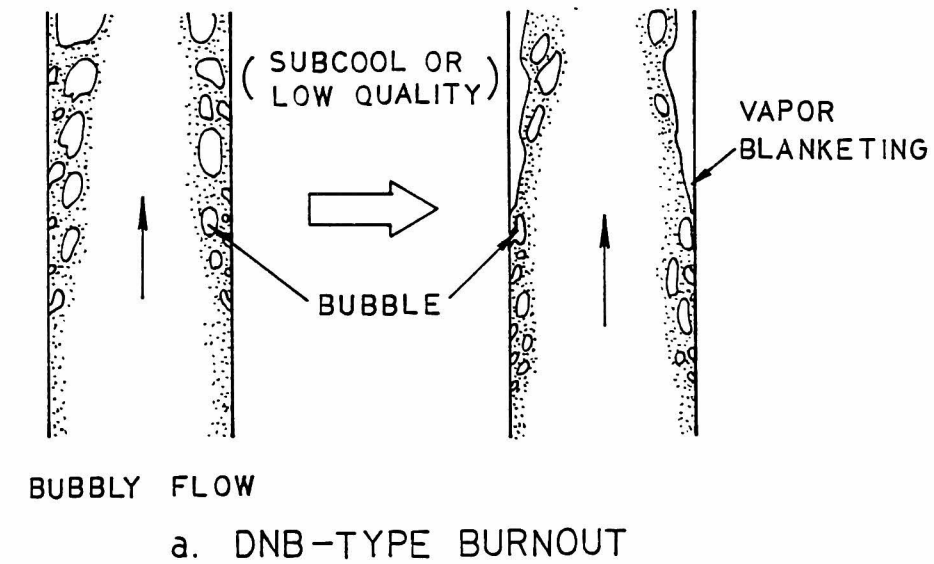


Figure 3 Basic burnout mechanisms in flow boiling.

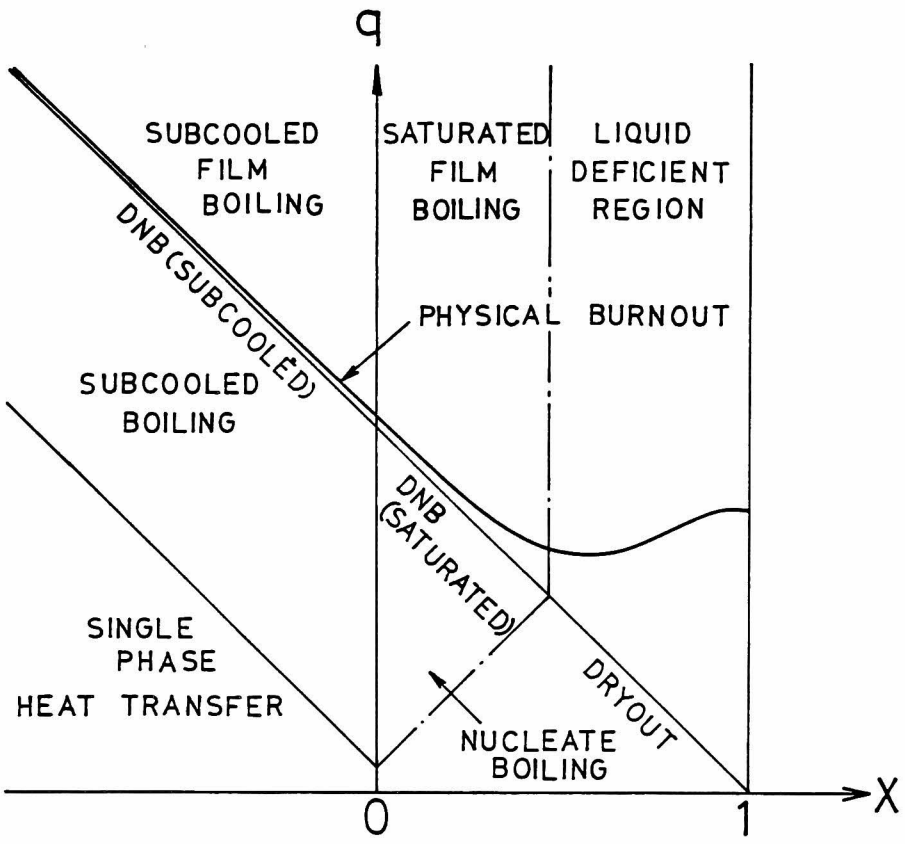


Figure 4 Burnout mechanisms as a function of quality with increasing heat flux as ordinate [4].

# CHAPTER II.

# TWO-PHASE FLOW REGIME TRANSITIONS

## II.1. INTRODUCTION

The complexity of gas-liquid two-phase flow arises from the fact that there exist interfaces between the two phases. The geometrical pattern of the interface in two-phase flow, which is reffered to as flow regime, varies depending on the volume fraction of each phases. Since the two-phases interact through the interface, the characteristics of the flow depend on the flow regime. In a boiling system, the heat and mass transfer rate also depends upon the flow regimes. Moreover, the flow regime plays an important role in boiling burnout phenomena. For example, the significance of the annular flow regime in high-quality burnout has been pointed out earlier. Therefore, it is of primary importance to know the flow regime at a given condition in describing two-phase flow.

Traditionally, flow regimes are identified from a flow-regime map obtained from experimental observations. Many flow-regime maps have been proposed using dimensional coordinates based on the liquid and gas superficial velocities [1-4]. Other investigators have attempted to correlate the transition boundaries by non-dimensional groups [5-9]. There have also been theoretical works [10-12] to predict from regimes. These conventional flow-regime maps are based primarily on the liquid and gas superficial velocities or the total mass velocity and the vapor quality. The flow regimes are the classifications of the geometrical structures of flow. Therefore, it is postulated that the flow

structures should depend directly on the geometrical parameter such as the void fraction and interfacial area. Under steady-state fully-developed conditions, it may be assumed that there exists a unique relation between the void fraction and the superficial velocities [2,3,14]. Therefore it can be said that these traditional approaches may be suitable for slow transients and near fully developed conditions, where a mixture model such as the drift-flux model [1] is sufficient. The discrepancies between these two different approaches can be significant near flow reversal conditions or under rapid transient conditions, though these differences have not yet been clearly demonstrated by specially designed experiments.

In view of these, new flow-regime criteria for upward gas-liquid flow in vertical tubes have been developed in this study. Four basic flow regimes designated by Hewitt and Hall-Taylor [13] as bubbly flow, slug flow, churn flow and annular flow, have been analyzed. These new criteria can be compared to existing flow-regime maps under steady-state conditions by using relative velocity correlations obtained previously by Ishii [14].

As regards to downflow, the burnout phenomenon is characterized better by the flow instabilities than by the flow regime transitions as will be discussed later. Therefore the flow-regime transitions for downflow are not considered here.

## II.2. CRITERIA FOR FLOW-REGIME TRANSITIONS

### II.2.1. Bubbly-Flow to Slug-Flow Transition

As studied by Radovicich and Moissis [15] and Griffith and Snyder [16], the transition from bubbly flow to slug flow in a tube occurs mainly due to agglomerations and coalescences of smaller bubbles into

cap bubbles. Once a cap bubble is formed, further coalescences follow in the wake region of a cap bubble. This transition occurs at the void fraction around 0.3. Radovicich and Moissis [15] showed qualitatively that the probability of collisions becomes very large at $\alpha \cong 0.3$, and they postulated this as a cause of the flow-regime transition. Dukler and Taitel [10] proposed $\alpha = 0.3$ as the criterion and then used a relative velocity correlation to convert it into a conventional form based on the superficial velocities of liquid and gas. Thus, following these observations, the criterion for the bubbly-to-slug flow transition can be given by

$$\alpha = 0.3 \ . \tag{1}$$

The value of 0.3 can also be obtained from a very simple geometrical consideration only. Suppose bubbles distribute themselves in a tetrahedral lattice pattern in which each bubble fluctuates. It is assumed that there is a sphere of influence around each bubble. Although these spheres of influence can overlap in certain situations, the summation of the sphere volumes equals the total volume of the mixture. The number of not only the collisions but also the coalescences is considered to become very large if the maximum possible gap L between two bubbles becomes less than a bubble diameter $2r_b$ as shown in Fig. 1. Under this condition, it is evident that the bubbles should deform considerably during each fluctuation. The above condition requires

$$\alpha = \left(\frac{2}{3}\right)^3 = 0.296 \simeq 0.3 \ . \tag{2}$$

In order to convert Eq.(1) into a conventional form based on the superficial velocities, we use the following relationship between $j_g$ and $j_f$, which is derived from the drift velocity for bubbly flow [14];

$$j_g/\alpha = C_0 j + \sqrt{2}\,(\sigma g \Delta\rho/\rho_f^2)^{1/4}\,(1-\alpha)^{1.75} \quad , \tag{3}$$

where $C_0$ is given by

$$C_0 = 1.2 - 0.2\sqrt{\rho_g/\rho_l} \qquad \text{for round tubes,} \tag{4}$$

$$= 1.35 - 0.35\sqrt{\rho_g/\rho_f} \qquad \text{for rectangular channels,} \tag{5}$$

and

$$j = j_g + j_f \quad . \tag{6}$$

Therefore, the relationship between $j_g$ and $j_f$ at the transition becomes

$$j_f = \left(\frac{3.33}{C_0} - 1\right) j_g - \frac{0.76}{C_0}\,(\sigma g \Delta\rho/\rho_f^2)^{1/4} \quad . \tag{7}$$

II.2.2. Slug-flow to Churn-flow Transition

The transition is postulated to occur when the mean void fraction over the entire region exceeds that over the slug-bubble section. This criterion can be visualized in an idealized pattern as follows. At just before the slug to churn flow transition, the slug bubbles are lined up right next to each other and the tail of the preceding bubble starts to touch the nose of the following bubble. Under this condition, the

liquid slugs become unstable to sustain their individual identity due to the strong wake effect. Then destructions and creations of liquid slugs follow. It is considered that physically this corresponds to the flow regime transition. The mean void fraction over the slug-bubble section $\alpha_m$ is obtained by a potential flow analysis applied to the film flow along the bubble until the film flow reaches the void fraction corresponding to the fully developed flow.

Consider the slug flow model as shown in Fig. 2. Except very near the nose of the bubble, the application of the Bernoulli equation yields the local void fraction at the distance h from the nose, thus

$$\alpha(h) = \frac{\sqrt{2gh\Delta\rho/\rho_f}}{\sqrt{2gh\Delta\rho/\rho_f} + (C_0-1)j + 0.35\sqrt{\Delta\rho gD/\rho_f}} \quad , \tag{8}$$

where the following equation for the slug-bubble velocity is used [14];

$$v_{gs} = C_0 j + 0.35\sqrt{\Delta\rho gD/\rho_f} \quad . \tag{9}$$

The mean void fraction is calculated by

$$\alpha_m = \frac{1}{L_b}\int_0^{L_b} \alpha(h)dh \quad , \tag{10}$$

where $L_b$ is the mean slug-bubble length. From Eqs.(8) and (10), the following equation is derived.

$$\alpha_m = 1 - 2X + 2X^2 \ln\left(1 + \frac{1}{X}\right) \quad , \tag{11}$$

where

$$X = \sqrt{\frac{\rho_f}{2g\Delta\rho L_b}} \left[ (C_0 - 1)j + 0.35\sqrt{\Delta\rho g D/\rho_f} \right] \quad . \tag{12}$$

Equation (11) is well approximated over the numerical values of $\alpha_m$ from 0.6 to 0.9 by the following expression:

$$\alpha_m = 1 - 0.813\, X^{0.75} \quad . \tag{13}$$

Now the mean slug-bubble length $L_b$ at the transition from the slug to churn flow regime may be estimated as follows. Somewhere below the nose of a slug bubble, the gravity force on the liquid film is completely balanced by the wall shear stress and the flow becomes fully developed. At a section below this point, there exists a small adverse pressure gradient for the downward liquid film flow. Since the liquid is no longer accelerating in the downward direction, the liquid film becomes unstable due to a flow separation and film instability. Thus, beyond the terminal velocity point of a film, interface disturbances will lead to a cut-off of the slug bubble. The force balance on the liquid film around the slug bubble gives

$$\frac{f}{2} \rho_f v_{fsb}^2 \pi D = \frac{2}{3} \Delta\rho g A (1-\alpha_{sb}) \quad , \tag{14}$$

The factor of 2/3 appears on the right hand side of the above equation due to the effect of the gravity on the wall shear [13,14]. The wall friction factor f is assumed to be in the form;

$$f = C_f \left[(1 - \alpha_{sb}) v_{fsb} D/\nu_f\right]^{-m} \quad . \tag{15}$$

Substituting Eq.(15) into Eq.(14) and solving for $v_{fsb}$, we obtain

$$v_{fsb} = (1-\alpha_{sb})^{\frac{1+m}{2-m}} \left[3C_f \, (D/\nu_f)^{-m} \, \rho_f/(\Delta\rho g D)\right]^{\frac{1}{m-2}} \quad . \tag{16}$$

The right hand side of the above equation can be eliminated by using the basic relationship for the two-phase mixture, i.e. Eq.(9) and the following equation,

$$v_{fsb} = \frac{\alpha_{sb} v_{gs} - j}{1 - \alpha_{sb}} \quad . \tag{17}$$

The resulting equation is

$$\alpha_{sb} = \frac{j + (1-\alpha_{sb})^{\frac{3}{2-m}} \left[3C_f \, (D/\nu_f)^{-m} \, \rho_f/(\Delta\rho g D)\right]^{\frac{1}{m-2}}}{C_0 j + 0.35\sqrt{\Delta\rho g D/\rho_f}} \quad . \tag{18}$$

Here we assume that m = 0.2 and $C_f$ = 0.046 for a turbulent flow [10]. In the presence of small bubbles in the liquid film section and due to its relatively large film thickness, the film behavior may be approximated by a turbulent flow model for most practical cases. Then Eq.(18) becomes

$$\alpha_{sb} = \frac{j + 3ab(1-\alpha_{sb})^{1.67}}{C_0 j + 0.35\, b} \quad , \tag{19}$$

where

$$a = [\Delta\rho g D^3/(\rho_f \nu_f^2)]^{1/18} \quad , \tag{20}$$

and

$$b = \sqrt{\Delta\rho g D/\rho_f} \quad . \tag{21}$$

Equation (19) can be solved if we use the approximation:

$$(1-\alpha_{sb})^{1.67} \simeq 0.25\ (1-\alpha_{sb}) \quad . \tag{22}$$

which is valid when $\alpha_{sb}$ is larger than 0.6.

Hence we obtain

$$\alpha_{sb} = \frac{j + 0.75ab}{C_0 j + 0.35b + 0.75ab} \quad . \tag{23}$$

On the other hand, Eq.(8) gives

$$\alpha(L_b) = \frac{y}{y + (C_0-1)j + 0.35b} \quad , \tag{24}$$

where

$$y = \sqrt{2\Delta\rho g L_b/\rho_f} \quad . \tag{25}$$

Based on the condition that $\alpha(L_b)$ be equal to $\alpha_{sb}$ at the tail end of the

slug bubble, we obtain

$$y = j + 0.75ab \quad , \tag{26}$$

or in a more explicit form, the solution for the slug bubble length becomes

$$\sqrt{2\Delta\rho g L_b/\rho_f} = j + 0.75\sqrt{\Delta\rho g D/\rho_f}\,[\Delta\rho g D^3/(\rho_f \nu_f^2)]^{1/18} \quad . \tag{27}$$

There exist several data on the slug-bubble length [5,17]. Although the general trends are the same among those data, the exact mean bubble lengths are different by as much as 100%. This indicates that the length depends on the development of the slug flow (injection, entry length, etc.). However, when this fact is recognized, Fig. 3 shows a reasonable comparison between Akagawa's data and $L_b$ predicted by Eq.(27).

Since it is assumed that the transition from the slug to churn flow regime occurs when the mean void fraction over the entire region reaches the mean void fraction in the slug-bubble section, the transition criterion becomes

$$\alpha \geq 1 - 0.813\left(\frac{(C_0-1)j + 0.35\sqrt{\Delta\rho g D/\rho_f}}{j + 0.75\sqrt{\Delta\rho g D/\rho_f}\,[\Delta\rho g D^3/(\rho_f \nu_f^2)]^{1/18}}\right)^{0.75} . \tag{28}$$

It is noted that for standard conditions, the term 1/18 power in the denominator in the above criterion may be further simplified. For

weakly viscous fluids such as water this term may be simply replaced by a constant value of 3, i.e.

$$(\Delta\rho g D^3/\rho_f \nu_f^2)^{1/18} \simeq 3$$

The above criterion is obtained from $\alpha \geqq \alpha_m$ where $\alpha_m$ is calculated from Eq.(13) together with Eqs.(12) and (27).

In order to compare Eq.(28) to existing data in $j_f - j_g$ plane, the following relationship from the drift-flux condition is used,

$$\alpha = \frac{j_g}{C_0 j + 0.35\sqrt{\Delta\rho g D/\rho_f}} \quad . \tag{29}$$

By using Eq.(29), the transition criterion can be recasted in terms of $j_g$ and $j_f$ under steady state fully-developed flow conditions.

II.2.3. Churn-flow to Annular-flow Transition

The criteria for this transition have been developed by Ishii [14], postulating two different mechanisms:

(1) Flow reversal in the liquid film section along large bubbles.

(2) Destruction of liquid slugs or large waves by entrainment or deformation.

The first mechanism assumes that, for the film section along large bubbles, the annular drift-velocity correlation can be used locally. This can be given [14] by

$$\frac{j_g}{\alpha} - j = \frac{1-\alpha}{\alpha + \left[\frac{1 + 75(1-\alpha)}{\sqrt{\alpha}} \cdot \frac{\rho_g}{\rho_f}\right]^{1/2}} \left[ j + \sqrt{\frac{\Delta\rho g D(1-\alpha)}{0.015\ \rho_f}} \right] \tag{30}$$

which can be obtained from a force balance. Hence by setting the flow

reversal condition in the film as $j_f = 0$,

$$j_g = \sqrt{\Delta\rho g D/\rho_g}\ \alpha^{1.25} \left[\frac{1-\alpha}{0.015[1+75(1-\alpha)]}\right]^{1/2} \quad . \tag{31}$$

However, in the range of $\alpha$ relevant to the present case, the churn to annular flow transition criterion can be approximated [14] by

$$j_g = \sqrt{\Delta\rho g D/\rho_g}\ (\alpha - 0.11) \quad , \tag{32}$$

where $\alpha$ should satisfy the condition given by Eq.(28).

On the other hand, the second criterion can be obtained from the onset of droplet entrainment [14]. The onset of entrainment criteria for film flow has been developed from a force balance on the liquid crest between the shearing force of the vapor drag and the retaining force of the surface tension. This is given by

$$\frac{\mu_f j_g \sqrt{\rho_g/\rho_f}}{\sigma} = N_{\mu f}^{0.8} \quad , \tag{33}$$

where

$$N_{\mu f} = \mu_f/[\rho_f \sigma \sqrt{\sigma/(g\Delta\rho)}]^{1/2} \tag{34}$$

for low viscous fluid ($N_{\mu f} < 1/15$) and at relatively high liquid Reynolds number ($Re_f > 1635$). It is considered that once the gas flux exceeds the value given above in the churn flow bubble section, the liquid waves and subsequently liquid bridges and slugs can be entrained

as small droplets. This will lead to the elimination of liquid slugs between large bubbles and to a continuous gas core. This entrainment-induced flow transition is given by the second criterion based on Eq.(33) as

$$j_g \geq (\sigma g \Delta\rho/\rho_g^2)^{1/4} N_{\mu f}^{-0.2} \quad . \tag{35}$$

The second criterion is applicable to a flow in a larger diameter tube given by

$$D > \sqrt{\sigma/(g\Delta\rho)}\, N_{\mu f}^{-0.4}/[(1-0.11\, C_0)/C_0]^2 \quad , \tag{36}$$

Therefore, the second criterion from the onset of entrainment is applicable to predict the occurrence of the annular-mist flow or to predict the churn-to-annular flow transition in a larger diameter tube.

Equation (35) can be compared to existing data if we use Eq.(30) when $\alpha < \alpha_m$ , and

$$\alpha = \frac{j_g}{C_0 j + \sqrt{2}\, (\sigma g \Delta\rho/\rho_f^2)^{1/4}} \quad , \tag{37}$$

when $\alpha > \alpha_m$ .

II.2.4. Flow Regime Map

A flow regime map can be drawn by using newly developed transition criteria. Figure 4 shows an example of flow regime map for air-water

flow in a 25.4mm I.D. tube at 25°C and atmospheric pressure.

Curve A on the map designates the bubble-to-slug flow transition which is predicted by Eq.(1). The locus of the curve depends only on the properties of both phases. The transition from the slug to churn flow occurs at curve B, based on Eq.(28). At high liquid and gas velocities, the slug flow is limited by curve D corresponding to Eq.(35). At higher gas velocities than curve D, liquid slugs will be disintegrated into liquid drops by entrainment, thus the annular-mist flow will be observed. However, in Region A, the void fraction is rather low, ranging from 0.3 to 0.7. Thus in this region the flow is so highly agitated that it may be difficult to distinguish between the slug or annular flow. Hence the flow may behave like a churn flow, although it appears to be paradoxical in terms of the standard behavior and definition of the churn flow. The churn to annular flow transition occurs at curve C predicted by Eq.(32). Curve C moves toward higher gas velocities when the tube diameter becomes larger, until the diameter reaches the value which satisfies inequality (36). Therefore, the annular flow which is seen in the region bounded by the curves B,C and D disappears when the diameter is larger than the limiting value.

## II.3. COMPARISON WITH EXISTING DATA

The newly developed flow regime criteria can be compared with existing data for air-water flow [1,2,4-7,11,12,18] and steam-water flow [19-21] under steady-state and fully-developed flow conditions, although the present criteria are not limited to these conditions.

In most cases, rather wide discrepancies will be observed in the location of the curves for experimental transition boundaries. This is due to the different methods of observations and definitions of the flow

regimes. Moreover, the transition phenomena themselves develop gradually and there are some history effects of upstream conditions. Consequently, some ambiguity is inevitable in determining the transitions. Therefore, the transition boundaries should be understood as a band with a certain width proportional to the uncertainty in determining the transition boundaries.

II.3.1. Air-water Flow at Atmospheric Pressure

Figure 5 shows the comparison of the bubbly-to slug flow transition for air-water flow at 25°C and atmospheric pressure in a 2.5cm I.D. tube. Although there are wide discrepancies in the location of the curves, the present criterion predicts intermediate location of the transition boundary. The discrepancy will be attributed mainly to the definition of the bubbly flow, that is, whether the bubbly flow includes cap bubbles or not. For example, the curve by Duns and Ros[6] corresponds to the boundary between Region I and II, following their terminology. According to their definition, Region I includes part of slug flow as defined by Govier and Aziz [2]. This may be the reason why the curve by Duns and Ros is located at relatively high gas velocity. Taking into account these fact, the comparison shown in Fig. 5 seems reasonable.

Figure 6 shows the boundaries for the slug-to-churn flow transition for air-water flow at 25°C and atmospheric pressure in a 2.5cm I.D. tube. The agreement between the present theory and the curve by Govier and Aziz [2] is good and the general trends of the curves which appear in the figure is well reproduced by the theory, except that some of the curves tend to depart from the others at high liquid superficial velocity. This discrepancy may be attributed to the difficulty in

discriminating between the churn and slug flow at higher liquid velocities.

The curves for the churn-to-annular flow transition are shown in Fig. 7. A remarkably good agreement is observed in the figure.

Figure 8 compares the present theory with the flow regime map by Govier and Aziz [2]. Overall agreement is reasonable. Figure 9 shows a good agreement between the present criteria and those of Dukler and Taitel [11]. This agreement is not surprising because the basic principles involved in defining the transition criteria are similar. Figure 10 shows the comparison between the present theory and that of Taitel et al. [12] In the bubbly flow region, they proposed the transition B above which finely dispersed bubbles exist, which the present theory does not distinguish. The transition A and C may correspond to the curve for the bubbly-to-slug flow transition by the present theory, although Taitel et al. [12] postulated the void fraction at the transition to be 0.25 for transition A and 0.52 for transition C instead of 0.3 in the present theory. There is a large disagreement in the boundary between the slug and churn flow at higher liquid volumetric fluxes. This may be attributed to the difference in the proposed basic mechanism of the slug-to-churn flow transition. That is, Taitel et al. characterized the churn flow as an entry region phenomenon associated with the existence of slug flow further along the pipe, whereas the present theory characterizes it as highly agitated Taylor bubbles and aerated liquid slugs at increased void fraction. In addition to this, it is very difficult to visually discriminate between these flow regimes at higher liquid velocities, as pointed out by Taitel et al. [12] Finally, the transition E corresponds to the boundary of annular flow which

agrees very well with the present criterion.

II.3.2. Steam-water Flow at High Pressures

As most of the maps for vapor-liquid flow are drawn as a relationship between the mass velocity G and the equilibrium vapor quality $x_e$, the theoretical maps in $j_g - j_f$ plane are transformed into those in $x_e - G$ plane. In those cases, the equilibrium vapor quality and the mass velocity are calculated by the following equations.

$$G = \rho_g j_g + \rho_f j_f \quad , \tag{38}$$

and

$$x_e = \rho_g j_g / G \quad . \tag{39}$$

The present theory is compared to the data of Bergles et al. [19] and Bennet et al. [20] for steam-water flow at high pressures in round tubes. Typical comparisons are shown in Figs. 11 and 12. The data were reproduced from the reference [19] in Fig. 11 together with the present flow maps in terms of the mass velocity and the exit vapor quality. The figure demonstrates fairly good agreement between the data and the present criteria. At high mass velocities, the froth flow was observed by Bergles et al. [19] This flow regime appears in the part of the annular flow region where the void fraction is rather low ($0.3 < \alpha < 0.7$) according to the present calculation. Here the region A on the present flow map, where the flow may behave like a highly agitated churn flow, may correspond to the froth flow regime.

The maps can also be plotted in terms of the superficial velocities

of both phases as shown in Fig. 13. As the experimental data are originally plotted in terms of the mass velocity versus equilibrium vapor quality, the superficial velocities for the data points are calculated from those parameters by assuming thermal equilibrium. However, provided that the subcooling is not very large, the calculated superficial velocities will be good estimates of the true values. It is interesting to note, by comparing Fig. 12 with, say, Fig. 8, that the locus of the curve for the bubbly-to-slug flow transition moves toward lower gas velocities at higher pressures.

An example of the map affected by subcooled boiling is shown in Fig. 14. The broken lines represent the transition boundaries reproduced from the data of Bergles et al. [19] for 3.4 MPa steam-water flow in a 29.9mm I.D. tube. The curves turn away from the theoretical map as the mass velocity is increased.

The figure shows that the use of thermal equilibrium quality may not be accurate for flow regime map when subcooled boiling occurs at higher mass velocities. In the present theory, the criteria for the flow regime transition are correlated in terms of the void fraction and the volumetric fluxes. In view of this, flowing quality will be more relevant to use in plotting the experimental data in the flow map [21] for non-equilibrium flow. The data in Fig.14 can be transformed to the map shown by the broken lines in which the flowing quality was estimated by using the Levy correlation [22] together with the Bowring correlation [23] for the subcooling at the point of bubble detachment. The dotted solid-line represents the bubbly-to-slug flow transition based on the thermal equilibrium quality. The figure shows the relevance of the use of the flowing quality in non-equilibrium (subcooled boiling) flow.

The comparison of the theory with the data for high pressure steam-water flow in a rectangular channel is presented in Figs. 15-19. The data were reproduced from the reference [24]. In these figures, the data are plotted in terms of mass velocity versus flowing quality. Hosler used flowing quality instead of thermal equilibrium quality in order to account for subcooled boiling and for some of the effects of heat flux, as mentioned by himself [24]. Those figures indicate that the general trends are very similar to those for steam-water flows in round tubes and are predicted reasonably well by the present theory, except that the agreement of the bubbly-to-slug flow transition is disappointing at 1.0 MPa. However, Hosler himself limited the applicable range of pressure to 2 to 14 MPa for use of his data with reasonable confidence.

The theory can be compared to those data in terms of the superficial velocities, too. The example is presented in Fig. 20. The theoretical flow regime maps indicate that the slug-to-annular flow transition occurs at lower gas velocities with increasing pressure, although the trend is less remarkable in the experimental data.

## II.4. SUMMARY AND CONCLUSIONS

New flow-regime criteria have been developed for a vertical upward flow, using direct geometrical parameters such as the void fraction. These new criteria can be compared to existing data under steady-state and fully-developed flow conditions by using relative velocity correlations obtained by Ishii [14].

Newly developed criteria have been compared with the conventional criteria and experimental data for atmospheric pressure air-water flows and high pressure steam-water flows in round tubes and a rectangular

channel. There exist wide discrepancies among the experimental data, not only due to the different methods of observations and definitions of the flow regimes but also due to the transition phenomena themselves which develop gradually. However, when these factors are considered, it should be said that the present criteria showed satisfactory agreements with those data.

It is also pointed out that the flowing quality is more suitable than the thermal equilibrium quality to correlate the flow regime transitions for a subcooled-boiling system. This is consistent with the statement that the void fraction should be used in flow regime criteria.

## NOMENCLATURE

$A$ : Flow area

$a$ : Non-dimensional group defined by Eq.(20)

$b$ : Dimensional group defined by Eq.(21)

$C_f$ : A constant

$C_0$ : Distribution parameter

$D$ : Hydraulic diameter

$f$ : Wall friction factor

$G$ : Mass velocity of two-phase mixture

$g$ : Gravity

$h$ : Distance from the nose of a slug bubble

$j$ : Volumetric flux (superficial velocity) of two-phase mixture

$j_k$ : Superficial velocity of k phase (k=g or f)

$L$ : Gap between two bubbles

$L_b$ : Mean slug bubble length

$m$ : A constant

$N_{\mu f}$ : Viscosity number

$p$ : Pressure

$r_b$ : Mean bubble radius

$v_{fsb}$ : Terminal film velocity in the slug-bubble section

$v_{gs}$ : Gas velocity in the slug bubble

$X$ : Parameter defined by Eq.(12)

$x_e$ : Thermal equilibrium quality

$y$ : Dimensional group defined by Eq.(25)

### Greek symbols

$\alpha$ : Void fraction

$\alpha_m$ : Mean void fraction

$\alpha_{sb}$ : Void fraction corresponding to the terminal film velocity $v_{fsb}$

$\Delta\rho$ : Absolute value of density difference

$\mu_f$ : Viscosity of liquid

$\nu_f$ : Kinematic viscosity of liquid

$\rho_k$ : Density of k phase (k=g or f)

$\sigma$ : Surface tension

Subscripts

b : Bubble

e : Thermal equilibrium

f : Liquid phase or friction

g : Gas phase

m : Mean

s : Slug bubble

sb : Tail-end of the slug bubble

## REFERENCES


[1] V.C. Sternling, "Two phase flow theory and engineering decision," award lecture presented at AIChE Annual Meeting, (Dec. 1965).

[2] G.W. Govier and K. Aziz, The flow of complex mixtures in pipes, Van Nostrand Reinhold, New York (1972).

[3] G.B. Wallis, One-dimensional two-phase flow, McGraw-Hill, New York (1972).

[4] G.F. Hewitt and D.N. Roberts, Studies of two-phase flow patterns by simultaneous X-ray and flash photography, UKAEA Report AERE-M2159 (1969).

[5] P. Griffith and G.B. Wallis, "Two-phase slug flow," J. Heat Transfer, 3, p.307 (1961).

[6] H. Duns, Jr. and N.C.J. Ros, "Vertical flow of gas and liquid mixtures from borcholes," Proc. 6th. World Petroleum Congress, Frankfurt (1963).

[7] T.L. Gould, "Vertical two-phase steam-water flow in geothermal wells," J. Petroleum Tech., 26, p.833 (1974).

[8] P.L. Spedding and V.T. Nguyen, "Regime maps for air water two phase flow," Chem. Engng. Sci., 35, p.779 (1980).

[9] J. Weisman and S.Y. Kang, "Flow pattern transitions in vertical and upwardly inclined lines," Int. J. Multiphase Flow, 7, p.271 (1981).

[10] A.E. Dukler and Y. Taitel, Flow regime transitions for vertical upward gas liquid flow : A preliminary approach through physical modeling, Progress report No.1, NUREG-0162, (1977).

[11] A.E. Dukler and Y. Taitel, Flow regime transitions for vertical upward gas liquid flow, Progress report No.2, NUREG-0163 (1977).

[12] Y. Taitel, D. Barnea and A.E. Dukler, "Modeling flow pattern transitions for steady upward gas-liquid flow in vertical tubes," AIChE J., 26[3], p.345 (1980).

[13] G.F. Hewitt and N.S. Hall-Taylor, Annular two-phase flow, Pergamon Press (1970).

[14] M. Ishii, One-dimensional drift-flux model and constitutive equations for relative motion between phases in various two-phase flow regimes, ANL Report ANL-77-47 (1977).

[15] N.A. Radovicich and R. Moissis, The transition from two-phase bubble flow to slug flow, MIT Report No.7-7633-22 (1962).

[16] P. Griffith and G.A. Snyder, A bubbly-slug transition in a high velocity two-phase flow, MIT Report No.5003-29 (1964).

[17] K. Akagawa, H. Hamaguchi and T. Sakaguchi, "Studies on the fluctuation of pressure drops in two-phase slug flow (Third report, Pressure recovery behind a bubble, and bubble and liquid slug lengths)," Trans. JSME, 36[289], p.1535 (1970).

[18] T. Oshinowo and M.E. Charles, "Vertical two-phase flow : Part II. Holdup and pressure drop," Can. J. Chem. Engng., 56, p.438 (1974).

[19] A.E. Bergles, J.P. Roos and J.G. Bourne, Investigation of boiling flow regimes and critical heat flux, NYO-3304-13 (1968).

[20] A.W. Bennet, G.F. Hewitt, H.A. Kearsey, R.K.F. Keeys and P.M.C. Lacey, Flow visualization studies of boiling at high pressure, UKAEA Report AERE-R4874 (1965).

[21] K. Sekoguchi, O. Tanaka, S. Esaki, N. Katsuki and M. Nakasatomi, "Prediction method of flow patterns in subcooled and low quality boiling regions," Trans. JSME, 46[409], p.1825 (1980).

[22] S. Levy, "Forced convection subcooled boiling -- Prediction of

vapor volumetric fraction," Int. J. Heat Mass Transfer, 10, p.951 (1967).

[23] R.W. Bowring, Physical model based on bubble detachment and calculations of steam voidage in the subcooled region of a heated channel, Report HPR-10, OECD Halden Report Project (1962).

[24] E.R. Hosler, "Flow patterns in high pressure two-phase (steam-water) flow with heat addition," Chem. Engng. Prog. Symp. Series, No.82, Vol.64, P.54 (1968).

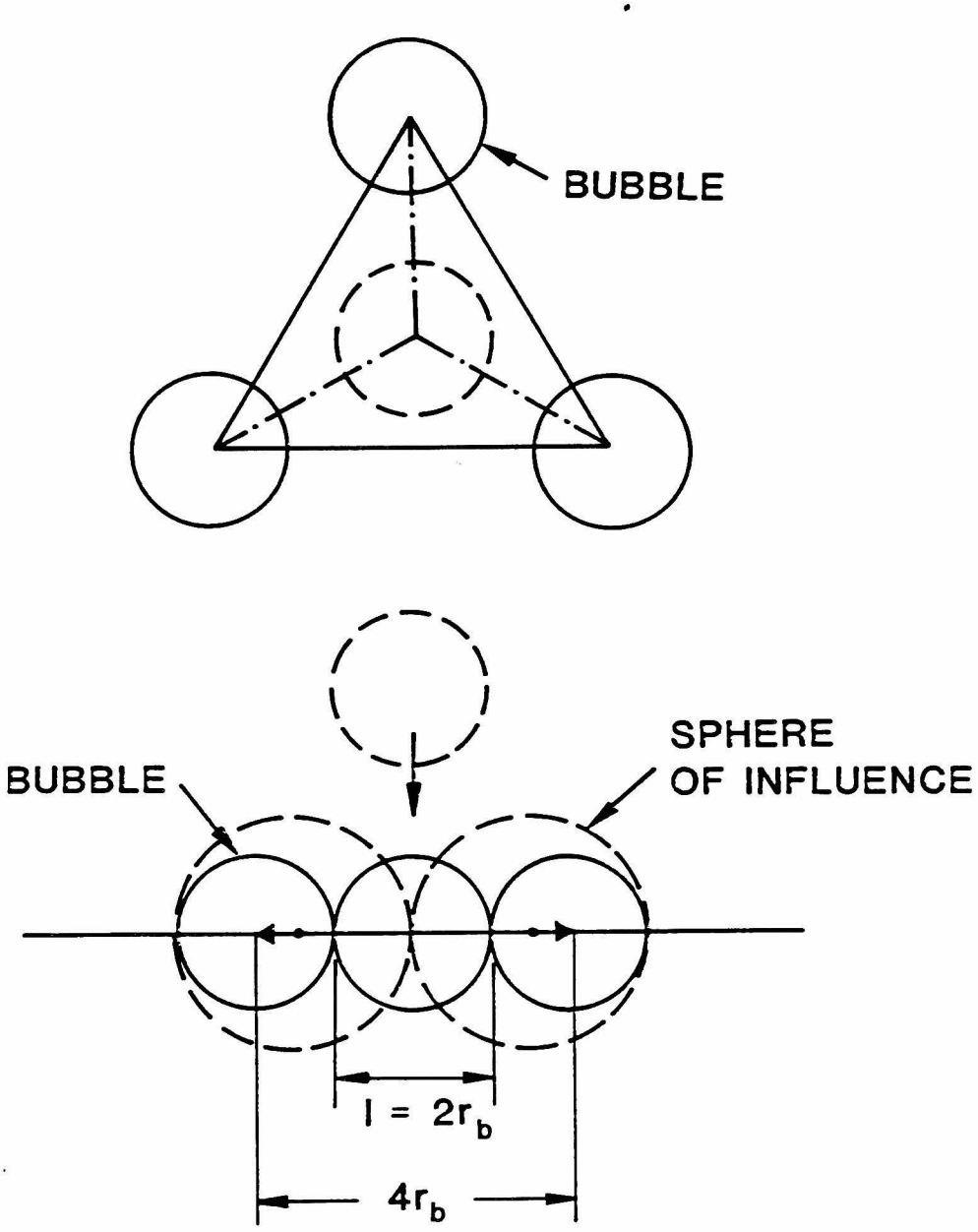


Figure 1 Bubble packing and coalescence pattern.

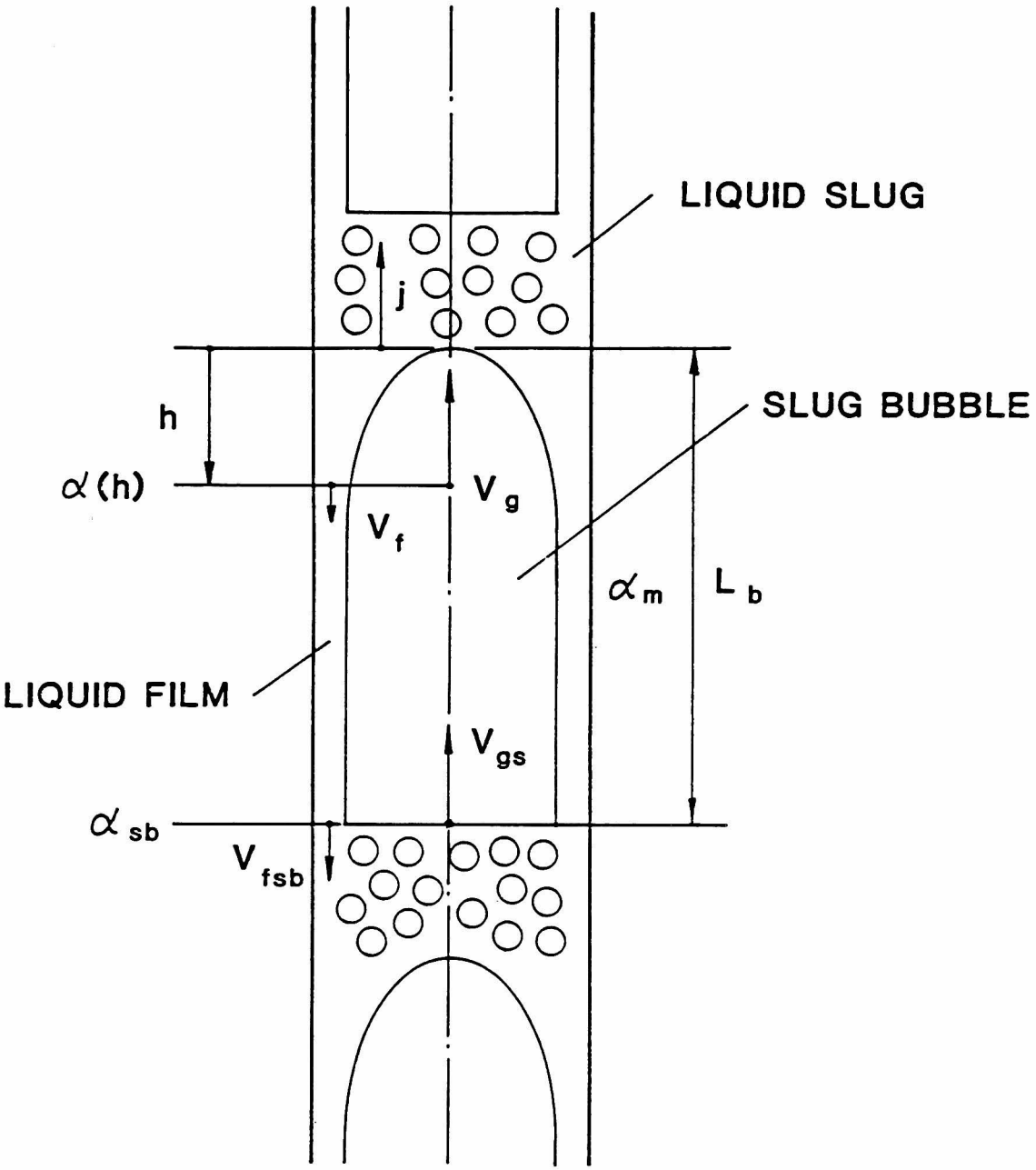


Figure 2 Slug flow model.

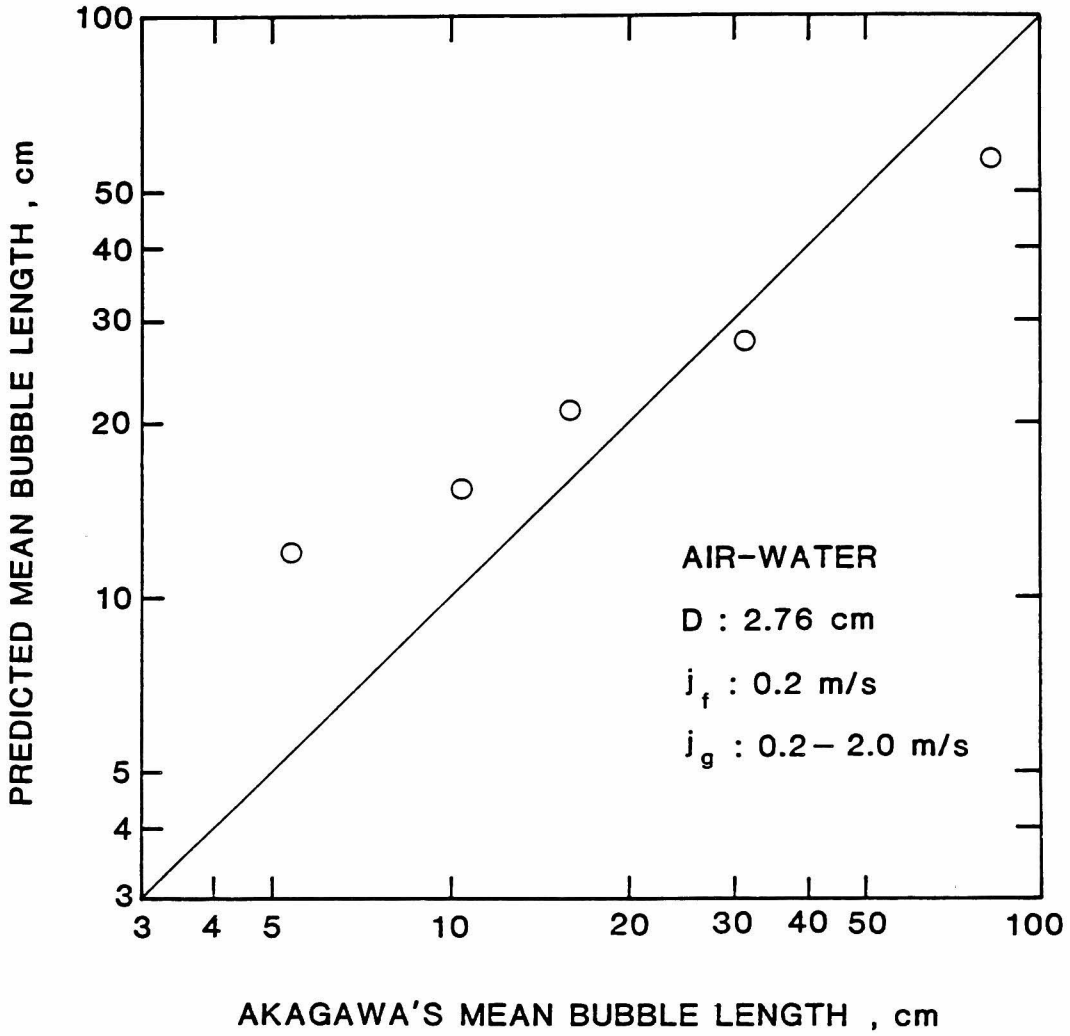


Figure 3 Comparison of mean bubble length to the experimental data by Akagawa et al. [17].

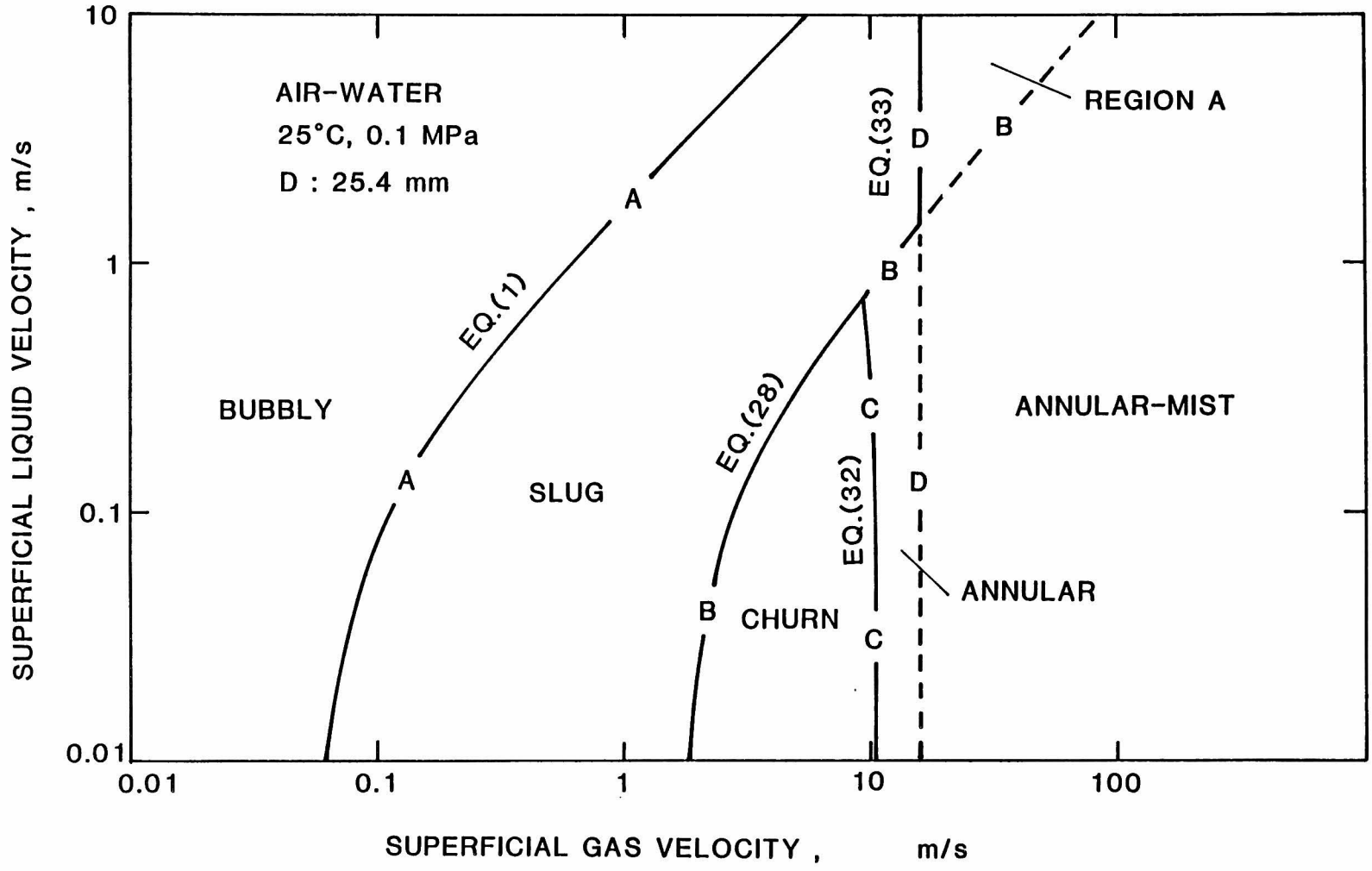


Figure 4 Flow regime map based on newly developed transition criteria.

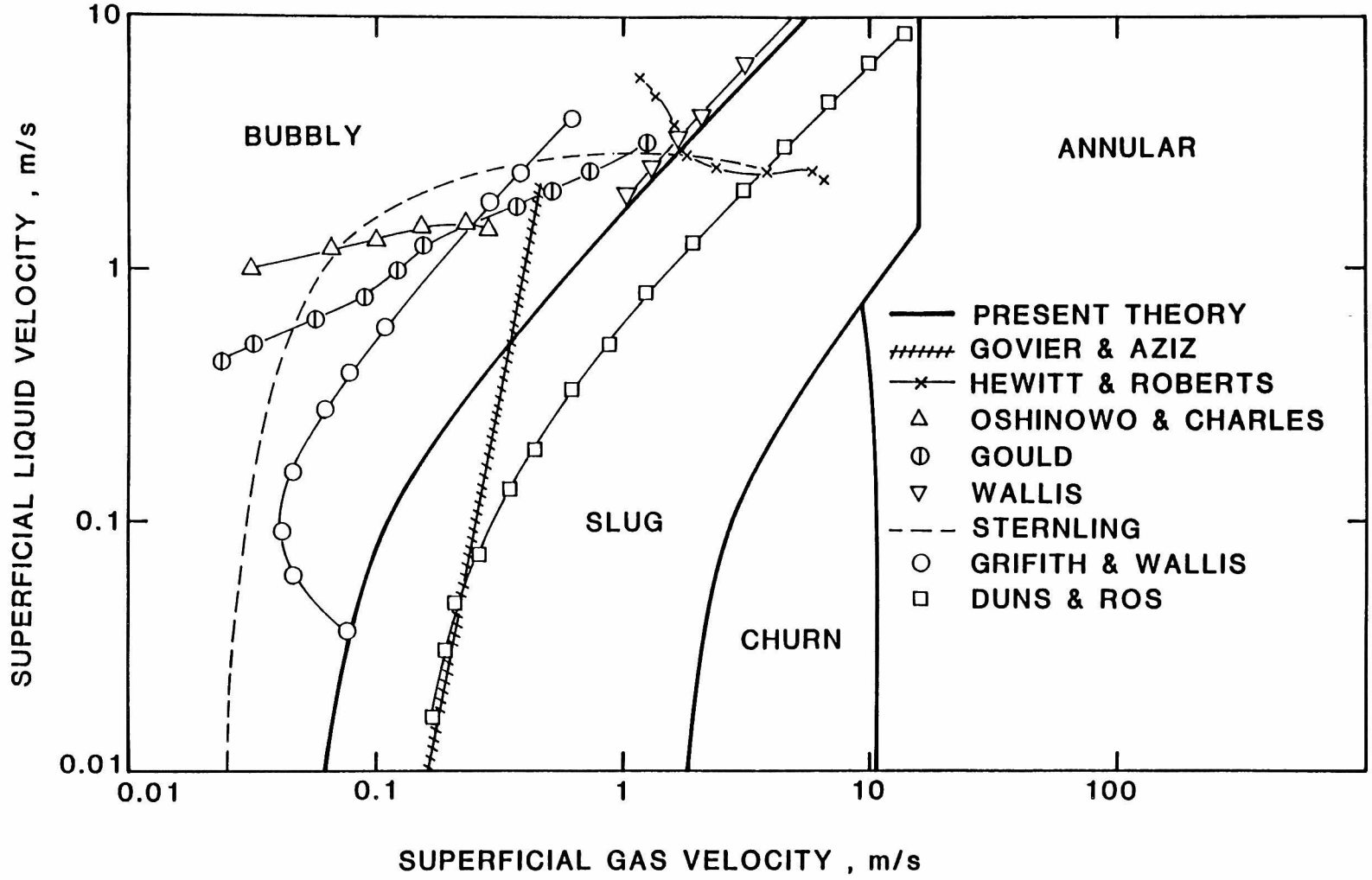


Figure 5 Comparison of the bubbly-to-slug flow transition for atmospheric air-water flow.

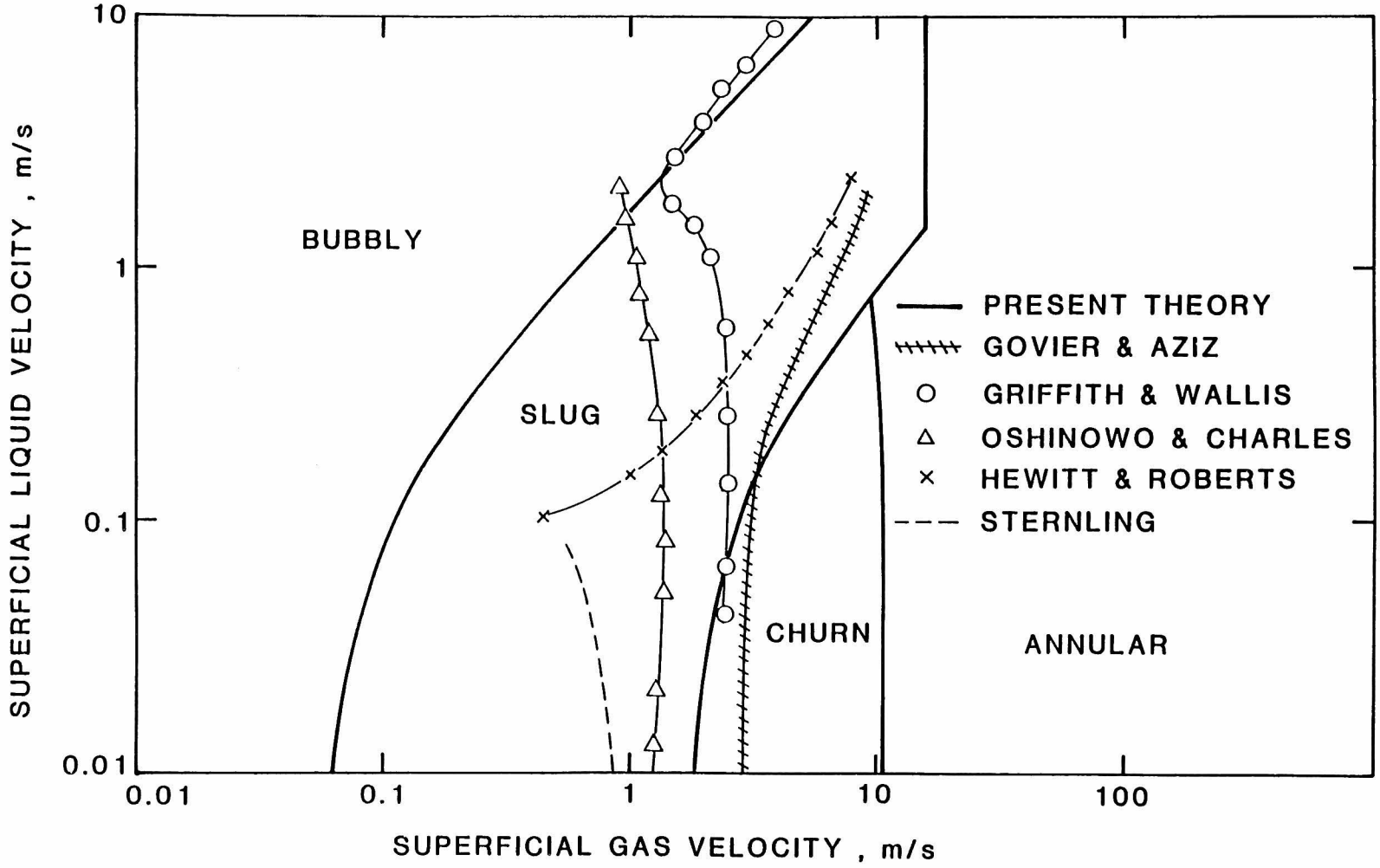


Figure 6 Comparison of the slug-to-churn flow transition for atmospheric air-water flow.

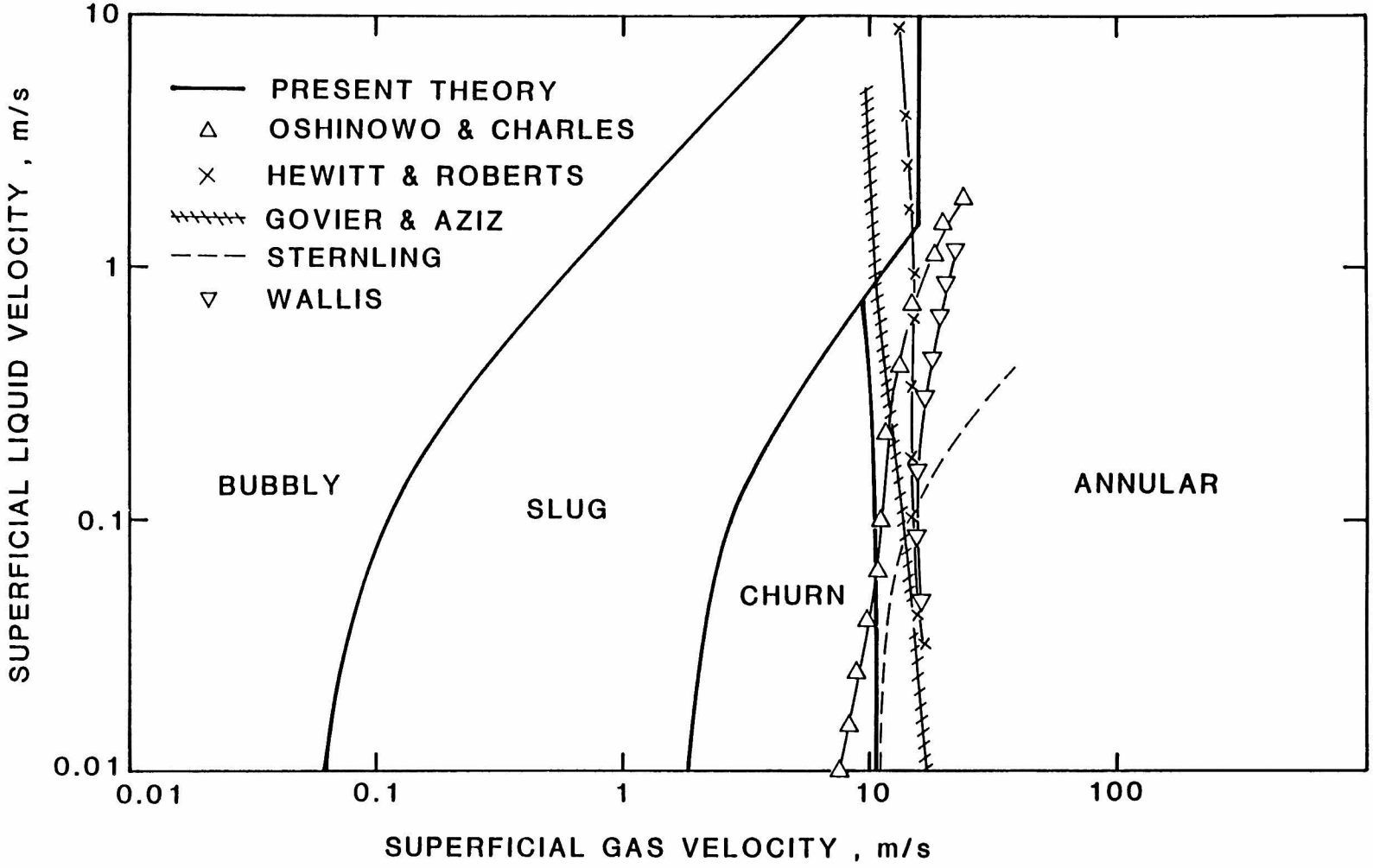


Figure 7 Comparison of the churn-to-annular flow transition for atmospheric air-water flow.

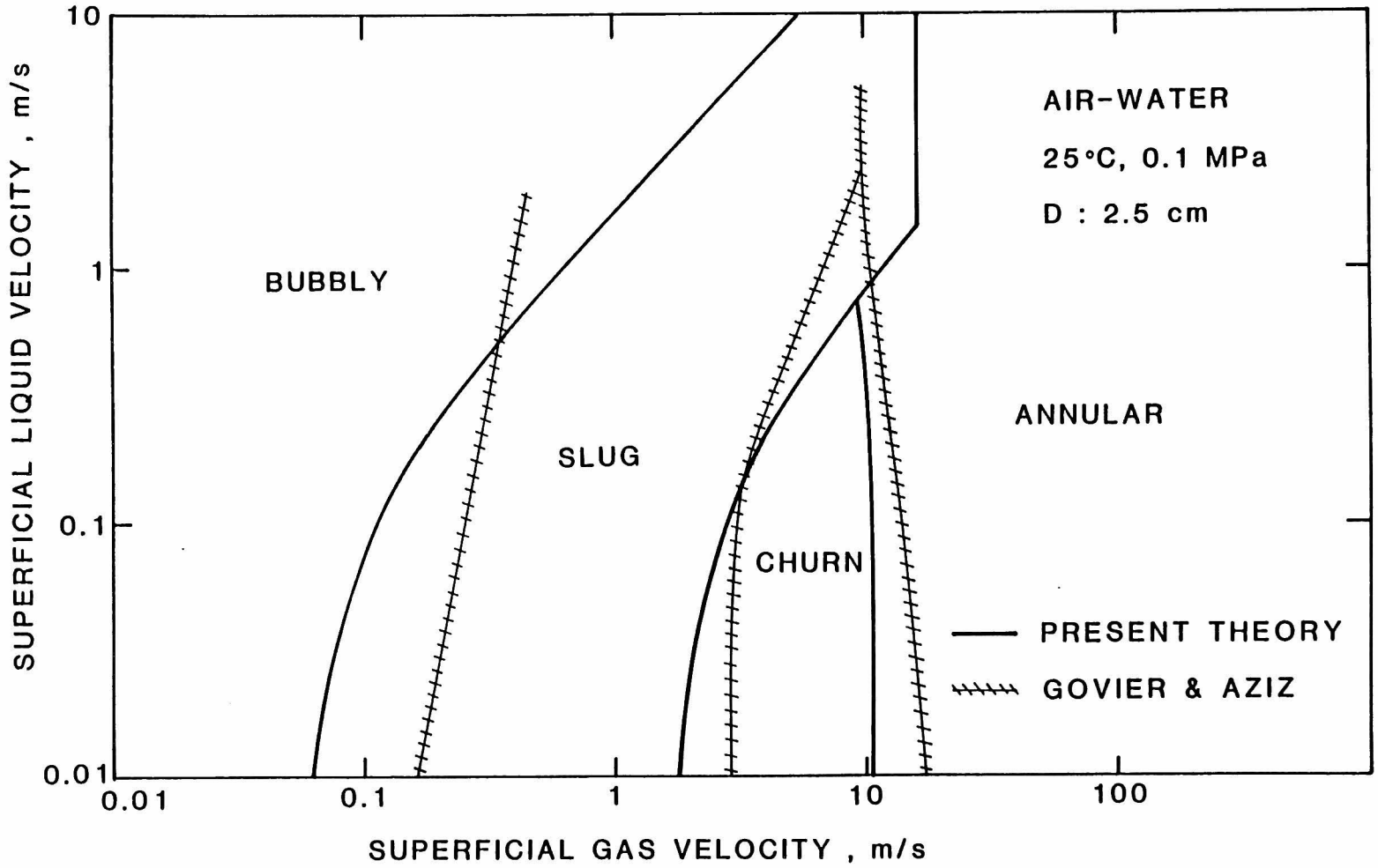


Figure 8 Comparison to the map of Govier and Aziz [2].

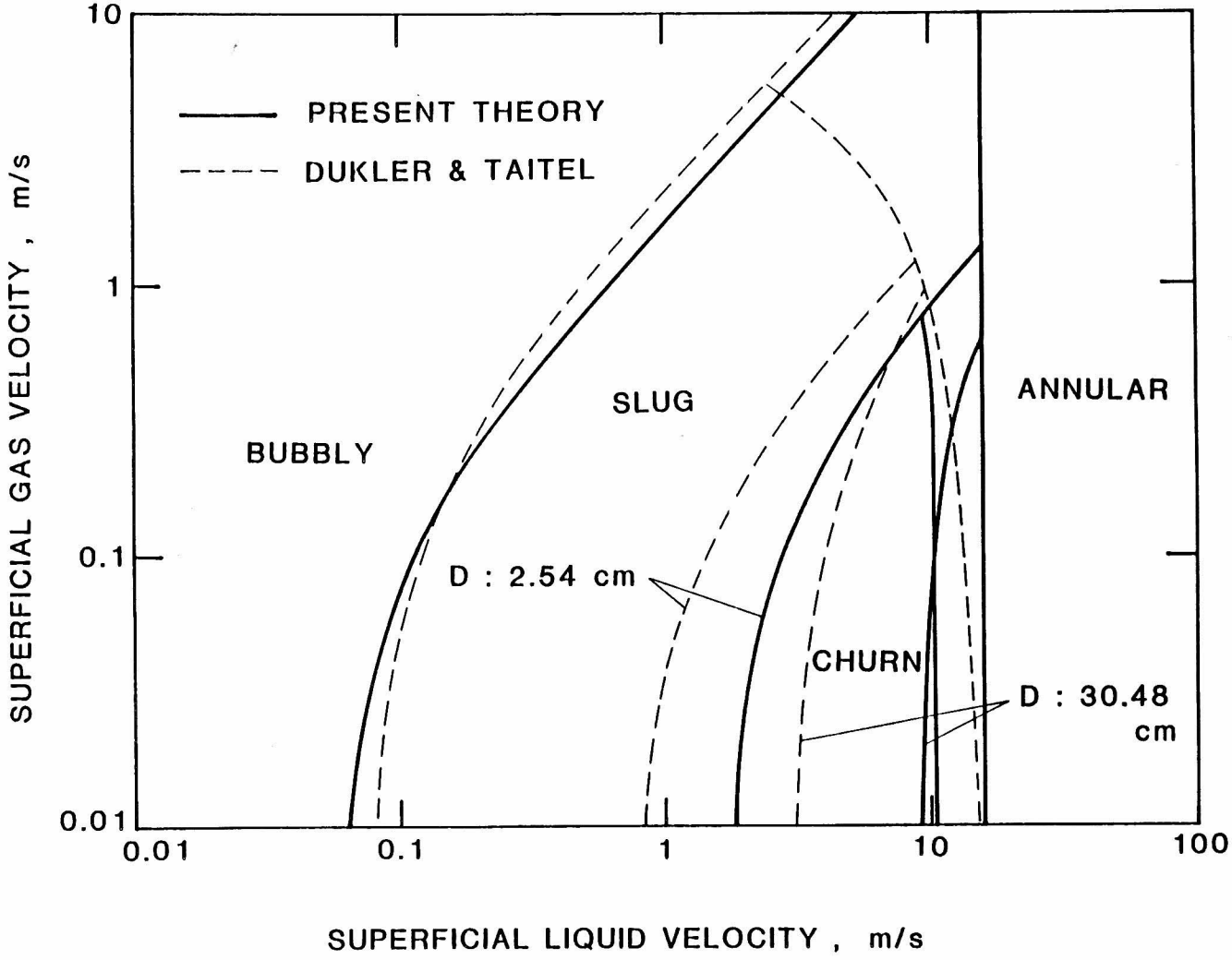


Figure 9 Comparison to the map of Dukler and Taitel [10].

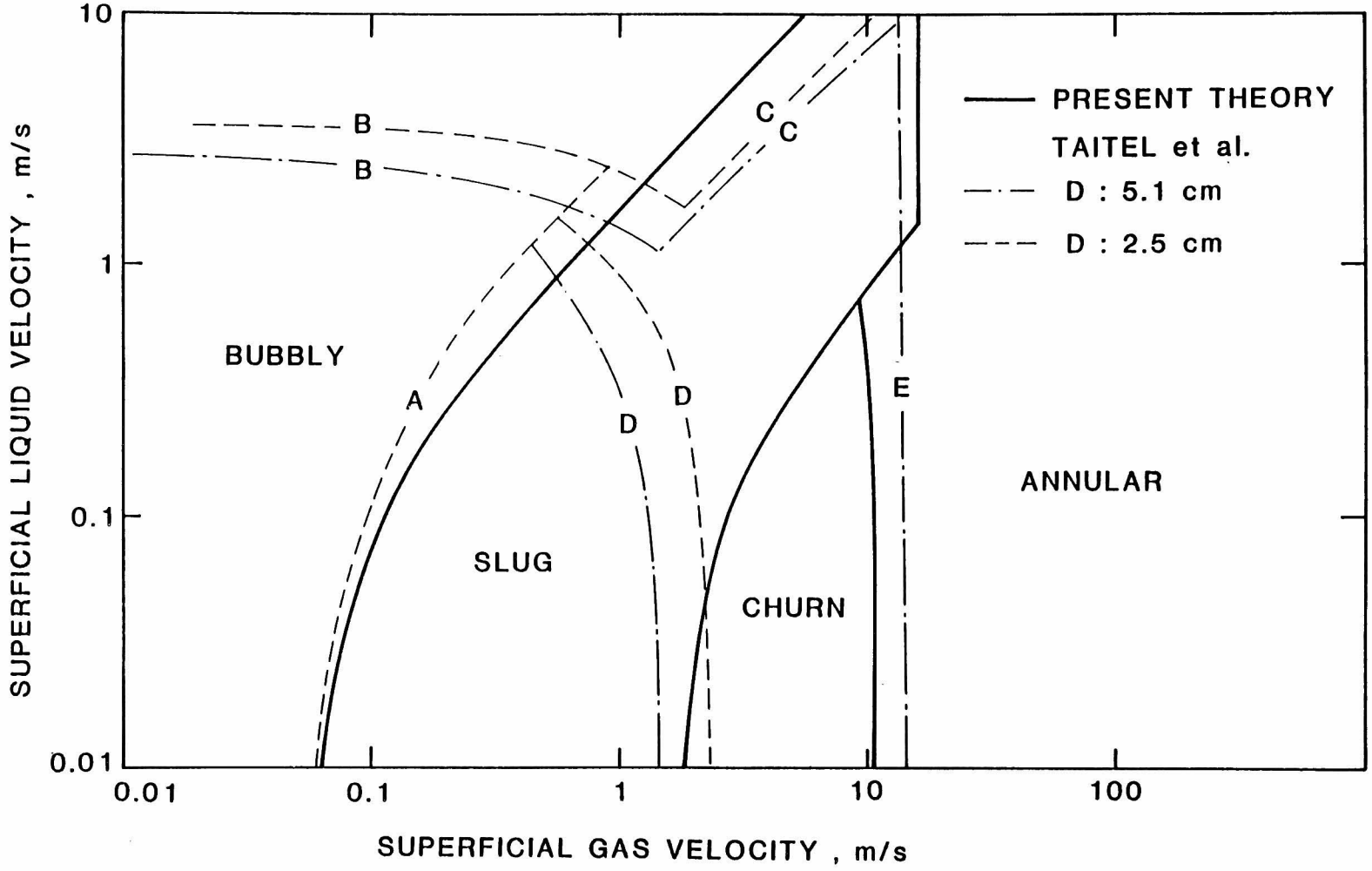


Figure 10 Comparison to the map of Taitel et al. [12] for water at 0.1 MPa and 25°C.

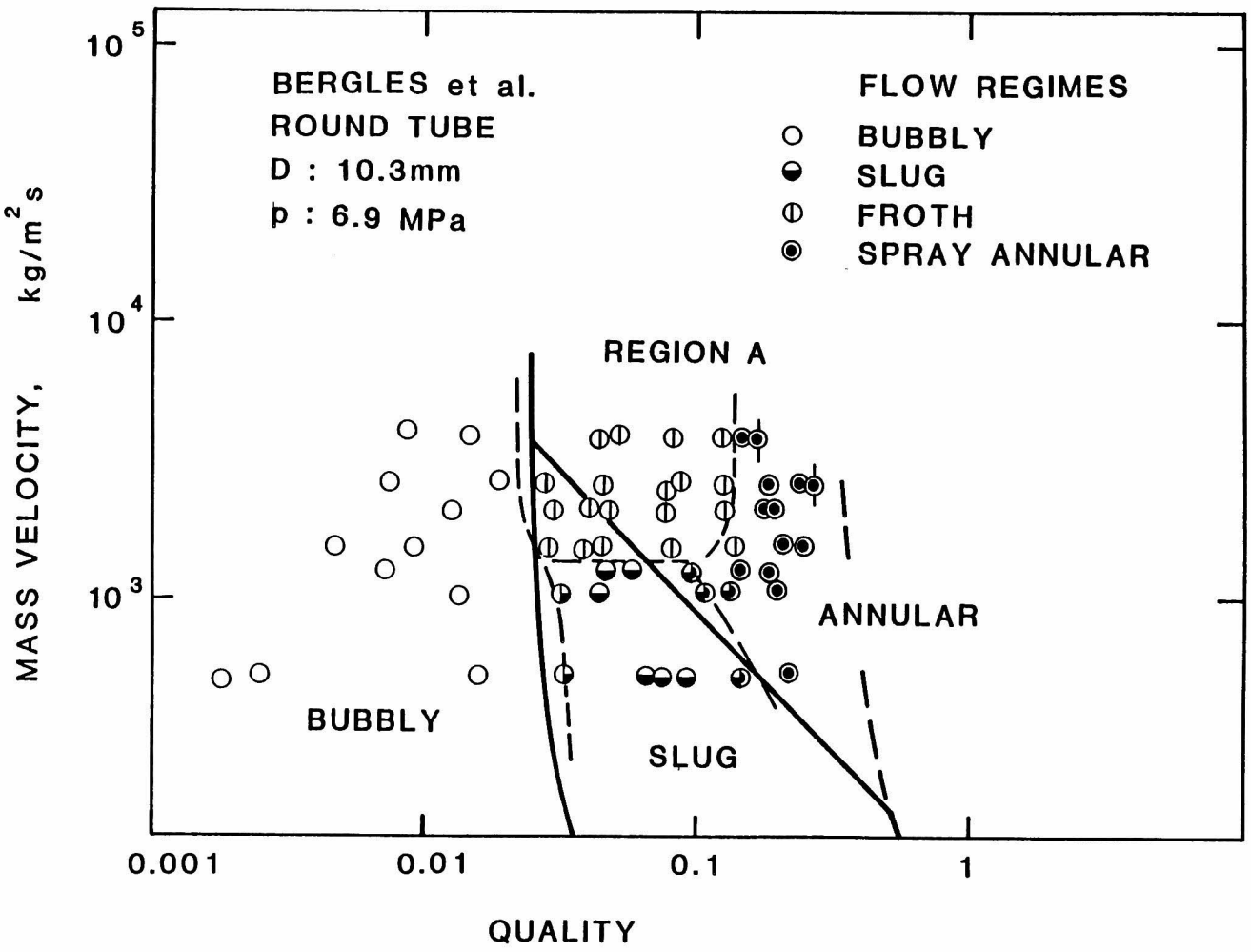


Figure 11 Flow regime map for steam-water flow at 6.9 MPa in a 10.3 mm ID tube, compared to the data of Bergles et al. [19].

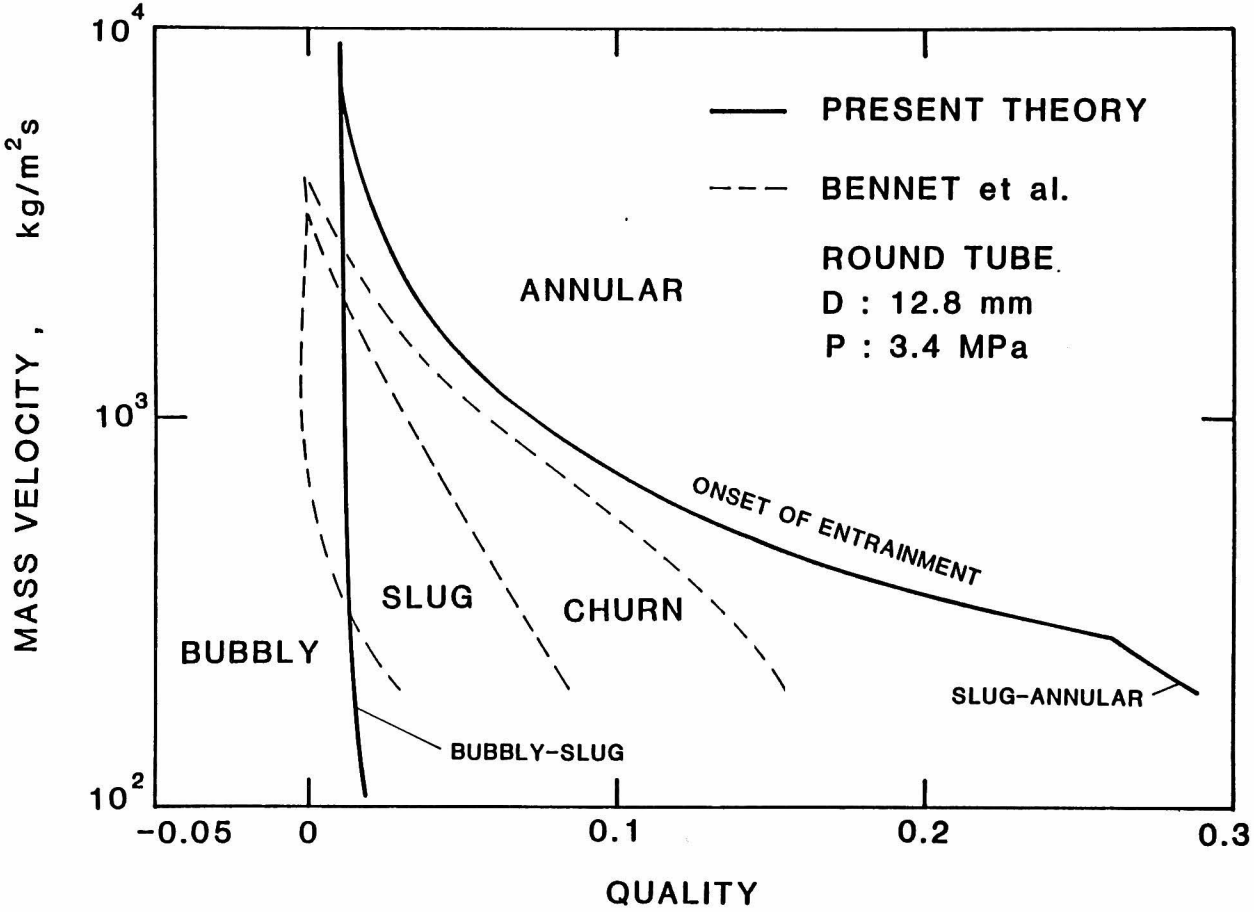


Figure 12 Semi-logarithmic flow regime map compared to the data of Bennet et al. [20] for subcooled flow boiling at 3.4 MPa.

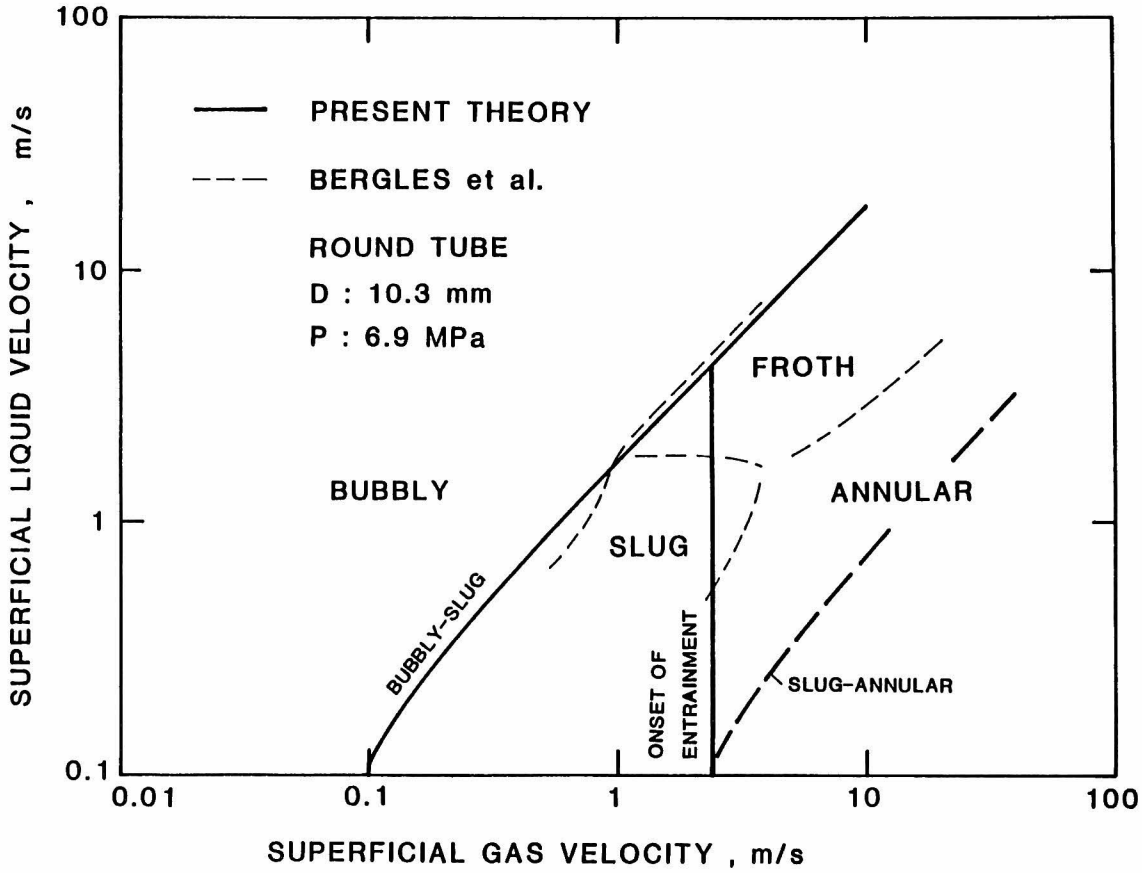


Figure 13 Comparison of the flow regime map in terms of the superficial velocities for steam-water flow at 6.8 MPa in a 10.3 mmID tube.

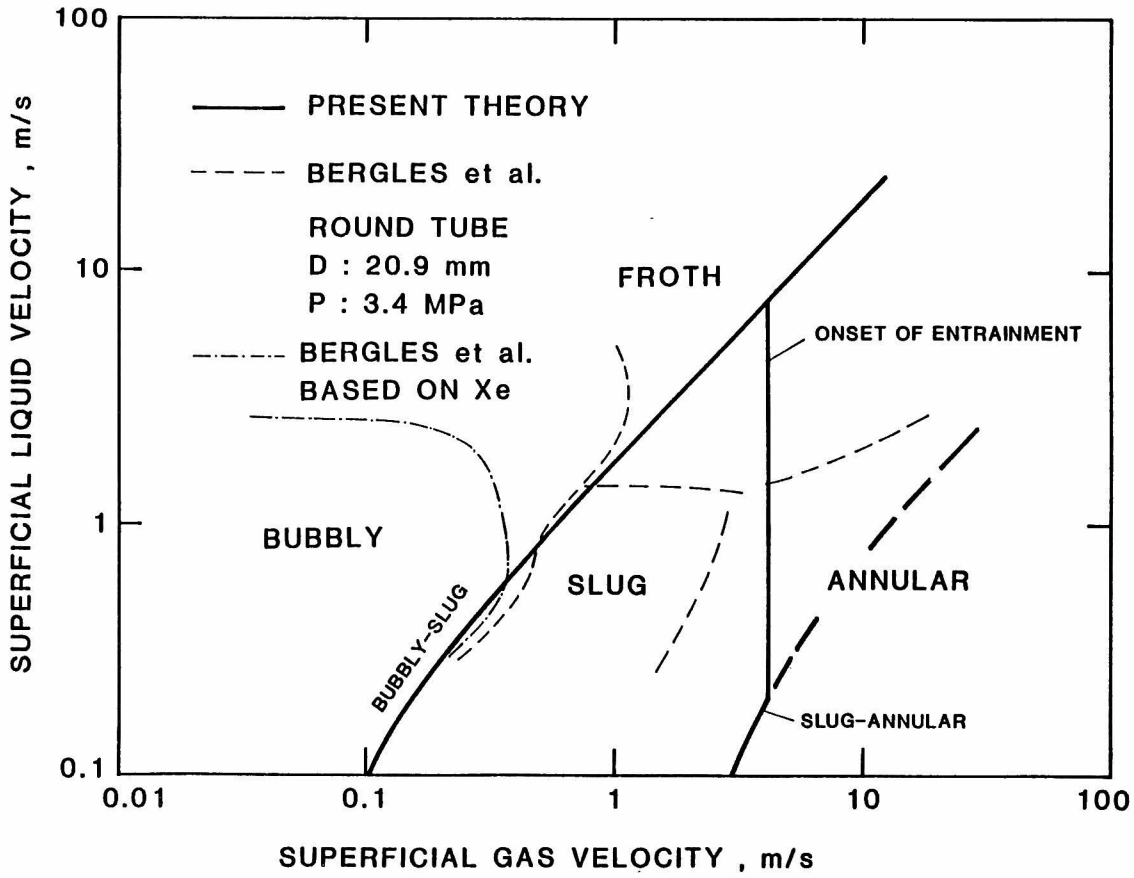


Figure 14 Comparison of the flow regime map in terms of the superficial velocities for steam-water flow at 3.4 MPa in a 20.9 mmID tube.

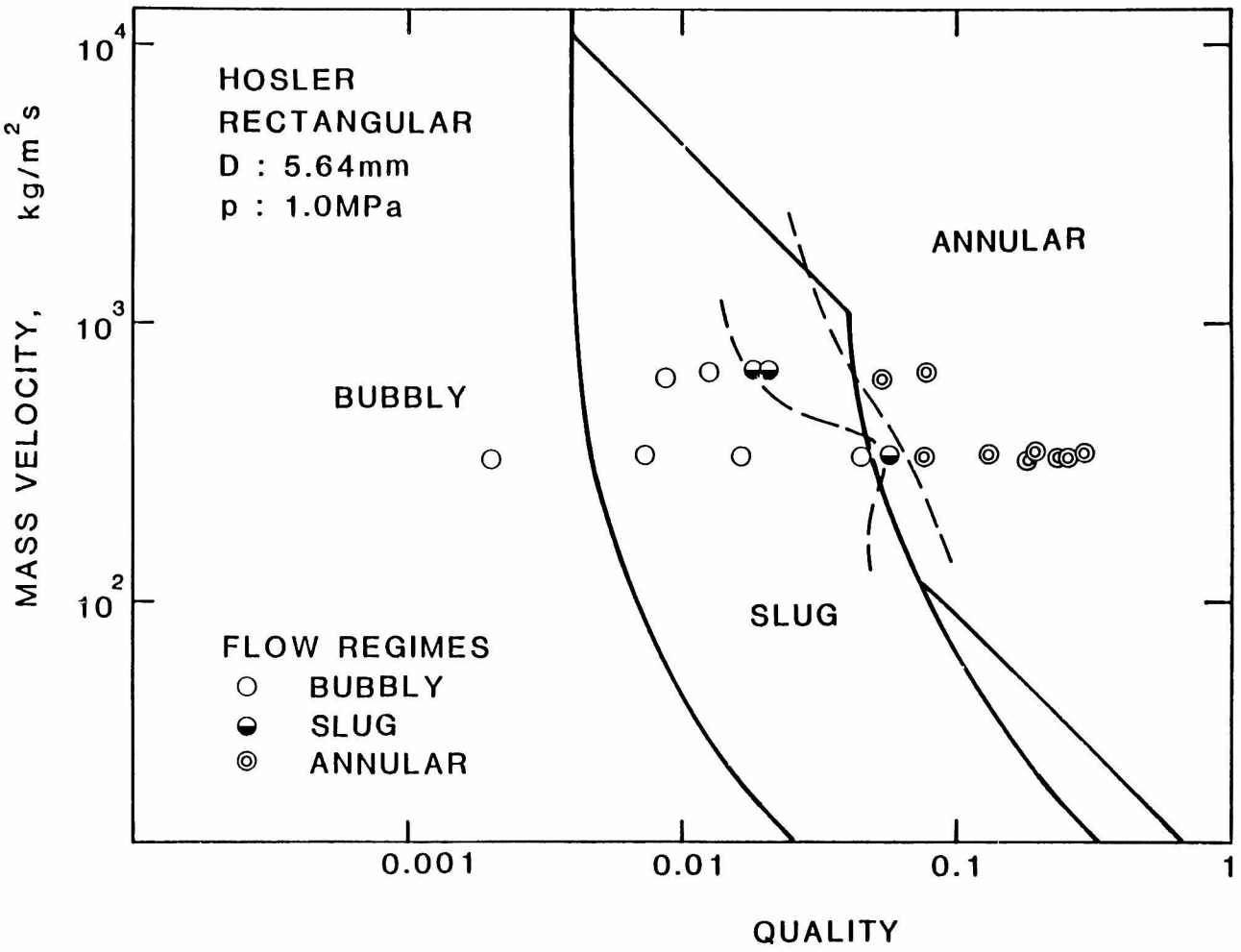


Figure 15 Comparison of the flow regime map for steam-water flow at 1.0 MPa in a rectangular channel (data taken by Hosler [24]).

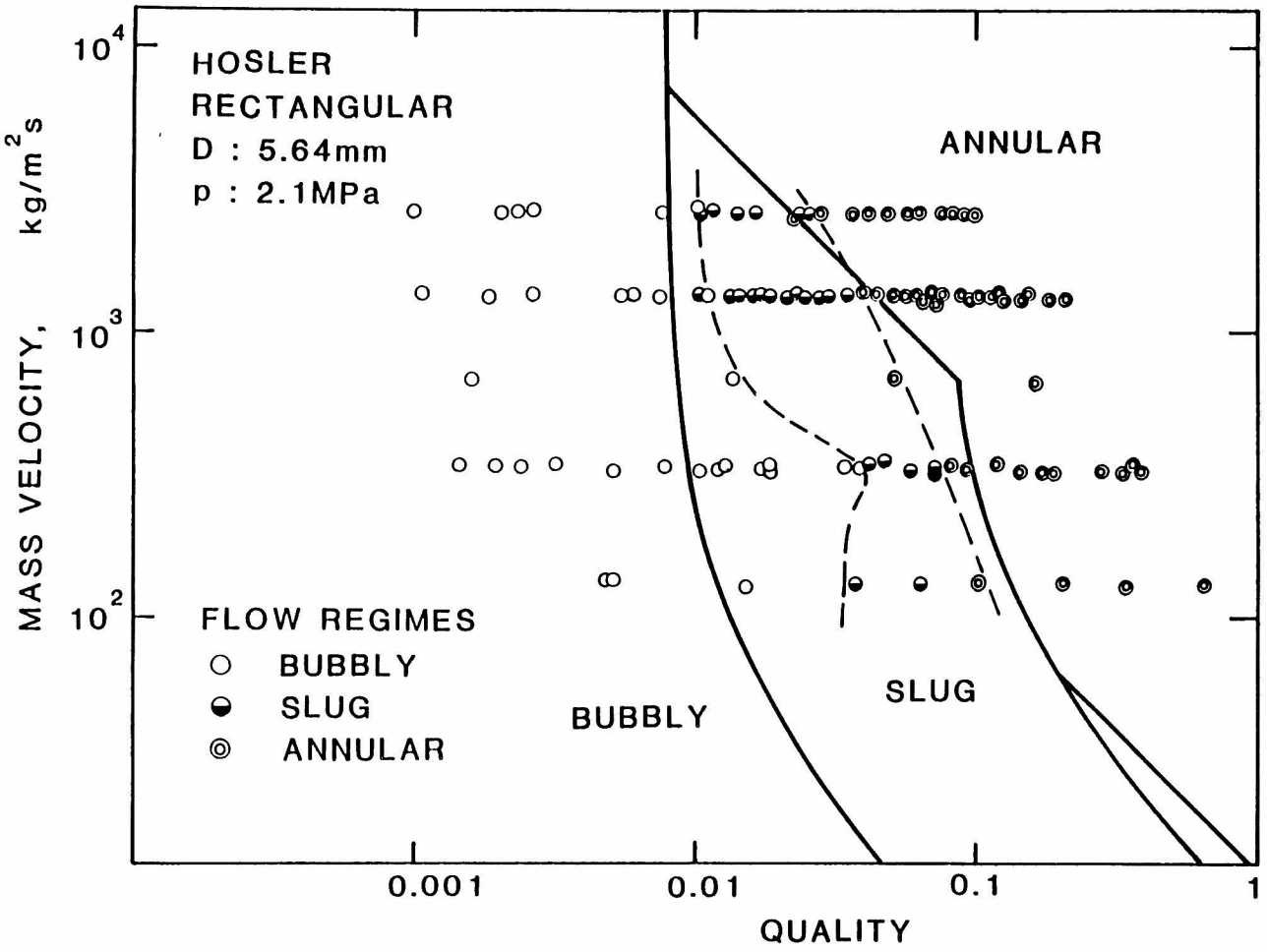


Figure 16 Comparison of the flow regime map for steam-water flow at 2.1 MPa in a rectangular channel (data taken by Hosler [24]).

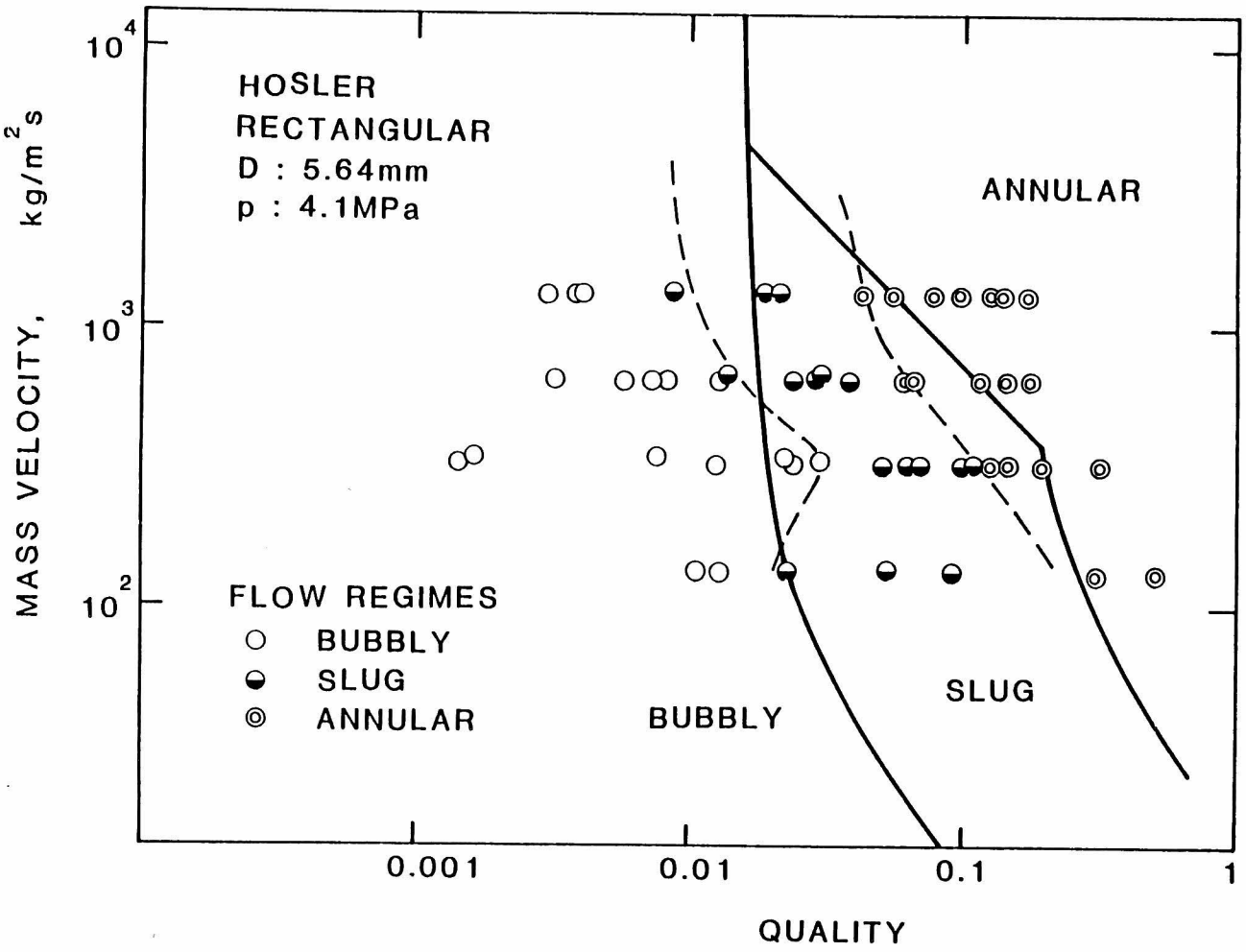


Figure 17 Comparison of the flow regime map for steam-water flow at 4.1 MPa in a rectangular channel (data taken by Hosler [24]).

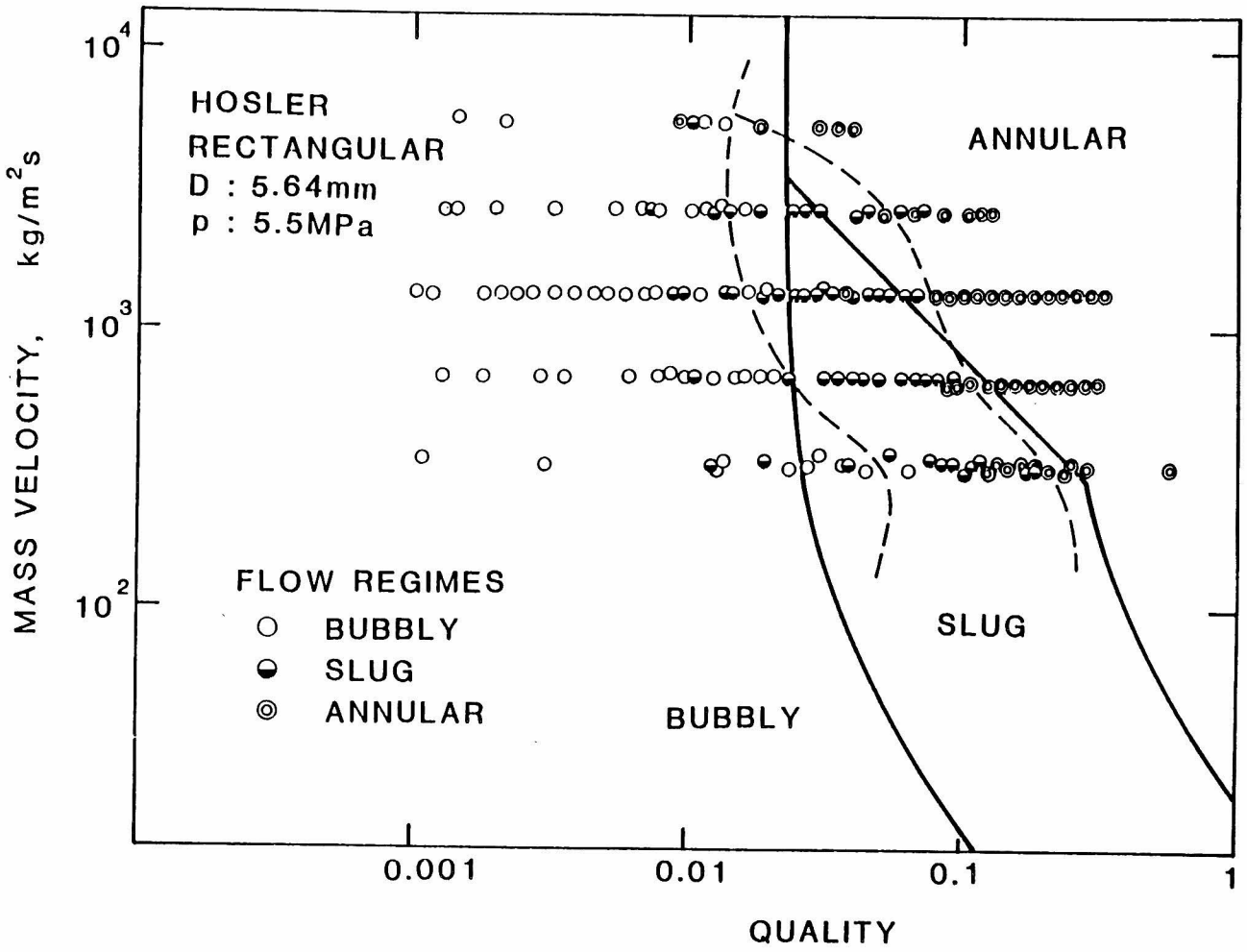


Figure 18 Comparison of the flow regime map for steam-water flow at 5.5 MPa in a rectangular channel (data taken by Hosler [24]).

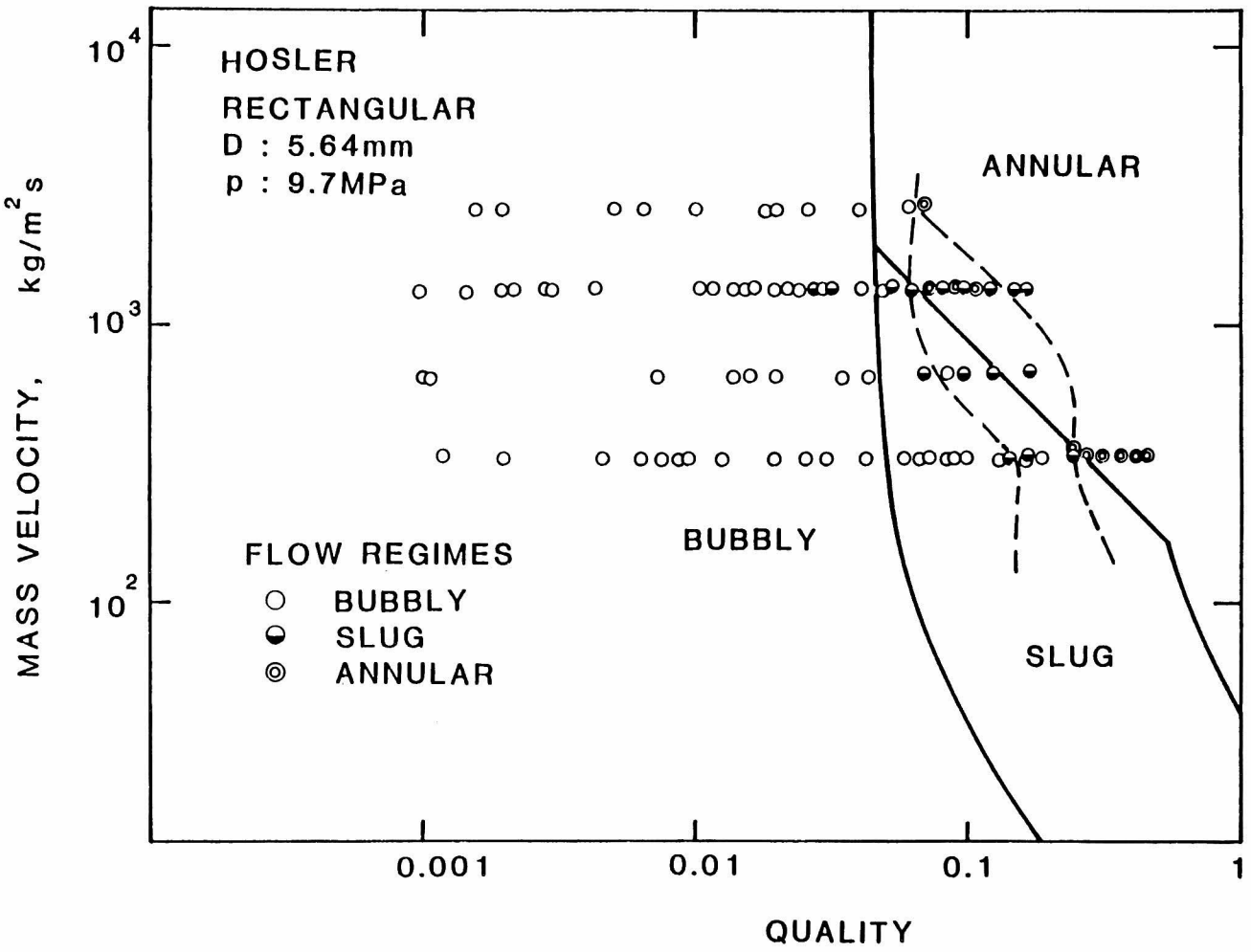


Figure 19 Comparison of the flow regime map for steam-water flow at 9.7 MPa in a rectangular channel (data taken by Hosler [24]).

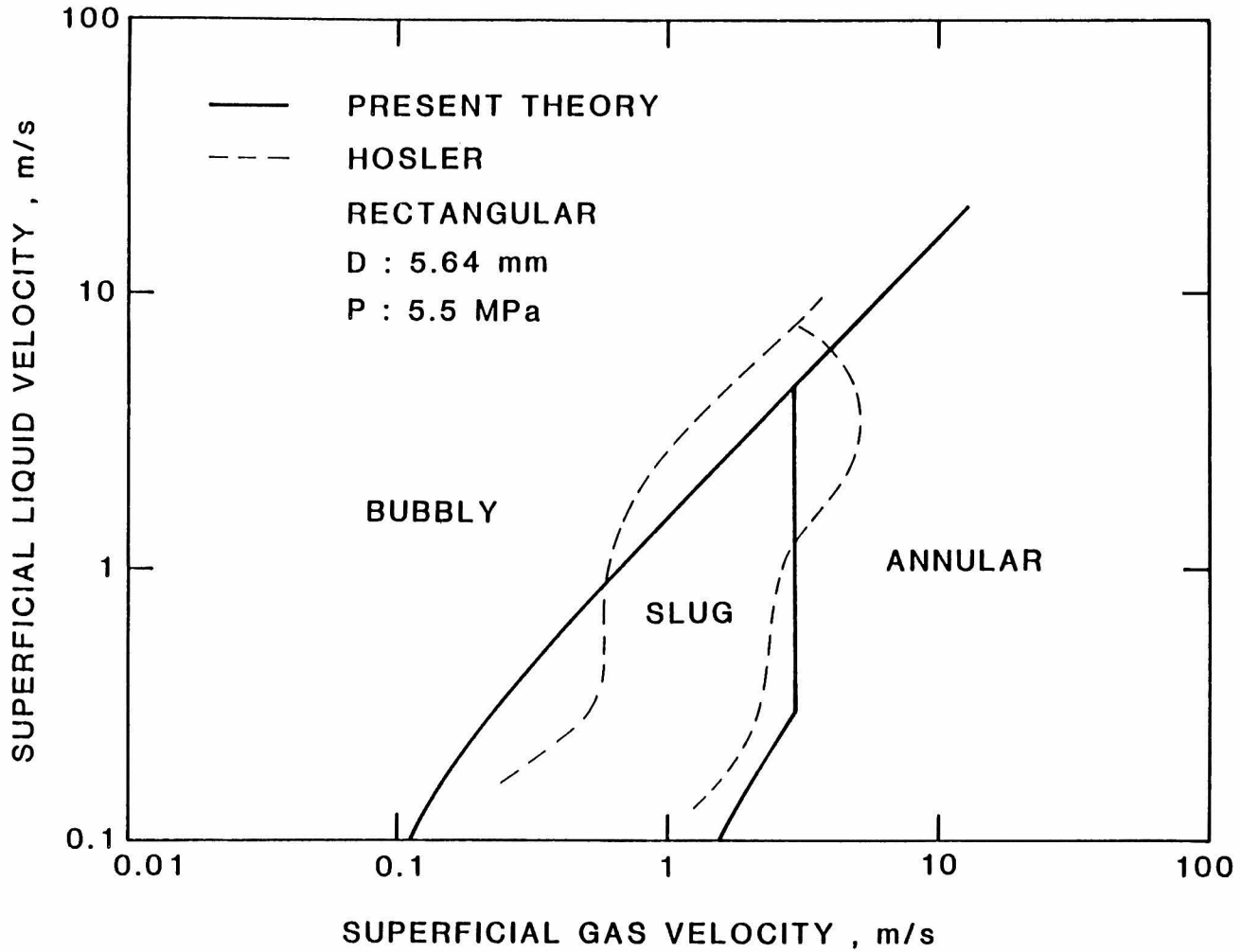


Figure 20 Flow regime map in terms of the superficial velocities for Hosler's data at 5.5 MPa [24].

# CHAPTER III.

# FLOODING AND FLOW REVERSAL

## III.1. INTRODUCTION

In a vertical countercurrent flow, the gas flows upward and the liquid downward. However, the range of the gas and the liquid flow rates in which the countercurrent flow appears is limited by the phenomena known as flooding or flow reversal [1], as illustrated in Fig. 1, i.e. if the gas flow rate is increased sufficiently, it limits the liquid flow rate. These phenomena have been studied extensively, earlier in chemical engineering industries in the interests of high heat and mass transfer rate encountered in chemical processes. Flooding and flow reversal are also important in thermosyphons because they impose the upper limit of heat transfer rate in such engineering equipments [2-8]. Recently, they have attracted the attention of many researchers in nuclear reactor applications with regards to the "countercurrent flow limitation (CCFL)" under loss of coolant accidents (LOCA) [9-15].

Many experimental and theoretical works have been performed on flooding and flow reversal phenomena in tubes [1,4,14-21]. The most widely used flooding correlation is the Wallis correlation [1] expressed as,

$$j_g^{*1/2} + m\, j_l^{*1/2} = C \ , \tag{1}$$

where

$$j_k^* = j_k \sqrt{\rho_k / \Delta\rho g D} \quad , \qquad (k = g \text{ or } l) \tag{2}$$

When the flow is turbulent, m is equal to unity. The value of C depends of the geometrical conditions of the channel and the way of mixing of the two phases. When the entrance is sharp-edged, C is 0.725 and for round-edged entrances C is between 0.88 and 1.

The flow reversal condition can be obtained by letting $j^*_1 = 0$, and we have

$$j_g^* = 0.5 \sim 1 \tag{3}$$

which means that the flow reversal condition depends on the tube diameter.

On the other hand, Pushkina and Sorokin [16] proposed for flow reversal the following equation which does not depend on the tube diameter;

$$\text{Ku (Kutateladze number)} = j_g(\rho_g^2/\sigma g\Delta\rho)^{1/4} = 3.2 \quad . \tag{4}$$

This apparent inconsistency was interpreted successfully by Wallis and Makkenchery [17]. Introducing the following dimensionless group:

$$D^* = D\sqrt{g\Delta\rho/\sigma} \quad . \tag{5}$$

the Kutateladze number is rewritten as

$$Ku = j_g^* \sqrt{D^*} \quad . \tag{6}$$

Then they postulated that when the Kutateladze number is less than 3.2

(i.e. for small D*), Eq.(3) holds and otherwise Eq.(4) is valid. Therefore the flow reversal condition for small D* becomes

$$j_g^* = Ku/\sqrt{D^*} = \text{const.} \tag{7}$$

A variety of models of flooding and flow reversal have been proposed, namely, the standing wave model [22], the viscous flow model [23], the potential flow model [4], the entrainment model [20], and more recently, the roll-wave model [15] and the separate flow model [21,24]. In this respect, Hewitt and Whalley [25] observed the flooding phenomena using the laser shadowgraph technique and pointed out that the rapid wave growth is the cause of flooding and the droplet entrainment is an effect of flooding.

Richter [15] considered the force balance acting on the liquid film and the roll wave. He obtained analytically the flooding and flow reversal criteria for round tubes and annuli. The average perimeter based on the arithmetic mean diameter was used as the characteristic length for annuli. The model reproduced successfully both the Wallis correlation [1], Eq.(3) and the Pushkina and Sorokin correlation [16], Eq.(4) as well as the experimental data on annuli [12,13] in relation to the CCFL problem in the downcomer of a pressurized water reactor.

Bharathan et al.[24] recently proposed the separate flow model considering the force balance acting on the annular liquid film and obtained the following relation for flooding.

$$\frac{2f_i j_g^{*2}}{\alpha^{5/2}} + \frac{2f_{wl} j_l^{*2}}{(1-\alpha)^2} = 1 - \alpha \quad . \tag{8}$$

The limiting values for $j^*_g$ and $j^*_l$ can be obtained as an envelope of curves drawn with the void fraction as a parameter, if the friction factors $f_i$ and $f_{wl}$ are given. They also derived an empirical correlation for the interfacial friction factor $f_i$ in vertical annular countercurrent flow, as follows:

$$f_i = 0.005 + a\,\delta^{*b} \quad , \tag{9}$$

where

$$\log_{10} a = -0.56 + \frac{9.07}{D^*} \quad , \tag{10}$$

$$b = 1.63 + \frac{4.74}{D^*} \quad , \tag{11}$$

$$\delta^* = \delta\sqrt{g\Delta\rho/\sigma} \quad . \tag{12}$$

In spite of all those investigations, it appears that there still remain several problems, such as the effect of channel length, the effect of two-dimensional flow, the effects of channel inlet and outlet conditions, the effect of condensation. As for thin rectangular channels which is similar to the coolant channels of a MTR-type research reactor, there are no data available on flooding and flow reversal, although they are important in relation to the minimum critical heat flux in such channels. Therefore this chapter mainly concerned with the flooding and flow reversal for air-water flow in thin rectangular channels, although the basic equations are derived each for a round tube, rectangular channel and annulus.

## III.2. THEORY

### III.2.1. Basic Equations for Round Tubes

Assuming uniform annular liquid film as shown in Fig. 2, the relationships among the pressure drop, gravity force and the shear stresses in the liquid film and the gas core are expressed as [26],

$$\frac{dp}{dz} + \rho_l g = \frac{\tau_i P_i}{(1-\alpha)A} - \frac{\tau_{wl} P_{wl}}{(1-\alpha)A} \quad , \tag{13}$$

$$\frac{dp}{dz} + \rho_g g = - \frac{\tau_i P_i}{\alpha A} \quad . \tag{14}$$

Eliminating the pressure drop term from Eqs.(13) and (14), we obtain

$$\Delta\rho g = \frac{4}{D(1-\alpha)}(\tau_i/\sqrt{\alpha} - \tau_{wl}) \quad , \tag{15}$$

where the following is assumed,

$$\frac{P_i}{P_{wl}} = 1 - \frac{2\delta}{D} \simeq \sqrt{\alpha} \quad . \tag{16}$$

The interfacial shear stress $\tau_i$ and the wall shear stress $\tau_{wl}$ can be written respectively as

$$\tau_i = \frac{f_i}{2} \rho_g v_r^2 \quad , \tag{17}$$

$$\tau_{wl} = \frac{f_l}{2} \rho_l v_l |v_l| - \frac{1}{3} \Delta\rho g \delta \quad , \tag{18}$$

where $v_l$ is negative for the falling liquid film.

The relative velocity $v_r$ and the velocities for the two phases $v_g$

and $v_l$ can be written in terms of the superficial velocities and the void fraction as

$$v_r = v_g - v_l \quad , \tag{19}$$

$$v_g = j_g/\alpha \quad , \tag{20}$$

$$v_l = j_l/(1-\alpha) \quad . \tag{21}$$

Substituting Eqs.(17) through (21) into Eq.(15) and rearranging, we obtain

$$\frac{3f_i\rho_g}{\Delta\rho g D\sqrt{\alpha}}\left(\frac{j_g}{\alpha} - \frac{j_l}{1-\alpha}\right)^2 - \frac{3f_{wl}\rho_l j_l|j_l|}{\Delta\rho g D(1-\alpha)^2} = 1 - \alpha \quad . \tag{22}$$

Now using the dimensionless superficial velocities defined by Eq.(2), we arrive at the following equation:

$$\frac{3f_i}{\alpha^{5/2}}\left(j_g^* - \frac{\alpha}{1-\alpha} j_l^*\sqrt{\rho_g/\rho_l}\right)^2 - \frac{3f_{wl}}{(1-\alpha)^2} j_l^*|j_l^*| = 1 - \alpha \quad . \tag{23}$$

The above equation can be rewritten as

$$j_g^* = \frac{\alpha}{1-\alpha} j_l^*\sqrt{\rho_g/\rho_l} + \sqrt{\frac{\alpha^{2.5}(1-\alpha)}{3f_i}\left[1 + \frac{3f_{wl}}{(1-\alpha)^3} j_l^*|j_l^*|\right]} \quad . \tag{24}$$

Substituting $j^*_l = 0$ into Eq.(24), we obtain the following for flow reversal condition.

$$j_g^* = \sqrt{\frac{\alpha^{2.5}(1-\alpha)}{3f_i}} \quad . \tag{25}$$

III.2.2. Basic Equations for Rectangular Channels

Based upon the observations in the experiment conducted with thin rectangular channels, it is assumed that the liquid flowing down on the wide side walls can be neglected compared to that on the narrower side walls, as illustrated in Fig. 3. The same procedure can be followed to obtain the equation for the rectangular channel. Thus the balance of force acting on the liquid film gives

$$\frac{dp}{dz} + \rho_l g = \frac{\tau_i}{\delta} - \frac{\tau_{wl}}{\delta} \quad . \tag{26}$$

As for the gas core, we have

$$\frac{dp}{dz} + \rho_g g = - \frac{\tau_i P_i}{\alpha A} - \frac{\tau_{wg} P_{wg}}{\alpha A} \quad . \tag{27}$$

Eliminating the pressure drop term from Eqs.(26) and (27) we obtain

$$\Delta\rho g = \frac{2\tau_i}{\alpha w(1-\alpha)} - \frac{2\tau_{wl}}{w(1-\alpha)} + \frac{\tau_{wg}}{s} \quad , \tag{28}$$

where the void fraction $\alpha$ is approximated by

$$\alpha = 1 - 2\,\delta/w \tag{29}$$

Here we assumed the same equations for the interfacial shear stress and the wall shear stress in the liquid film as given earlier, i.e. Eqs.(17) and (18), respectively. The wall shear stress in the gas core is given in the same manner. Then

$$\tau_{wg} = \frac{f_g}{2} \rho_g v_g^2 \quad . \tag{30}$$

Using Eqs.(19) through (21) and substituting Eqs.(17),(18) and (30) into Eq.(28) we obtain

$$\frac{3f_i\rho_g}{2\Delta\rho g w \alpha}\left(\frac{j_g}{\alpha} - \frac{j_1}{1-\alpha}\right)^2 - \frac{3f_{w1}\rho_1 j_1|j_1|}{2\Delta\rho g w(1-\alpha)^2} + \frac{3f_g\rho_g j_g^2}{2\Delta\rho g w\alpha^2}\cdot\frac{w}{2s}(1-\alpha) = 1-\alpha \quad . \tag{31}$$

Equation (31) can be rewritten by using the non-dimensional superficial velocities,

$$j_g^* = j_g\sqrt{\rho_g/(2\Delta\rho g w)} \quad , \tag{32}$$

$$j_1^* = j_1\sqrt{\rho_1/(2\Delta\rho g w)} \quad , \tag{33}$$

and therefore,

$$\frac{3f_i}{\alpha}\left(\frac{j_g^*}{\alpha} - \frac{j_1^*}{1-\alpha}\sqrt{\rho_g/\rho_1}\right)^2 - \frac{3f_{w1}j_1^*|j_1^*|}{(1-\alpha)^2} + \frac{3f_g w}{2s\alpha^2} j_g^{*2}(1-\alpha) = 1-\alpha \quad . \tag{34}$$

Equation (34) can be rearranged for $j^*_g$, hence

$$j_g^* = \frac{\alpha j_1^*}{1-\alpha}\sqrt{\rho_g/\rho_1} + \sqrt{\frac{\alpha^3(1-\alpha)}{3f_i}\left[1 + \frac{3f_{w1}j_1^*|j_1^*|}{(1-\alpha)^3} - \frac{3f_g w}{2s\alpha^2} j_g^{*2}\right]} \quad . \tag{35}$$

For flow reversal condition, letting $j^*_1 = 0$, we have

$$j_g^* = \sqrt{\frac{\alpha^3(1-\alpha)}{3f_i}\left[1 - \frac{3f_g w}{2s\alpha^2} j_g^{*2}\right]} \quad . \tag{36}$$

It should be noted here that Eqs.(35) and (36) are very similar to those for round tubes if we use 2w as the characteristic length, except the power of the void fraction and the additional term due to wall friction in the gas core.

III.2.3. Basic Equations for Annuli

The same procedures can be followed to obtain the equations for annuli in which case the following assumptions are made:

(1) The gap of the annulus is small compared to the diameters of the inner and the outer walls.

(2) The thickness of the liquid films on the inner and the outer walls are equal and small compared to the gap of the annulus, hence

$$\delta/D << \delta/s << 1 \quad , \tag{37}$$

where

$$D = \frac{D_i + D_o}{2} \quad , \tag{38}$$

and the following approximation holds:

$$1 - \alpha = 2\delta/s \quad . \tag{39}$$

(3) The interfacial shear stress in the inner and the outer liquid

films are equal, thus

$$\tau_{ii} = \tau_{io} = \tau_i \quad . \tag{40}$$

(4) The wall shear stress in the liquid films are equal, thus

$$\tau_{wli} = \tau_{wlo} = \tau_{wl} \quad . \tag{41}$$

Based on the above assumptions, we obtain the following equation:

$$\frac{3f_i\rho_g}{2\Delta\rho gs\alpha}\left(\frac{j_g}{\alpha} - \frac{j_1}{1-\alpha}\right)^2 - \frac{3f_{wl}\rho_1 j_1|j_1|}{2\Delta\rho gs(1-\alpha)^2} = 1 - \alpha \quad . \tag{42}$$

Here we define the non-dimensional superficial velocities by

$$j_g^* = j_g\sqrt{\rho_g/(2\Delta\rho gs)} \quad , \tag{43}$$

$$j_1^* = j_1\sqrt{\rho_1/(2\Delta\rho gs)} \quad , \tag{44}$$

From Eqs.(44) through (45), we obtain

$$j_g^* = \frac{\alpha j_1^*}{1-\alpha}\sqrt{\rho_g/\rho_1} + \sqrt{\frac{\alpha^3(1-\alpha)}{3f_i}\left[1 + \frac{3f_{wl}j_1^* j_1^*}{(1-\alpha)^3}\right]} \quad , \tag{45}$$

and for flow reversal condition, we have

$$j_g^* = \sqrt{\frac{\alpha^3(1-\alpha)}{3f_i}} \quad . \tag{46}$$

Therefore the similar equations to those for round tubes are obtained if

we use the hydraulic equivalent diameter 2s.

III.2.4. Relation between Superficial velocities and Void Fraction

Having basic equations for liquid films, the conditions for flooding and flow reversal can be obtained if the wall and interfacial friction factors are given and if another relationship between the void fraction and the superficial velocities at the occurrence of flooding is known. However, it is difficult at the present time to obtain the general solution of the problem because it appears that the flooding conditions differ from one channel geometry and another and the available correlations are applicable only to a limited range of parameters. For this reason it may be relevant at this time to derive the flooding conditions using an appropriate phenomenological modeling which is based upon the experimental observation.

Before solving the equation, it is interesting to look into the relationship between the void fraction and the superficial velocities predicted by the basic equations. For simplicity we consider here the flow reversal condition for round tubes, i.e. Eq.(25). Richter [15] and Bharathan et al.[24] used essentially the same basic equations as Eq.(25). The only difference is a factor 2/3 multiplied in the root of Eq.(25). Taitel et al.[21] obtained a slightly different equation, assuming a laminar flow in the film, which can be rewritten as follows:

$$j_g^* = \sqrt{\frac{\alpha^2(1-\alpha)}{3f_i}\left[1 + \frac{48\nu_l j_l^*}{D(1-\alpha)^3\sqrt{\rho_l/(\Delta\rho g D)}}\right]} \quad . \tag{47}$$

For flow reversal condition, letting $j^*_l=0$, we have

$$j_g^* = \sqrt{\frac{\alpha^2(1-\alpha)}{3f_i}} \quad . \tag{48}$$

When the void fraction is close to unity, Eq.(48) is essentially the same as Eq.(25).

The interfacial friction factor for rough annular film was obtained by Wallis [1], which is given by

$$f_i = 0.005\ [1 + 75(1 - \alpha)] \quad . \tag{49}$$

Richter [15] used the following relation,

$$f_i = 0.008\ [1 + 75(1 - \alpha)] \quad . \tag{50}$$

Taitel et al.[21] used the empirical correlation for interfacial friction factor of Bharathan et al. [24], i.e. Eq.(9). Using these equations, the curve for $j^*_g$ versus $1-\alpha$ can be drawn as given in Fig. 4. It can be seen that the curve predicted by Eq.(25) with Eq.(49) is close to that of Richter [15]. The prediction by Taitel et al.[21] gives higher $j^*_g$ at low $1-\alpha$ and lower $j^*_g$ at higher $1-\alpha$ compared to the others. The curve predicted by Eq.(25) with $f_i=0.005$ is also shown in the figure which shows that the assumption $f_i=0.005$ gives far high $j^*_g$ at the void fractions lower than 0.98. Therefore, it can be said that the relation between $j^*_g$ and the void fraction is sensitive to the interfacial friction factor. This indicates that it is important to use appropriate equations under given conditions in order to derive the flooding conditions from the basic equations.

## III.3. EXPERIMENT

### III.3.1. Test Section

In order to obtain the flooding velocities for air-water flow in

thin rectangular channels, an experiment has been performed. Three test sections with thin rectangular channel were employed in the experiment. The width of these test sections is 40 mm and the gap 1.5, 2.4 and 5.0 mm. The gap is kept close to the nominal value by sandwiching machined aluminum spacer between two acrylic plates, resulting in the above described thin rectangular channels. The 2.4 mm gap is the same as that employed in the burnout experiment which will be discussed in Chapter VI. The length of the test section is 470 mm, which has a 130 mm long, tapered entrance region in order that the disturbance to the liquid film in introducing air into the test section is as small as possible. Since the test section wall is transparent, the observation of the flow regime is possible.

The top of the test section is so called sharp-edged flange which is connected to the upper plenum which serves as the water reservoir and the gas-liquid separator. The plenum is furnished with the water inlet and the overflow.

The bottom of the test section is connected to the mixing chamber and the measuring cylinder.

III.3.2. Test Apparatus

The test apparatus is schematically depicted in Fig. 5. Compressed air was reserved in the reservoir and supplied to the test section through the regulating valve. The air flow rate was measured with a float-type flowmeter. The reference temperature and pressure were measured in the mixing chamber with an Alumel-Chromel thermocouple and a Bourdon-tube type pressure gauge, respectively.

Air was introduced into the test section through the tapered entrance region at the bottom and exits at the top into the atmosphere.

Tap water was supplied to the upper plenum. The amount of water which was allowed to flow downward by the countercurrent air flow was reserved in the measuring cylinder. The remainder was drained from the overflow. The distance from the top of the test section to the overflow can be set either at 300, 400 or 600 mm.

### III.3.3. Test Procedure

First, air flow rate is regulated to a given value. After the measuring cylinder is emptied, the drain valve closed. Then water is supplied to the upper plenum. The measurement is made after the water level in the upper plenum and the flow regime in the test section become steady. The water flow rate is calculated from the measured time to fill a known volume in the measuring cylinder with water that was allowed to flow through the test section. In calculating the flow rate, the correction is needed due to the air volume which is expelled by the water entering the measuring cylinder.

## III.4. RESULTS AND DISCUSSIONS

### III.4.1. Visual Observations

Observed flow pattern of countercurrent flow in a thin rectangular channel is shown in Fig. 7. Most of the liquid entering the test section appears to flow down along the narrow side walls. The liquid films on the narrow side walls are rather thick whereas those on the wide side walls are so thin that unwetted patches sometimes appear on the surface. In the case shown in Fig. 7, the most of the surface on the wide side wall is unwetted.

Based upon the visual observations, it appears that the flooding velocities are controlled mainly by the rapid growth of large disturbance waves at the top of the test section. Therefore, the liquid film

down the top is rather smooth. Countercurrent air and water strongly interact at the top probably due to the sudden enlargement of the flow area. The disturbance wave grows untill its crest touches that on the opposite side of the channel and form a liquid bridge. Then the bridge is broken up into droplets, and again another disturbance wave grows. This type of flooding will be referred to as top flooding from now on.

The other type of flooding was also observed by completely filling the measuring cylinder and the mixing chamber with water so that the net flow rate in the test section is zero. Typical flow pattern is shown in Fig. 8. In this case, the liquid films on the narrow side walls are thick and large disturbance waves are generated at the bottom. These disturbance waves grow rapidly to form thick liquid bridges. They are blown upward by the air stream. It appears that the liquid circulates within the test section, i.e. the liquid flows down along the narrow side walls, reaches the bottom and then are carried upward in the disturbance waves, the liquid bridges and the thin climbing liquid films along the wide side walls. This type of flooding will be referred to as bottom flooding, here. At higher air velocities, the disturbance waves or liquid bridges are torn up into droplets, as shown in Fig. 9. In this case, the upper portion of the wide side walls are unwetted and only small droplets are deposited on the surface.

The above two observations indicate that it is important in analyzing the flooding phenomenon and burnout due to flooding to specify which mechanism is dominant. As will be described later in Chapter VI, a flooding similar to the bottom flooding was observed at the complete bottom blockage condition in the burnout experiment with thin rectangular channels. In that case, a burnout occurred when sufficient liquid

was not supplied to the heated wall by the falling film on the narrow side walls.

III.4.2. Flooding Velocities

Since the flooding velocities are often correlated in terms of $j^*_g{}^{1/2}$ and $j^*_l{}^{1/2}$, the experimental data are plotted in the same manner. As discussed previously, $j^*_g$ and $j^*_l$ are defined by Eqs.(32) and (33) for rectangular channels.

The flooding velocities for the test section with 5 mm gap are shown in Fig. 10, in which the effect of the water depth above the test section appears to be small. Therefore, the water depth was kept at 400 mm in the subsequent runs.

The data taken with three test sections are compared in Fig. 11, together with the prediction by the Wallis correlation [1]. The measured flooding velocities are generally lower than the Wallis correlation. The data for the gap 2.4 mm appear to be slightly larger than the others although no systematic dependency on the gap is evident.

III.4.3. Countercurrent Flow Envelope

If the friction factors are known, the basic equation for annular film, Eq.(35) for rectangular channel generates the curves for $j^*_g$ versus $j^*_l$ with the void fraction as a parameter. The envelope of these curves corresponds to the theoretical countercurrent flow limit [24]. Hence, we calculate the envelope for each test section and compare with the experimental data. Here, we assume Eq.(49) for the interfacial friction factor and the Blasius equation for the wall friction factors, given by

$$f_{wl} = 0.0791\ Re_l^{-0.25} \quad , \tag{51}$$

where

$$Re_l = \frac{\rho_l |v_l| \delta}{\mu_l} \quad , \tag{52}$$

and

$$f_g = 0.0791 \, Re_g^{-0.25} \quad , \tag{53}$$

$$Re_g = \frac{2\rho_g v_g s}{\mu_g} \quad . \tag{54}$$

The results of the calculations are shown for each test section in Figs. 12, 13 and 14. The figures indicate that the theoretical limit is more than two times higher than the measured flooding velocities, the difference being larger at higher liquid velocities. The discrepancy can be explained by the fact that the flooding velocities in this case are limited by the onset of large disturbance waves at the top.

III.4.4. Comparison with Other Works

No correlation for flooding is available at the present time for thin rectangular channels. However, one may use those for round tubes with 2w as the characteristic length, taking account of the similarity of the basic equations. As mentioned before, the flooding occurred due to the onset of large disturbance waves. Hence, first, we use Richter's theory [15] which is based on the roll wave (disturbance wave) mechanism. The result is expressed as

$$\frac{f_{wl}}{4} N_B^3 \, j_g^{*6} \, j_l^{*2} + f_{wl} N_B \, j_g^{*4} + 150 \, f_{wl} j_g^{*2} = 1 \quad , \tag{55}$$

where $N_B$ is the Bond number defined by

$$N_B = (2w)^2 \frac{\Delta\rho g}{\sigma} \quad , \tag{56}$$

and

$$f_{wl} = 0.008 \quad . \tag{57}$$

Imura et al.[4] derived the following relation between the flooding velocities based on the potential theory:

$$v_g + v_l = \sqrt{\frac{\sigma}{\rho_g}\left(k - \frac{1}{R-\delta}\right)} \quad , \tag{58}$$

The second term in the right hand side can be omitted for a rectangular channel. The wave number k is given by

$$k = \frac{\zeta}{\delta} \quad , \tag{59}$$

where the parameter $\zeta$ was determined empirically [4], and is given by

$$\zeta = 0.046 \left(\frac{\rho_l g D^2}{\sigma}\right)^{0.5} (\mu_l/\mu_g)^{0.12} \quad . \tag{60}$$

Here, we assume that Eq.(60) can be applied to rectangular channels if we put 2w into D. The film thickness is calculated by using the following equations [4]:

$$\delta = \left(\frac{3\nu_l^2}{g}\right)^{1/3} Re_l^{1/3} \qquad (Re_l < 400) \tag{61}$$

$$\delta = 0.369 \left( \frac{3\nu_l^2}{g} \right)^{1/3} Re_l^{1/2} \qquad (Re_l \geq 400) \qquad (62)$$

Figure 15 shows the comparison between these theory and the data as well as the Wallis correlation [1]. These theories appear to overpredict the flooding velocities. This result indicates that we may not use the equations for round tubes by simply replacing the characteristic length, probably because the flow is not uniform in circumference in rectangular channels whereas a uniform liquid film can be expected in round tubes. At this time the present data are approximately correlated by the Wallis equation with C = 0.6.

## III.5. CONCLUSIONS

The results obtained in this chapter are summarized as follows:

(1) The basic relation between the superficial velocities in annular flow and countercurrent flow are derived by considering the balance of forces acting on the liquid film and the gas core, for three basic channel geometries, i.e. round tubes, rectangular channels and annuli. The resultant equations for each channel geometries are similar to each other if one uses the diameter for a round tube, 2w for a rectangular channel and 2s for an annulus as the characteristic length.

(2) The visual observations revealed that the flooding velocities in thin rectangular channels were controlled by the onset of large disturbance waves at the top of the test section. Thus the liquid film downstream appeared to be rather smooth. The most of the liquid entering the test section is carried in the falling film along the narrow side walls.

(3) On the other hand, at zero net liquid flow conditions, i.e. when

the bottom condition of the channel allows no liquid flow down, large disturbance waves are generated at the bottom. The thick liquid films on the narrow side walls are highly agitated to form liquid bridges which break up to generate droplet entrainment.

(4) The flooding velocities obtained for the thin rectangular channels are lower than predicted by the existing equations for round tubes. The present data are tentatively correlated by the Wallis correlation [1] with C = 0.6.

## NOMENCLATURE

| | | |
|---|---|---|
| $A$ | : | Flow area |
| $a$ | : | Constant for the interfacial friction factor given by Bharathan et al.[24] |
| $b$ | : | Constant for the interfacial friction factor given by Bharathan et al.[24] |
| $C$ | : | Parameter for the flooding correlation of Wallis [1] |
| $D$ | : | Tube diameter or characteristic length |
| $D^*$ | : | Dimensionless tube diameter |
| $D_i$ | : | Inner diameter of annulus |
| $D_o$ | : | Outer diameter of annulus |
| $f_i$ | : | Interfacial friction factor |
| $f_g$ | : | Wall friction factor in gas phase |
| $f_{wl}$ | : | Wall friction factor in liquid phase |
| $g$ | : | Gravity |
| $j_k$ | : | Superficial velocity or volumetric flux of the k phase (k=g or 1) |
| $j^*_k$ | : | Dimensionless superficial velocity of the k phase (k=g or 1) |
| $Ku$ | : | Kutateladze number |
| $k$ | : | Wave number |
| $m$ | : | Parameter used in the flooding correlation of Wallis |
| $N_B$ | : | Bond number |
| $P_i$ | : | Wetted perimeter of the gas-liquid interface |
| $P_{wg}$ | : | Wetted perimeter of the gas-wall contact |
| $P_{wl}$ | : | Wetted perimeter of the liquid-wall contact |
| $dP/dz$ | : | Pressure drop |
| $R$ | : | Radius |
| $Re_g$ | : | Gas phase Reynolds number |
| $Re_l$ | : | Liquid film Reynolds number |
| $s$ | : | Gap of annulus or rectangular channel |
| $v_k$ | : | Velocity of the k phase (k=g or 1) |
| $v_r$ | : | Relative velocity of the two phases |
| $w$ | : | Width of rectangular channel (wider span) |
| $z$ | : | Distance along the stream |

Greek Symbols

$\alpha$ : Void fraction

$\delta$ : Film thickness

$\delta^*$ : Dimensionless film thickness

$\Delta\rho$ : Difference of the densities of the two phases

$\zeta$ : Parameter for wave number given by Imura et al.[4]

$\mu_k$ : Viscosity of the k phase (k=g or l)

$\nu_l$ : Kinematic viscosity of liquid

$\rho_k$ : Density of the k phase (k=g or l)

$\sigma$ : Surface tension

$\tau_i$ : Interfacial shear stress

$\tau_{ii}$ : Interfacial shear stress in the liquid film on the inner wall

$\tau_{io}$ : Interfacial shear stress in the liquid film on the outer wall

$\tau_{wg}$ : Wall shear stress at the gas-liquid contact

$\tau_{wl}$ : Wall shear stress in the liquid film

$\tau_{wli}$ : Wall shear stress in the liquid film on the inner wall

$\tau_{wlo}$ : Wall shear stress in the liquid film on the outer wall

Subscripts

g : Gas phase

i : inner or interface

l : liquid phase

o : outer

w : wall

## REFERENCES


[1] G.B. Wallis, One-dimensional Two-phase Flow, McGraw-Hill, New York (1969).

[2] P. Griffith, W.A. Schumann and A.D. Neustal, "Flooding and burn-out in closed-end vertical tubes," Two Phase Fluid Flow Symposium, Paper No.5, Inst. Mech. Engrs., London (1962).

[3] W.J. Frea, "Two phase heat transfer and flooding in counter current flow," 4th. Int. Heat Transfer Conference, Paris, Paper No.B5.10 (1970).

[4] H. Imura, H. Kusuda and S. Funatsu, "Flooding velocity in a countercurrent annular two-phase flow," Chem. Engng. Sci., 32, pp.79-87 (1977).

[5] Z. Nejat, "Maximum heat flux for countercurrent two phase flow in a closed end vertical tubes," 6th. Int. Heat Transfer Conference, Toronto, Canada, Paper No.FB-29 (1978).

[6] S.N. Faynzilberg, N.Yu. Koloskova and M.G. Semena, "Correlation of experimental data on the maximum heat fluxes in two-phase thermosyphons," Heat Transfer - Soviet Research, 11[2], pp.119-122 (1979).

[7] M.K. Bezrodnyy, S.N. Faynzil'berg and YE.A. Kondrusik, "Investigation of the maximum heat transfer in annular two-phase thermosyphons," Heat Transfer - Soviet Research, 12[1], pp.118-123 (1980).

[8] T. Fukano, S.J. Chen and C.L. Tien, "Operating limits of the closed two-phase thermosyphon," Proc. ASME-JSME Thermal Engineering Conference, Honolulu, Hawaii, Vol.1, pp.95-101 (1983).

[9] P. Griffith, J.F. Pearson and R.J. Lepkowski, "Critical heat flux during a loss-of-coolant accident," Nucl. Safety, 18[3], pp.298-305 (1977).

[10] J.A. Block and G.B. Wallis, "Heat transfer and fluid flows limited by flooding," Heat Transfer : Research and Application, AIChE Symposium Series, No.174, Vol.74, pp.73-82 (1978).

[11] P. Griffith, C.T. Avedisian and J.P. Walkush, "Counterflow critical heat flux," ibid., pp.149-155 (1978).

[12] C.J. Crowley, J.A. Block and P.H. Rothe, An evaluation of ECC penetration data using two scaling parameters, CREARE TN-233 (1976).

[13] R.P. Collier, J.S. Liu, J.A. Dworak, A. Segev and L.J. Flanigan, Steam water mixing and system hydrodynamics problem, NUREG/CR-2011, NUREG/CR-0565 (1978).

[14] Y. Sudo and A. Ohnuki, "Mechanism of falling water limitation under counter-current flow through single vertical flow path," Trans. JSME, Ser.B, 49[444], pp.1685-1694 (1983) in Japanese.

[15] H.J. Richter, "Flooding in tubes and annuli," Int. J. Multiphase Flow, 7[6], pp.647-658 (1981).

[16] O.L. Pushkina and Y.L. Sorokin, "Breakdown of liquid film motion in vertical tubes," Heat Transfer - Soviet Research, 1[5], pp.56-64 (1969).

[17] G.B. Wallis and S. Makkenchery, "The hanging film phenomenon in vertical annular two phase flow," J. Fluids Engng., 98, pp.297-298 (1974).

[18] G.B. Wallis and J.T. Kuo, "The behavior of gas-liquid interfaces in vertical tubes," Int. J. Multiphase Flow, 2, pp.521-536 (1976).

[19] S. Suzuki and T. Ueda, "Behavior of liquid films and flooding in counter-current two-phase flow -- Part 1. Flow in circular tubes," Int. J. Multiphase Flow, 3, pp.517-532 (1977).

[20] A.E. Dukler and L. Smith, Two-phase interactions in counter-current flow studies of the flooding mechanism, NUREG/CR-0617 (1977).

[21] Y. Taitel, D. Barnea and A.E. Dukler, "A film model for the prediction of flooding and flow reversal for gas-liquid flow in vertical tubes," Int. J. Multiphase Flow, 8[1], pp.1-10 (1982).

[22] C.J. Shearer and J.F. Davidson, "The investigation of a standing wave due to gas blowing upwards over a liquid film; Its relation to flooding in wetted-wall columns," J. Fluids Mech., 22, Part 2, pp.321-335 (1965).

[23] A.G. Cetinbudaklar and G.J. Jameson, "The mechanism of flooding in vertical counter-current two-phase flow," Chem. Engng. Sci., 24, pp.1669-1680 (1969).

[24] D. Bharathan and G.B. Wallis, "Air-water countercurrent annular flow," Int. J. Multiphase Flow, 9[4], pp.349-366 (1983).

[25] G.F. Hewitt and P.B. Whalley, "Advanced optical instrumentation methods," Int. J. Multiphase Flow, 6, pp.139-156 (1980).

[26] M. Ishii, One-dimensional drift-flux model and constitutive equations for relative motion between phases in various two-phase flow regimes, ANL-77-47 (1977).

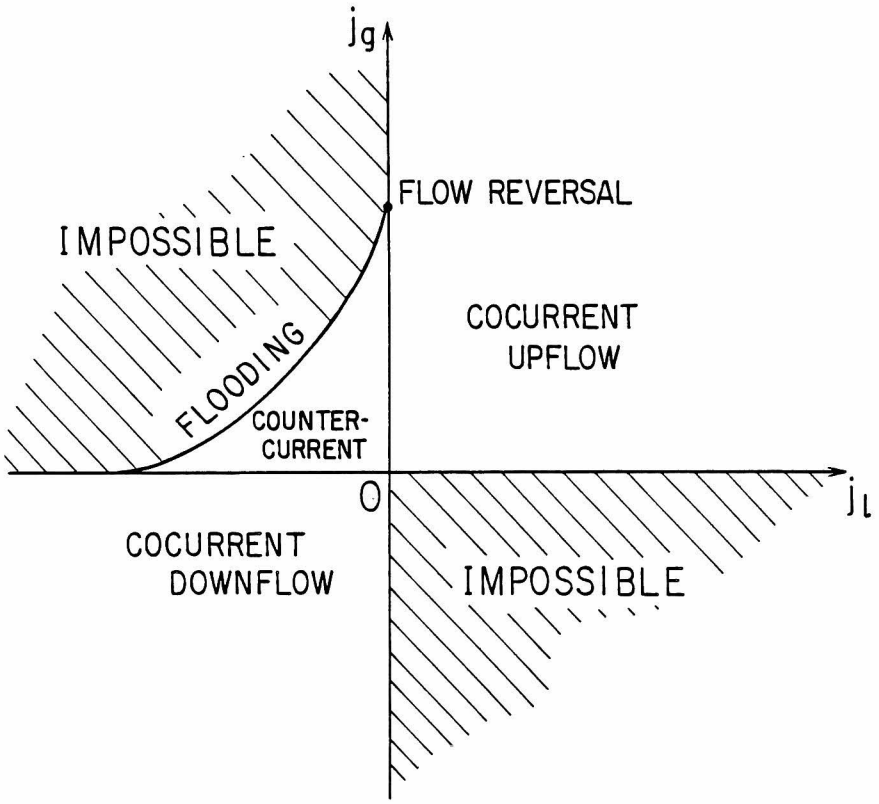


Figure 1 Boundary of countercurrent gas-liquid two-phase flow.

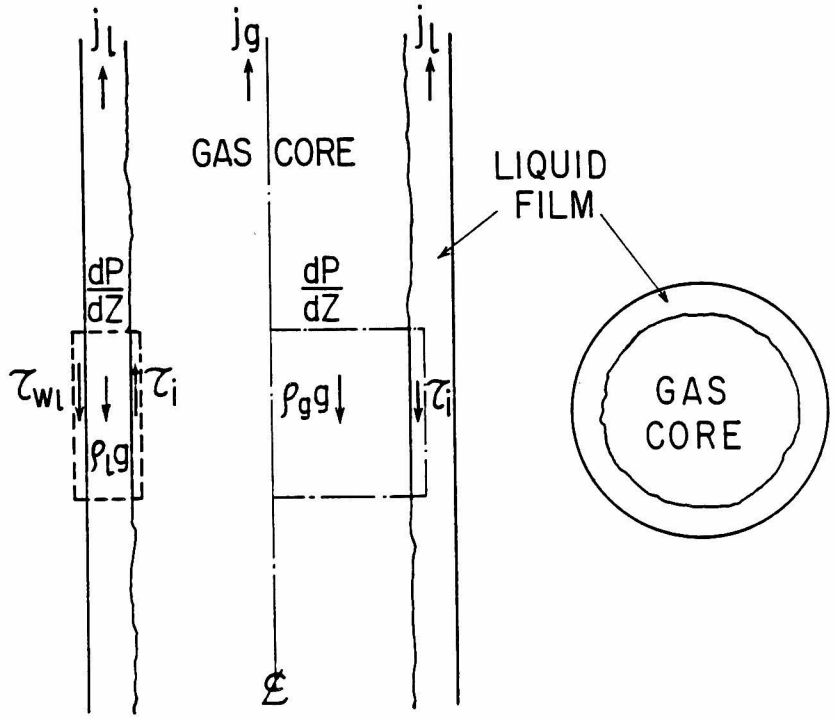


Figure 2 Annular film model in a round tube.

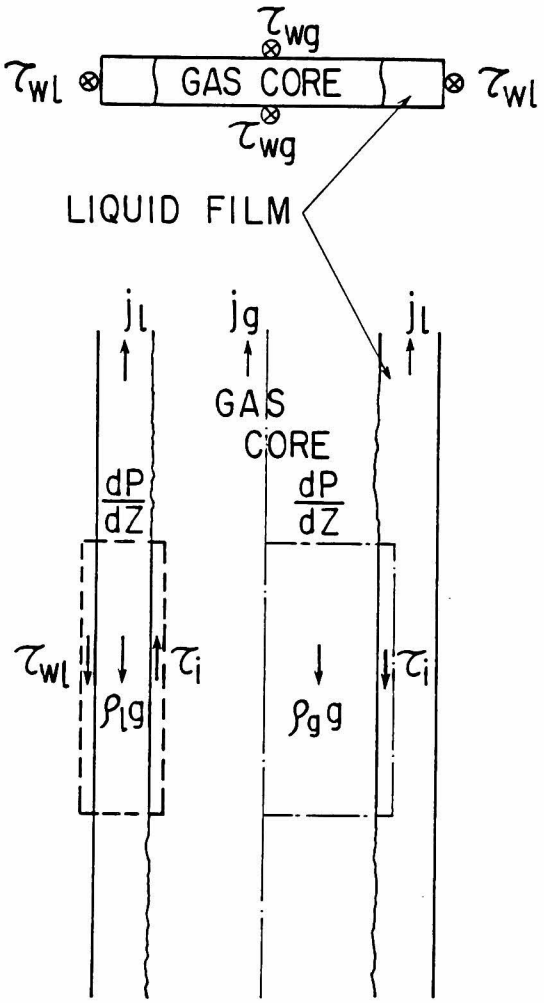


Figure 3 Film model in a thin rectangular channel.

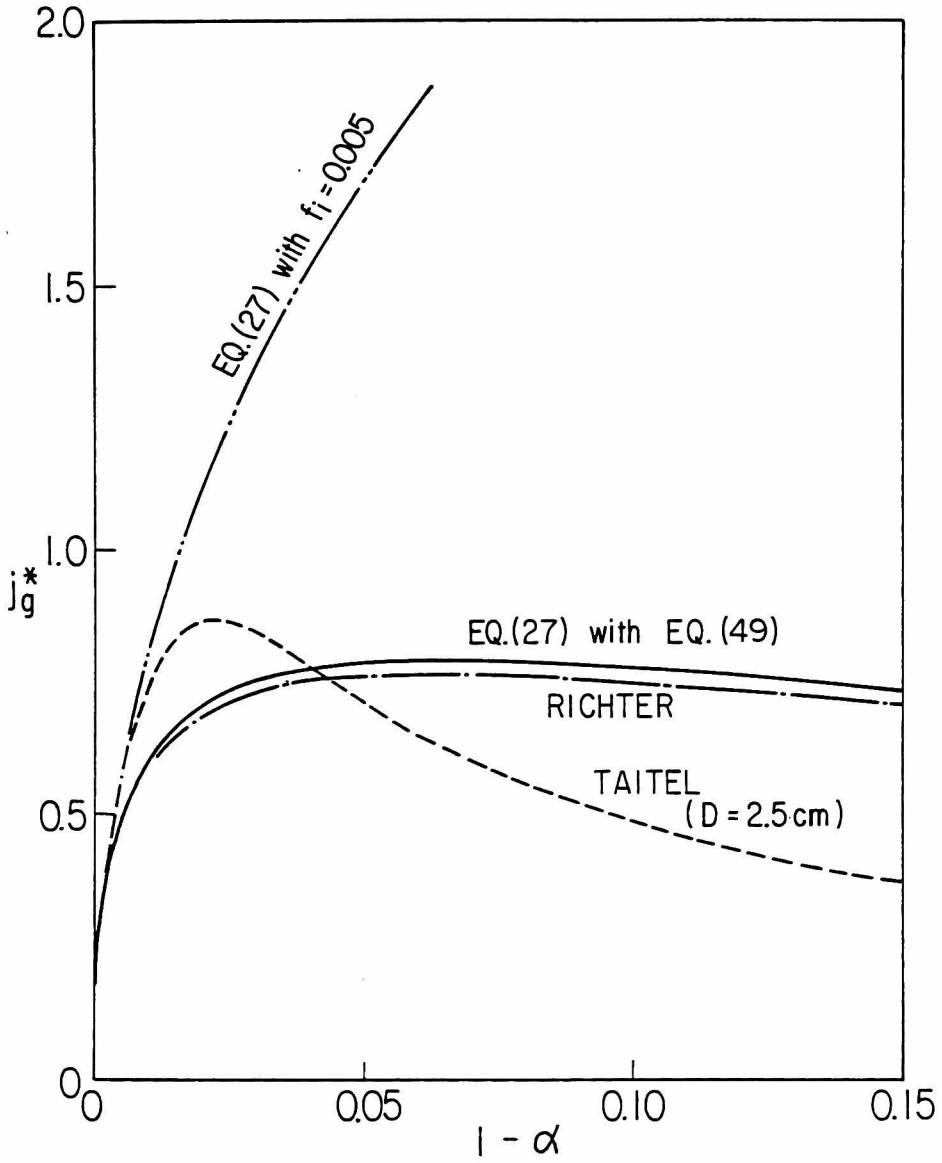


Figure 4 Predicted relationship between the non-dimensional superficial velocity and the liquid volumetric fraction.

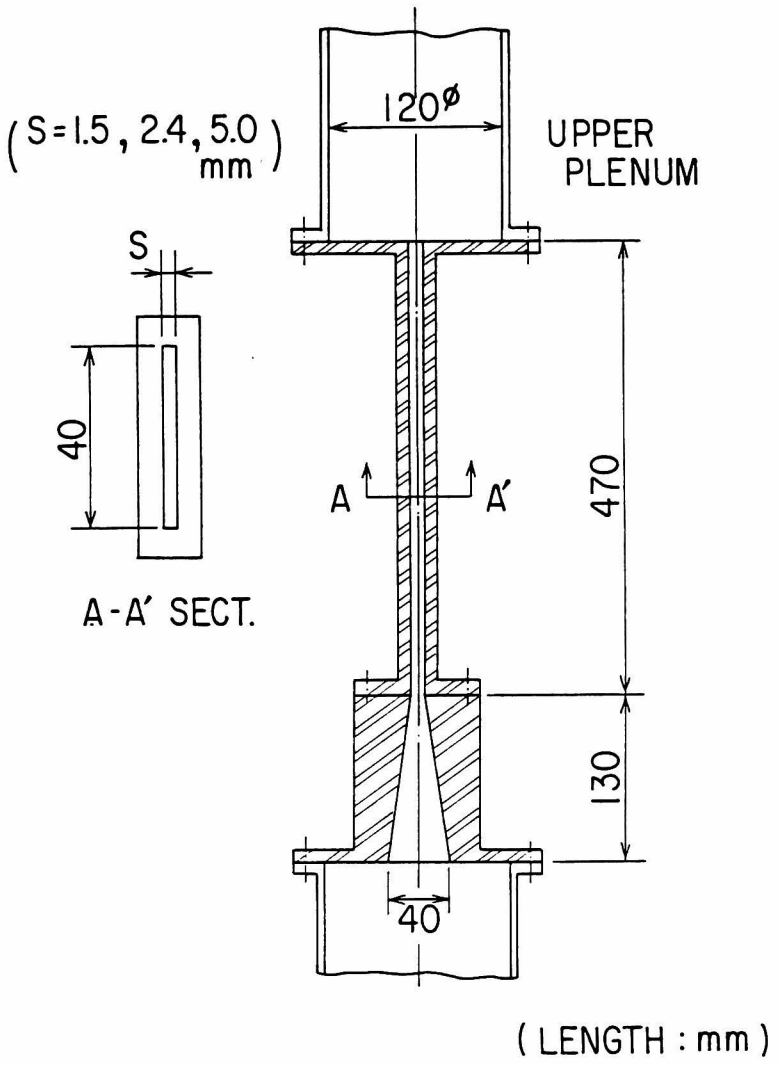


Figure 5 Test section employed in the flooding experiment.

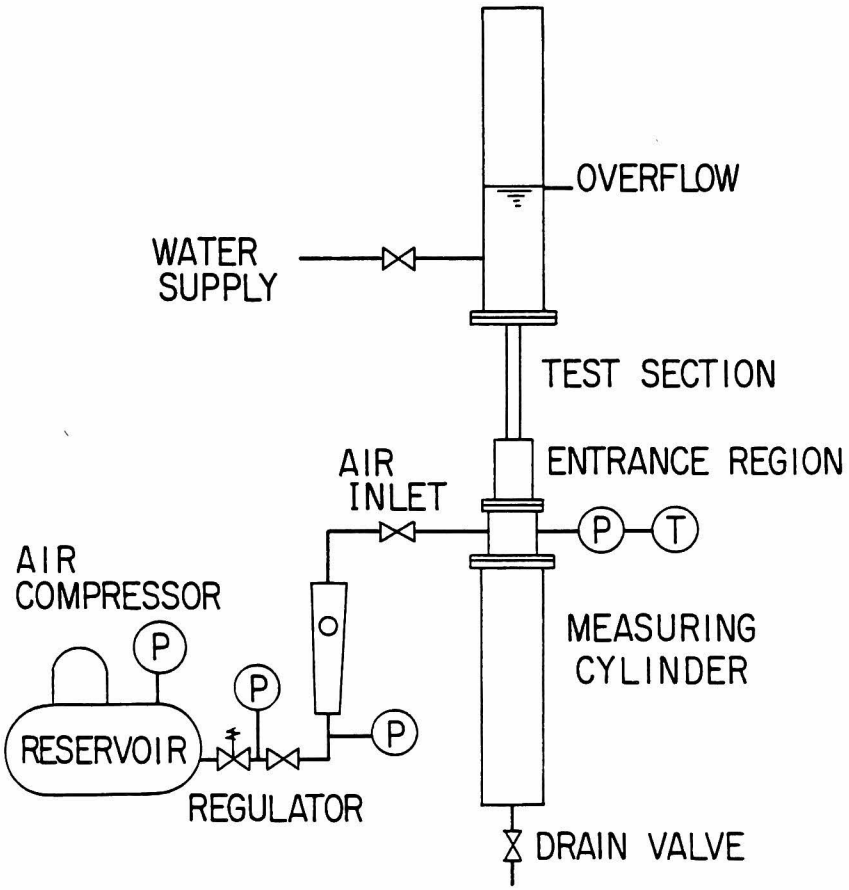


Figure 6 Schematic showing of the test apparatus.

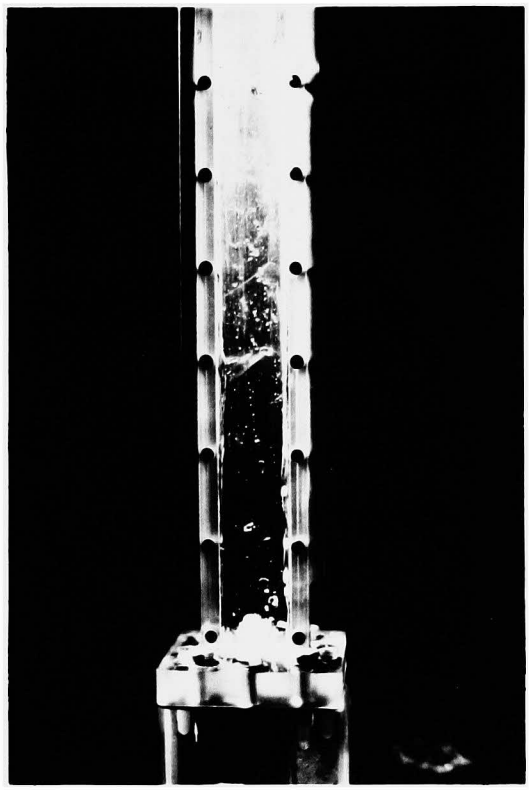

Figure 7 Pattern of countercurrent flow in a thin rectangular channel, flooding at the top.

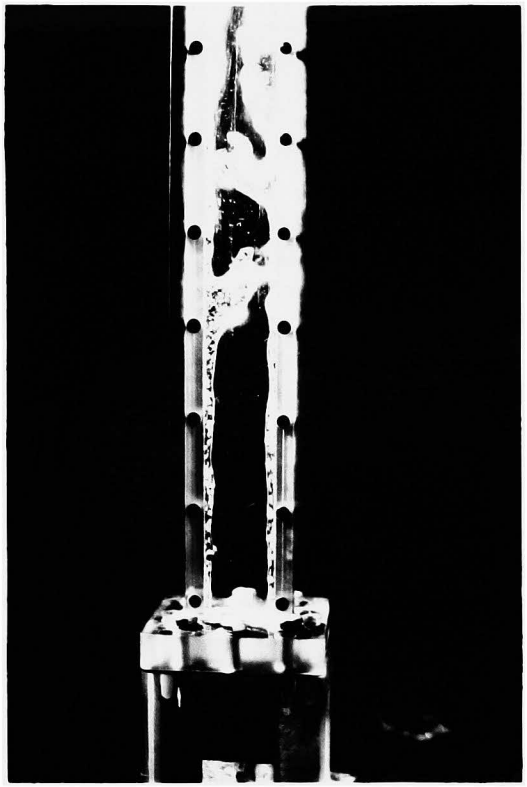

Figure 8 Pattern of countercurrent flow in a thin rectangular channel at the complete bottom blockage, flooding at the bottom.

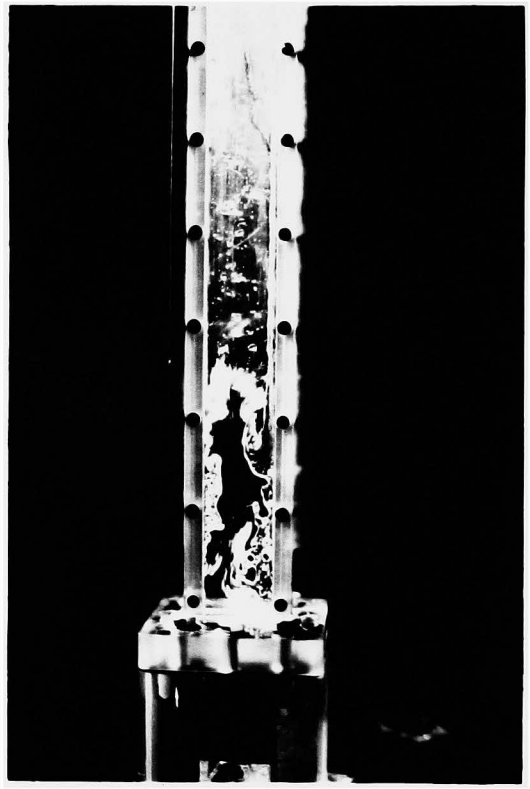

Figure 9 Pattern of countercurrent flow in a thin rectangular channel at the complete bottom blockage, near flow reversal condition.

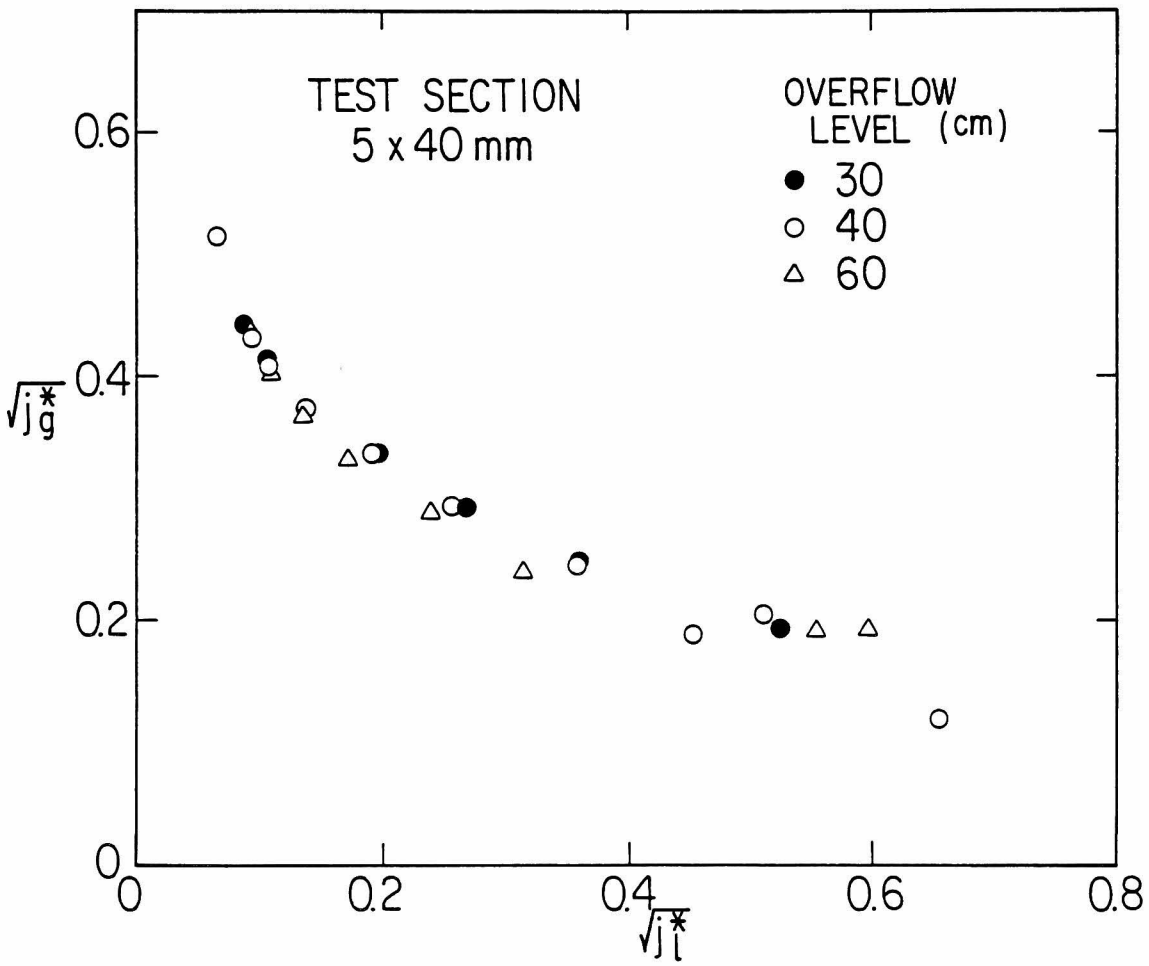


Figure 10. Flooding velocities for the test section with 5 mm gap, showing the effect of water height above the top of the test section.

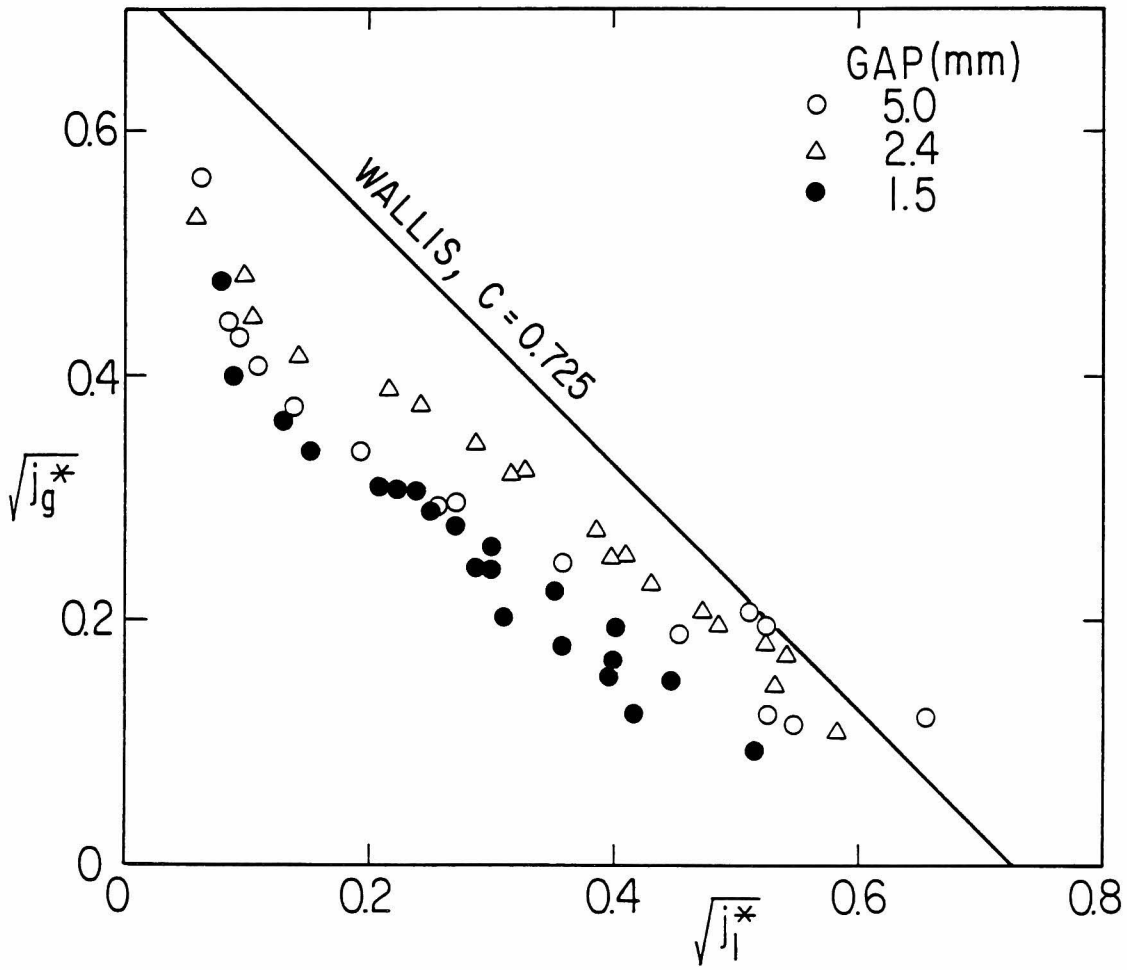


Figure 11 Comparison of the flooding velocities for three test sections and the Wallis correlation [1].

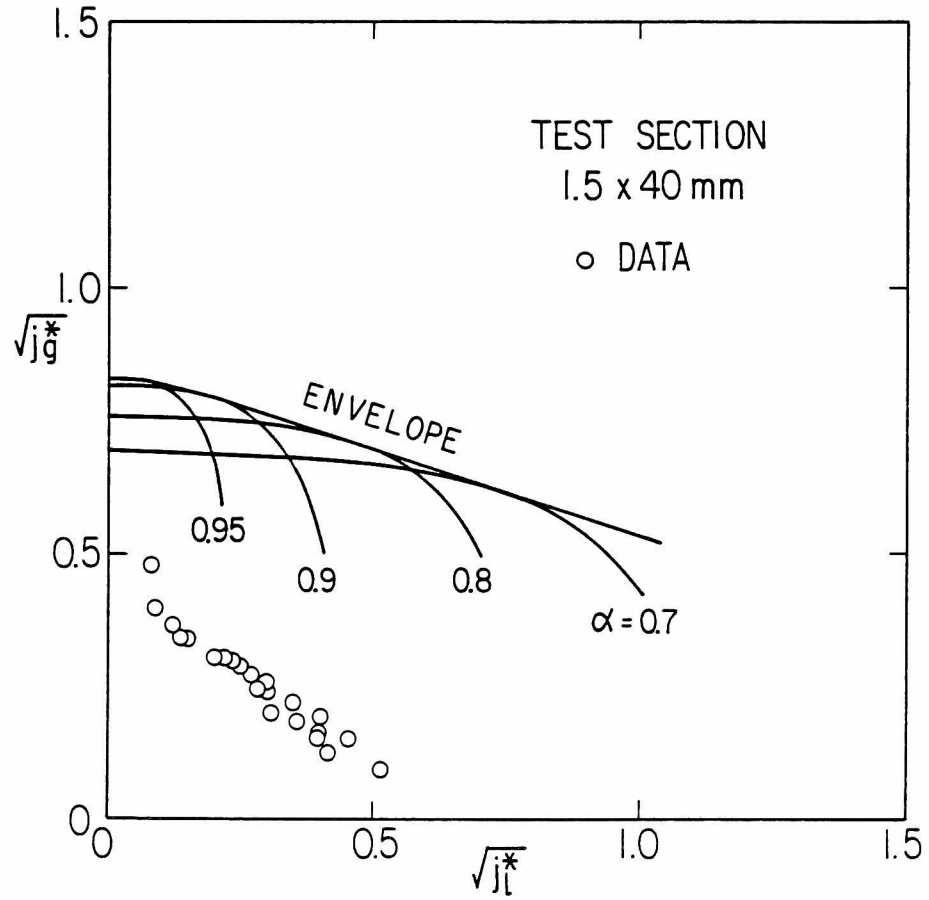


Figure 12 Countercurrent flow limit for the test section with 1.5 mm gap.

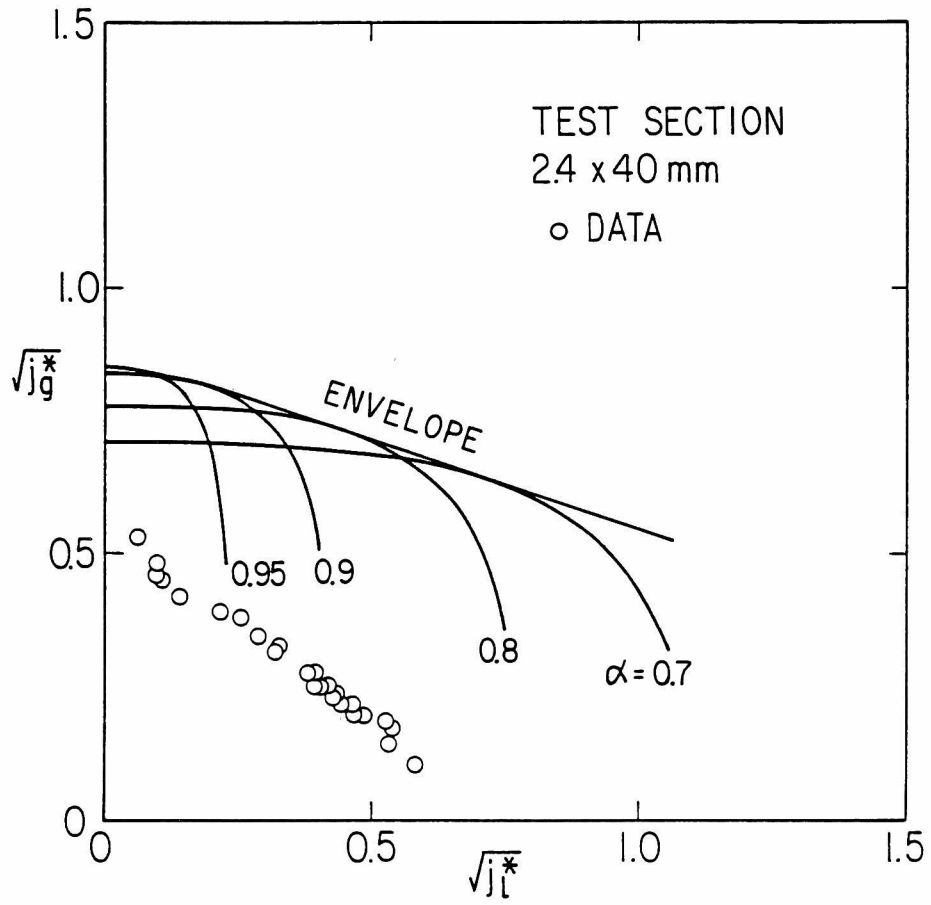


Figure 13 Countercurrent flow limit for the test section with 2.4 mm gap.

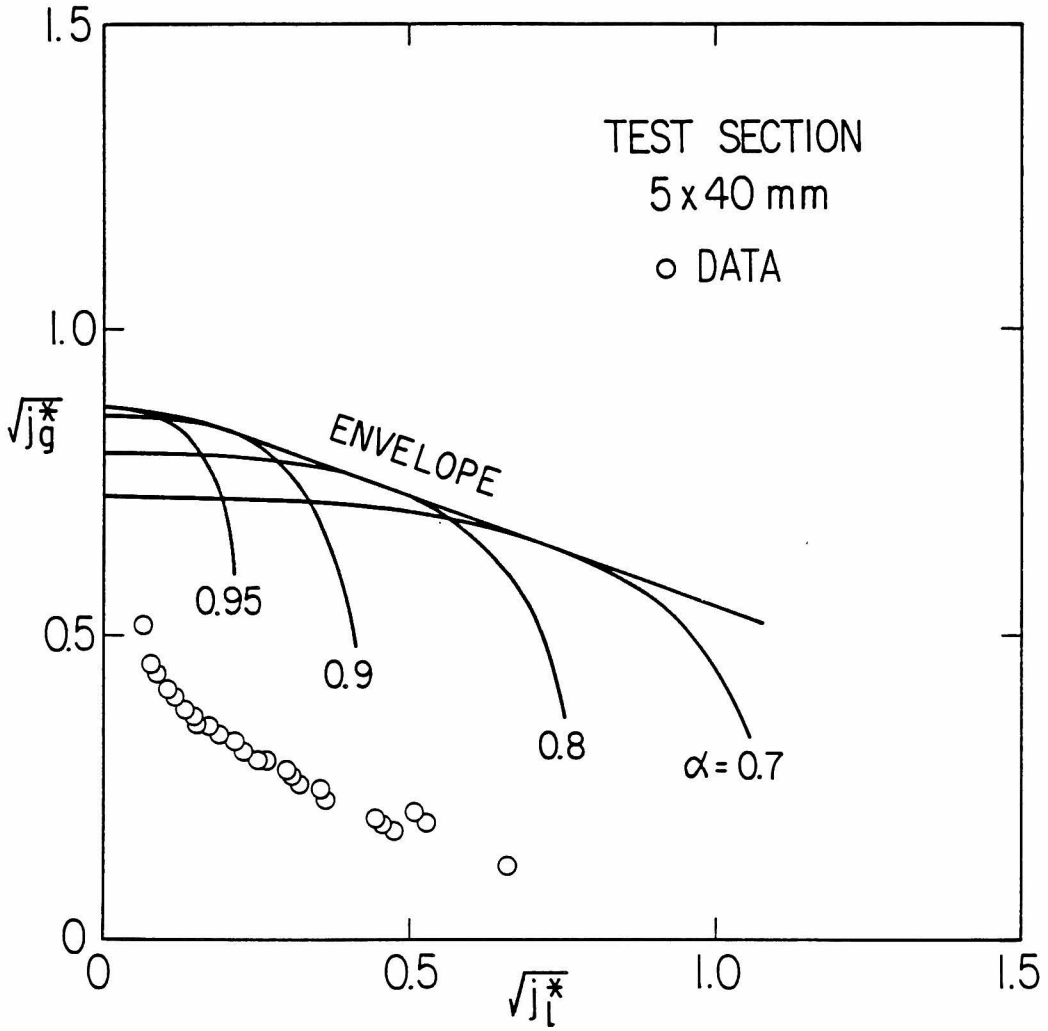


Figure 14 Countercurrent flow limit for the test section with 5.0 mm gap.

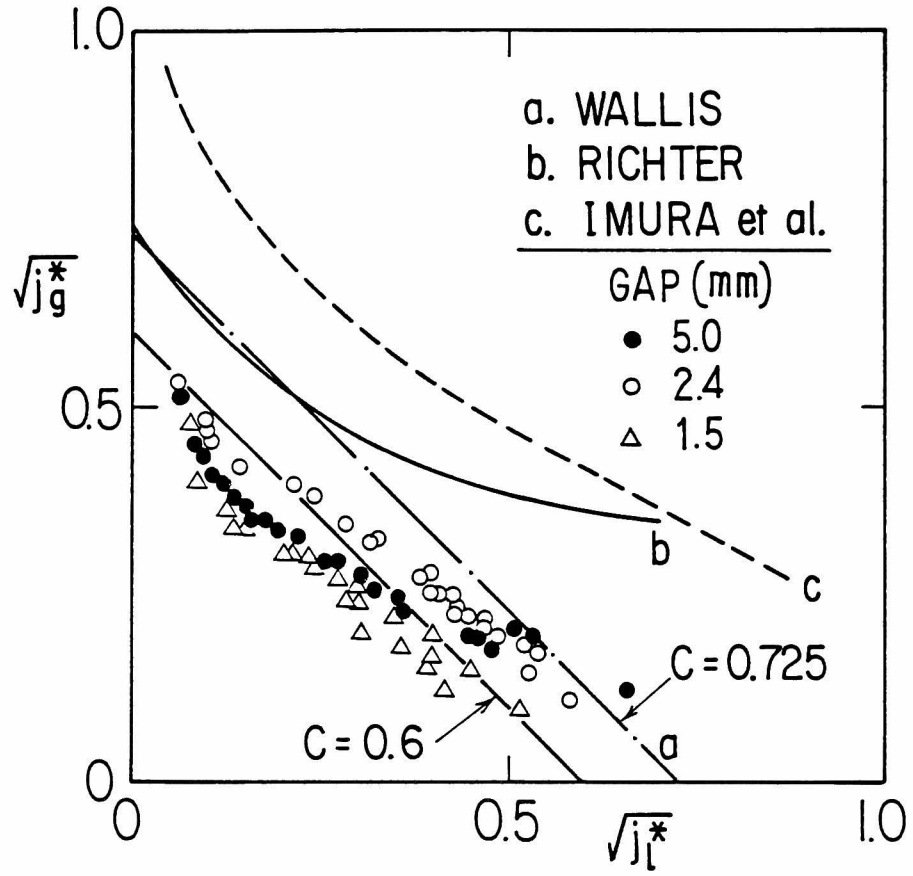


Figure 15 Comparison of flooding velocities with existing correlations.

# CHAPTER IV.

# CRITICAL HEAT FLUX UNDER LOW FLOW CONDITIONS IN A VERTICAL ANNULUS

## IV.1. INTRODUCTION

The occurrences of burnout in natural convection boiling can be very important in relation to the safety of various types of liquid cooled nuclear reactors under a number of different accident conditions. It is noted that milder accidents which lead to the decay heat removal by near natural convection boiling have much higher probability than those of severe accidents extensively studied recently. Furthermore, the break-down of natural convection boiling which results in dryout and burnout of heated surface in these conditions can lead to very significant consequences.

A number of works have been performed on the CHF for water flowing in annular channels [1-10]. However, only few data are available for the CHF at low-flow-rate and low-pressure conditions[11], because most of those are concerned with the CHF for high pressure systems in relation to the core cooling of a light water reactor (LWR) [4-9] or with the CHF for subcooled boiling at high flow conditions [1-3].

In view of the above, an experimental study has been performed on the CHF at low flow rates typical of natural convection conditions for water flowing in an annulus at atmospheric pressure. An internally heated annular test section was employed in order that the observation of the flow regimes at burnout could be made.

## IV.2. CRITICAL HEAT FLUX EXPERIMENT

### IV.2.1. Test Loop

The test loop initially set up for Freon-11 blowdown tests [12] at Argonne National Laboratory in the U.S. was modified for this study as shown in Fig. 1. It consisted of a test section, upper and lower plena, hot and cold legs, a downcomer, a bypass loop, a circulating pump, flow control valves and a turbine flow meter. The test loop was thermally insulated by Fiberglass material except the test section.

The test section is made of an 86 cm-long, 2.05 cm-OD, directly heated, Type 304 stainless steel tube and a 0.9 m-long, 2.60 cm-ID transparent Pyrex pipe. Twenty-two 0.762 mm-OD, Chromel-Alumel thermocouples were spot-welded onto the inside wall of the stainless steel tube as shown in Fig. 2. The detail of the test section was already described in the literature [12].

The downcomer consisted of a 180 cm-long, 15 cm ID stainless steel tube flanged at both ends, equipped with a cooling coil of a 12 m-long, 3 mm-ID copper tube, a 5 kW immersion heater, a steam release valve and a water supply.

A 1.58 cm-ID stainless steel flexible tube was installed in the hot and the cold leg to allow thermal expansion and to avoid the vibration of the test section induced by the pump during forced circulation experiments. The cold leg consisted of two parallel flow paths, one for natural circulation and the other for forced convection. A pump capable of delivering up to 0.5 l/min of water was installed in the latter cold leg.

### IV.2.2. Experimental Procedure

Before starting the measurements, the water in the test loop was

heated up with the immersion heater and the test section heater. During the heatup operation, the power to the test section was kept so low as not to cause dryout on the surface of the heated wall. Power to the test section was supplied by a 20-V, 1500-A, dc power supply. To protect the test section from physical burnout, nine temperature controllers were set to trip the power at a heated-wall temperature of 200°C. The detail of the controllers also appear in the literature [12]. The power to the test section was calculated by measuring the voltage drop across the test section and that across an on-line shunt rated at 50 mV/2000 A.

The loop was filled with ion-exchanged water to a level several centimeters above the hot leg which was observed in the glass tube attached to the downcomer. To avoid overpressure in the loop, the vent valve on top of the downcomer was left open during the experiment. Thus all the measurements were performed under atmospheric pressure.

The water flow rate into the test section was controlled by the valves installed in the cold leg. Test condition covered natural circulation, forced circulation and zero net flow with the inlet valve fully closed. The water flow rate was measured by a turbine flowmeter. The flowmeter was calibrated within 4%.

The temperatures were recorded by a digital recorder. As dry patches were more frequently observed in the surface near the upper end of the heated wall, the temperature at the location of TC 22 was recorded also by a strip chart. A large abrupt increase in the temperature trace was recognized as an evidence of dryout as well as the actuation of the power trip circuit.

In order to observe flow regimes over a wider range of water flow

rate, the flowmeter was replaced by a 1.58 cm-ID pipe in earlier runs, thus reducing the resistance to the flow. In these runs, the flow rate was estimated from the axial profile of the heated-wall temperature, assuming that the single phase heat transfer coefficient was constant over the non-boiling region. If this was true, the water flow rate should be proportional to the reciprocal of the temperature rise along the test section.

## IV.3. EXPERIMENTAL RESULTS

### IV.3.1. Flow Regimes at Burnout

At an early stage of the heatup, the initiation of boiling occurred suddenly with a large slug bubble, followed by intermittent bubble formation. During this period, highly agitated inlet flow was observed as shown in Fig. 3. As the flow approached steady, smaller bubbles were generated more frequently, resulting in a more stable flow.

No significant difference in flow regimes between natural circulation and forced circulation was noticed in the test section. Observed flow regimes are shown in Fig. 4 in comparison with the flow regime map predicted by the previously obtained criteria for flow-regime transitions. The bubbly flow was observed only at low heat flux and large inlet subcooling. The slug flow which appeared in the figure was characterized by the periodic slug bubble formation, although the shape of the bubbles were disturbed by boiling. In the churn flow regime, slug-like bubbles were entirely deformed and less periodic and liquid bridging was typically observed. Dry patches appeared on the surface of the heated wall in this flow regime, though they were quenched away mainly by the passage of liquid bridges. The temperature rise due to dry patch formation was found in the strip chart as shown in Fig. 5.

As the steam quality increased, the liquid bridging became less frequent. Falling liquid film as well as climbing film was observed at low mass velocities. Those liquid film, however, did not seem thick enough to quench dry patches, thus permanent dryout of the heated wall followed. A typical reading of the heated-wall temperature during the dryout is shown in Fig. 5. Some investigators pointed out that the burnout at high steam quality was caused by a film dryout in the annular flow [13-16]. The same mechanism of burnout was observed also in this study, however, it occurred just after the transition from the churn to annular flow at very low inlet mass velocity and low pressure. This is exhibited also in Fig. 4.

IV.3.2. Critical Heat Flux

The critical power to the test section is plotted against mass velocity in Fig. 6. The figure indicates that the critical heat flux for a given test section is well correlated by the mass velocity. The effect of inlet subcooling is not clear in the data. There are no remarkable differences in the critical power results between natural circulation and forced circulation conditions.

It is also suggested that there is a threshold heat flux for burnout to occur. The visual observation confirmed that the occurrence of burnout at zero net flow (complete bottom blockage) is closely related to the flooding phenomenon at the upper end of the test section [17-23]. The critical power to the test section can be estimated using the Wallis correlation for flooding as follows [21,24],

$$j_g^{*1/2} + j_f^{*1/2} = C \quad , \tag{1}$$

where

$$j_g^* = j_g\sqrt{\rho_g/(\Delta\rho gD)} \quad , \tag{2}$$

$$j_f^* = j_f\sqrt{\rho_f/(\Delta\rho gD)} \quad , \tag{3}$$

The numerical value of C is 0.725 for sharp-edged entrances and 0.88 to 1.0 for round-edged entrances. Assuming that the incoming liquid is saturated, we obtain

$$Q = Ah_{fg}\rho_g j_g \quad . \tag{4}$$

Equations (1) through (4) and the mass balance equation yield the following result for the flooding limited power to the test section.

$$Q = \frac{C^2 h_{fg} A\sqrt{\rho_g g\Delta\rho D}}{[1 + (\rho_g/\rho_f)^{1/4}]^2} \quad . \tag{5}$$

From Eq.(5) the critical power to the test section is estimated to be 1.0 to 1.9 kW which agrees well with the results shown in Fig. 6.

As was mentioned in the previous section, the burnout at low mass velocities occurred due to churn to annular flow transition. The criterion for the transition has been developed previously in Chapter II based upon the flow reversal condition within the liquid film in the churn-flow bubble section. The criterion can be expressed as

$$j_g\sqrt{\rho_g/(\Delta\rho gD)} = \alpha - 0.11 \qquad (\alpha \geq \alpha_m) \tag{6}$$

where

$$\alpha_m = 1 - 0.813 \left[ \frac{(C_0 - 1)j + 0.35\sqrt{\Delta\rho g D/\rho_f}}{j + 0.75\sqrt{\Delta\rho g D/\rho_f} \left( \frac{g\Delta\rho D^3}{\rho_f \nu_f^2} \right)^{1/18}} \right]^{0.75} \tag{7}$$

Here the void fraction $\alpha$ is given based on the drift velocity for the churn flow regime as

$$\alpha = \frac{j_g}{C_0\, j + \sqrt{2} \left( \frac{\sigma g \Delta\rho}{\rho_f^2} \right)^{1/4}} \quad . \tag{8}$$

The distribution parameter $C_0$ is given for a pipe by [25]

$$C_0 = 1.2 - 0.2\sqrt{\rho_g/\rho_f} \tag{9}$$

The energy balance in the test section is expressed by

$$Q = (h_{fg}\rho_g j_g + \Delta h_i G)\, A \quad . \tag{10}$$

Using the relationship for $j_g$ , $j_f$ and $j$ , and from Eq.(10), the following equations can be derived:

$$j_g = \frac{Q}{A h_{fg} \rho_g} - \frac{\Delta h_i}{h_{fg}} \frac{G}{\rho_g} \quad , \tag{11}$$

$$j = \frac{Q\Delta\rho}{A h_{fg} \rho_g \rho_f} + \left( 1 - \frac{\Delta h_i}{h_{fg}} \frac{\Delta\rho}{\rho_g} \right) \frac{G}{\rho_f} \quad . \tag{12}$$

Now we introduce the following non-dimensional groups:

$$q^* = \frac{Q}{h_{fg} A_h \sqrt{\lambda \rho_g g \Delta\rho}} \quad , \tag{13}$$

$$G^* = \frac{G}{\sqrt{\lambda \rho_g g \Delta\rho}} \quad , \tag{14}$$

$$D^* = D/\lambda \quad , \tag{15}$$

where $\lambda$ is the Taylor-wave length scale given by

$$\lambda = \sqrt{\sigma/(g\Delta\rho)} \quad . \tag{16}$$

The non-dimensional group, Eq.(13) is originally derived by Zuber [26] and Kutateladze [27] from the consideration on the hydraulic instability. Using Eqs. (13) through (16), Eqs. (11) and (12) can be rewritten as

$$j_g = J\sqrt{\lambda g \Delta\rho/\rho_g} \quad , \tag{17}$$

$$j = \left( J \frac{\Delta\rho}{\rho_f} + \frac{\rho_g}{\rho_f} G^* \right) \sqrt{\lambda g \Delta\rho/\rho_g} \quad , \tag{18}$$

where

$$J = q^* A_h/A - \frac{\Delta h_i}{h_{fg}} G^* \quad . \tag{19}$$

In this study, $\Delta h_i/h_{fg}$ was large enough compared to $\rho_g/\Delta\rho$, then the

second term on the right hand side of Eq.(18) can be neglected.

$$j \simeq J \frac{\Delta\rho}{\rho_f} \sqrt{\lambda g \Delta\rho / \rho_g} \quad . \tag{20}$$

Finally, from Eqs.(6) and (8) we obtain

$$J = \sqrt{D^*} \left( \frac{J}{C_0 \, J \frac{\Delta\rho}{\rho_f} + \sqrt{2\rho_g / \rho_f}} - 0.11 \right) \quad . \tag{21}$$

Equation (21) can be solved with the condition $\alpha > \alpha_m$ to give

$$J = \frac{1}{2} \left( \frac{\rho_f \sqrt{D^*}}{C_0 \Delta\rho} - \frac{\sqrt{2\rho_f \rho_g}}{C_0 \Delta\rho} - 0.11\sqrt{D^*} \right)$$

$$+ \frac{1}{2} \left[ \left( \frac{\rho_f \sqrt{D^*}}{C_0 \Delta\rho} - \frac{\sqrt{2\rho_f \rho_g}}{C_0 \Delta\rho} - 0.11\sqrt{D^*} \right)^2 - 0.4 \frac{\sqrt{2D^* \rho_f \rho_g}}{C_0 \Delta\rho} \right]^{1/2} \quad . \tag{22}$$

For low pressure steam-water flow, $\rho_g / \rho_f$ can be neglected in Eq.(22) and $\Delta\rho \cong \rho_f$ , then

$$J \simeq \left( \frac{1}{C_0} - 0.11 \right) \sqrt{D^*} \quad , \tag{23}$$

or more explicitly,

$$q^* = \frac{A}{A_h} \left[ \frac{\Delta h_i}{h_{fg}} G^* + \left( \frac{1}{C_0} - 0.11 \right) \sqrt{D^*} \right] \quad . \tag{24}$$

In terms of the critical heat flux, Eq.(24) becomes

$$q_c = \frac{A}{A_h}\left[\Delta h_i\, G + \left(\frac{1}{C_0} - 0.11\right) h_{fg}\sqrt{\rho_g \Delta\rho g D}\right] \quad . \tag{25}$$

Comparison of q* predicted by Eq.(24) with the experimental data can be found in Fig. 7 which shows a reasonable agreement between them.

## IV.4. DISCUSSIONS

### IV.4.1. Burnout Mechanisms

Barnard et al.[28] investigated dryout at low flow rate for an upward flow of Freon-113 in a vertical tube. They classified the burnout mechanisms into five types. When the flow passages are substantially filled with liquid, the burnout will occur due to the vapor production by boiling which prevents liquid from reaching the heated surface. This is the pool-boiling burnout. Flooding limited burnout occurs at zero net flow through the flow passage when the vapor flow prevents a sufficient downward flow of liquid. When the flow rate through the flow passage is not zero but very low, all the liquid entering the passage from the bottom will be evaporated and the vapor flow will prevent liquid flowing down from the top. This type of burnout is called a circulation and flooding limited burnout. As the flow rate from the bottom increases, the vapor flow becomes sufficiently high to prevent any liquid flowing down the flow passage from the top. In this case, dryout occurs when the vapor quality approaches to unity. This is called a circulation limited burnout which was referred to as the high-quality CHF in Chapter I. For higher flow rates, a substantial amount of the liquid will be entrained by the vapor flow, which causes dryout at vapor qualities less than unity. This is called entrainment

limited burnout. The last two types have often been referred to as a basic mechanism of burnout in annular two-phase flow [13-16].

However, the observation in this study indicated the possibility of burnout caused by the flow-regime transition from churn to annular flow as was discussed in the previous section. This type of burnout occurred over the same range of mass velocity as circulation limited burnout. At the present, the boundary between these two different types of burnout cannot be predicted with high certainty. It will be interesting to note that film dryout did cause the burnout due to the churn-to-annular flow transition but liquid film still remained on the unheated wall in that case.

IV.4.2. CHF Correlations

IV.4.2.1. Pool boiling CHF

Zuber [26] and Kutateladze [27] proposed essentially the same correlation for pool-boiling CHF, given by

$$q = K\, h_{fg}\rho_g(\sigma g^2 \Delta\rho/\rho_g^2)^{1/4}\left(\frac{\rho_f}{\rho_f + \rho_g}\right)^n \quad . \tag{26}$$

Zuber derived this equation from the consideration on the stability of vapor-liquid interface [26]. On the other hand, Kutateladze obtained it by correlating the experimental data using non-dimensional parameters. Thus he found that

$$K = 0.16 \text{ and } n = 0 \quad .$$

Then Eq.(26) can be rewritten by using the non-dimensional groups

defined by Eqs.(13) through (16) as

$$q^* = 0.16 \quad . \tag{27}$$

IV.4.2.2. Flooding CHF

The heat flux at burnout due to flooding can be calculated by Eq.(5), which is expressed in a non-dimensional form as follows,

$$q^* = C^2\zeta \quad , \tag{28}$$

where

$$\zeta = \frac{A\sqrt{D^*}}{A_h[1 + (\rho_g/\rho_f)^{1/4}]^2} \quad . \tag{29}$$

In terms of the CHF, this criterion becomes

$$q_c = \frac{A}{A_h} \frac{C^2 h_{fg}\sqrt{\rho_g \Delta\rho g D}}{[1 + (\rho_g/\rho_f)^{1/4}]^2} \quad . \tag{30}$$

A reasonable agreement between Eq.(28) and the experimental data under various conditions [17-19, 28] is shown in Fig. 8. As Block and Wallis [21] pointed out, the CHF tends to be constant for small L/D which means that the burnout is limited by the local heat flux. Then it may be deduced that the pool-boiling type burnout will occur in a very short tube. The transition from the pool-boiling type to flooding limited CHF can be calculated from Eqs.(27) and (28) as

$$C^2\zeta = 0.16 \quad . \tag{31}$$

Thus the non-dimensional CHF q* for these two regimes can be given as a function of $\zeta$ as illustrated in Fig. 8.

In the previous section Eq. (24) was derived as the CHF caused by churn-to-annular flow transition. The criterion for the transition is based on the assumption that liquid film flow changes the direction from downward to upward at transition. Thus, when G* = 0 in Eq.(24), it should give the flooding condition. Actually, when G* = 0, Eq.(24) becomes

$$q^* = \frac{A}{A_h}\left(\frac{1}{C_0} - 0.11\right)\sqrt{D^*} \quad . \tag{32}$$

Comparing Eqs.(28), (29) and (32), we obtain

$$C^2 = \left(\frac{1}{C_0} - 0.11\right)\left[1 + (\rho_g/\rho_f)^{1/4}\right]^2 \quad . \tag{33}$$

For water under atmospheric pressure, the numerical value of the right hand side in Eq.(33) is 0.97 which agrees well with that of $C^2$ given by Wallis [24].

Furthermore in a very rapid transient it can be said that the flow may not develop to the flooding condition. In such a case, the pool-boiling type CHF criterion may still be used for a short time period.

IV.4.2.3. Circulation and flooding limited CHF

The model for this regime is illustrated in Fig. 9. Now we postulate that all the liquid entering the heated section from the bottom is evaporated and the liquid from the top is limited by flooding due to high steam flow, resulting in a dryout on the heated surface.

The heat balance can be expressed as

$$Q = A\ (h_{fg}\rho_g j_g + \Delta h_i G) \quad . \tag{34}$$

and

$$\rho_g j_g = \rho_g j_{gc} + \rho_f j_f \quad . \tag{35}$$

Here $\rho_f j_f$ is the liquid mass flux from the top and $\rho_g j_{gc}$ is the total evaporated mass flux from the bottom. From the assumption that all the liquid entering from the bottom is evaporated, we obtain

$$G = \rho_g j_{gc} \tag{36}$$

Using non-dimensional groups defined previously, Eqs.(1), (35) and (36) yield,

$$(1 - \sqrt{\rho_g/\rho_f})\ j_g^* - 2Cj_g^{*1/2} + \frac{G^*}{\sqrt{D^*}}\sqrt{\rho_g/\rho_f} + C^2 = 0 \quad . \tag{37}$$

Equation (37) is a quadratic form of $j_g^{*\frac{1}{2}}$ and has real solutions if

$$C^2 \geq (1 - \sqrt{\rho_g/\rho_f})\ G^*\sqrt{D^*} \quad . \tag{38}$$

Inequality (36) is met when

$$j_f^* = (j_g^* - G^*/\sqrt{D^*})\sqrt{\rho_g/\rho_f} \geq 0 \quad . \tag{39}$$

Equations (1)-(3) require that

$$j_g^{*1/2} = \frac{C}{1 + (\rho_g/\rho_f)^{1/4}} \quad , \tag{40}$$

when G* approaches to zero. Therefore we arrive at the solution

$$j_g^{*1/2} = \frac{C - \sqrt{C^2\sqrt{\rho_g/\rho_f} - (1 - \sqrt{\rho_g/\rho_f})\, G^*\sqrt{\rho_g/(\rho_f D^*)}}}{1 - \sqrt{\rho_g/\rho_f}} \quad . \tag{41}$$

Finally, non-dimensional heat flux is derived by using Eqs.(34) and (41) together with the definition of non-dimensional groups.

$$q^* = \frac{A\sqrt{D^*}}{A_h}\left[\left(\frac{C}{1+\sqrt[4]{\rho_g/\rho_f}}\right)^2\left(\frac{1-\sqrt[4]{\rho_g/\rho_f}\sqrt{1-(\sqrt{\rho_f/\rho_g}-1)G^*\sqrt{\rho_g/(\rho_f D^*)}/C^2}}{1 - \sqrt[4]{\rho_g/\rho_f}}\right)^2 + \frac{\Delta h_i}{h_{fg}}\frac{G^*}{\sqrt{D^*}}\right] \quad . \tag{42}$$

IV.4.2.4. Circulation limited CHF (high-quality CHF)

This type of burnout is characterized by complete evaporation of the liquid entering from the bottom and no liquid flow from the top. Therefore, letting

$$j_f^* = (j_g^* - G^*/\sqrt{D^*})\sqrt{\rho_g/\rho_f} = 0 \quad , \tag{43}$$

and

$$j_g^* = C^2 \quad . \tag{44}$$

in Eq. (39), we obtain for CHF,

$$q^* = \frac{A}{A_h} G^* \, (1 + \Delta h_i / h_{fg}) \quad . \tag{45}$$

It should be noted here that for the channel with an unheated wall, it is possible that there still remains a liquid film on the unheated wall when a burnout occurs. In such cases, the exit quality at burnout (critical quality, $x_c$) can be much less than unity, i.e. Eq.(45) can be rewritten as

$$q^* = \frac{A}{A_h} G^* \, (x_e + \Delta h_i / h_{fg}) \tag{46}$$

and Eq.(42) should be also changed accordingly.

IV.4.2.5. Entrainment limited CHF

There have been some attempts to calculate the CHF in this regime using annular flow model [14-16]. Whalley et al.[29] obtained an encouraging result from their analysis. However, no generalized correlation has been presented in an explicit form. An example of entrainment limited burnout was given by Barnard et al.[28] for Freon-113 in round tubes. They interpreted their experimental results using annular flow model of Whalley et al.[29] assuming a simple empirical equation for entrainment fraction. Their data on mass velocity versus critical quality at burnout are plotted in Fig. 10, in comparison with the flow regime map previously obtained. The figure shows that the most of the data of CHF fall in the annular-mist flow

regime, which is consistent with the observation in the experiment [28]. The relationship between the CHF and the mass velocity for Freon-113 is shown in a non-dimensional form in Fig. 11. Some existing CHF correlations are also shown in the figure.

The Katto correlation scheme was developed from a wide variety of experimental data for forced circulation CHF in round tubes using a dimensional analysis [30] and later modified for annuli [10]. The equation for the L-regime becomes

$$\frac{q}{h_{fg}G} = C_L\left(\frac{\sigma\rho_f}{G^2L}\right)^{0.043}\frac{D}{L}\,(1 + 1.16\Delta h_i/h_{fg}) \quad , \tag{47}$$

where $C_L$ = 0.34 for Freon and = 0.25 otherwise, or in a non-dimensional form used in this study

$$q^* = C_L\,\frac{D}{L}\left(\frac{\rho_f\lambda}{\rho_g L}\right)^{0.043} G^{*0.914}\;(1 + 1.16\Delta h_i/h_{fg}) \quad . \tag{48}$$

Equation (48) is similar to Eq.(45) as the term $(\rho_f\lambda/\rho_g/L)^{0.043}$ is close to unity. This agrees with Katto's statement that the burnout in the L-regime is caused mainly by the dryout of the liquid film on the heated surface when the fraction of liquid entrained in the gas core is small. Another Katto's equation is, for the H-regime,

$$\frac{q}{h_{fg}G} = 0.1\,(\rho_g/\rho_f)^{0.133}\left(\frac{\sigma\rho_f}{G^2L}\right)^{1/3}\frac{1 + K_H\Delta h_i/h_{fg}}{1 + 0.0031\;L/D} \quad , \tag{49}$$

where

$$K_H = 1.8\left(\frac{L/D}{130}\right)^{-5\rho_g/\rho_f} \tag{50}$$

for $\sigma\rho_f/G^2L < 3 \times 10^{-6}$ , and

$$K_H = 0.075 \left( \frac{L/D}{130} \right)^{-5\rho_g/\rho_f} \left( \frac{\sigma\rho_f}{G^2L} \right)^{-1/4}$$

for $\sigma\rho_f/G^2L < 3 \times 10^{-6}$ .

Equation (49) is expressed in an analogous form to Eq.(48) as

$$q^* = 0.1\, G^{*1/3}\, (\lambda/L)^{1/3}\, (\rho_f/\rho_g)^{0.2}\, \frac{1 + K_H\, \Delta h_i/h_{fg}}{1 + 0.0031\, L/D} \quad . \qquad (51)$$

Katto interpreted that the burnout in the H-regime was affected by hydrodynamic instability. However, it can be seen from the figure that the entrainment-limited burnout data of Barnard et al.[28] are well reproduced by these correlations.

The broken lines in Fig. 11 represent the boundaries between the churn flow regime and the annular flow regime predicted by Eq.(24). The equation was derived assuming that $\Delta h_i/h_{fg}$ is large enough compared to $\rho_g/\Delta\rho$. The test condition of Barnard et al.[28] meets with this condition. However, the figure shows that the measured CHF is far above the churn-to- annular flow transition boundary. The bold line in Fig. 11 represents the onset of entrainment based on the criterion developed by Ishii et al.[31]. According to the criterion, liquid entrainment will occur when the following inequalities are met,

$$\frac{\mu_f j_g}{\sigma} \sqrt{\rho_g/\rho_f} > 11.78\, N_\mu^{0.8}\, Re_f^{-1/3} \quad , \qquad (52)$$

for $Re_f < 1635$, and

$$\frac{\mu_f j_g}{\sigma}\sqrt{\rho_g/\rho_f} > N_\mu^{0.8} \quad . \tag{53}$$

for $Re_f > 1635$ where $N_\mu$ is a viscosity number defined by

$$N_\mu = \frac{\mu_f}{\sqrt{\rho_f \sigma \lambda}} \quad , \tag{54}$$

and

$$Re_f = \frac{\rho_f j_f D}{\mu_f} \quad . \tag{55}$$

Inequalities (52) and (53) can be rewritten by using the definition of non-dimensional groups, and become

$$J(G^* - J)^{1/3} > 11.78\, N_\mu^{2/15}\, D^{*-1/3}\, (\rho_f/\rho_g)^{1/6} \tag{56}$$

for $Re_f < 1635$, and

$$J > N_\mu^{-0.2} \tag{57}$$

for $Re_f > 1635$ where J is defined by Eq.(19). Inequality (56) can be solved numerically by an iterative calculation. A rough estimate, however, can be obtained from the following expression, though it gives only a neccessary condition for Inequality (56).

$$q^* < \frac{A}{A_h}\left[(1 + \Delta h_i/h_{fg})\, G^* - \frac{1.63 \times 10^3}{G^{*3}}\, N_\mu^{2/5}\, D^{*-1}\sqrt{\rho_f/\rho_g}\right] \quad . \tag{58}$$

Inequality (57) also can be rewritten more explicitly as,

$$q^* > \frac{A}{A_h}\left[\frac{\Delta h_i}{h_{fg}} G^* + N_\mu^{-0.2}\right] \quad . \tag{59}$$

As shown in Fig. 11, Inequalities (56) and (57) predict the onset of entrainment to be very close to the churn-to-annular flow transition for this case.

IV.4.3. Discussions

The experimental data obtained from this study are compared with several CHF correlations [10, 28, 32-34] in Fig. 12. The Macbeth correlation [32,33] and the Lowdermilk correlation [34] were originally developed for round tubes. Hence the hydraulic equivalent diameter which appears in the equations was replaced by the heated equivalent diameter for this case. Their correlation consists of two equations: One for the low velocity regime and the other for the high velocity regime in the same manner as the Katto correlation scheme [10]. Barnett correlated experimental data for internally heated annuli assuming a similar form of correlation to that of Macbeth, however, the applicable range is limited to rather high mass velocities.

In Fig. 12, one sees that the data are well correlated by Eq.(24) which has been derived from the criterion for churn-to-annular flow transition. On the other hand, the conventional correlations for high-quality CHF predict much larger CHF than the data, although the correlations agree well with each other. As pointed out earlier, these correlations are valid for entrainment-limited burnout. However, Fig. 12 indicates the existence of different mechanism of dryout. The criterion to specify which mechanism should take place under a given condition is not known at the present time. It is interesting to note that no onset of entrainment is expected in the present case according to the

criterion of Ishii [31] whereas the onset of entrainment is predicted to follow immediately after the churn-to-annular flow transition in the case shown in Fig. 10. Observations in previous works [13-16] revealed that the entrainment and the deposition of liquid droplets could be a controlling factor for film dryout. In other words, we cannot expect droplet quenching in this case, in addition to the reduction of amount of liquid available for cooling of heated surface due to the existence of unheated surface.

Another factor that we should consider is the effect of system pressure on the flow regime transition. For example, the Barnett data for water at 7 MPa in an annulus with approximately the same hydraulic diameter as the present study can be well correlated by the high-quality CHF correlations [4,10] as shown in Fig. 13. It is interesting to note that in this case the churn-annular boundary disappears and the slug-annular boundary appears instead. Therefore, such burnout mechanism as was observed in the present study may be a phenomenon characteristic of low pressure systems.

## IV.5. CONCLUSIONS

An experiment has been performed for water flowing upward in an annulus at low flow rates and the data were compared with existing CHF correlations. The following conclusions can be drawn from the above discussions;

(1) The CHF at zero net flow (complete bottom blockage) can be predicted by flooding correlation which gives much lower CHF for large L/D than pool-boiling CHF.

(2) Visual observation revealed that the burnout at low mass velocities occurred due to liquid film dryout upon the flow regime transition

from the churn to annular flow.

(3) The CHF due to churn-to-annular transition coincides with the flooding CHF at very low mass velocities while it approaches to the condition of zero exit quality at high mass velocities

(4) No difference is observed in the CHF between natural convection and forced convection given the same flow rate.

## NOMENCLATURE

$A$ : Flow area

$A_h$ : Heated area

$C$ : Constant which appears in the flooding correlation

$C_L$ : Constant in the Katto L-regime correlation

$C_0$ : Distribution parameter

$D$ : Hydraulic diameter

$D_h$ : Heated equivalent diameter

$D^*$ : Non-dimensional hydraulic diameter defined by Eq.(15)

$G$ : Mass velocity

$G^*$ : Non-dimensional mass velocity defined by Eq.(14)

$g$ : Gravity

$h_{fg}$ : Latent heat of vaporization

$\Delta h_i$ : Inlet subcooling (enthalpy)

$J$ : Non-dimensional parameter defined by Eq.(19)

$j$ : Volumetric flux of two-phase mixture

$j_k$ : Superficial velocity (volumetric flux) of k phase (k=g or f)

$j_k^*$ : Non-dimensional superficial velocity of k phase (k=g or f)

$j_{gc}$ : Superficial velocity of vapor entering the heated section from the bottom

$K$ : A constant

$L$ : Heated length

$N_\mu$ : Viscosity number as defined by Eq.(54)

$n$ : A constant

$Q$ : Total heat input

$q_c$ : Critical heat flux

$q^*$ : Non-dimensional CHF defined by Eq.(13)

$Re_f$ : Liquid Reynolds number defined by Eq.(55)

$Z$ : Distance from the bottom in the flow direction

### Greek symbols

$\alpha$ : Void fraction

$\alpha_m$ : Mean void fraction in a slug bubble section

$\Delta\rho$ : Difference of the densities of the two phases

$\zeta$ : Non-dimensional parameter defined by Eq.(29)

$\lambda$ : Length scale of the Taylor wave

$\mu_k$ : Viscosity of k phase

$\nu_k$ : Kinematic viscosity of k phase

$\rho_k$ : Density of k phase

$\sigma$ : Surface tension

Subscripts

c : Critical condition

f : Liquid phase

g : Gas or vapor phase

i : Inlet

## REFERENCES


[1] S. Mirshak, W.S. Durant and R.H. Towell, Heat flux at burnout, DP-355 (1959).

[2] R.L. Menegus, Burnout of heating surfaces in water, DP-363 (1959).

[3] D.H. Knoebel, S.D. Harris and B. Crain, Jr., Forced convection subcooled critical heat flux, DP-1306 (1973).

[4] P.G. Barnett, A correlation of burnout data for uniformly heated annuli and its use for predicting burnout in uniformly heated rod bundles, AEEW-R463 (1966).

[5] P.G. Barnett, A comparison of the accuracy of some correlations for burnout in annuli and rod bundles, AEEW-R558 (1968).

[6] E. Jansen and J.A. Kervinen, Burnout conditions for single rod in annular geometry, GEAP-3899 (1963).

[7] S. Bertoletti, G.P. Gaspari, C. Lombardi, G. Peterlongo, M. Silvestri and F.A. Tacconi, "Heat transfer crisis with steam water mixtures," Energie Nucleare, 12, p.121 (1965).

[8] G.F. Hewitt, H.A. Kearsy and J.G. Collier, Correlation of critical heat flux for the vertical flow of water in uniformly heated channels, AERE-5590 (1970).

[9] K.M. Becker, A correlation for burnout predictions in vertical rod bundles, S-349 (1966).

[10] Y. Katto, "Generalized correlation of critical heat flux for the forced convection boiling in vertical uniformly heated annuli," Int. J. Heat Mass Transfer, 22, p.575 (1979).

[11] J.T. Rogers, M. Salcudean and A.E. Tahir, "Flow boiling critical heat fluxes for water in a vertical annulus at low pressure and

velocities," Proc. 7th. Int. Heat Transfer Conference, Munich, Vol.4, Paper No.FB-28, p.339 (1982).

[12] J.C.M. Leung, Occurrence of critical heat flux during blowdown with flow reversal, ANL-77-4 (1977).

[13] G.F. Hewitt, H.A. Kearsy, P.M.C. Lacey and D.J. Pulling, "Burnout and nucleation in climbing film flow," Int. J. Heat Mass Transfer, 8, p.793 (1965).

[14] G.F. Hewitt and N.S. Hall-Taylor, Annular two-phase flow, Pergamon Press, Oxford (1970).

[15] D. Butterworth and G.F. Hewitt, Two-phase flow and heat transfer, Oxford University Press, Oxford (1977).

[16] J.G. Collier, Convective boiling and condensation, McGraw-Hill, London (1972).

[17] P. Griffith, W.A. Schumann and A.D. Neustal, "Flooding and burnout in closed-end vertical tubes," Two-phase fluid flow symposium, Paper No.5, Inst. Mech. Engrs., London (1962).

[18] W.J. Frea, "Two-phase heat transfer and flooding in counter current flow," 4th. Int. Heat Transfer Conference, Paris, Paper No.B5.10 (1970).

[19] H. Kusuda and H. Imura, "Stability of a liquid film in a counter-current annular two-phase flow," Bull. of JSME, 17[114], p.1613 (1974).

[20] Z. Nejat, "Maximum heat flux for countercurrent two-phase flow in a closed end vertical tube," 6th. Int. Heat Transfer Conference, Toronto, Canada (1978).

[21] J.A. Block and G.B. Wallis, "Heat transfer and fluid flows limited by flooding," AIChE Symposium Series, No.174, Vol.74, p.73 (1978).

[22] P. Griffith, C.T. Avedisian and J.P. Walkush, "Counterflow critical heat flux," ibid., p.149 (1978).

[23] M.K. Bezrodny, S.N. Faynzilberg and YE.A. Kondrusik, "Investigation of the maximum heat transfer in annular two-phase thermosyphons," Heat Transfer - Soviet Research, 12[1], p.118 (1980).

[24] G.B. Wallis, Flooding velocities for air and water in vertical tubes, AEEW-R123 (1971).

[25] M. Ishii, One-dimensional drift-flux model and constitutive equations for relative motion between phases in various two-phase flow regimes, ANL-77-47 (1977).

[26] N. Zuber, Hydrodynamic aspects of boiling heat transfer, AECU-4439 (1959).

[27] S.S. Kutateladze, Heat transfer in condensation and boiling, AEC-tr-3770 (1959).

[28] D.A. Barnard, F.R. Dell and R.A. Stinchcombe, Dryout at low mass velocities for an upward boiling flow of Refrigerant-113 in a vertical tube, AERE-R7726 (1973).

[29] P.B. Whalley, P. Hutchinson and G.F. Hewitt, "The calculation of critical heat flux in forced convection boiling," 5th. Int. Heat Transfer Conference, Tokyo, Paper No.b6.11 (1974).

[30] Y. Katto, "A generalized correlation of critical heat flux for the forced convection boiling in vertical uniformly heated round tube, Int. J. Heat Mass Transfer, 21, p.1527 (1978).

[31] M. Ishii and M.A. Grolmes, Inception criteria for droplet entrainment in two-phase concurrent film flow," AIChE J., 21, p.308 (1975).

[32] R.V. Macbeth, Burnout analysis. Part 4: Application of local

conditions hypothesis to world data for uniformly heated round tubes and rectangular channels, AEEW-R267 (1963).

[33] R.V. Macbeth, "The burnout phenomenon in forced-convection boiling," Advances in Chemical Engineering, 7 (1968).

[34] W.H. Lowdermilk, C.D. Lanzo and B.L. Siegel, Investigation of boiling burnout and flow stability for water flowing in tubes, NACA-TN-4382 (1958).

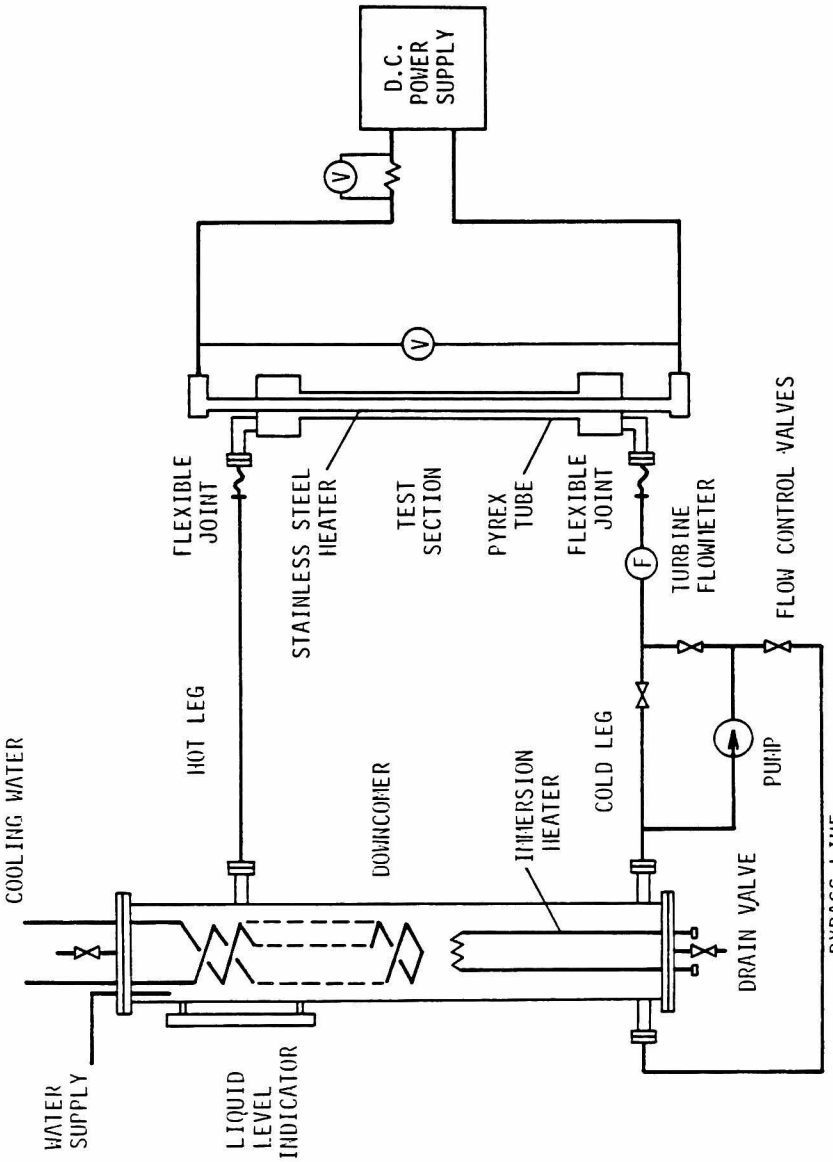


Figure 1 Schematic showing of the test rig.

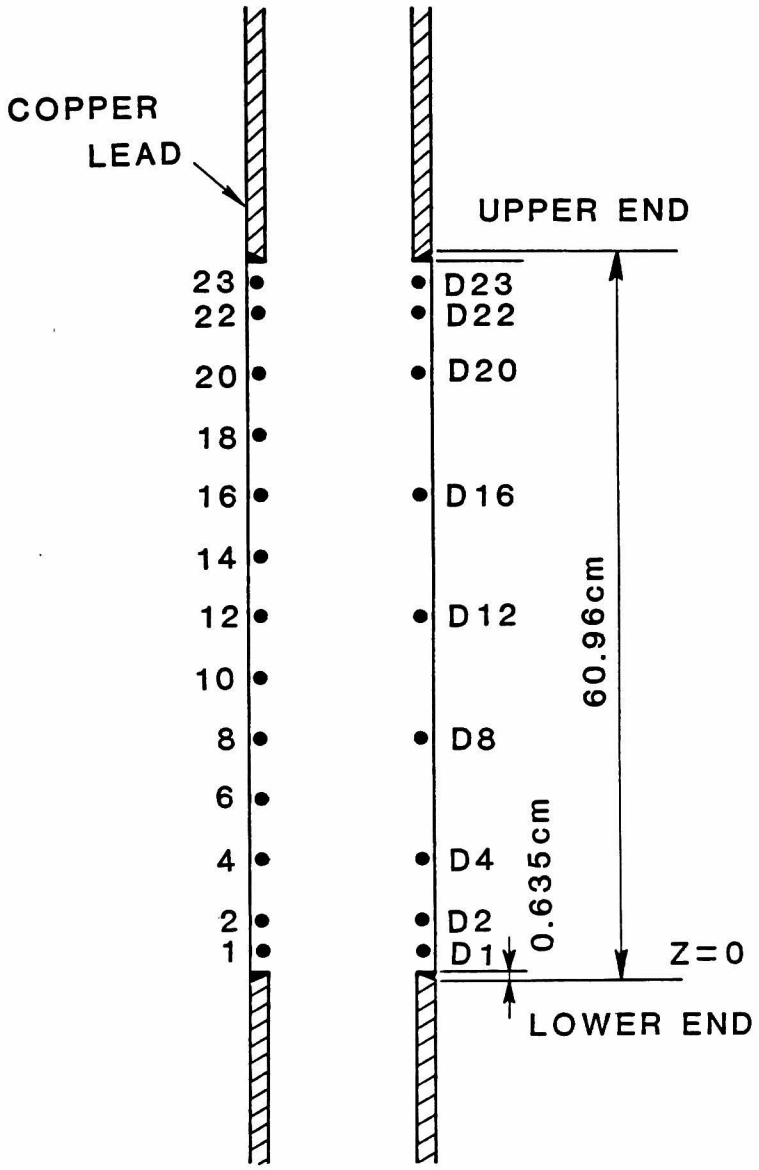


Figure 2 Thermocouple locations. The numbers denote the distance from z = 0 measured in inch.

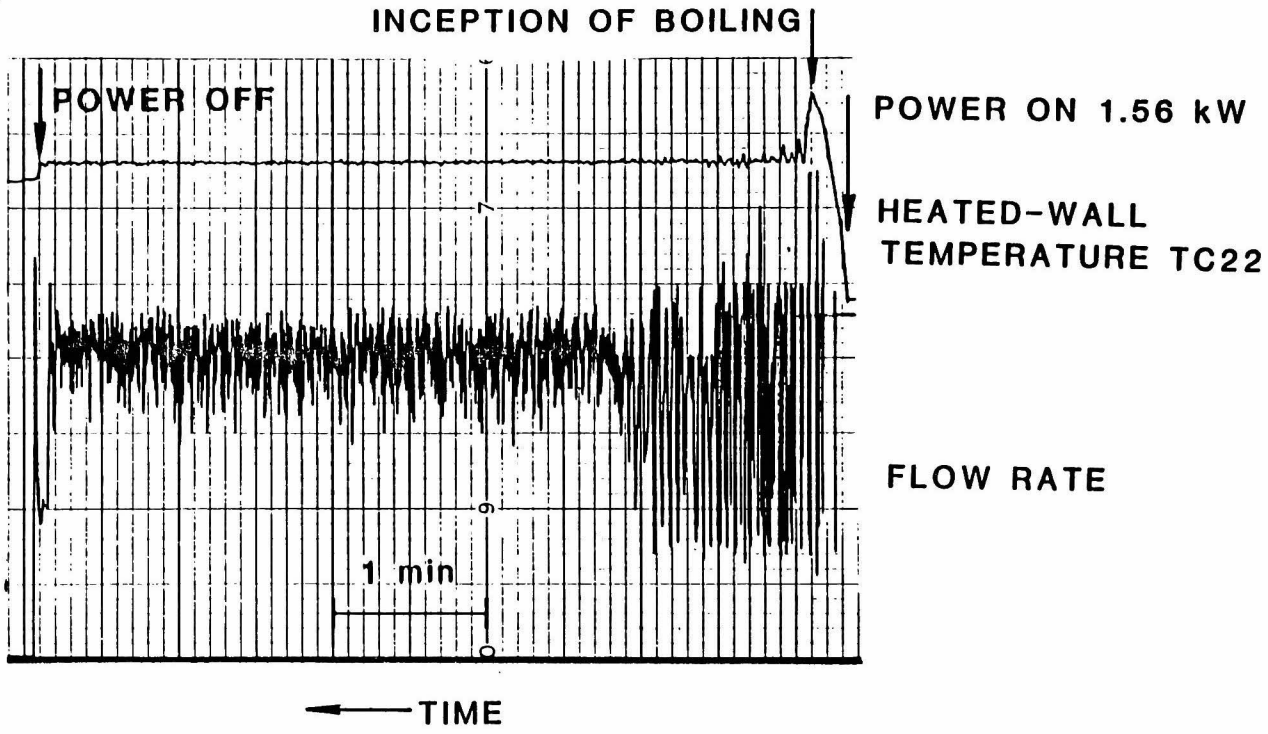


Figure 3 Heated-wall temperature and flow-rate traces at an early stage of heatup.

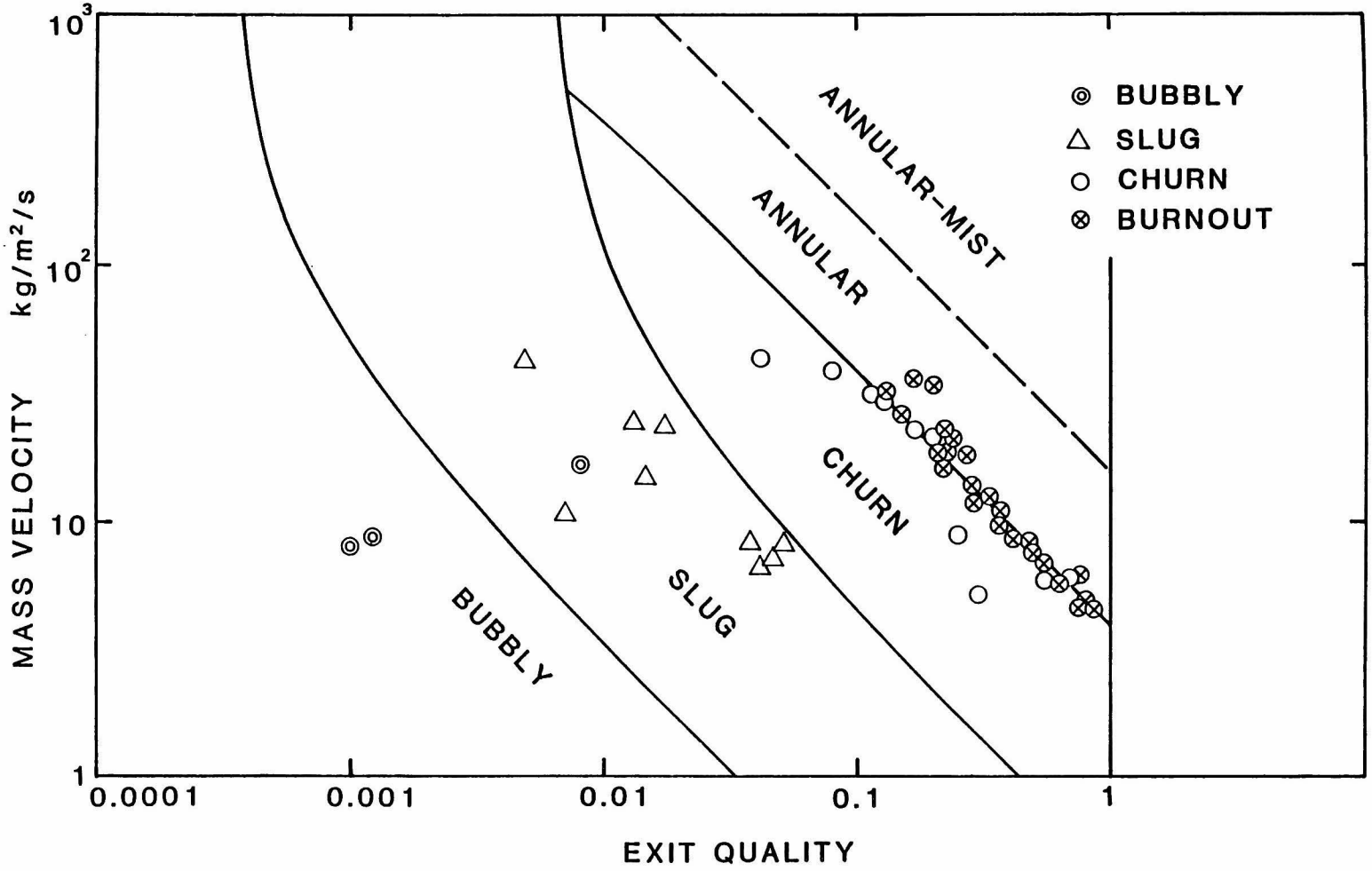


Figure 4 Test conditions plotted in the flow regime map based on the new criteria developed in Chapter II.

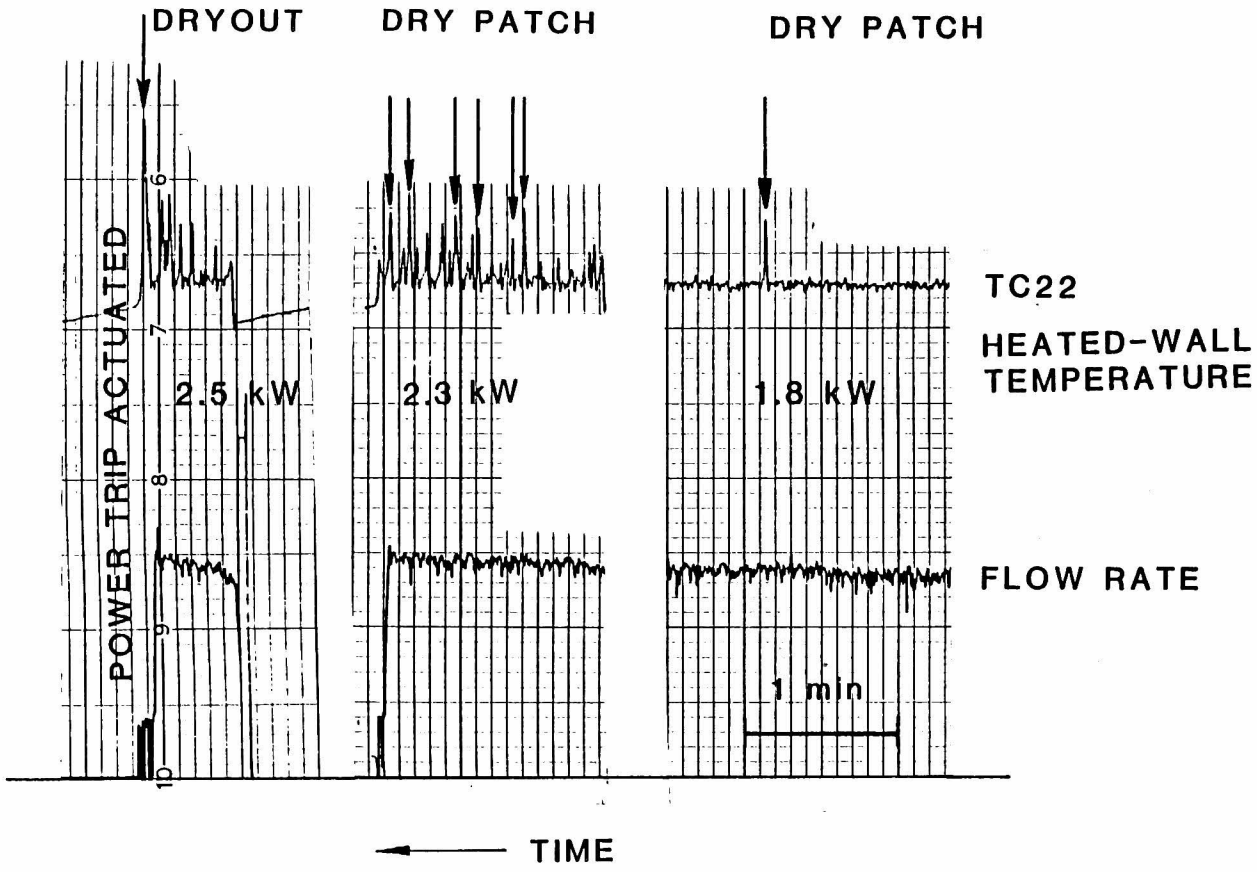


Figure 5 Typical heated-wall temperature and flow-rate traces which resulted in a dryout.

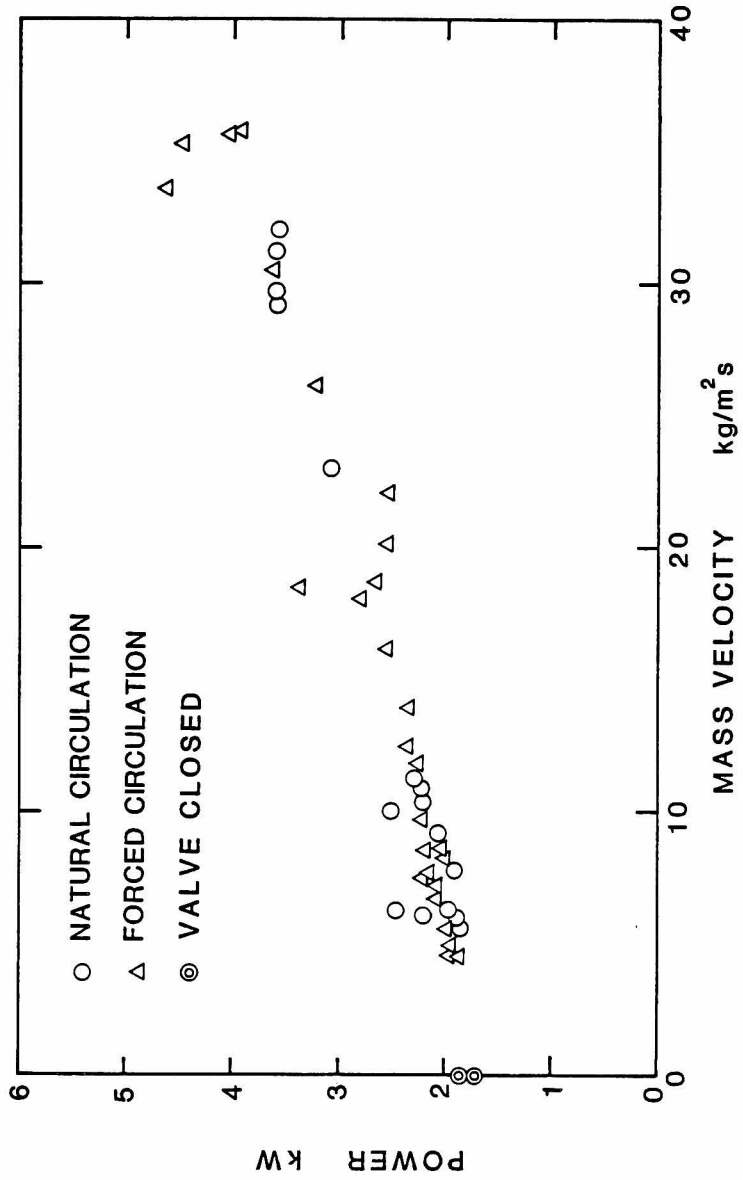


Figure 6 Measured critical power to the test section as a function of mass velocity.

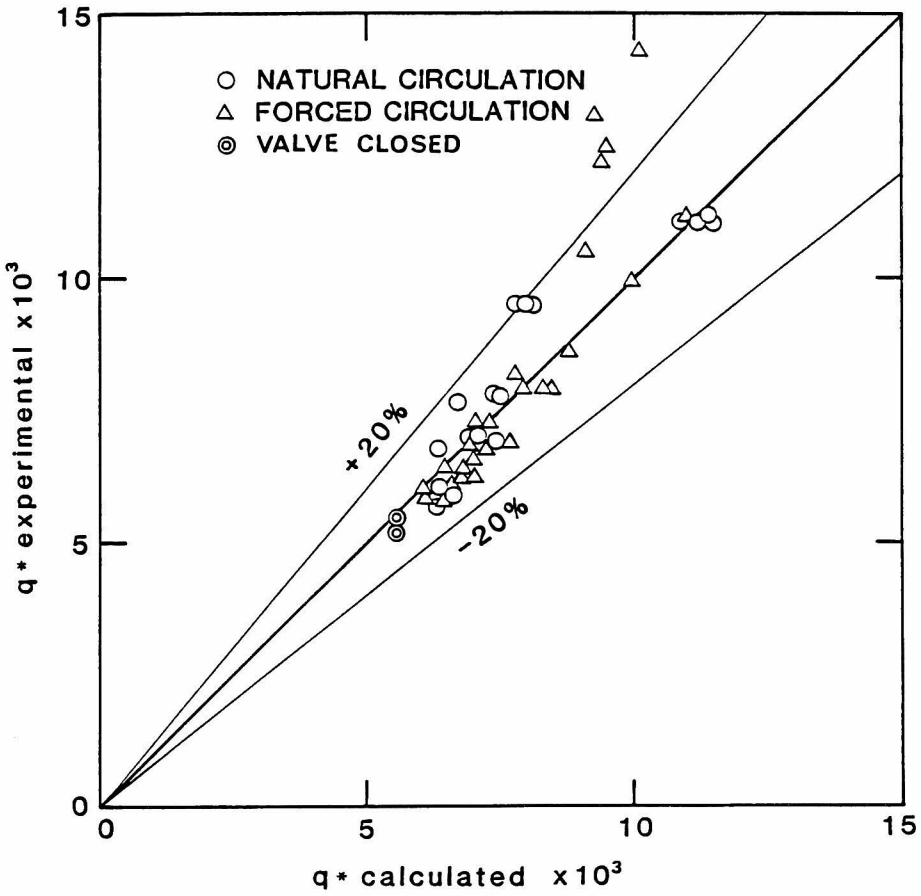


Figure 7 Comparison of predicted non-dimensional CHF with the experimental data.

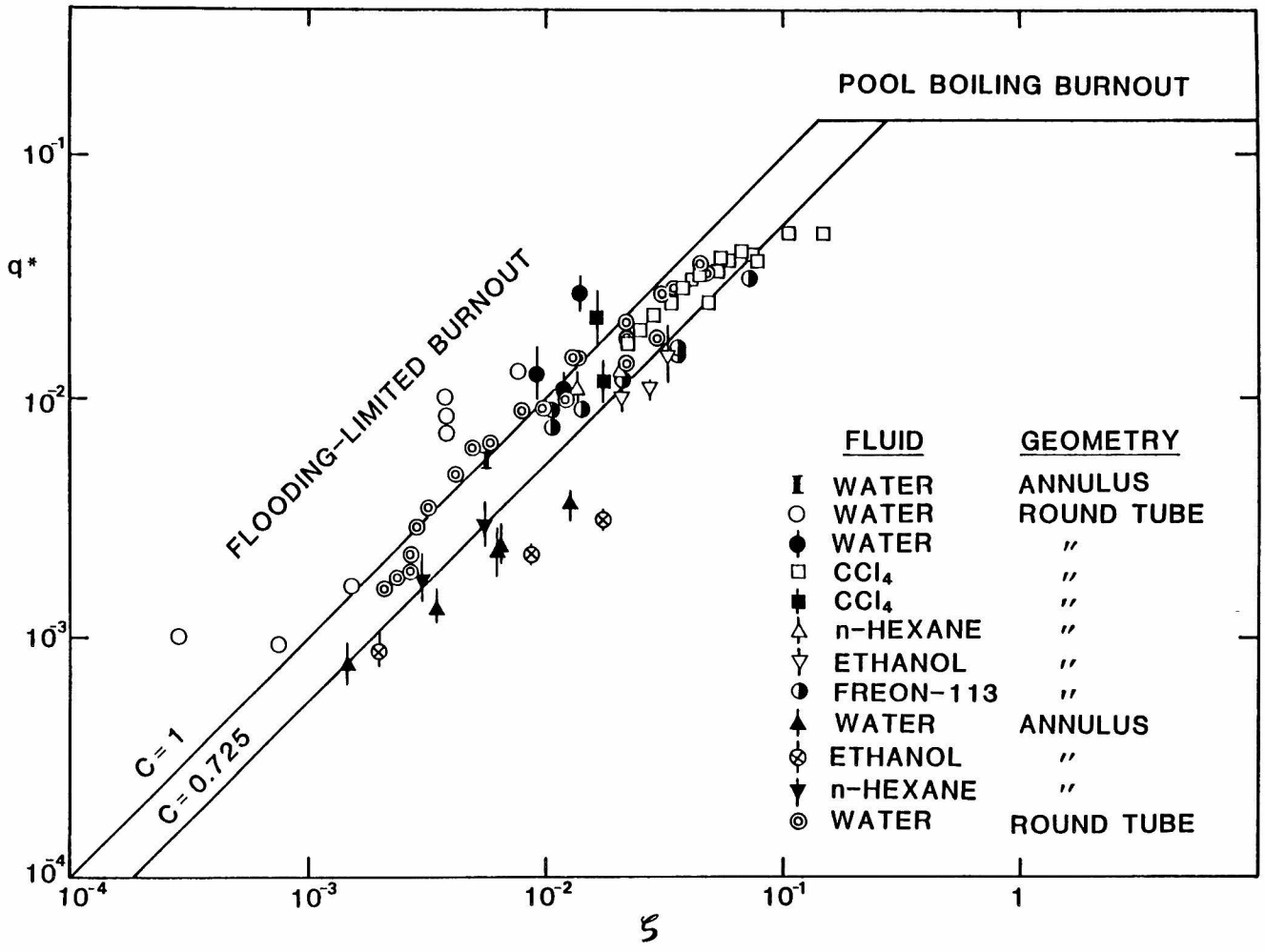


Figure 8 Non-dimensional CHF versus parameter $\zeta$ for flooding limited burnout.

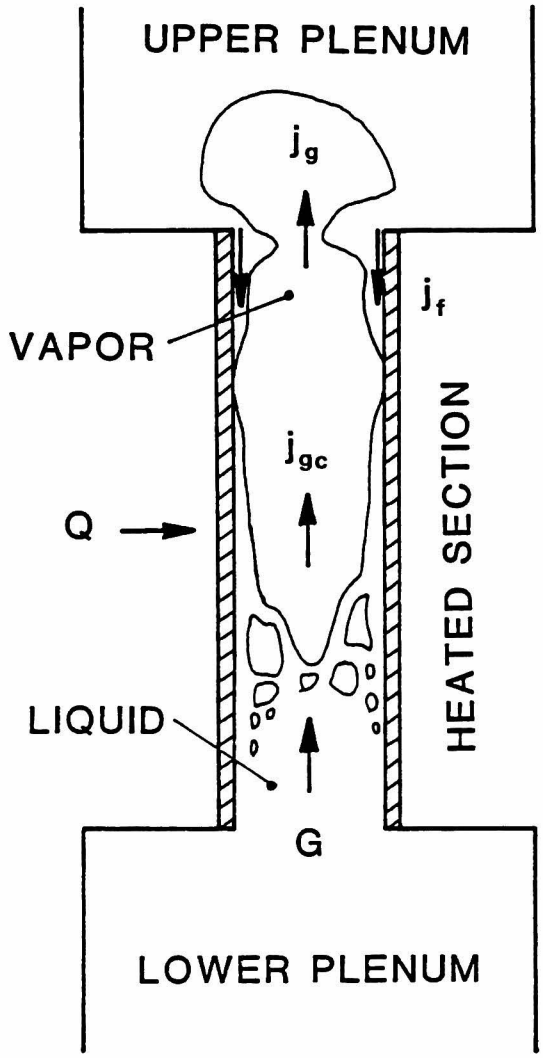


Figure 9 Model for circulation and flooding limited burnout.

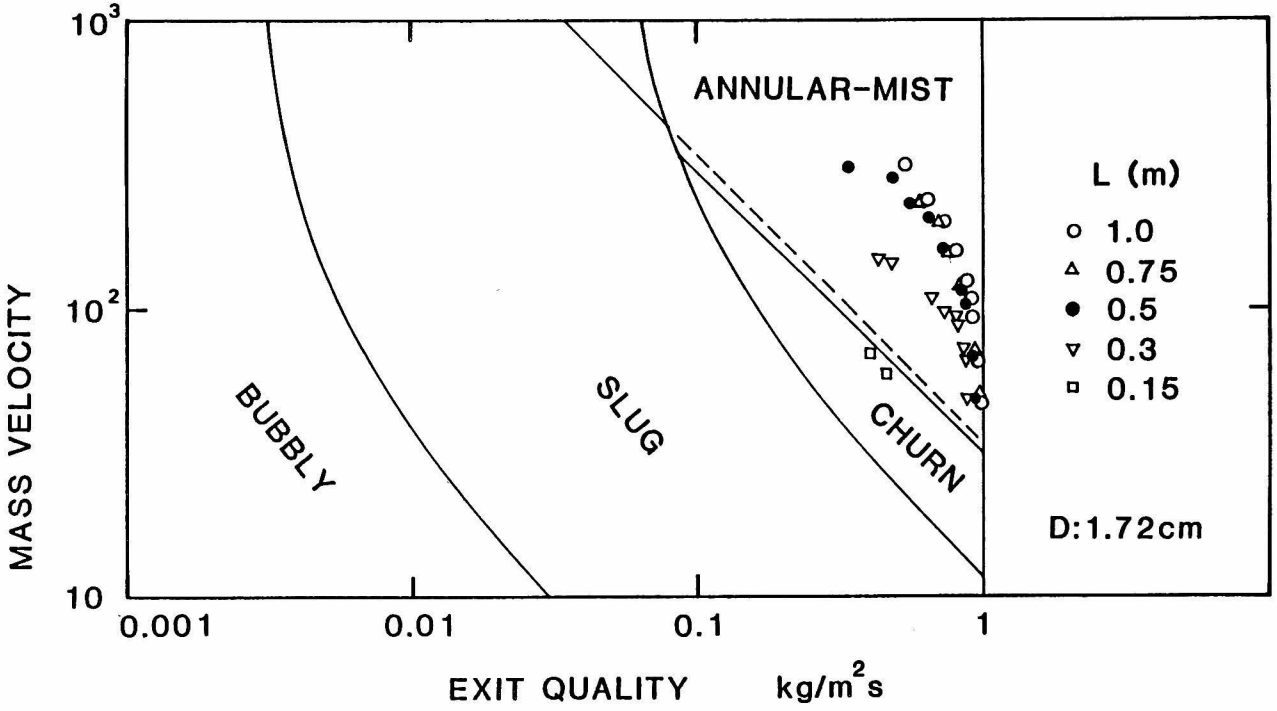


Figure 10 Critical heat flux data of Barnard et al. [20] for Freon-113 plotted in the flow regime map based on the newly developed criteria.

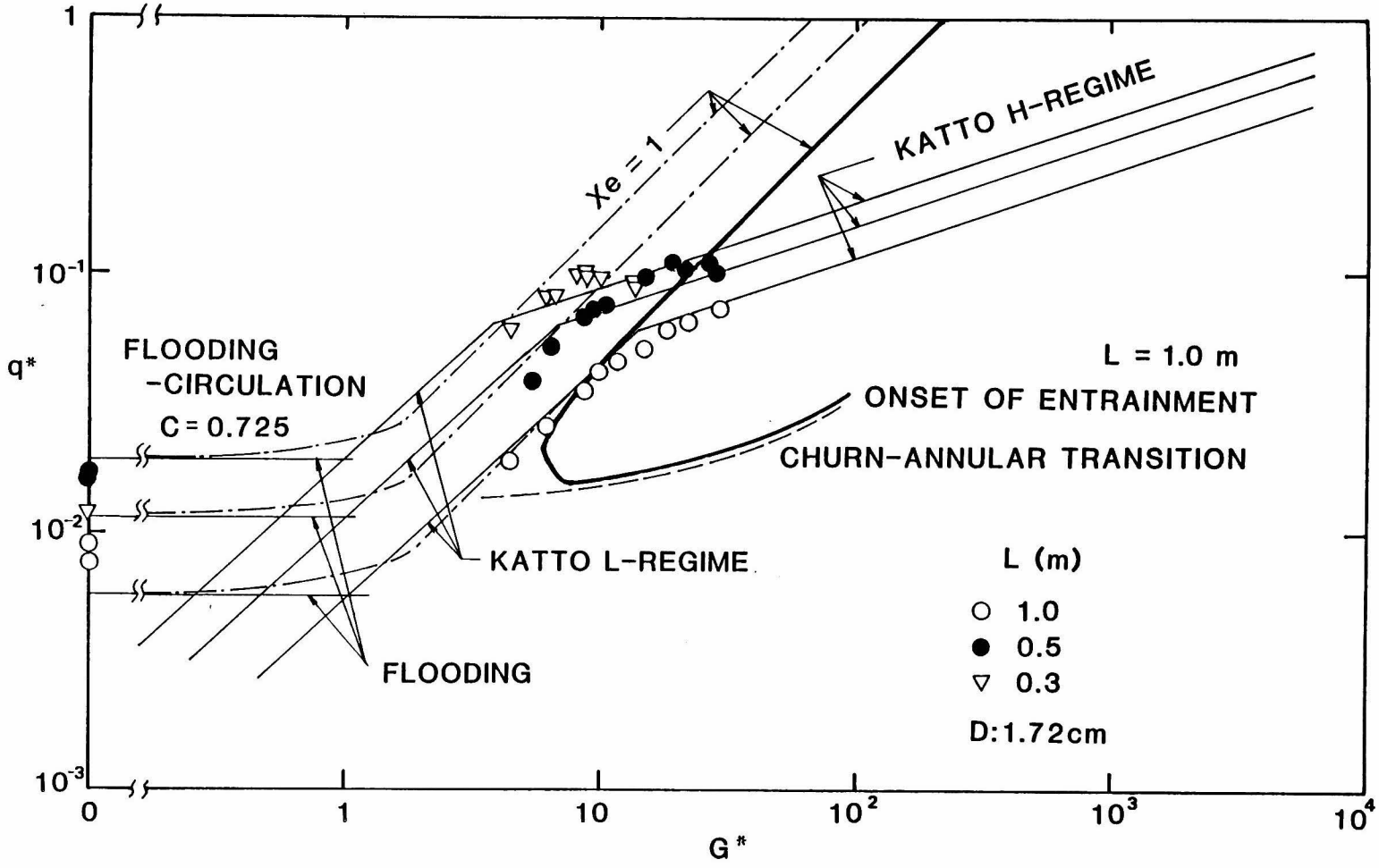


Figure 11 Critical heat flux data of Barnard et al. [20] for Freon-113 compared with several correlations.

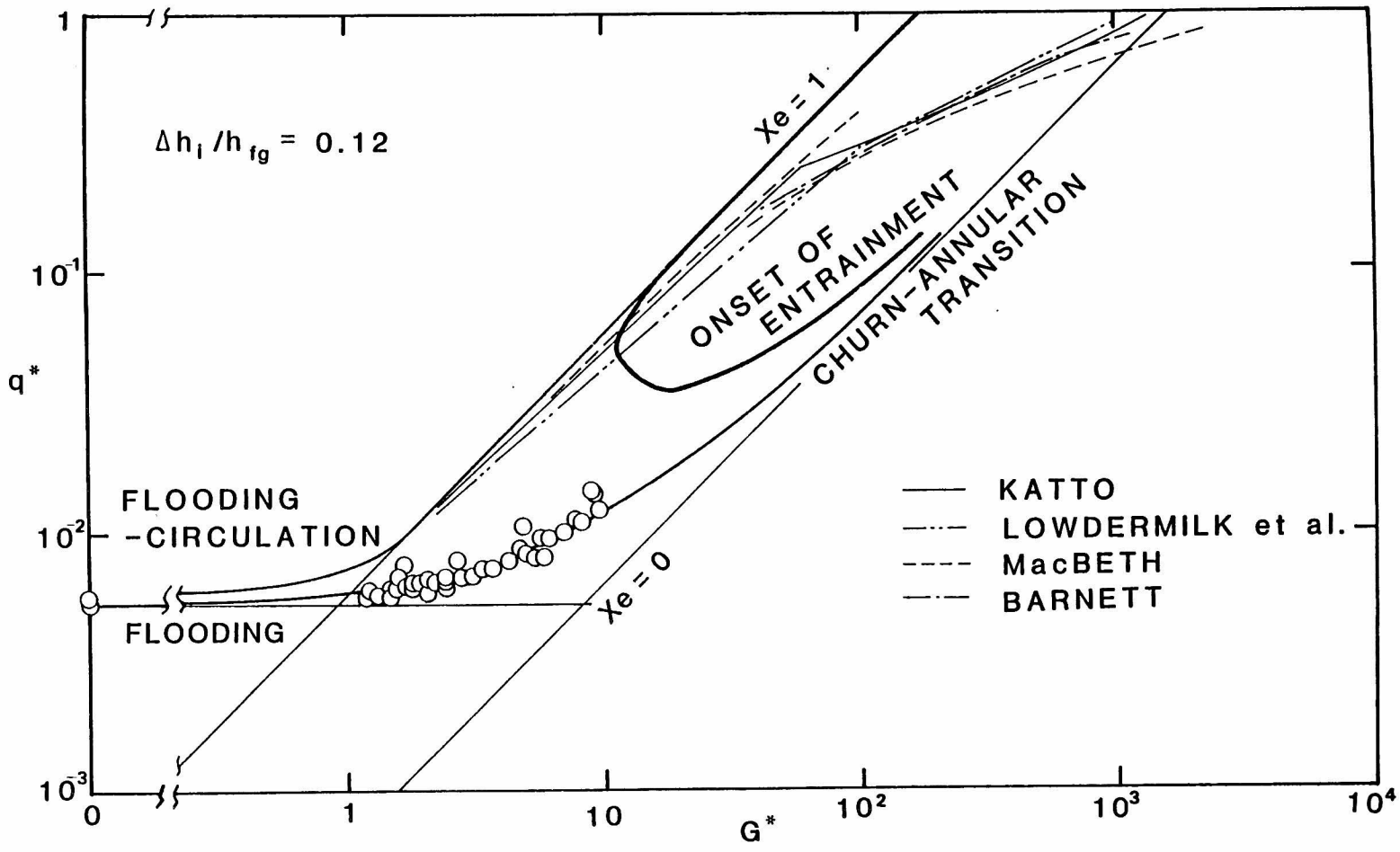


Figure 12 Comparison of the experimental data with several CHF correlations at low pressure and low mass velocities.

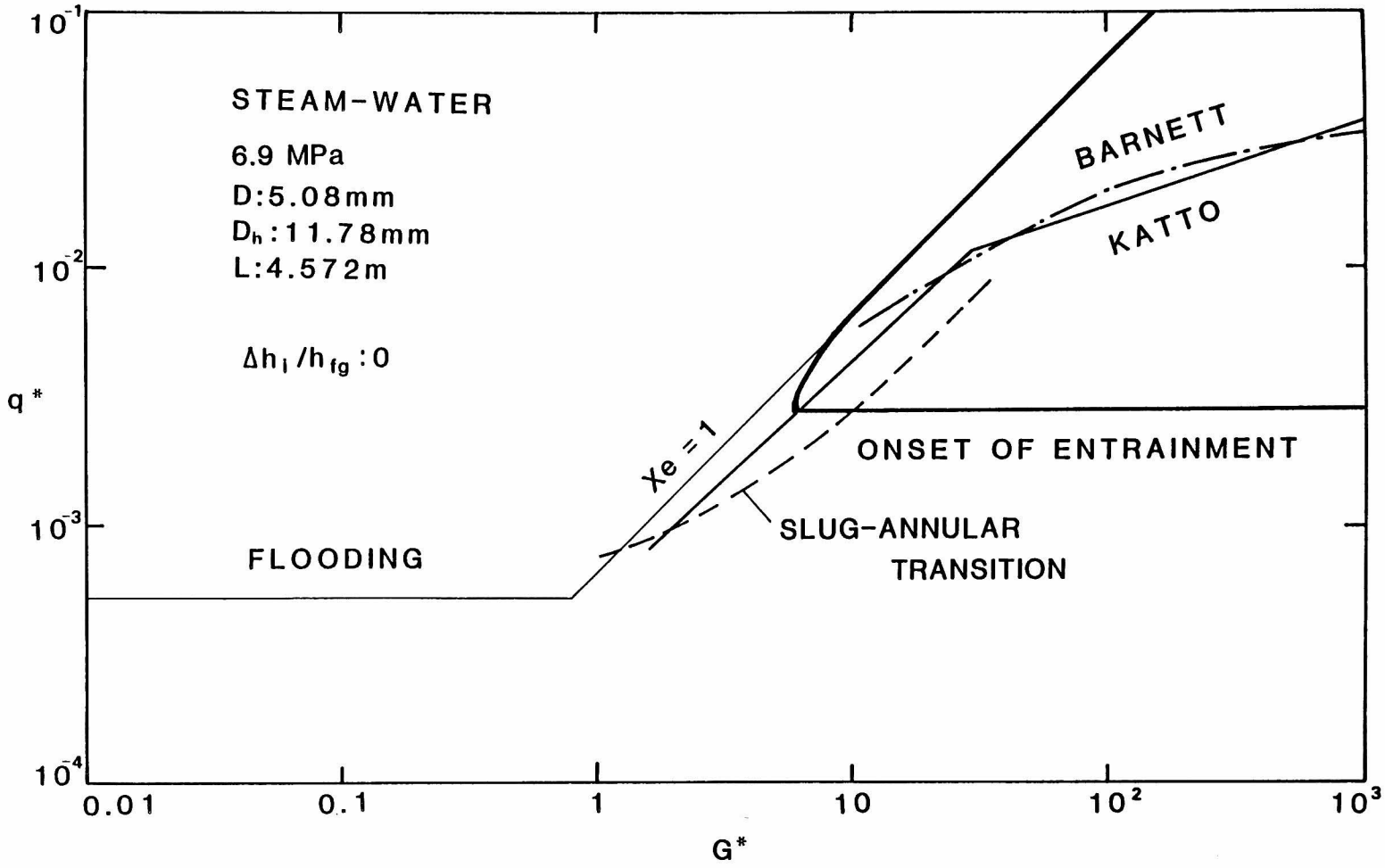


Figure 13 Predicted CHF at low mass velocities and high pressure in comparison with the annular-flow boundary.

# CHAPTER V.

# CRITICAL HEAT FLUX IN ROUND TUBES

## V.1. INTRODUCTION

Numerous and extensive works have been performed on burnout phenomenon in round tubes during two and a half decades. A number of comprehensive reviews on the subject also have been published so far [1-8]. Since the CHF problem has been investigated particularly in the development of nuclear reactors in which the main concerns have been the maximum power extractable from the reactor, much effort has been devoted to the development of the design correlations for CHF predictions at such high-flow-rate/high-pressure conditions as expected in light water reactors (LWR).

On the other hand, less works have been done on CHF at low flow rates. In 1958, Lowdermilk et al.[9] studied burnout phenomenon for water flowing in tubes. For stable flow conditions, they obtained two regimes of burnout, namely the low-velocity/high-exit-quality region and the high-velocity/low-exit-quality region. Later, Macbeth [10] and Thompson and Macbeth [11] compiled world data for water in uniformly heated tubes and correlated them based on the assumption that CHF is linear with the critical quality $x_c$ at given mass velocity, i.e.

$$q_c = F_1(G,P,D) - F_2(G,P,D)\, x_c \quad . \tag{1}$$

Low mass velocity regime and high mass velocity regime were defined and the coefficients given separately for each regimes. Since their

correlations were, however, defined by several constants at each of several pressure levels, interpolation or extrapolation is necessary to use them at pressures other than those given.

Recently, Katto [12] developed a new dimensionless correlation applicable to fluids other than water, in which four major CHF regimes, i.e. L-regime, H-regime, N-regime and HP-regime, were identified. Katto interpreted the burnout in the L-regime as almost complete evaporation of liquid entering the heated section and that in the H-regime as entrainment and deposition-controlled burnout [13]. In the former, the burnout occurs at high exit quality, whereas in the latter the critical quality at burnout decreases because of the reduction of film flow rate due to liquid entrainment.

With all these investigations, it is only recent that the emphasis is given to CHF at very low mass velocities, flow stagnation and flow reversal conditions, of interest for steam generators with natural convection and for nuclear reactors in accident conditions, such as a loss-of-coolant accident (LOCA) [5,6]. Barnard et al. [14] investigated CHF for Freon-113 flowing in tubes near atmospheric pressure and at mass velocities from zero to 320 $kg/m^2s$. They discussed five possible mechanisms of burnout at zero and low mass velocities, namely pool-boiling CHF, zero-circulation and flooding-limited CHF, circulation and flooding-limited CHF, circulation-limited CHF and entrainment- limited CHF. They concluded that CHF at zero inlet mass velocity occurred due to flooding and pool-boiling CHF. For low mass velocities, CHF occurred due to complete evaporation or entrainment-limited mechanism.

There exists little literature on CHF for downflow [15-17]. Blumenkrantz and Gambill [15] observed downflow CHF several-fold lower

than upflow CHF at very low mass velocities of water. Downflow CHF obtained by Cumo et al.[16] for Freon-12 was about 11% lower than upflow CHF with the conditions otherwise the same. The lower values of downflow CHF may be attributed to the buoyancy effects. However, there still remains a possibility that some flow instabilities were involved particularly in the experiment of Blumenkrantz and Gambill [15] with low pressure water.

It is noted that the above mentioned results for upflow were obtained under stable-flow conditions. That is, the test section was suitably isolated from the other part of the test loop by providing, for example, a large inlet throttling. However, it is generally known that boiling channels are subject to various flow instabilities, which may be the cause of premature burnout [9],[18-24]. The premature burnout occurs due to liquid starvation caused by the temporary reduction of the flow rate during the instability.

Lowdermilk et al. [9] conducted an experiment with water flowing vertically in round tubes to study the effects of upstream compressibility and inlet throttling on the stability of flow and CHF. They demonstrated that the flow became unstable and consequently the CHF decreased with larger upstream compressibility and less inlet throttling.

Maulbetsch and Griffith [21] studied experimentally and analytically both flow excursion and pressure-drop oscillations. From these studies, it was shown that these instabilities most likely cause burnout at lower heat flux than stable-flow CHF. It was also shown that the upstream compressibility worked as an energy storage mechanism in pressure-drop oscillations and those flow instabilities could be

effectively controlled by providing a large inlet throttling just prior to the heated section.

Although a large number of investigators have been performed on CHF for water flowing in round tubes as described so far, it can be said that:

> Transient conditions, particularly the LOCA characteristics of low velocity, flow stagnation, and flow reversal, are not well understood. Reference steady-state critical-heat-flux data for low velocities and pressures are needed.

as stated by Bergles [5]. In view of these, experiments have been performed with water flowing in a round tube at low-flow-rate and low-pressure conditions to study the effects on CHF, of buoyancy (i.e. upflow and downflow), upstream compressibility (upper and lower plena) and inlet valve throttling. Critical heat flux at complete bottom blockage also has been measured. Furthermore, CHF versus mass-velocity curves are compared with observed flow-stability boundaries at given inlet water temperatures.

## V.2. EXPERIMENT

### V.2.1. Test Section

Test section is made of a 6 mm-ID, 1 mm-thick stainless steel tube as shown in Fig. 1. A copper electrode is silver-soldered to each end of the test section. The length of the heated section is 344 mm. The test section is mounted in the loop with suitable fittings and Tefron bushing as electrical insulator. Ten Chromel-Alumel thermocouples are spot-welded onto the outside wall of the stainless steel tube. The thermocouple locations are shown in Fig. 1. These thermocouples are connected to burnout detectors which actuate the relay to switch off the power to the test section when any of the wall temperatures rise beyond the preset value. The stainless steel tube is heated electrically by a

d.c. power supply and water flows inside. The whole test section is thermally insulated with asbestos ribbon.

V.2.2. Test Loop

Test loop consists of a test section, an upper and a lower plenum, a downcomer (water tank), a bypass, a circulating pump, flow control valves, three turbine flowmeters and a pipeline connecting these components as shown in Fig. 2. The loop is filled with ion-exchanged water, which was degassed by boiling prior to the experiment. Water is circulated by a centrifugal pump whose characteristic is known. The flow orientation in the test section can be set either upward or downward with four stop valves in the loop.

Three geometrical arrangements for the test section were employed. In the first series of experiment, the test section was mounted in the loop simply using standard tube fittings and joints in order that there remained as small compressible volume as possible. A throttle valve was installed at the bottom of the test section. The second series of experiment was conducted with a plenum at the top and the bottom of the test section. The volume of the plenum is $1077cm^3$. In the third series, a surge tank was connected to the loop upstream of the test section. The volume of the surge tank was about $300cm^3$, but the volume of air in it was changeable.

V.2.3. Instrumentation

The flow rate to the test section was measured with two turbine flowmeters installed parallel to each other in the loop. The electrical outputs from these turbine flowmeters were recorded on a strip chart which enabled us to read the average flow rate as well as to observe the fluctuations.

The water temperatures were measured at the inlet and outlet of the test section, downstream of the flowmeters and in the downcomer with Chromel-Alumel thermocouples. The heated-wall temperatures were measured with ten Chromel-Alumel thermocouples spot-welded onto the heater as mentioned before. All these temperatures were also recorded on a strip chart or with a digital printer.

The pressure in the loop was measured with a Bourdon-tube type gauge installed in the upstream of the test section.

V.2.4. Test Procedure

Prior to the experiment, the water in the loop was circulated and boiled for about half an hour for degassing, since the existence of non-condensible gas reduces the CHF considerably. Then the valves were set to obtain the desired flow orientation.

The flow rate was regulated in two ways, namely, either by inlet-valve throttling with all the bypass closed or by throttling the valve downstream of the flowmeters with the inlet valve and the bypass valve open. The former case corresponds to a "stiff" system though not completely stiff, whereas the latter case corresponds to a "soft" system.

Critical heat flux was measured at given flow rates and inlet water temperatures. The inlet water temperature was kept constant by using the cooling pipe in the downcomer and the heat input to the test section. The exit pressure was always kept near atmospheric by keeping the relief valve open on top of the downcomer during the experiment. At each given flow rates, the power to the test section was gradually increased by small steps until a burnout occurred.

The determination of the occurrence of burnout is based on the

actuation of any one of the burnout detectors, which actuate a relay to switch off the power to the test section as soon as the wall temperatures rise beyond a preset value due to the occurrence of burnout. The preset levels of the detectors were so changed in each run as to trip the circuit right due to burnout. Since the wall temperatures were recorded on a strip chart, the occurrence of burnout was observed also from the abrupt increase in the temperature traces.

The heat flux was calculated from the voltage drops across the test section and the calibrated on-line shunt of the power supply assuming a uniform heat flux. The critical heat flux is defined by the heat flux just before the occurrence of rapid temperature excursion.

As will be described later various flow instabilities were encountered. In such cases as the instability directly resulted in burnout, the flow rate corresponding to the CHF was determined by the readings just before the occurrence of the instability. However, there were other case in which the flow rate decreased to another meta-stable point and held at that level for a while before burnout resulted. In those cases, both the initial and the last flow rates were used as a reference in correlating the CHF.

## V.3. RESULTS AND DISCUSSIONS

### V.3.1. Overall Behavior of CHF

The overall behavior of CHF as a function of mass velocity is shown in Fig. 3 for the test section without plenum under "stiff" conditions, i.e. with large inlet throttling. Here, the positive and the negative mass velocities denote upflow and downflow, respectively, while zero inlet mass velocity means the complete blockage of the test channel at the bottom.

It can be seen from the figure that the curves are almost symmetrical about the line with zero mass velocity, which indicates that the effects of buoyancy is small for a stiff system. In both upflow and downflow, CHF increases linearly as the mass velocity increases at very low mass velocities. There is a minimum in CHF (ranging from 0.06 to 0.08 $MW/m^2$) at zero inlet mass velocity. The effect of inlet water temperature is small in this range of parameters. However, at high mass velocities (namely, larger than 200 $kg/m^2s$), the gradient of the curves decreases remarkably and the effect of inlet water temperature becomes obvious. At the highest mass velocities, there are some indications that the gradient of the curves increase again with increasing mass velocity.

It has been recognized that in a "soft" system, flow instabilities may cause the CHF to decrease substantially. Figure 4 and 5 exemplify the premature burnout due to flow instabilities when the system is operated with less inlet restriction. The reduction in the CHF is larger at lower mass velocities. However, at the lowest mass velocities, two curves appear to merge. This may be attributed mainly to the large pressure drop across the turbine flowmeter compared to the pressure drop in the heated section for very low flow measurement. The figures also show that the curve for the soft system is not symmetrical but the CHF is lower for downflow, which indicates that the effect of buoyancy becomes important at very low flow rates.

The flow instabilities prior to burnout were observed in flow rate traces. A typical flow rate trace of unstable flow which resulted in a burnout is shown in Fig. 6(a). A flow rate trace of stable burnout is also presented in Fig. 6(b). The amplitude of the fluctuation in the

flow rate is much larger in the former case in which the burnout occurred due to unstable flow. The amplitude of the flow rate trace increases with increasing power to the test section. Figure 7 shows the variation of root-mean-square (r.m.s.) amplitude of the output from the flowmeter with increasing heat flux at given mass velocities. The effect of inlet throttling is also shown there. The r.m.s. amplitude of the flow rate increases sharply just before the occurrence of burnout and the sharp increase in the amplitude occurs at lower heat flux in a soft system.

The effect of buoyancy on the CHF can be remarkable in the test section with upper and lower plena, as illustrated in Fig. 8. In upflow, the curves for CHF versus mass velocity are almost unchanged. However, the curves for downflow appears to be entirely different. The critical heat flux remains low up to the mass velocity of about 200 $kg/m^2s$, beyond which the gradient of the curves increases. At high mass velocities, however, the gradient of the curves decreases again. From the visual observation in the experiment conducted with rectangular channels which will be described in Chapter VI, Low CHF at very low downflow is attributed to the bubble stagnation in the heated section. The critical mass velocity to stagnate bubbles is estimated from the bubble drift velocity in the churn flow regime [25], as will be discussed in the subsequent chapter. Thus the equation becomes

$$G_c = -\sqrt{2}\ (\rho_1^2 \sigma g \Delta\rho)^{1/4}/C_0 \quad , \tag{2}$$

where the negative sign represents downflow and the distribution parameter $C_0$ for a round tube is given by [25]

$$C_0 = 1.2 - 0.2 \sqrt{\rho_g/\rho_l} \quad . \tag{3}$$

Using Eq.(2) the critical mass velocity to stagnate bubbles in the present system becomes -179 kg/m$^2$s, which roughly agrees with the mass velocity at which the curves change their gradient as shown in Fig. 8. In addition to this, the shape of the curves is very similar to those which will be presented for rectangular channels in Chapter VI, in which case the visual observation revealed that such CHF curve was caused by the bubble stagnation.

From these figures, it can be said that the CHF decreases substantially due to unstable flow and the effect of buoyancy destabilizes the flow markedly, leading to further decrease in CHF. The effect of plenum is not evident in upflow, whereas it appears to be dramatic in downflow. The critical heat flux dropped as much as one fifth of that for the stiff system. This may be explained by the destabilizing effect of buoyancy in downflow and the upstream compressibility. In fact, there possibly remained a certain amount of gas in the upper plenum which served as an upstream compressibility in the downflow experiment.

It is known that an upstream compressibility works as an energy storage mechanism to excite pressure-drop oscillations [21]. In order to observe this phenomenon, a compressible volume (about 140cc of air in the surge tank) was connected to the loop immediately upstream of the test section and the CHF measured. In some cases, sustained flow oscillations with large amplitudes arose with a small increase in the heat input, and the flow rate dropped to another level gradually as the heat input was increased, keeping the inlet throttling constant. An example is illustrated in Fig. 9. This phenomenon is different from that

shown in Fig. 6(a) in which a burnout initiated directly after the occurrence of flow excursion. The period of the sustained flow oscillations is estimated to be a few seconds and the exit quality is not very high but positive. This type of flow instability will be discussed later.

The results of CHF in the test section with the compressible volume are shown in Figs. 10, 11 and 12. The triangles in the figures are the data plotted in terms of the initial mass velocity and the solid triangles in terms of the mass velocity just before the burnout when the above mentioned flow instabilities are encountered. It is clearly shown that the upstream compressibility causes a burnout at much lower heat flux than the stable CHF in view of initial mass velocity, however, the data approaches to the stable CHF in terms of the mass velocity just before the burnout.

V.3.2. Minimum CHF due to Flooding

In Figs. 3 through 6, a minimum CHF is observed at zero inlet mass velocity, i.e. at the complete bottom blockage condition. This flow condition is similar to those encountered in those systems as closed-end thermosyphon reboilers. Critical heat flux in such systems has been already studied by many authors. From these studies, it has been recognized that burnout occurs due to flooding. Critical heat flux due to flooding can be calculated from the Wallis correlation [26] for flooding velocities, hence

$$q_{cF} = \frac{C^2 h_{fg} A \sqrt{\rho_g g \Delta\rho D}}{A_H [1 + (\rho_g/\rho_l)^{1/4}]^2} \qquad (4)$$

where the constant C takes the value between 0.725 and 1 depending on

the entrance geometry. If we assume that C=1 and use it in Eq.(4), CHF becomes 0.043 $MW/m^2$ which is about a half of the experimental data.

In stead of Eq.(4), CHF due to flooding can be calculated using previously obtained relation between the gas and the liquid superficial velocities in the annular liquid-film flow. From the force balance acting on the liquid film and postulating an uniform film, the relationship can be expressed as

$$j_g^* = \frac{\alpha}{1-\alpha} j_l^* \sqrt{\rho_g/\rho_l} + \sqrt{\frac{\alpha^3(1-\alpha)}{3f_i\sqrt{\alpha}} \left[ 1 + \frac{3f_l}{(1-\alpha)^3} j_l^* |j_l^*| \right]} \quad , \quad (5)$$

where the non-dimensional superficial velocities for the two phases are defined by

$$j_g^* = j_g \sqrt{\rho_g/(\Delta\rho g D)} \quad , \quad (6)$$

$$j_l^* = j_l \sqrt{\rho_l/(\Delta\rho g D)} \quad . \quad (7)$$

The interfacial friction factor $f_i$ and the wall friction factor for the liquid film are defined by [25]

$$\tau_i = \frac{f_i}{2} \rho_g (v_g - v_l)^2 \quad , \quad (8)$$

$$\tau_{wl} = \frac{f_l}{2} \rho_l v_l^2 - \frac{1}{3}\Delta\rho g \delta \quad . \quad (9)$$

In Eq.(5), the superficial velocities are positive for upflow. At flooding-limited burnout, all the liquid flowing down may be almost dried out, therefore the following conditions can be assumed:

$$j_l^* << j_g^* \ , \quad \tau_{wl} << \tau_i \text{ and } \alpha \simeq 1. \tag{10}$$

Thus one can approximate Eq.(5) by

$$j_g^* = \sqrt{\frac{1-\alpha}{3f_i}} \ . \tag{11}$$

The interfacial friction factor $f_i$ at flooding has been obtained for round tubes by Bharathan et al.[27], as given by

$$f_i = 0.005 + a\ \delta^{*b} \ , \tag{12}$$

where

$$\log_{10} a = -0.56 + 9.07/D^* \ , \tag{13}$$

$$b = 1.63 + 4.74/D^* \ , \tag{14}$$

$$\delta^* = \delta\sqrt{g\Delta\rho/\sigma} \ , \tag{15}$$

$$D^* = D\sqrt{g\Delta\rho/\sigma} \ . \tag{16}$$

The void fraction can be approximated for thin liquid film by

$$1 - \alpha = 4\delta^*/D^* \ . \tag{17}$$

From Eqs.(11), (12) and (17), we arrive at the equation:

$$j_g^* = \sqrt{\frac{4\ \delta^*/D^*}{0.015\ (1 + 200\ a\ \delta^{*b})}} \ . \tag{18}$$

The non-dimensional film thickness $\delta^*$ can be eliminated from Eq.(18) by using the following relationship for falling film obtained by Wallis [26]:

$$\delta^*/D^* = 0.063 \, |j_1^*|^{2/3}. \tag{19}$$

At flooding burnout conditions, it may be assumed that all the liquid flowing down from the top is evaporated in the heated section so that the mass fluxes for two phases are equal. therefore,

$$\rho_g j_g = - \rho_1 j_1 \quad , \tag{20}$$

or alternatively

$$j_1^* = - j_g^* \sqrt{\rho_g/\rho_1} \quad . \tag{21}$$

With Eqs.(19) and (21), Eq.(18) can be solved numerically. Thus we obtain for the present test section, $j^*_g = 1.23$ ($j_g = 30.8$ m/s). When $\delta^*$ is small. the term $200a\delta^{*b}$ can be neglected compared to unity, which implies that the interfacial friction factor takes a constant value 0.005. Then Eq.(18) can be approximated by

$$j_g^* \simeq 8(\rho_g/\rho_1)^{1/4} \quad . \tag{22}$$

For the present case, Eq.(22) gives the value of $j^*_g$ to be 1.3 which agrees with the numerical solution of Eq.(18), therefore Eq.(22) is a reasonable approximation of Eq.(18). It should be noted, however, that

Eq.(22) may not be applicable when the viscosity is not small because it assumes a turbulent film in Eq.(19).

Having the value of $j^*_g$, one may calculate CHF due to flooding as follows. Assuming saturated liquid entering the heated section, the heat balance gives the following equation.

$$A_H q_{cF} = A h_{fg} \rho_g j_g \quad . \tag{23}$$

Equation (23) can be rewritten in a non-dimensional form as

$$q_{cF}^* = \frac{A}{A_H} j_g^* \sqrt{D^*} = \frac{D}{4L_H} j_g^* \sqrt{D^*} \quad , \tag{24}$$

where

$$q_{cF}^* = q_{cF} / (h_{fg} \sqrt{\lambda \rho_g g \Delta\rho}) \quad , \tag{25}$$

$$\lambda = \sqrt{\sigma / (g \Delta\rho)} \quad . \tag{26}$$

It is interesting to note here that the right hand side of Eq.(24) can be expressed in terms of the Kutateladze number defined by

$$Ku = j_g^* \sqrt{D^*} \quad , \tag{27}$$

hence,

$$q_{cF}^* = \frac{A}{A_H} Ku = \frac{D}{4L_H} Ku \quad . \tag{28}$$

Pushkina and Sorokin [28] obtained the criterion for flow reversal in terms of the Kutateladze number which is given by

$$Ku = 3.2 \quad . \tag{29}$$

It was pointed out earlier [29] that Eq.(29) is valid when D* is large.

Since Eq.(29) gives limiting condition for liquid penetration into the test section, it may be considered that the upper limit of flooding CHF is given by

$$q_{cF}^* = 3.2 \frac{A}{A_H} \quad . \tag{30}$$

From Eq.(24), we finally find that $q^*_{cF} = 8.33 \times 10^{-3}$ or $q_{cF} = 0.071$ MW/m$^2$, which agrees satisfactorily with the experimental results. If we use Eq.(22) instead of the numerical solution, the approximate equation for flooding CHF becomes

$$q_{cF}^* \simeq \frac{2D}{L_H}\left(\frac{\rho_g}{\rho_1}\right)^{1/4}\sqrt{D^*} \quad , \tag{31}$$

which gives $q^*_{cF} = 8.5 \times 10^{-3}$.

It should be noted here that the discrepancy between Eq.(4) and the experimental data can not be interpreted satisfactorily at present. However, it may be attributed to the effects of various parameters such as the tube diameter, length, inlet and outlet geometries, properties of the liquid and the gas and even the material of the tube wall. Further studies are needed on this point.

### V.3.3. CHF Correlations

#### V.3.3.1. Correlation of the present data

In order to correlate CHF, it will be convenient to use the following non-dimensional groups which were introduced previously.

$$q^* = q/(h_{fg}\sqrt{\lambda\rho_g g\Delta\rho}) \quad , \tag{32}$$

$$G^* = G/\sqrt{\lambda\rho_g g\Delta\rho} \quad . \tag{33}$$

Following these definitions, the pool-boiling CHF correlation [30,31] which has been chosen as the reference CHF in this study is expressed simply by

$$q_c^* = 0.16 \quad . \tag{34}$$

For stable upflow CHF, the Katto correlation [12] appears to be applicable. In the Katto correlation scheme, four CHF regimes are identified, namely, L-regime, H-regime, N-regime and HP-regime. Since the HP-regime appears only in high pressure systems, it may be excluded here. For each regime, a correlation is given in terms of the following non-dimensional groups:

$$q_c/h_{fg}G,\ \rho_l/\rho_g,\ \sigma\rho_l/G^2L_H \text{ and } L_H/D \ .$$

The first one is called the Boiling number. In the L-regime, CHF occurs due to complete evaporation of liquid film on the heated surface and is correlated by

$$\frac{q_{cL}}{h_{fg}G} = 0.25\,\frac{D}{L_H}\left(\frac{\sigma\rho_l}{G^2L_H}\right)^{0.043}(1 + 1.16\Delta h_i/h_{fg}) \quad , \tag{35}$$

which can be rewritten as

$$\frac{q_{cL}^*}{G^*} = 0.25\,\frac{D}{L_H}\left(\frac{\rho_l\lambda}{\rho_g L_H}\right)^{0.043} G^{*-0.086}\,(1 + 1.16\Delta h_i/h_{fg}) \, . \tag{36}$$

In the H-regime, the CHF is limited by liquid entrainment and is correlated by

$$\frac{q_{cH}}{h_{fg}G} = 0.10\,(\rho_g/\rho_l)^{0.133}\left(\frac{\sigma\rho_l}{G^2L_H}\right)^{1/3}\,\frac{1 + K_H\Delta h_i/h_{fg}}{1 + 0.0031\,L_H/D} \quad , \tag{37}$$

or using Eqs.(32) and (33),

$$\frac{q_{cH}^*}{G^*} = 0.10\,(\rho_l/\rho_g)^{0.2}\left(\frac{\lambda}{L_H G^{*2}}\right)^{1/3}\,\frac{1 + K_H\Delta h_i/h_{fg}}{1 + 0.0031\,L_H/D} \quad , \tag{38}$$

Here $K_H$ is given by

$$K_H = 1.8\left(\frac{L_H/D}{130}\right)^{-5\rho_g/\rho_l}$$

when $\sigma\rho_l/G^2L_H < 3 \times 10^{-6}$, and

$$K_H = 0.075\left(\frac{L_H/D}{130}\right)^{-5\rho_g/\rho_l}\left(\frac{\sigma\rho_l}{G^2L_H}\right)^{-1/4} \quad , \tag{39}$$

when $\sigma\rho_l/G^2L_H \geqq 3 \times 10^{-6}$.

The CHF correlation in the N-regime is given by

$$\frac{q_{cN}}{h_{fg}G} = 0.098\ (\rho_g/\rho_l)^{0.133} \left( \frac{\sigma\rho_l}{G^2 L_H} \right)^{0.433} \frac{(L_H/D)^{0.27}}{1 + 0.0031\ L_H/D} \quad , \tag{40}$$

or alternatively,

$$\frac{q_{cN}^*}{G^*} = 0.098\ (\rho_g/\rho_l)^{0.2} \left( \frac{\lambda}{L_H G^{*2}} \right)^{0.433} \frac{(L_H/D)^{0.27}}{1 + 0.0031\ L_H/D} \quad . \tag{41}$$

The effect of inlet subcooling $\Delta h_i/h_{fg}$ was not specified by Katto because of insufficient experimental data.

The present experimental data are plotted in terms of the Boiling number q*/G* and the non-dimensional mass velocity G* in Fig. 13 through 16 in comparison with the Katto correlation. In those figures, the flooding line is expressed by

$$q_{cF}^* = 0.0083 \tag{42}$$

which was obtained previously. The lines for zero exit quality ($x_e = 0$) and the exit quality equal to unity ($x_e = 1$) are calculated assuming thermal equilibrium and given by

$$\frac{q^*}{G^*} = \frac{D}{4L_H} (x_e + \Delta h_i/h_{fg}) \quad . \tag{43}$$

It can be seen from these figures that the data of the Boiling number versus the non-dimensional mass velocity fall along two curves: The curve at lower mass velocities agrees well with the Katto L-regime correlation, while the one at higher mass velocities is roughly parallel to the curve for the pool-boiling CHF. No difference is obvious between

the data obtained by using the test section with and without plena in upflow. In Figs. 13 and 15, the data under the soft condition are also plotted. The data for this case are again correlated by two curves, though the locus of the line at higher mass velocities is shifted toward lower heat flux.

There appears to be a small dependency on the inlet subcooling. The CHF data which fall along the curve parallel to the curve for pool-boiling CHF are plotted against the inlet subcooling in Fig. 17. Then the CHF in this region may be correlated tentatively by the following equation:

$$q_c^* = q_{c0}^* \left[1 + 12 \left(\Delta h_i / h_{fg}\right)^2\right] \quad . \tag{44}$$

The value of $q^*_{c0}$ depends on how the system is stable, and is 0.155 and 0.061 for the present stiff and soft systems, respectively.

Since the CHF, even for the present "stiff" system, is as much as three-fold lower than the stable-flow CHF predicted by the Katto correlation, it is probable that the present test loop has been totally affected by the flow instabilities. It is also pointed out that the gradient of the line at high mass velocity and high heat flux is close to that of the Katto N-regime line. In the region where the N-regime CHF appears, the heat flux is so high that once a small disturbance in the flow rate would cause vapor-blanketing, the heated surface could not be quenched any more and DNB-type burnout would result.

At the highest mass velocities concerned, there are some indications that the CHF tends to fall along the line for zero exit quality or slightly below (see, for example, the data for the soft system in

Figs. 13 and 15). This turned out to be closely related to the onset of flow instability which will be discussed later.

Similar figures are obtained for downflow as shown in Figs. 18 through 21. The critical heat flux at low mass velocities are roughly reproduced by the Katto L-regime correlation but they are as much as 30% lower than the prediction. The difference becomes smaller as the mass velocity increases. This is because the effect of buoyancy is more significant at lower mass velocities. When the mass velocity becomes still higher, the data reach the point at which they transfer to another line, which is parallel to that for the pool-boiling CHF and is given by Eq.(44). The constant $q^*_{co}$ is 0.0153 and 0.046 for the soft system with and without plenum, respectively. As the data points further proceed along the line given by Eq.(44) with increasing mass velocity, they encounter a turning point again after which the CHF takes the value close to the line for zero exit quality.

In Figs. 19 and 20, the dotted solid-line represents the transition boundary from the churn to the annular flow regime, which is previously obtained and approximately given by

$$q^* = q_{cF}^* + \frac{A}{A_H}\frac{\Delta h_i}{h_{fg}} G^* \quad . \tag{45}$$

In this case, the flooding term $q^*_{cF}$ is given by Eq.(42). The data denoted by circles indicate that burnout occurs in the annular flow regime or on its boundary at lower mass velocities. However, at higher mass velocities, burnout may occur in the churn or slug flow regime. A similar figure can be drawn based on the data for a round tube (2.44 mm -ID, $L_H/D$ = 100) obtained by Lowdermilk a et al.[9] as given in Fig. 22.

The stable-flow CHF agrees well with the Katto L-regime correlation at lower mass velocities but at higher mass velocities, it is rather higher than the H-regime correlation. The effects of compressible volume, as also shown there, is the same as observed in the present experiment.

V.3.3.2. Comparison with other correlations

The present data are compared with three high-quality CHF correlations, i.e. the Lowdermilk correlation [9], the Macbeth correlation [10] and the Katto correlation [12], and one subcooled-boiling CHF correlation by Zenkevich [32]. The results are plotted in terms of the non-dimensional CHF q* and the non-dimensional mass velocity G*. Figures 23 through 25 give the comparisons for the upflow at the inlet temperatures 30, 40 and 60°C, respectively. Figure 26 presents the results for the inlet temperature 85°C. The results for the downflow will be found in Figs. 27 through 29. The legend for the numbers to identify the curves is given in Fig. 23 and is common to Figs. 23 through 29.

For the upflow CHF, it can be said that the data which fall in the lower mass velocity regime (for example, the Katto L-regime) agree well with the corresponding high-quality CHF correlations. On the other hand, the location of the data in the higher mass velocity regime is shifted from those toward lower heat flux and mass velocity. The extent of the shift depends on the system characteristics such as inlet throttling and upstream compressibility, as was already discussed. The data at high mass velocity and low exit quality seem to agree with or slightly lower than the Zenkevich correlation [32]. This point will be discussed again later in relation to flow instabilities.

The line numbered 6 in Fig. 23 represents the natural circulation

CHF predicted by the Katto and Kawamura correlation [33]. The predicted value is much higher than the flooding CHF. Therefore a natural convection test was conducted in the present series of the experiment with all the valves on line open except the bypass valves. The results are marked with dotted circles. As the flow was unstable, the range of the flow rate at burnout is shown by a bar. It can be seen that the natural convection CHF agrees reasonably well with the Katto L-regime correlation. Therefore, in Katto-Kawamura's experiment, the CHF may not have been caused by flooding but by complete evaporation in low flow boiling.

As regards to the downflow, Figs. 27 through 28 indicate that the CHF in low mass velocity regime can be reproduced by the high-quality CHF correlations, although the predicted values are as much as 30% higher than the experimental data at very low mass velocities because of the buoyancy effect. However, in a soft system, the transition to the high mass velocity regime is likely to occur at low mass velocity. Particularly, in the test section with an upper plenum, the downflow CHF is kept low until the mass velocity increases to the transition boundary from the churn to annular flow regime or the line for zero exit quality is encountered. After the transition, the CHF increases along the line representing zero exit quality and it seems that the CHF may increase along the curve predicted by Zenkevich correlation [32] at much higher velocities.

V.3.4. Relation between the CHF and Flow Instabilities

V.3.4.1. Observed flow instabilities

The CHF observed in the present experiment appears to be considerably affected by various flow instabilities. In that case, the temporary reduction of the flow rate due to instability causes total

liquid starvation which may lead to a premature burnout as a consequence.

Two types of flow instabilities were recognized. One is the flow excursion in which a small increase in heat flux at constant valve-throttling causes a sudden non-recurrent reduction of the inlet flow rate and, as a consequence, a burnout. Typical traces illustrating burnout due to the flow excursion have been shown in Fig. 6(a). The others are oscillating instabilities. The most common among them will be the density-wave oscillation and the pressure-drop oscillation [33-35]. These oscillatory instabilities do not always cause burnout, but the amplitude is so large that it may cause the vibrations of the components in the system.

The flow excursion was first analyzed by Ledinegg [36] and the criterion for the instability was given by

$$\left(\frac{\partial \Delta p}{\partial G}\right)_{int} \leq \left(\frac{\partial \Delta p}{\partial G}\right)_{ext} \quad . \tag{46}$$

This means that the flow excursion occurs when the slope of the internal pressure-drop versus flow-rate curve becomes smaller (more negative) than the external pressure-drop versus flow-rate curve (or pump characteristic). This is illustrated in Fig. 30. In order to identify the flow excursion, a case shown in Fig. 31 has been analyzed, in which case the bypass valves were closed and the flow rate was adjusted with the inlet valve. As the pressure drops across the test section and the inlet valve were not measured, they were estimated from the known pump characteristic and measured single-phase flow rate after shutting down the power to the test section due to burnout. Since the resistance

coefficient of the flowmeters were known, the resistance coefficient of the inlet valve can be calculated assuming the following form.

$$\Delta p_{ext}\ (G) = \Delta p_{int}\ (G) = K_i \frac{G^2}{\rho_1} + \frac{f_1 G^2}{2D\rho_1} (L_H + L_U) + K_e \frac{G^2}{\rho_1} \quad . \qquad (47)$$

Here the first term on the right hand side represents the inlet pressure loss which includes the resistances at the flowmeter and the inlet valve. The second term is the frictional pressure loss in the heated and upper unheated sections, and the third term the exit pressure loss. The exit resistance coefficient $K_e$ is chosen as 0.5 and the inlet resistance coefficient $K_i$ determined from the experiment. The single phase friction factor $f_1$ is obtained from

$$f_1 = 0.3164\ Re_1^{-0.25} \quad , \qquad (48)$$

where

$$Re_1 = GD/\mu_1 \quad . \qquad (49)$$

Two-phase pressure drop is given by

$$\Delta p_{int} = K_i \frac{G^2}{\rho_{1i}} + \frac{f_1 G^2 L_B}{2D\rho_{1i}} + \Delta p_{TPF} + \Delta p_G + \Delta P_e + \Delta p_A \quad . \qquad (50)$$

The exit pressure loss $\Delta p_e$ can be calculated by [8]

$$\Delta p_e = K_e \left( 1 + \frac{\Delta\rho}{\rho_g} x_e^{1.5} \right) G^2/\rho_{1i} \quad , \tag{51}$$

where the exit quality is

$$x_e = \frac{4Lq}{h_{fg}DG} - \frac{\Delta h_i}{h_{fg}} \quad . \tag{52}$$

The gravity term $\Delta p_G$ is roughly estimated from

$$\Delta p_G = \rho_1 g \ (L_H + L_U) - \Delta\rho g \alpha_H \ (L_H + L_U - L_B) \tag{53}$$

where $\alpha_H$ is the average void fraction in the boiling region. It is assumed that the average void fraction $\alpha_H$ is calculated using the average quality in the heated section and from the homogeneous flow model, hence,

$$\alpha_H = \frac{1}{1 + \frac{1 - 0.5\ x_e}{0.5\ x_e} \cdot \frac{\rho_g}{\rho_1}} \quad . \tag{54}$$

The above simplification turned out to produce no significant errors in the final results for the present case. Another simplification is to assume that the acceleration term $\Delta p_A$ can be neglected because it is canceled out due to condensation in the downstream of the loop, as stated by Ishii et al.[37]. Approximate equation for the two-phase friction terms was also given by Ishii et al.[37] based on the homogeneous-flow model and is expressed as

$$\Delta p_{TPF} = \frac{f_1 G^2}{2D\rho_{1i}} \left[ \frac{\left(1 + \frac{\Delta\rho}{\rho_g}\frac{x_e}{2}\right)(L_H - L_B)}{\left(1 + \frac{\Delta\mu}{\mu_g}\frac{x_e}{2}\right)^{0.25}} + \frac{\left(1 + \frac{\Delta\rho}{\rho_g} x_e\right) L_U}{\left(1 + \frac{\Delta\mu}{\mu_g} x_e\right)^{0.25}} \right] . \qquad (55)$$

A sample calculation has been performed for the case shown in Fig. 31. The result of the calculation is given in Fig. 32. Since the pump used in the experiment is capable of large flow rate, the external pressure-drop versus flow-rate curve becomes flat in the range of flow rate concerned. The curves for the external pressure drop have a negative slope region, thus the flow excursion is predicted to occur at the heat flux of 1.5 $MW/m^2$ and the mass velocity of 1750 $kg/m^2s$, which are in good agreement with the measured CHF and mass velocity, 1.47 $MW/m^2$ and 1749 $kg/m^2s$, respectively.

Another example is for the density-wave oscillations. Typical traces for this instability are presented in Fig. 33, and the predicted internal pressure-drop curves are shown in Fig. 34. The internal pressure-drop curves has a positive slope in this case because of large inlet throttling, thus no flow excursion is expected. The burnout locus marked with cross-in-circle is at the mass velocity 477 $kg/m^2s$ on the curve for the CHF 1.44 $MW/m^2$, whereas the predicted operating point at that heat flux is at the mass velocity 440 $kg/m^2s$. The stability boundary of the density wave oscillation can be obtained from the simple criterion of Ishii and Zuber [38], as given by

$$x_e \leq \frac{2\left(K_i + \frac{f_m L}{2D} + K_e\right)}{1 + \frac{1}{2}\left(\frac{f_m L}{2D} + 2K_e\right)} \cdot \frac{\rho_g}{\Delta\rho} \qquad (56)$$

where the two-phase friction factor $f_m$ can be calculated from Eq.(55) and the following equation:

$$\frac{f_m L}{2D} = \frac{\rho_l}{G^2} \Delta p_{TPF} \quad . \tag{57}$$

Equations (56) and (57) predict for the case given in Fig. 34 that the density wave oscillations occurs when the exit quality is larger than 0.025 at heat flux 1.44 $MW/m^2$. Since the exit quality at burnout is 0.94, the density-wave oscillations are likely to occur in the case shown in Fig. 34.

Somewhat more complex flow oscillations, as shown in Fig. 35, were observed in the test section with an upstream compressibility and with the bypass fully open. According to the analysis on the pressure-drop oscillations by Maulbetsch and Griffith [21], the pressure drop in the portion downstream of the compressible volume is considered in this case. The resultant pressure-drop versus flow-rate curves are as shown in Fig. 36. Maulbetsch and Griffith [21] pointed out that when the compressible volume was significantly large, the CHF always occurred at the minimum in the pressure-drop versus flow-rate curve. Therefore, it is expected in this case that the flow instability occurs at the point marked with cross-in-circle in Fig. 36, at which point the mass velocity is 1990 $kg/m^2s$ and the heat flux 1.38 $MW/m^2$. These values are reasonably close to the measured heat flux, 1.23 $MW/m^2$ at the onset of instability, the CHF 1.67 $MW/m^2$ and the initial mass velocity 1924 $kg/m^2s$. The stability boundary for the density wave oscillations predicted by Eq.(56) is also shown in Fig. 35. It is indicated that the operating point is likely to enter the region where the density-wave

oscillations are possible, after the onset of flow excursion. It appears that the stored energy in the compressible volume worked to retard the flow excursion. Therefore, it may be concluded that the instability is the pressure-drop oscillations followed by the density wave oscillations.

In the downflow experiment conducted with the upper plenum, periodic, low frequency oscillations were encountered, as depicted in Fig. 37. The period of the oscillations varied from several seconds to a few minutes which decreased with increasing mass velocity. In this case, the upper plenum may have served as an energy storage mechanism for the sustained oscillation. Predicted pressure-drop versus flow-rate curves are given in Fig. 38. The external pressure drop was calculated as the pump head minus the pressure loss from the outlet of the pump to the inlet of the upper plenum. The operating point marked with cross-in-circle which is close to the condition observed at the occurrence of burnout is in the negative slope region on the pressure-drop versus flow-rate curve. Therefore, this may be a pressure-drop oscillation, though it is considerably affected by the buoyancy acting on the bubbles particularly at low mass velocities.

V.3.4.2. Relation between the CHF and the stability boundaries

In this section, observed stability boundaries are compared to the CHF data in order to provide better understanding of burnout mechanisms. In Figs. 39 and 40, the stability boundaries both for upflow and downflow under stiff conditions are plotted in terms of the non-dimensional heat flux versus mass velocity. At low mass velocities, the flow is stable or the onset of flow instability is not obvious, and the CHF is well correlated by the stable-flow CHF correlations. Typical traces

under such conditions are shown in Fig. 6(b). At high mass velocities, however, the density-wave oscillations with large amplitudes, as given in Fig. 7, are encountered and the CHF decreases considerably from the stable-flow CHF. The traces for this case are shown in Fig. 33. As the mass velocity further increases, the density-wave oscillations are followed by the flow excursion which directly leads to burnout. At the highest mass velocities where the exit quality is near zero or slightly negative, the flow excursion occurs with no obvious preceding density-wave oscillations.

Similar stability map is obtained for upflow in the soft system and in the test section with upstream compressibility, although the boundaries are moved toward lower heat flux and mass velocity, as is shown in Figs. 41 through 44. In upflow with upstream compressibility, the pressure-drop oscillations followed by the density-wave oscillations appear at high mass velocities, as shown in Fig. 34. The stability boundaries for downflow in the soft system is shown in Fig. 45, which is very similar to that for corresponding upflow case, although the downflow appears to be less stable than the upflow.

When the upper plenum serves as a large upstream compressibility in downflow, a different stability map is obtained, as illustrated in Figs. 46 and 47. The pressure-drop oscillations, sometimes mixed with the density-wave oscillations, are observed prior to the burnout. The stability boundary is close to the line for zero exit quality. The critical heat flux is also close to the same line at higher mass velocity, which is consistent with the observation by Maulbetsch and Griffith [21].

## V.4. CONCLUSIONS

As has been described so far, the CHF at atmospheric pressure is significantly affected by the effects of buoyancy and various flow instabilities. These effects on the CHF are summarized as follows:

(1) The stable-flow CHF at low mass velocities can be well correlated by the conventional high-quality correlations, such as the Katto correlation [12]. In downflow, however, the CHF is as much as 30% lower than the upflow CHF at very low mass velocities due to the effect of buoyancy.

(2) The flow becomes unstable at lower mass velocity and heat flux by providing upstream compressibility, less inlet throttling and bypass, which cause the substantial reduction of CHF. The decreased CHF falls roughly around the line for constant heat flux, which is also approximately parallel to the lines predicted by the Katto H-regime and N-regime correlations. The locus of the line, however, is shifted toward lower heat flux and mass velocity depending on how the system is unstable. The CHF in this regime appears to be affected significantly by the density-wave oscillations.

(3) Due to the buoyancy effect the downflow is less stable than the upflow. Particularly when the test section has an upper plenum, the latter works as an effective upstream compressibility to induce the pressure-drop oscillations. The CHF in this case is kept almost constant at very low heat flux until the mass velocity exceeds the critical value to stagnate bubbles or the exit quality approaches to zero.

(4) At higher mass velocities, the lines for the above mentioned

unstable CHF intersect the zero-exit-quality line around which the minimum in the internal pressure-drop versus flow-rate curve occurs. Beyond this mass velocity, the CHF increases along the line for zero exit quality, irrespective of the flow orientation. In this regime, CHF occurs mainly due to flow excursion.

(5) There appears to be a minimum CHF as a function of mass velocity, which can be calculated from the flooding or flow reversal conditions. It turned out that all the data which suffered flow instabilities fall in the region which was bounded by the stable-flow CHF lines, the flooding or flow reversal line, and the line corresponding to the minimum in the internal pressure-drop versus flow-rate curve.

From these results, it may be concluded that the CHF at low flow rate and low pressure conditions is largely affected by various flow instabilities. At lower heat flux, the basic mechanism of the burnout will be the dryout or breakdown of the liquid film on the heated surface, which is caused by the deficiency of the liquid in the heated section and may be controlled by such hydrodynamical phenomena as flooding or flow reversal, entrainment and deposition of liquid droplets. Such flow instabilities as the density-wave oscillations, the pressure-drop oscillations and the flow excursion can reduce the effective film flow rate, thus leading to premature burnout.

When both the mass velocity and the heat flux are high, and the exit quality is near zero, the flow excursion appears to be the dominant phenomenon to cause burnout. The flow excursion leads to total liquid starvation and causes dryout over the wide area of the heated surface.

The Zenkevich correlation [32] for subcooled forced-convection CHF appears to reproduce the CHF well in this region. When the heat flux is sufficiently high, say, higher than the pool-boiling CHF, a temporary reduction of flow rate due to flow instability would initiate vapor-blanketing which can not be quenched by the subsequent increase of the flow rate. In that case, a DNB-type burnout will result.

## NOMENCLATURE

$A$ : Flow area

$A_H$ : Heated area

$a$ : A constant which appears in the equation for the friction factor by Bharathan et al.[27]

$b$ : Constant used in the equation for interfacial friction factor by Bharathan et al.[27]

$C$ : Constant for flooding correlation by Wallis [26]

$C_0$ : Distribution parameter

$D$ : Tube diameter

$D^*$ : Non-dimensional tube diameter defined by Eq.(16)

$F_1$, $F_2$ : Functions of G, p and D in the Macbeth correlation

$f_i$ : Interfacial friction factor

$f_l$ : Liquid phase friction factor

$f_m$ : Two-phase friction factor

$G$ : Mass velocity

$G^*$ : Non-dimensional mass velocity defined by Eq.(33)

$G_c$ : Critical mass velocity to cause bubble stagnation

$g$ : Gravity

$h$ : Enthalpy

$h_{fg}$ : Latent heat of vaporization

$\Delta h_i$ : Inlet subcooling (enthalpy)

$j_k$ : Superficial velocity (volumetric flux) of k phase (k=g or l)

$j^*_k$ : Non-dimensional superficial velocity of k phase (k=g or l)

$K_e$ : Exit resistance coefficient

$K_H$ : Non-dimensional parameter for the effect of inlet subcooling in the Katto H-regime correlation

$K_i$ : Inlet resistance coefficient

Ku : Kutateladze number

$L$ : Length

$L_B$ : Length of the non-boiling region

$L_H$ : Heated length

$L_u$ : Length of unheated region

$p$ : Pressure

$\Delta p$ : Pressure drop

$\Delta p_A$ : Pressure loss due to acceleration

$\Delta p_e$ : Pressure loss at the exit

$\Delta p_{ext}$ : External pressure drop (supply pressure drop)

$\Delta p_G$ : Pressure drop due to gravity

$\Delta p_{int}$ : Internal pressure drop (system-demand pressure drop)

$\Delta p_{TPF}$ : Frictional pressure loss of two-phase flow

: Slope of the internal pressure-drop versus mass velocity curve

: Slope of the external pressure-drop versus mass velocity curve

$q$ : Heat flux

$q_c$ : Critical heat flux

$q_{cF}$ : Critical heat flux due to flooding

$q_{cH}$ : Critical heat flux in the Katto H-regime

$q_{cL}$ : Critical heat flux in the Katto L-regime

$q_{cN}$ : Critical heat flux in the Katto N-regime

$q^*$ : Non-dimensional heat flux defined by Eq.(32)

$q^*_{c0}$ : Non-dimensional CHF at saturated condition

$Re_l$ : Liquid Reynolds number

$T_{in}$ : Inlet water temperature

$v_k$ : Velocity of k phase (k=g or l)

$x_c$ : Critical quality at burnout

$x_e$ : Exit quality

Greek symbols

$\alpha$ : Void fraction

$\alpha_H$ : Average void fraction in the heated section

$\delta$ : Liquid film thickness

$\delta^*$ : Non-dimensional liquid film thickness

$\rho_k$ : Density of k phase (k=g or l)

$\rho_{li}$ : Density of the liquid at the inlet

$\Delta\rho$ : Difference of the density between two phases

$\mu_k$ : Viscosity of k phase (k=g or l)

$\Delta\mu$ : Difference of the viscosity between the two phases

$\lambda$ : Length scale of the Taylor wave defined by Eq.(26)

$\sigma$ : Surface tension

$\tau_i$ : Interfacial shear stress

$\tau_{wl}$ : Wall shear stress for liquid phase

Subscripts

A : Acceleration

B : Non-boiling region

c : Critical

e : Exit

ext : External

F : Flooding

fg : Difference between the liquid and the gas

G : Gravity

g : Gas phase

H : Heated region or the Katto H-regime

i : Inlet

in : Inlet

int : Internal

L : The Katto L-regime

l : Liquid phase

m : Two-phase mixture

N : The Katto N-regime

u : Unheated region

w : Wall

0 : Zero inlet subcooling

## REFERENCES


[1] W.R. Gambill, "Burnout in boiling heat transfer - Part I : Pool boiling systems," Nucl. Safety, 9[5], pp.351-362 (1968).

[2] W.R. Gambill, "Burnout in boiling heat transfer - Part II : Subcooled forced-convection systems," Nucl. Safety, 9[6], pp.467-480 (1968).

[3] A.E. Bergles, "Burnout in boiling heat transfer. Part I : Pool-boiling systems," Nucl. Safety, 16[1], pp.29-42 (1975).

[4] A.E. Bergles, "Burnout in boiling heat transfer. Part II : Subcooled and low-quality forced-convection systems," Nucl. Safety, 18[2], pp.154-167 (1977).

[5] A.E. Bergles, "Burnout in boiling heat transfer. Part III : High-quality systems," Nucl. Safety, 20[6], pp.671-689 (1979).

[6] V. Marinelli, "Critical heat flux : A review of recent publications," Nucl. Technology, 34, pp.135-171 (1977).

[7] L.S. Tong, Boiling heat transfer and two-phase flow, John Wiley & Sons, New York (1965).

[8] J.G. Collier, Convective boiling and condensation, McGraw-Hill, London (1972).

[9] W.H. Lowdermilk, C.D. Lanzo and B.L. Siegel, Investigation of boiling burnout and flow stability for water flowing tubes, NACA-TN4382 (1958).

[10] R.V. Macbeth, Burnout analysis, Part IV, Application of a local conditions hypothesis to world data for uniformly heated tubes and rectangular channels, AEEW-R267 (1963).

[11] B. Thompson and R.V. Macbeth, Boiling water heat transfer burnout

in uniformly heated round tubes : A compilation of world data with accurate correlations, AEEW-R356 (1964).

[12] Y. Katto, "A generalized correlation of critical heat flux for the forced convection boiling in vertical uniformly heated round tubes," Int. J. Heat Mass Transfer, 21[12], pp.1527-1542 (1978).

[13] Y. Katto, "An analytical investigation of CHF of flow boiling in uniformly heated vertical tubes with special reference to governing dimensionless groups," Int. J. Heat Mass Transfer, 25[9], pp.1353-1361 (1982).

[14] D.A. Barnard, F.R. Dell and R. Stinchcombe, R.S.100 : Dryout at low mass velocities for an upward boiling flow of refrigerant-113 in a vertical tube, AERE-R7726 (1974).

[15] A.R. Blumenkrantz and W.R. Gambill, "Buoyancy effects on thermal burnout with downflow of water in vertical channels," cited by W.R. Gambill in Reference [2].

[16] M. Cumo, R. Bertoni, R. Cipriani and G. Palazzi, "Upflow and downflow burnout," Inst. Mech. Engrs. Conference Publications, 1977-8, pp.183-192 (1977).

[17] G.J. Kirby, R. Staniforth and J.H. Kinneir, A visual study of forced convection boiling, Part 2. Flow patterns and burnout for a round test section, AEEW-R506 (1967).

[18] V.I. Aladiev, Z.L. Miropolsky, V.E. Doroschuk and M.A. Styrikovich, "Boiling crisis in tubes," Proc. Int. Heat Transfer Conference, Publ. by ASME (1961).

[19] A.E. Bergles, "Subcooled burnout in tubes of small diameter," ASME Paper No.63-WA-182 (1963).

[20] R.S. Daleas and A.E. Bergles, "Effects of upstream compressibility

on subcooled critical heat flux," ASME Paper No.65-HT-67 (1965).

[21] J.S. Maulbetsch and P. Griffith, "System-induced instabilities in forced convection flows with subcooled boiling," Proc. 3rd. Int. Heat Transfer Conference, Chicago, Vol.4, pp.247-257 (1966).

[22] A.E. Bergles, R.F. Lopina and M.P. Fiori, "Critical-heat flux and flow-pattern observations for low-pressure water flowing in tubes," I. Heat Transfer, ,pp.69-74 (1967).

[23] F. Mayinger, O. Schad and E. Weiss, Research into the critical heat flux (burnout) in boiling water, EURAEC-1620 (1966).

[24] D.B. Collins, M. Gacesa and C.B. Parsons, "Study of onset of premature heat transfer crisis during hydrodynamic instability in a fullscale reactor channel," ASME Paper No.71-HT-11 (1971).

[25] M. Ishii, One-dimensional drift-flux model and constitutive equation for relative motion between phases in various two-phase flow regimes, ANL-77-47 (1977).

[26] G.B. Wallis, One dimensional two-phase flow, McGraw-Hill, New York (1967).

[27] D. Bharathan and G.B. Wallis, "Air-water countercurrent annular flow," Int. J. Multiphase Flow, 9[4], pp.349-366 (1983).

[28] O.L. Pushkina and Yu.L. Sorokin, "Breakdown of liquid film motion in vertical tubes," Heat Transfer - Soviet Research, 1[5], pp.56-64 (1969).

[29] G.B. Wallis and S. Makkenchery, "The hanging film phenomenon in vertical annular two phase flow," J. Fluids Engng., 98, pp.297-298 (1974).

[30] S.S. Kutateladze, Heat transfer in condensation and boiling, AEC-tr-3770 (1959).

[31] N. Zuber, Hydrodynamic aspects of boiling heat transfer, AECU-4439 (1959).

[32] B.A. Zenkevich, "The generalization of experimental data on critical heat fluxes in forced convection of subcooled water," J. Nucl. Energy, Part B : Reactor Technology, 1, pp.130-133 (1959).

[33] J.A. Bouré, A.E. Bergles and L.S. Tong, "Review of two-phase flow instability," Nucl. Engng. Design, 25, pp.165-192 (1973).

[34] M. Ishii, Study on flow instabilities in two-phase mixtures, ANL-76-23 (1976).

[35] S. Kakaç and T.N. Veziroglu, A review of two-phase flow instabilities," in Advances in two-phase flow and heat transfer, Vol.II, ed. S. Kakaç and M. Ishii, Martinus Nijhof Publ., pp.577-667 (1983).

[36] M. Ledinegg, "Instability of flow during natural and forced circulation," Die Wärme, 61, p.8 (1938).

[37] M. Ishii and H.K. Fauske, "Boiling and dryout behavior in a liquid-metal fast breeder reactor subassembly bundle under low heat flux and low flow conditions," Nucl. Sci. Engng., 84, pp.131-146 (1983).

[38] M.Ishii and N. Zuber, "Thermally induced flow instabilities in two-phase mixtures," 4th. Int. Heat Transfer Conference, Paris, Paper No.B5.11 (1970).

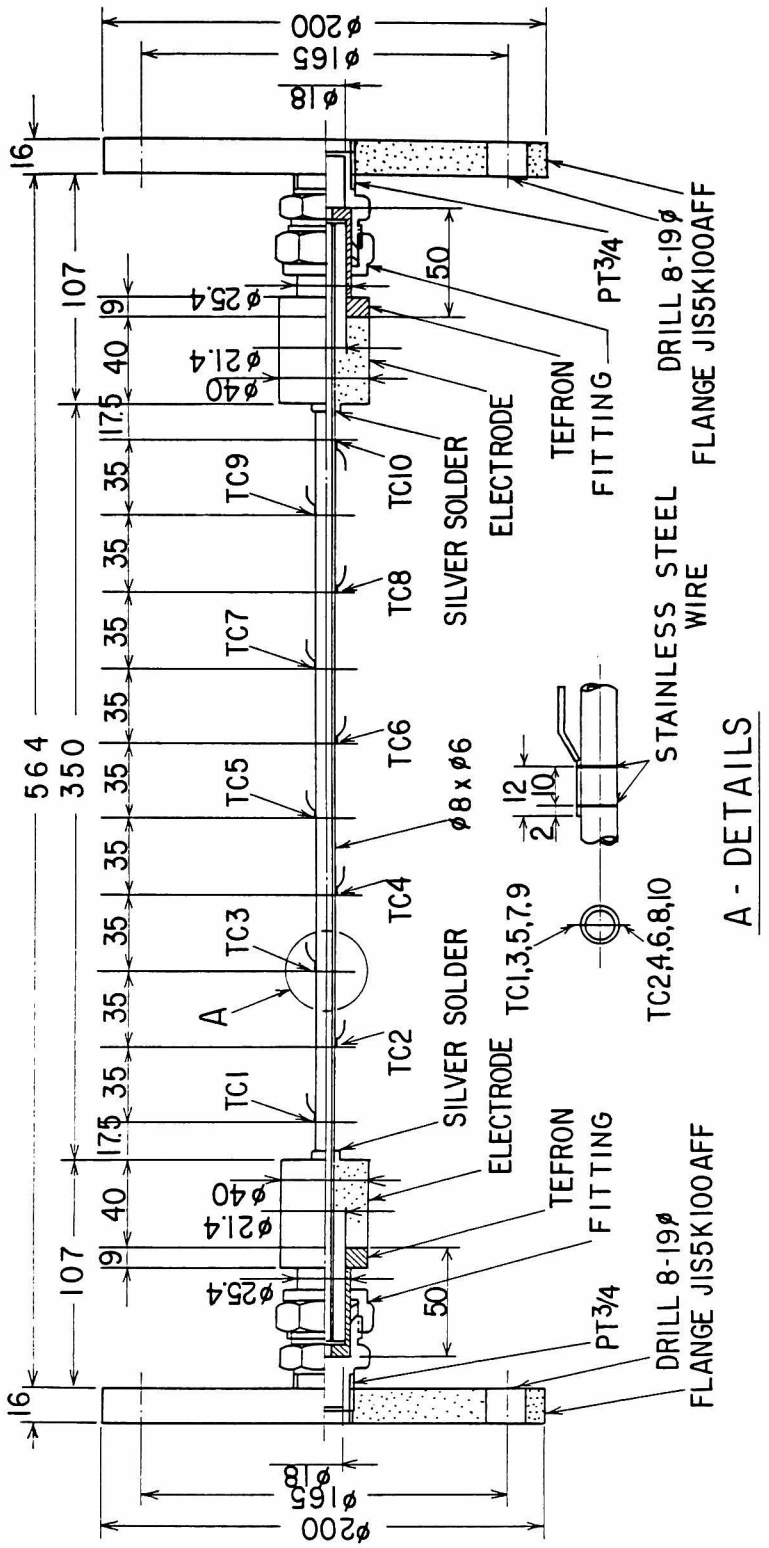


Figure 1 Test section with round tube heater.

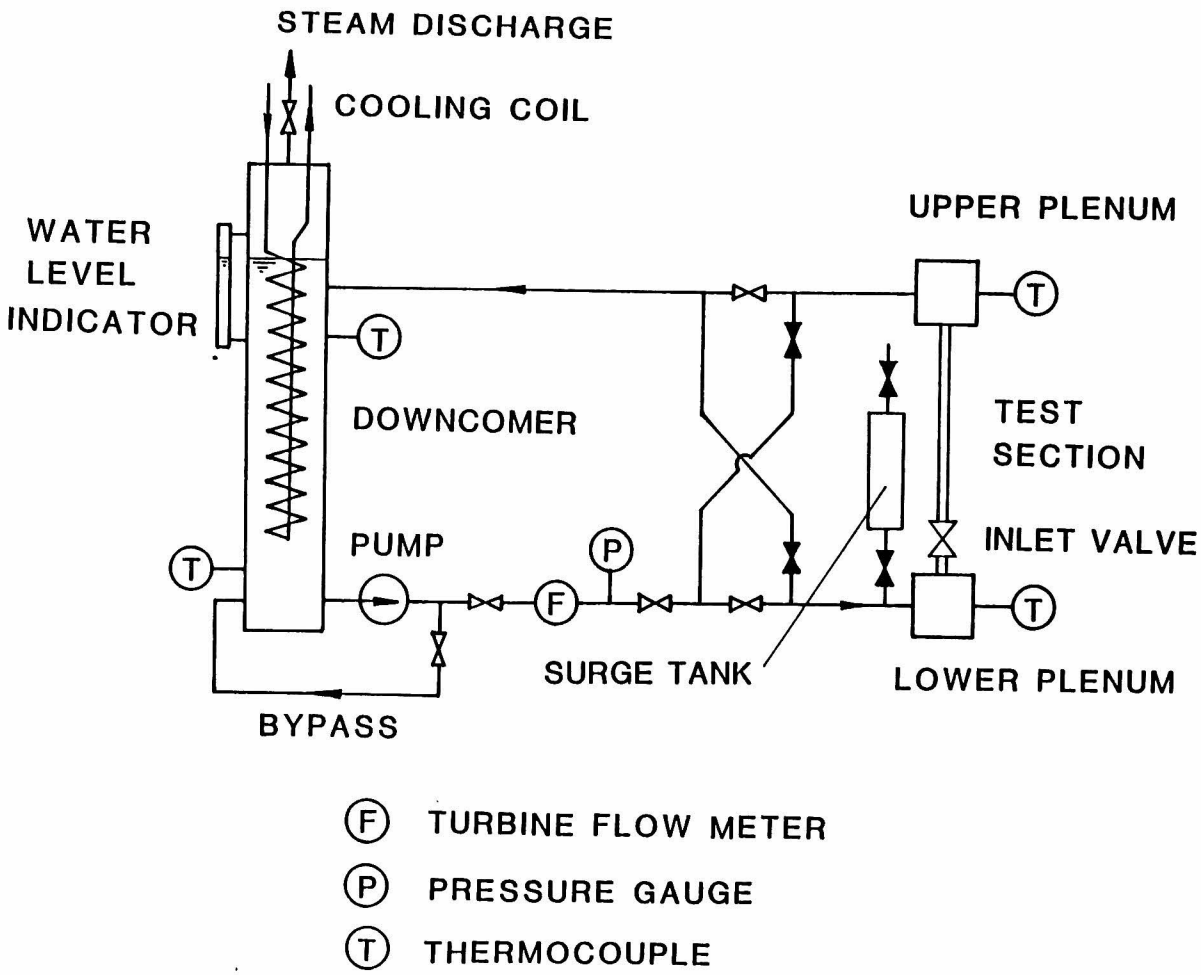


Figure 2 Schematic showing of the test loop employed in the round tube experiment.

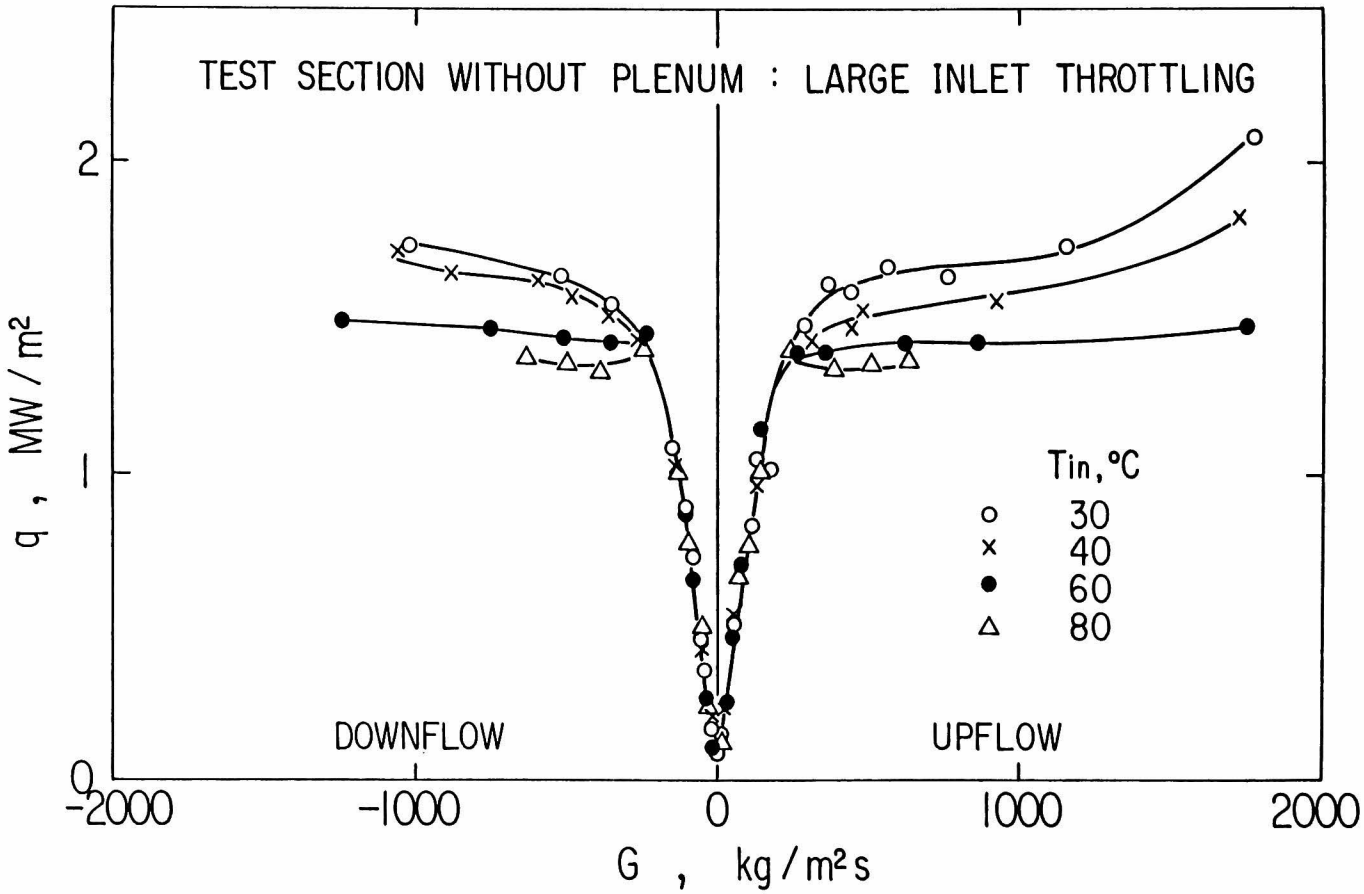


Figure 3 Overall behavior of CHF as a function of mass velocity for the test section without plenum under "stiff" condition.

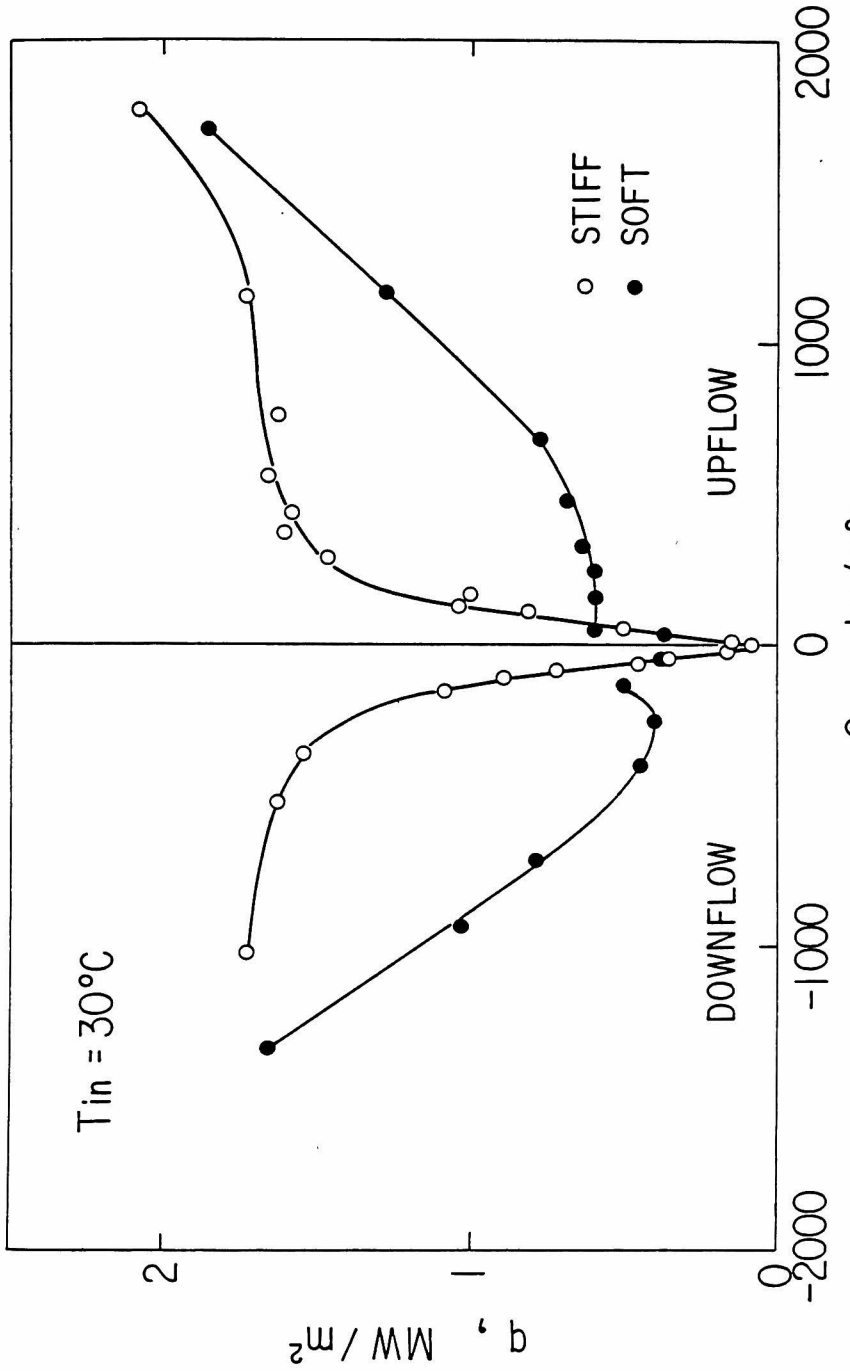


Figure 4 Effects of inlet throttling on the overall behavior of CHF at inlet water temperature 30°C.

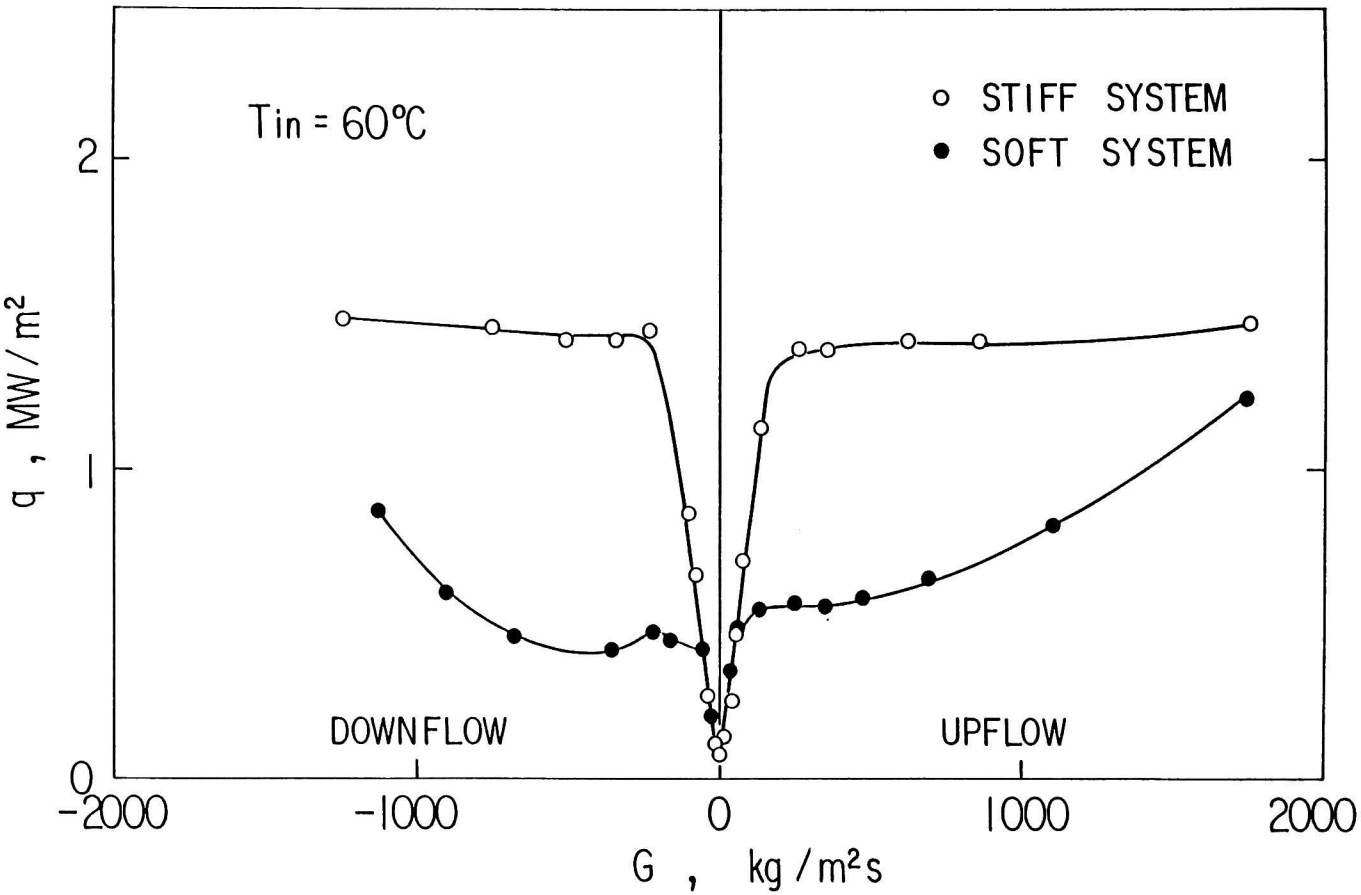


Figure 5 Effects of inlet throttling on the overall behavior of CHF at inlet water temperature 60°C.

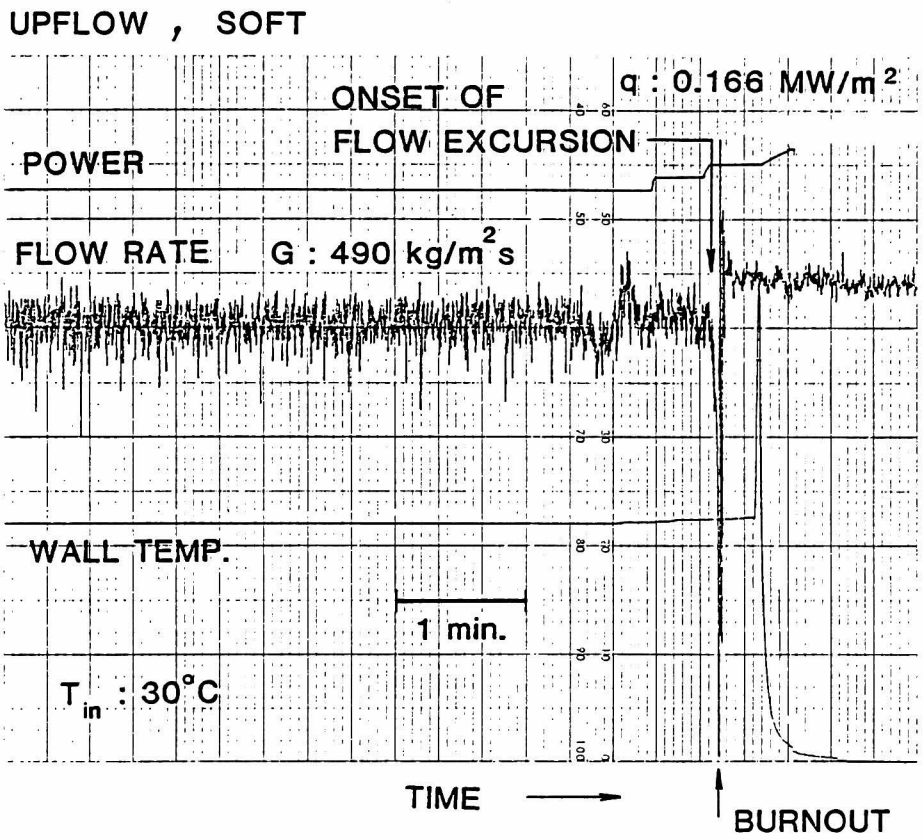


Figure 6(a) Flow-rate trace at burnout due to flow excursion.

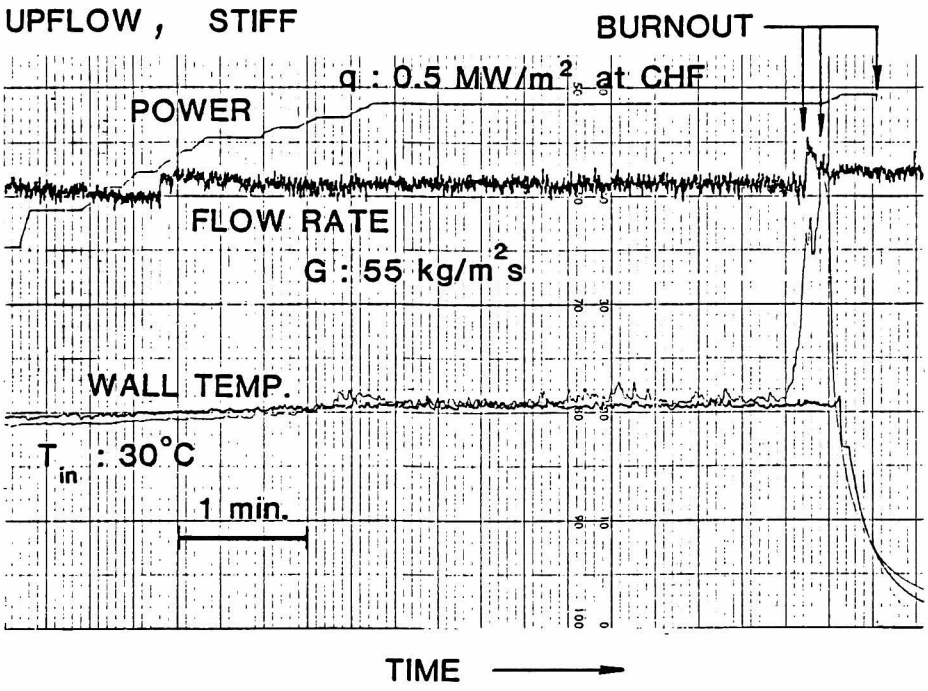


Figure 6(b) Typical traces at stable-flow burnout.

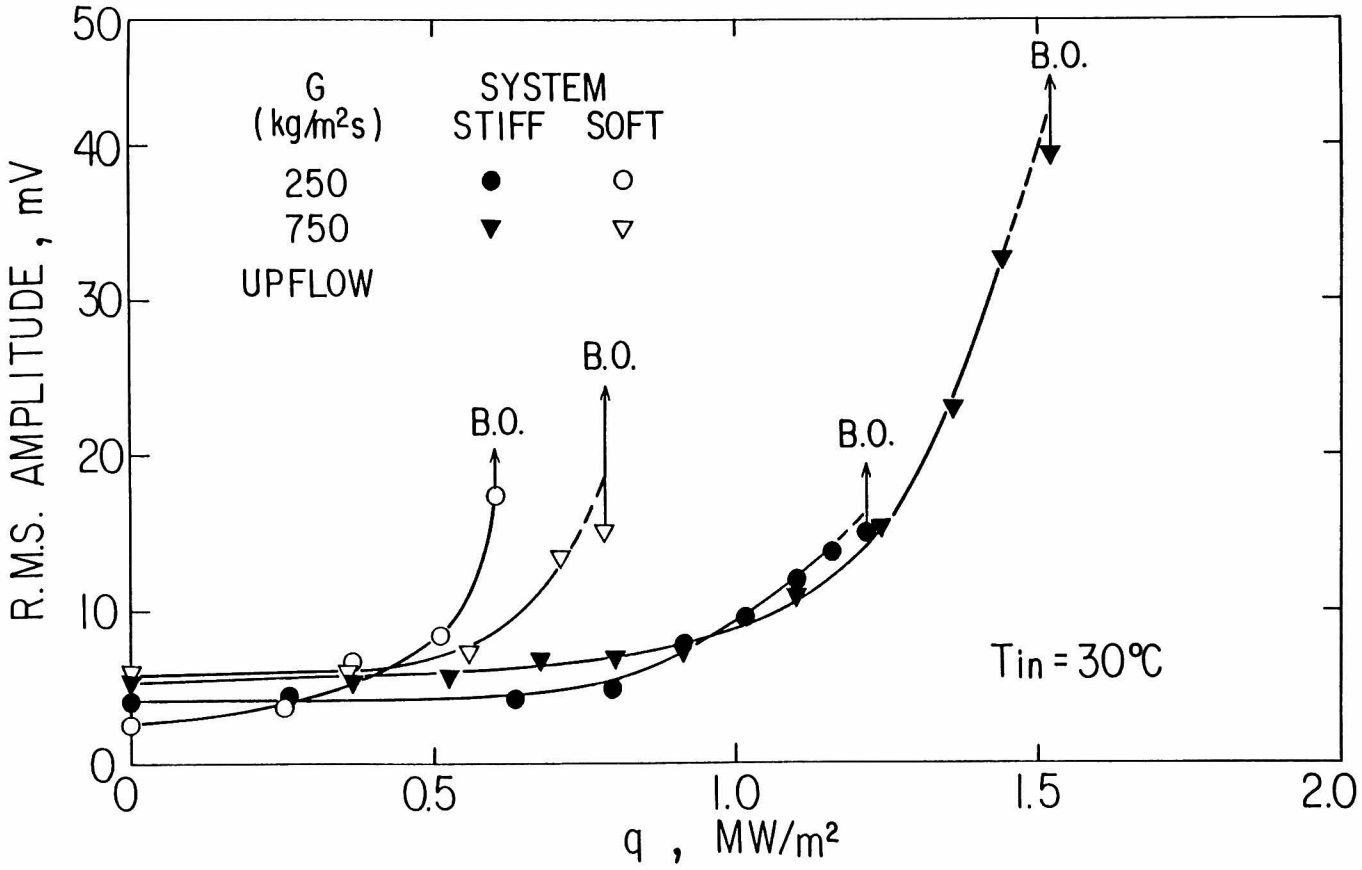


Figure 7 Effect of inlet throttling on the r.m.s. amplitude of the flowmeter output as a function of heat flux.

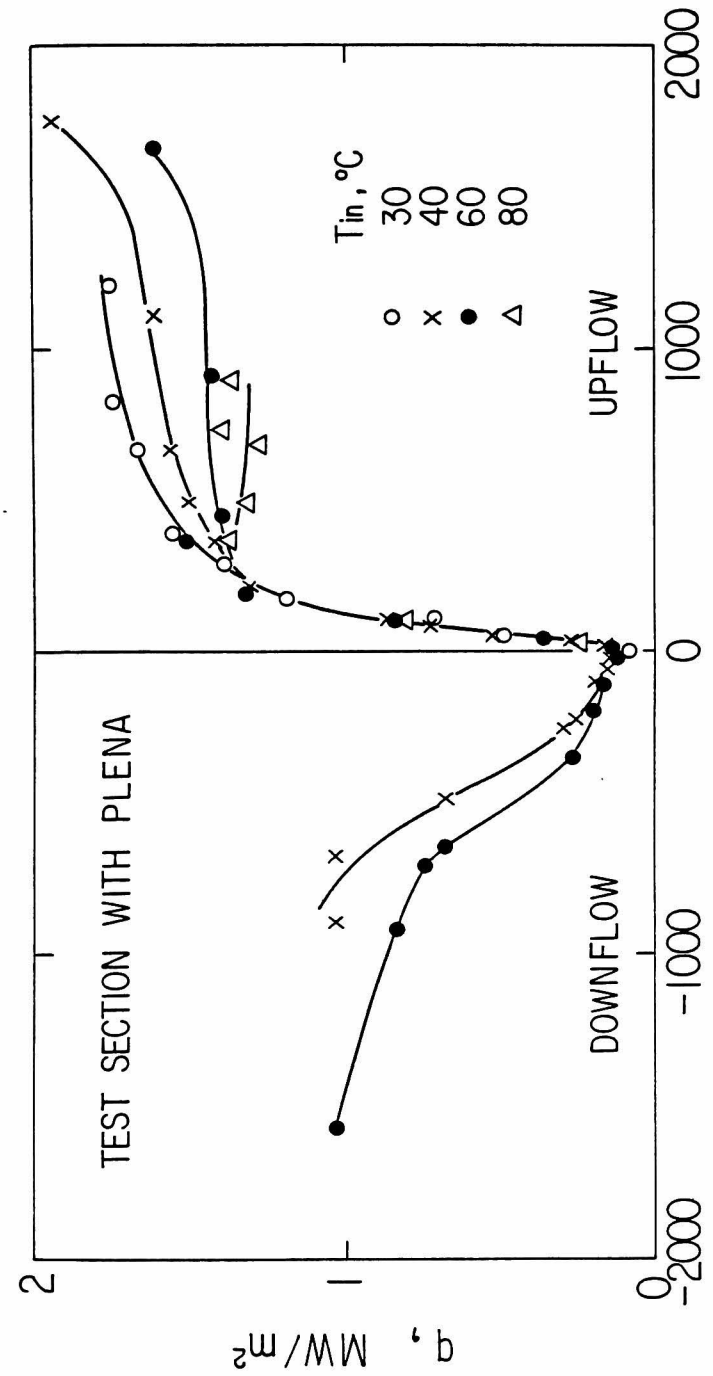


Figure 8 Overall behavior of CHF as a function of mass velocity for the test section with upper and lower plena.

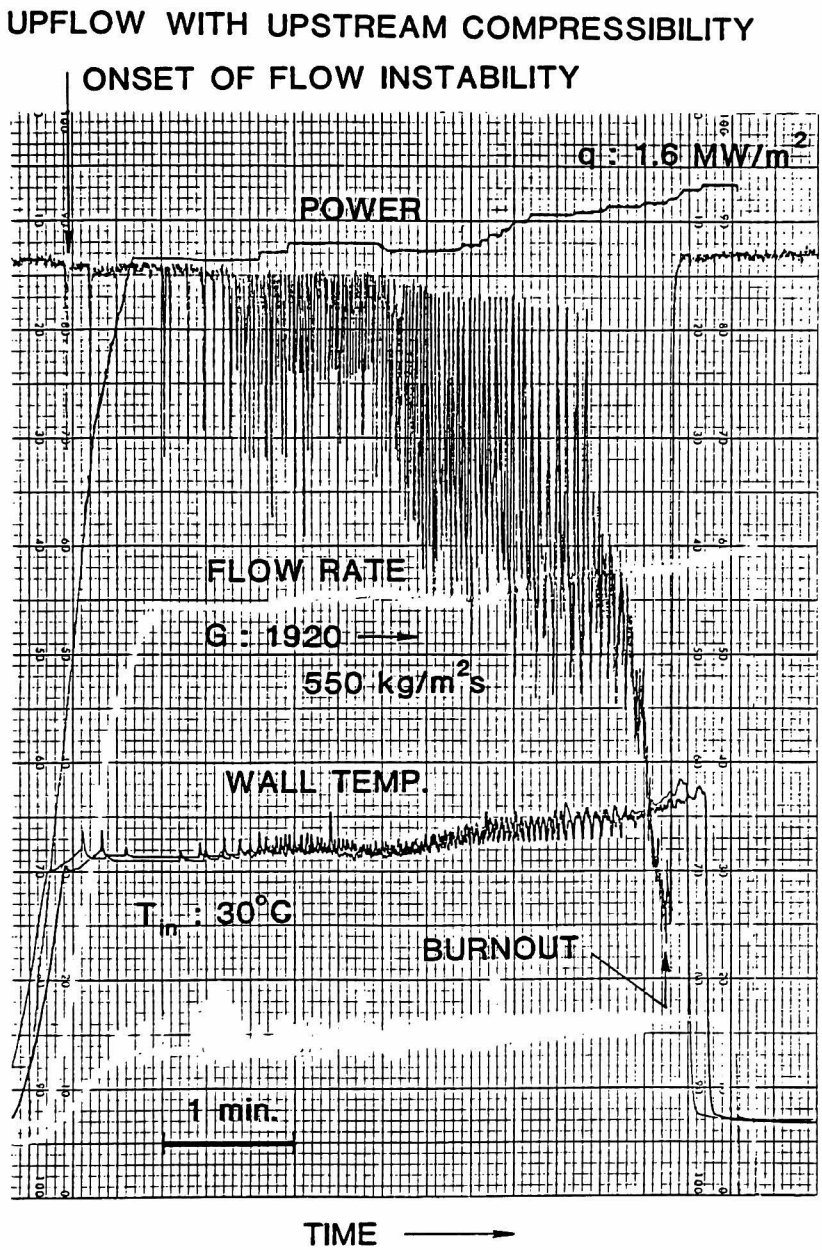


Figure 9 Complex flow instability in upflow affected by the upstream compressibility.

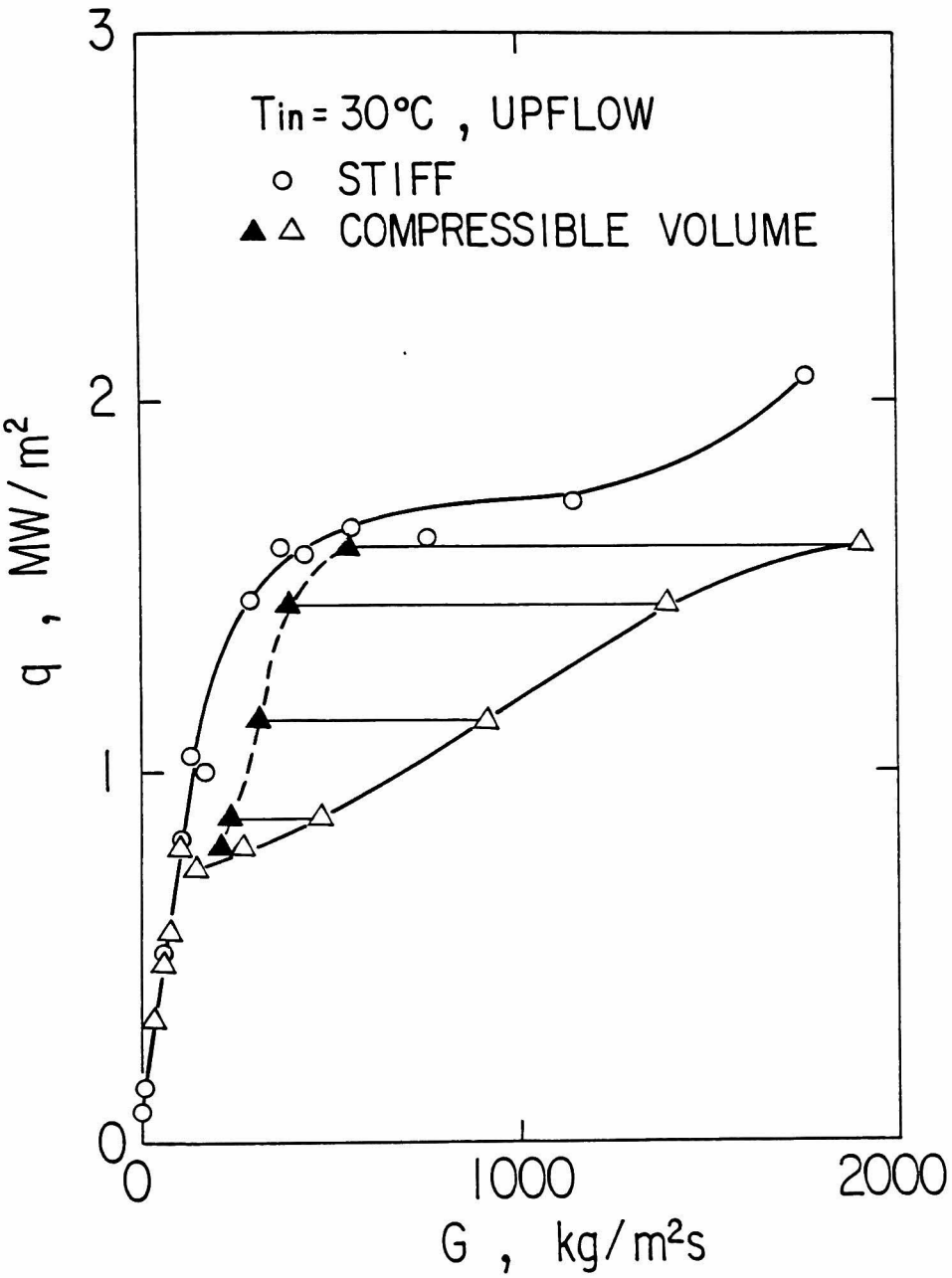


Figure 10 Effect of compressible volume on CHF for upflow at inlet temperature 30°C.

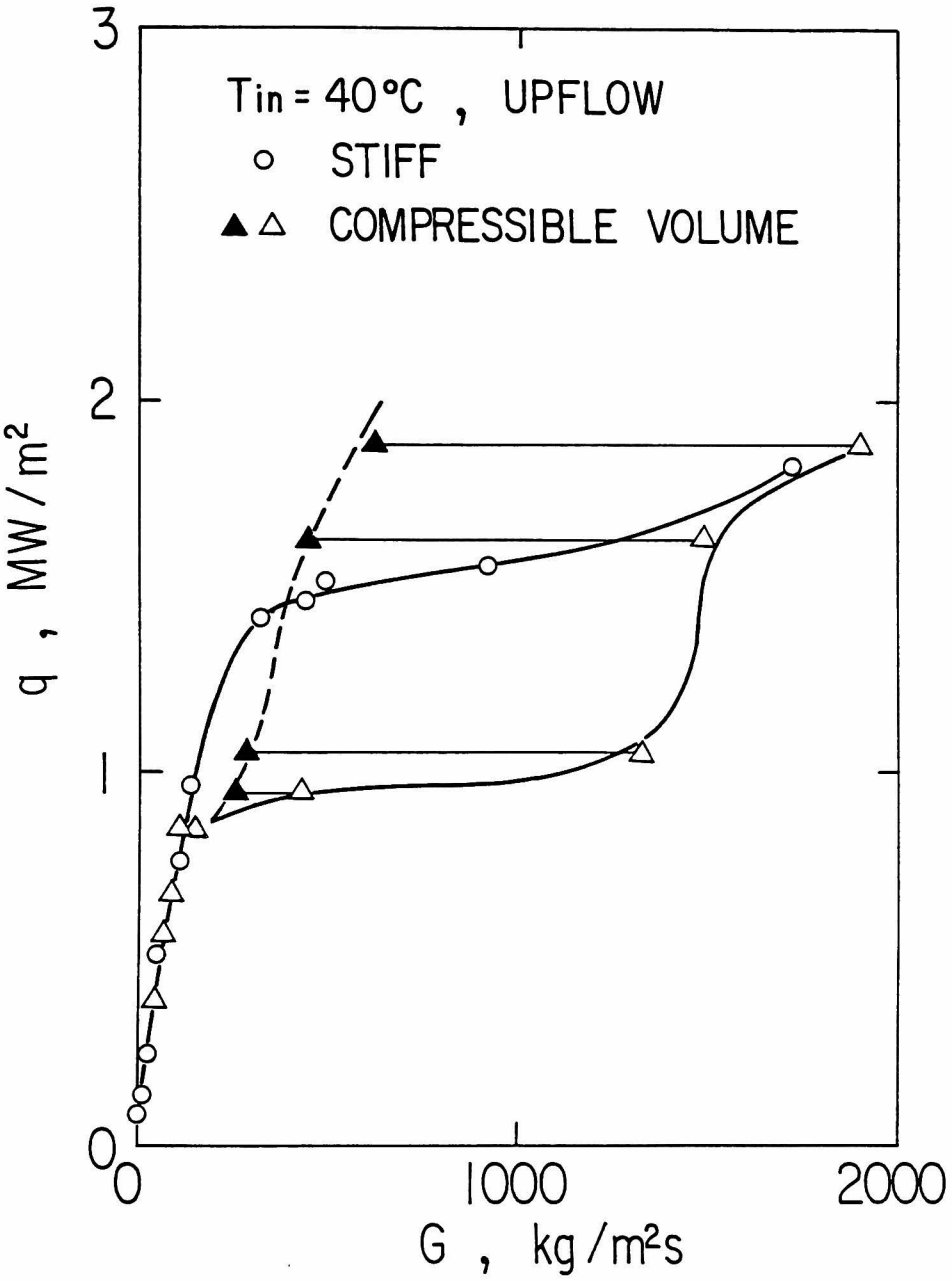


Figure 11 Effect of compressible volume on CHF for upflow at inlet temperature 40°C.

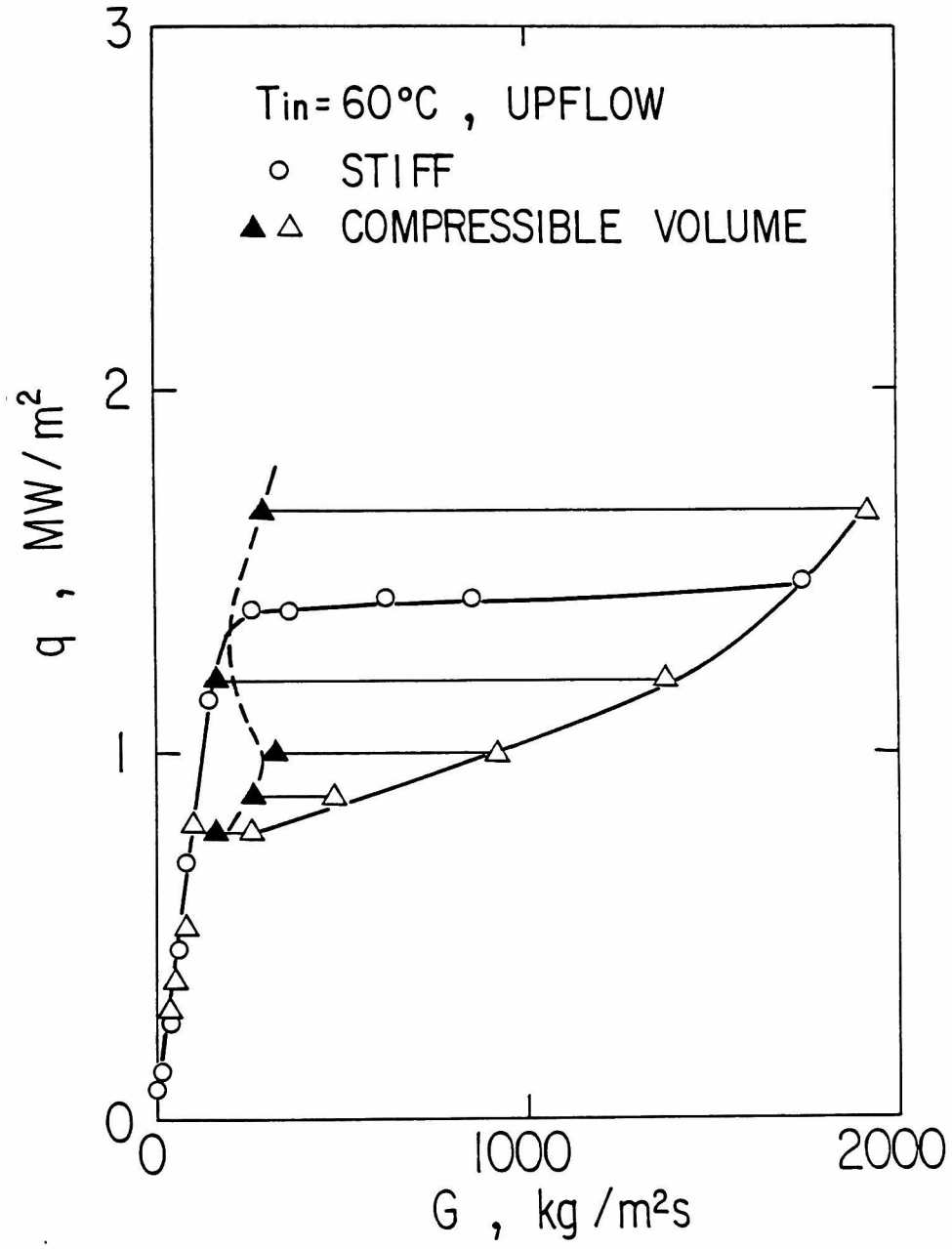


Figure 12 Effect of compressible volume on CHF for upflow at inlet temperature 60°C.

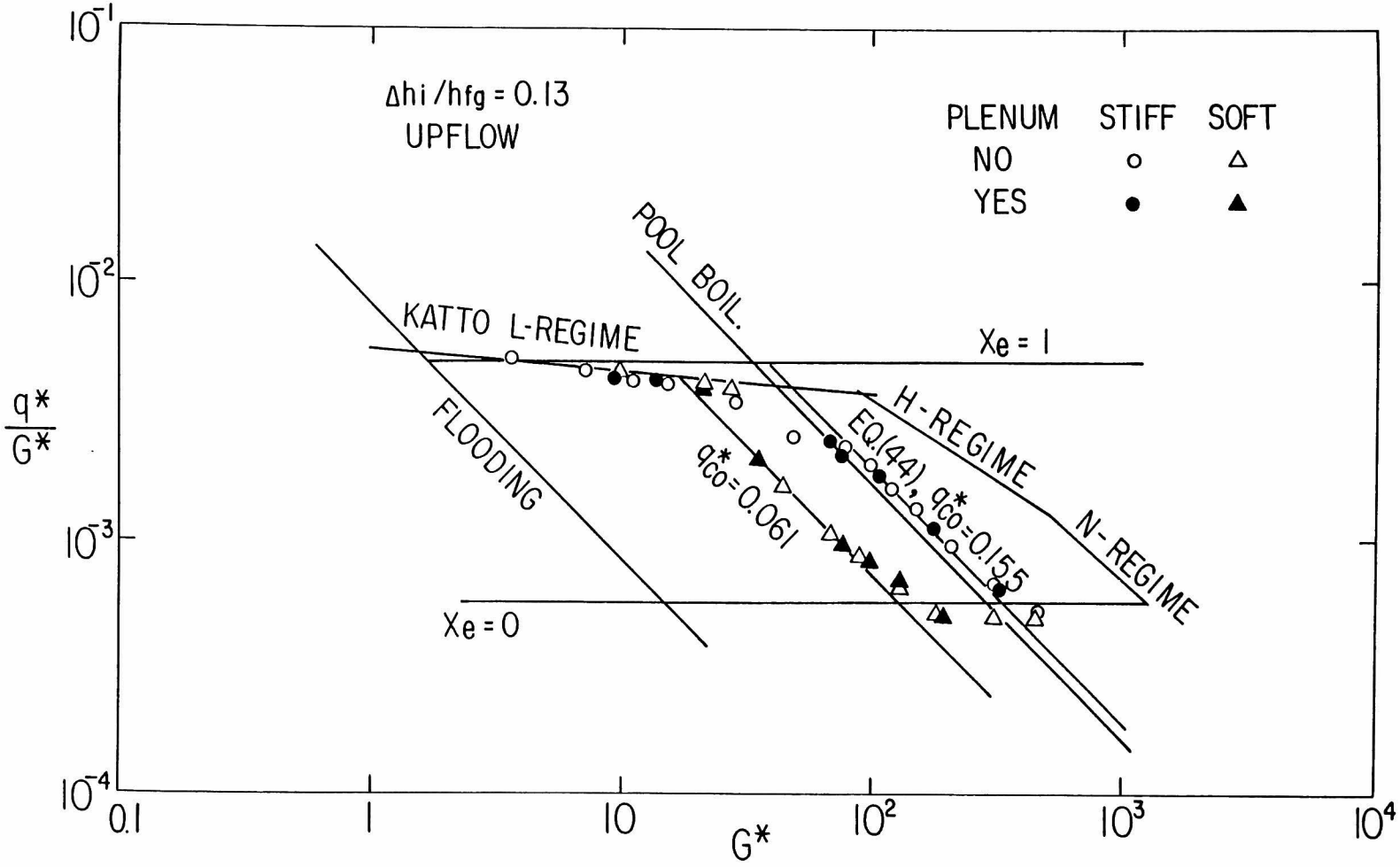


Figure 13 Correlation of upflow CHF data in terms of the boiling number and the non-dimensional mass velocity at inlet temperature 30°C.

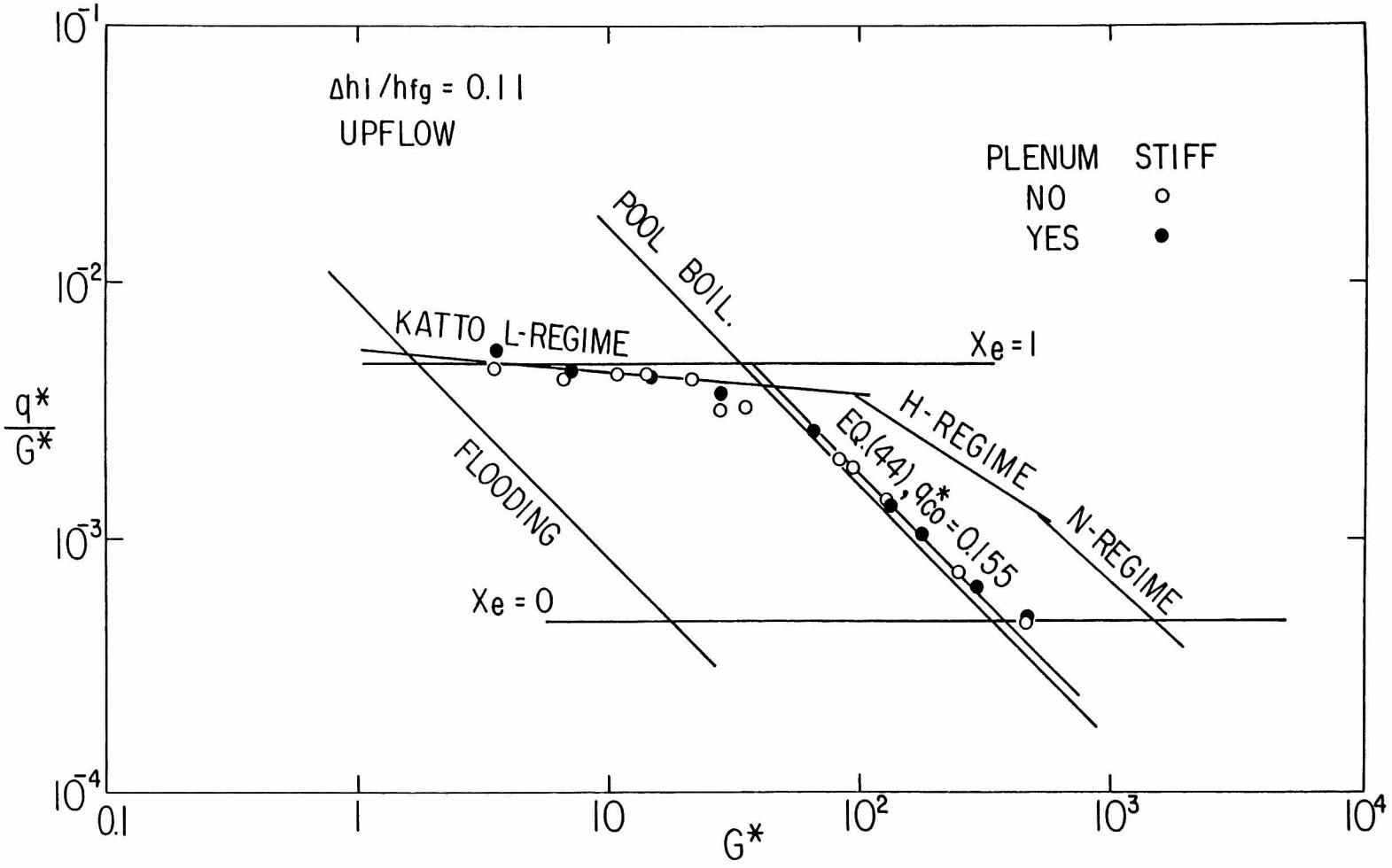


Figure 14 Correlation of upflow CHF data in terms of the boiling number and the non-dimensional mass velocity at inlet temperature 40°C.

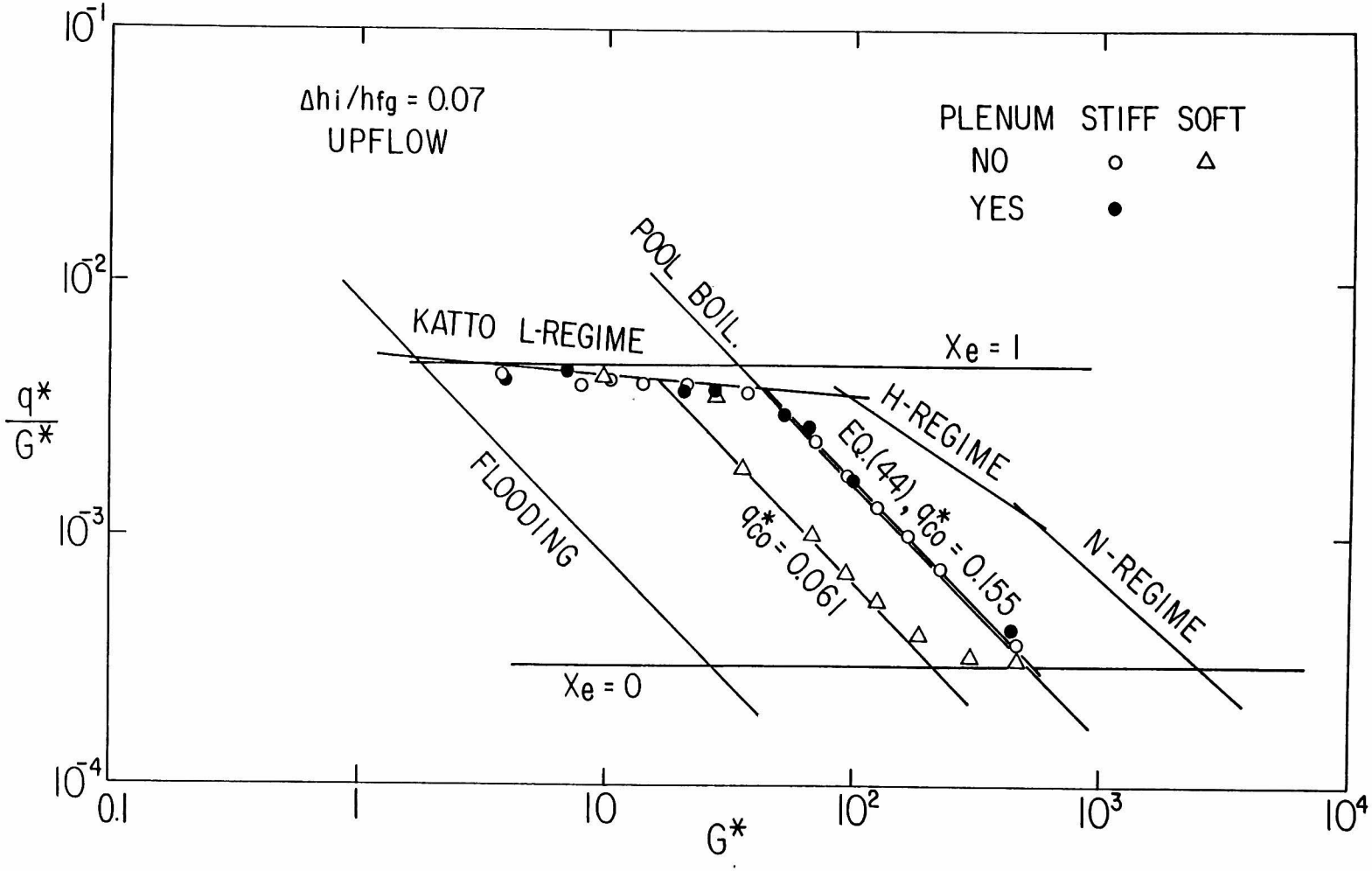


Figure 15 Correlation of upflow CHF data in terms of the boiling number and the non-dimensional mass velocity at inlet temperature 60°C.

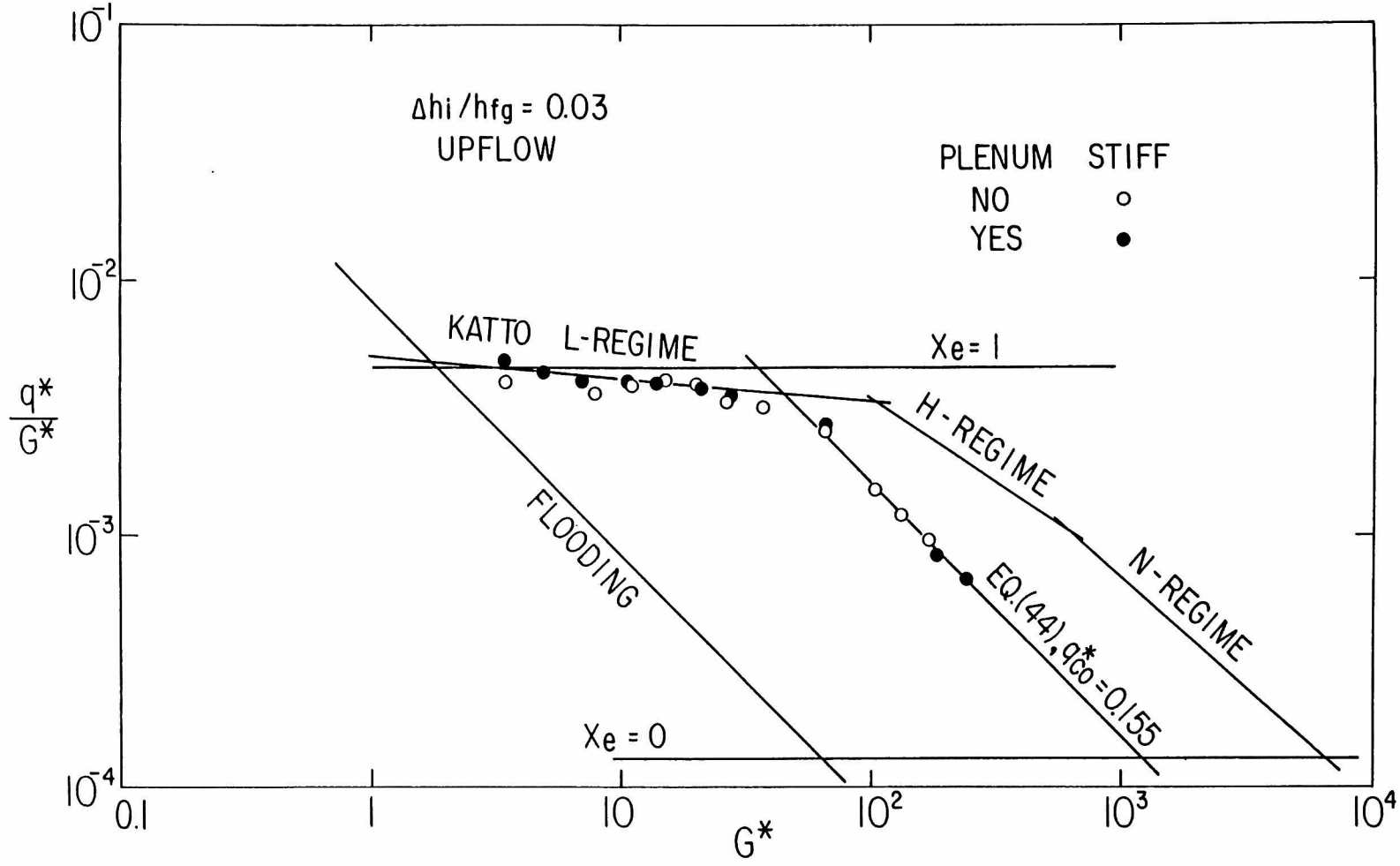


Figure 16 Correlation of upflow CHF data in terms of the boiling number and the non-dimensional mass velocity at inlet temperature 80°C.

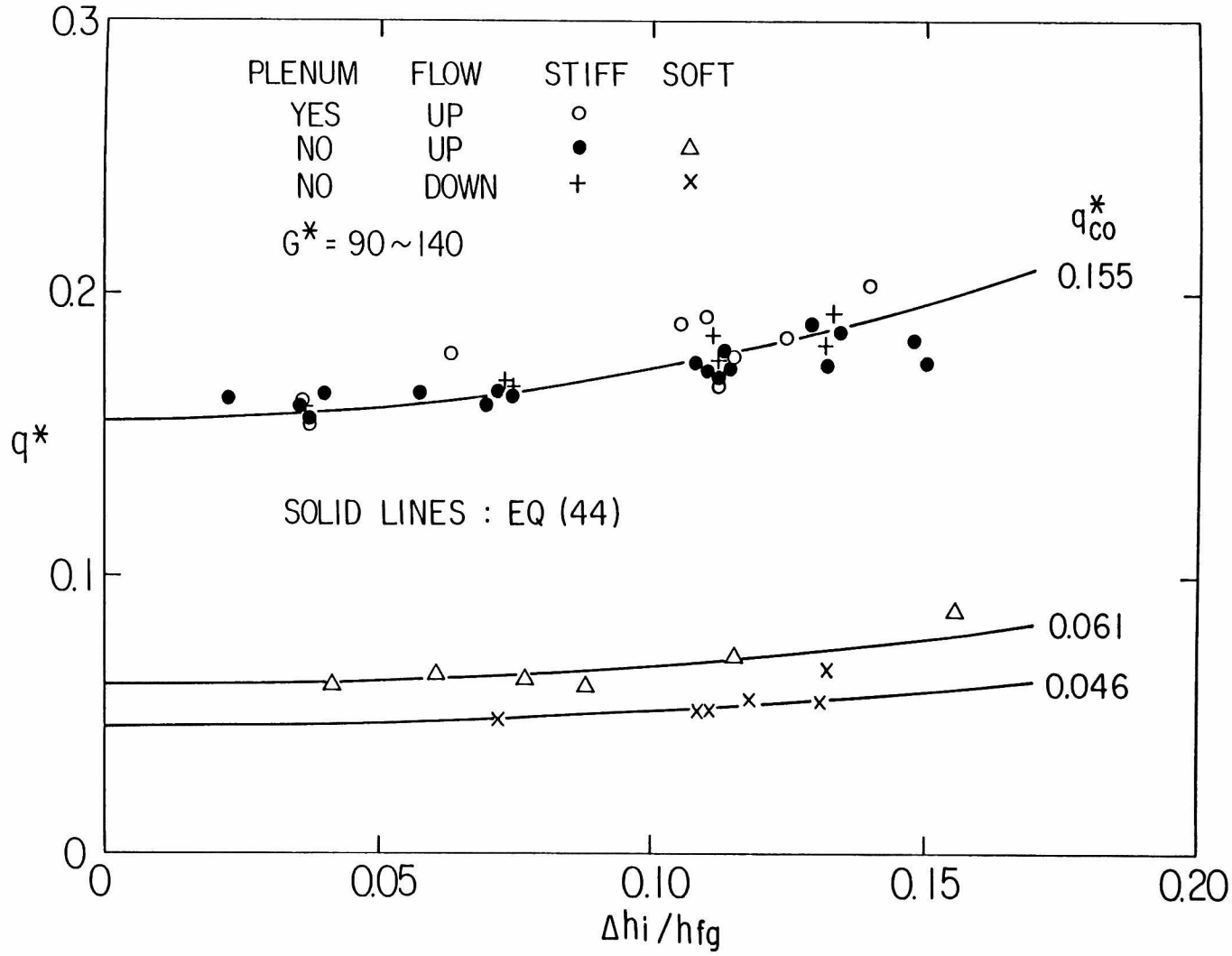


Figure 17 Effect of inlet subcooling on the CHF at higher mass velocities.

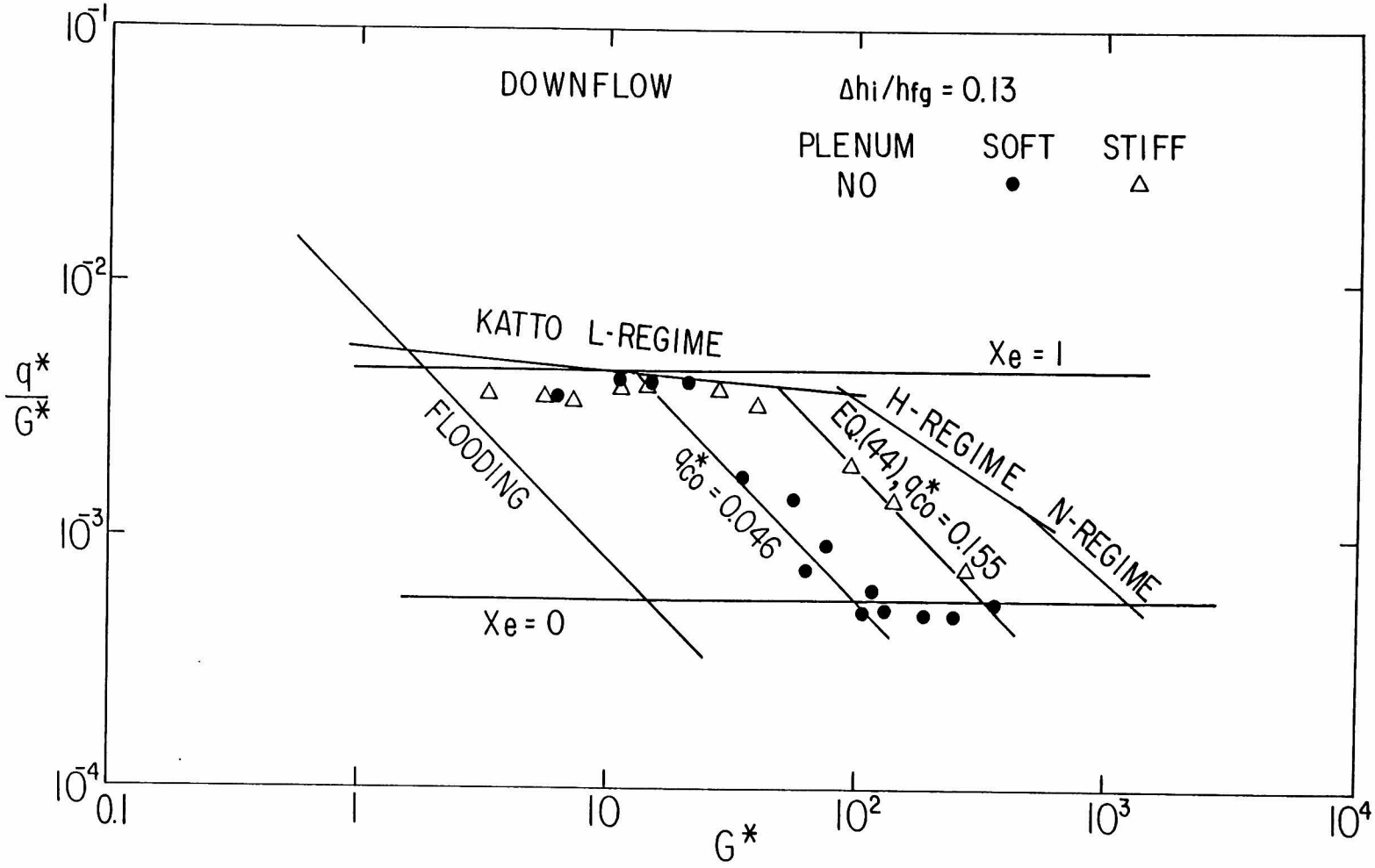


Figure 18 Correlation of downflow CHF data in terms of the boiling number and the non-dimensional mass velocity at inlet temperature 30°C.

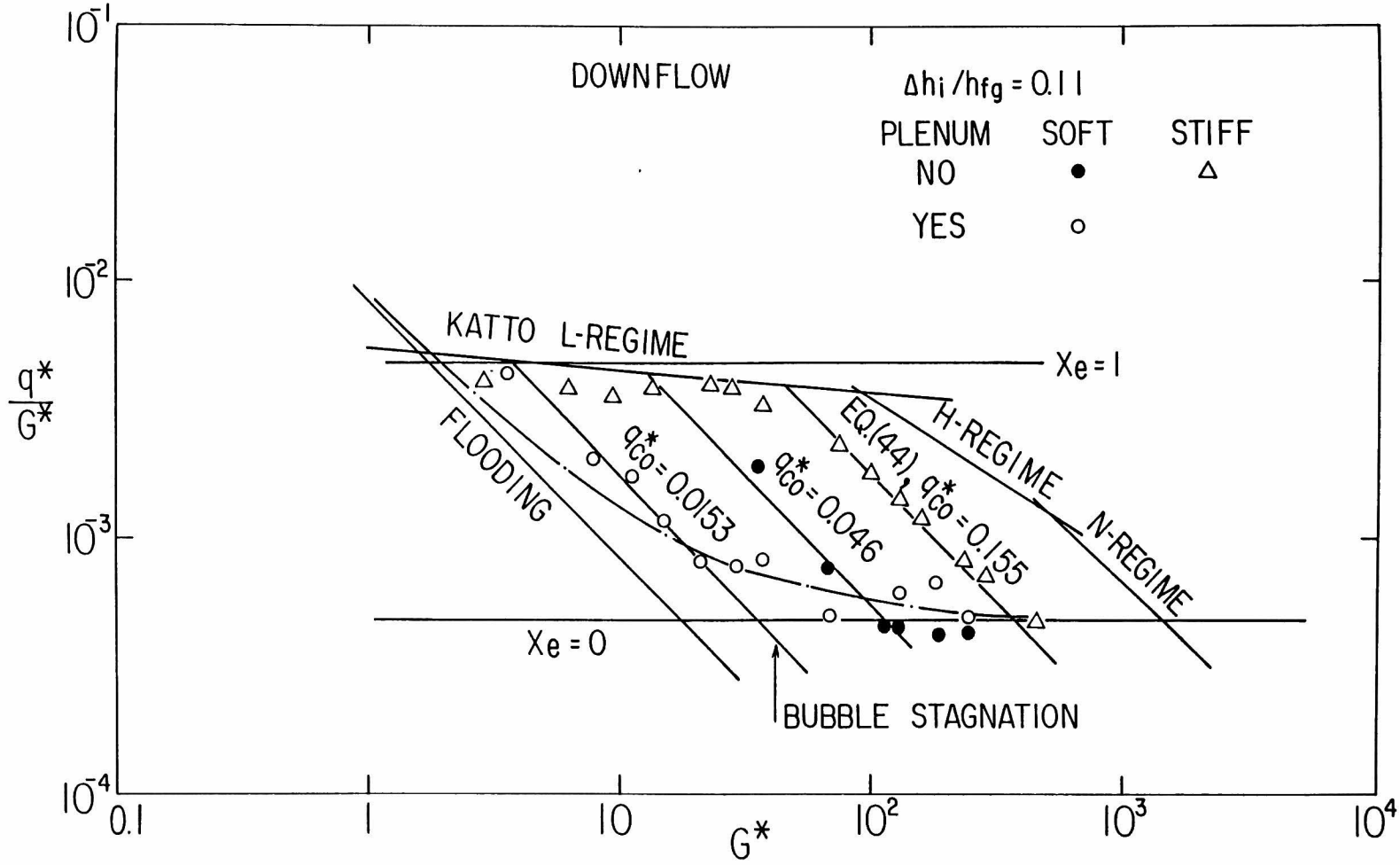


Figure 19 Correlation of downflow CHF data in terms of the boiling number and the non-dimensional mass velocity at inlet temperature 40°C.

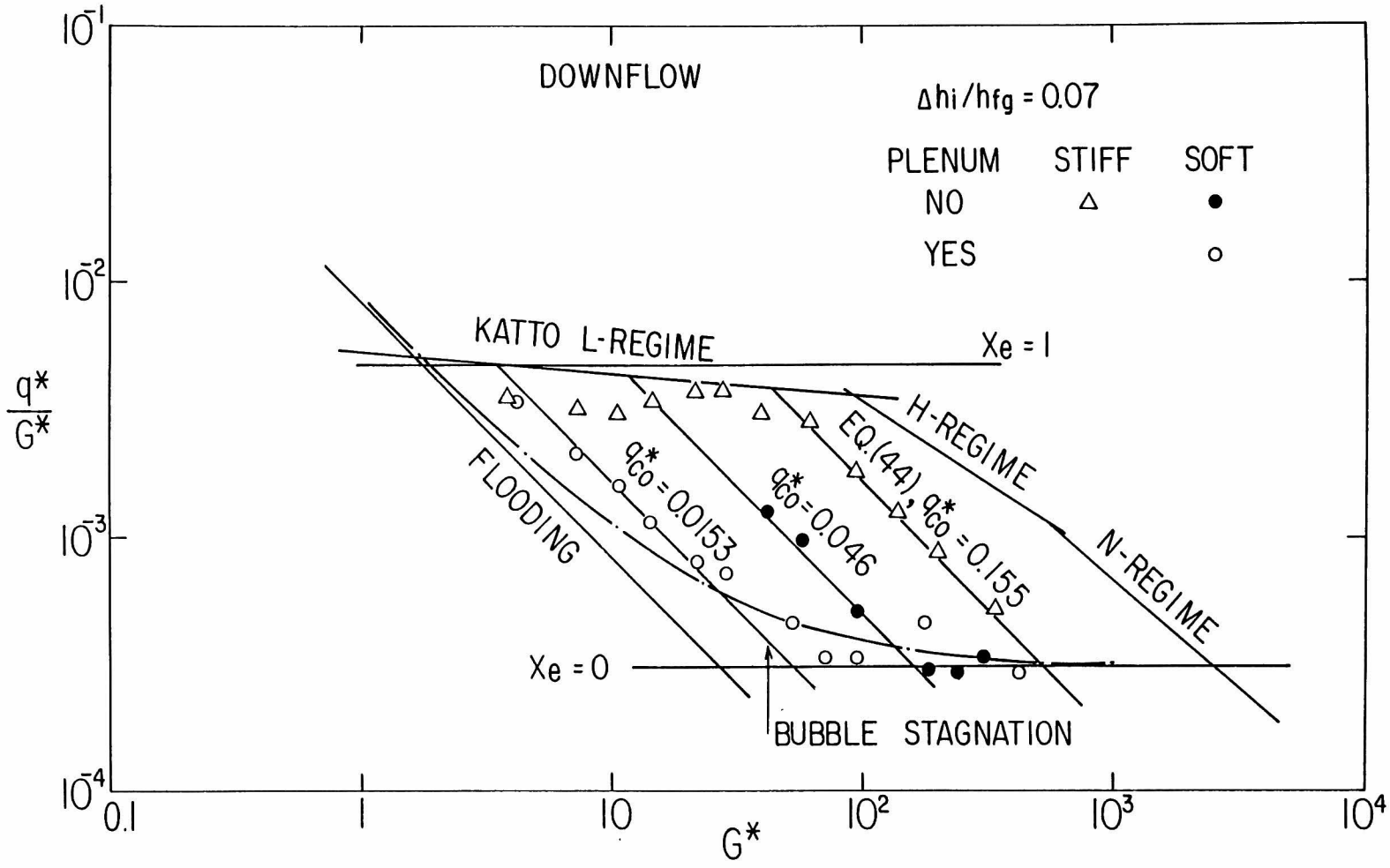


Figure 20 Correlation of downflow CHF data in terms of the boiling number and the non-dimensional mass velocity at inlet temperature 60°C.

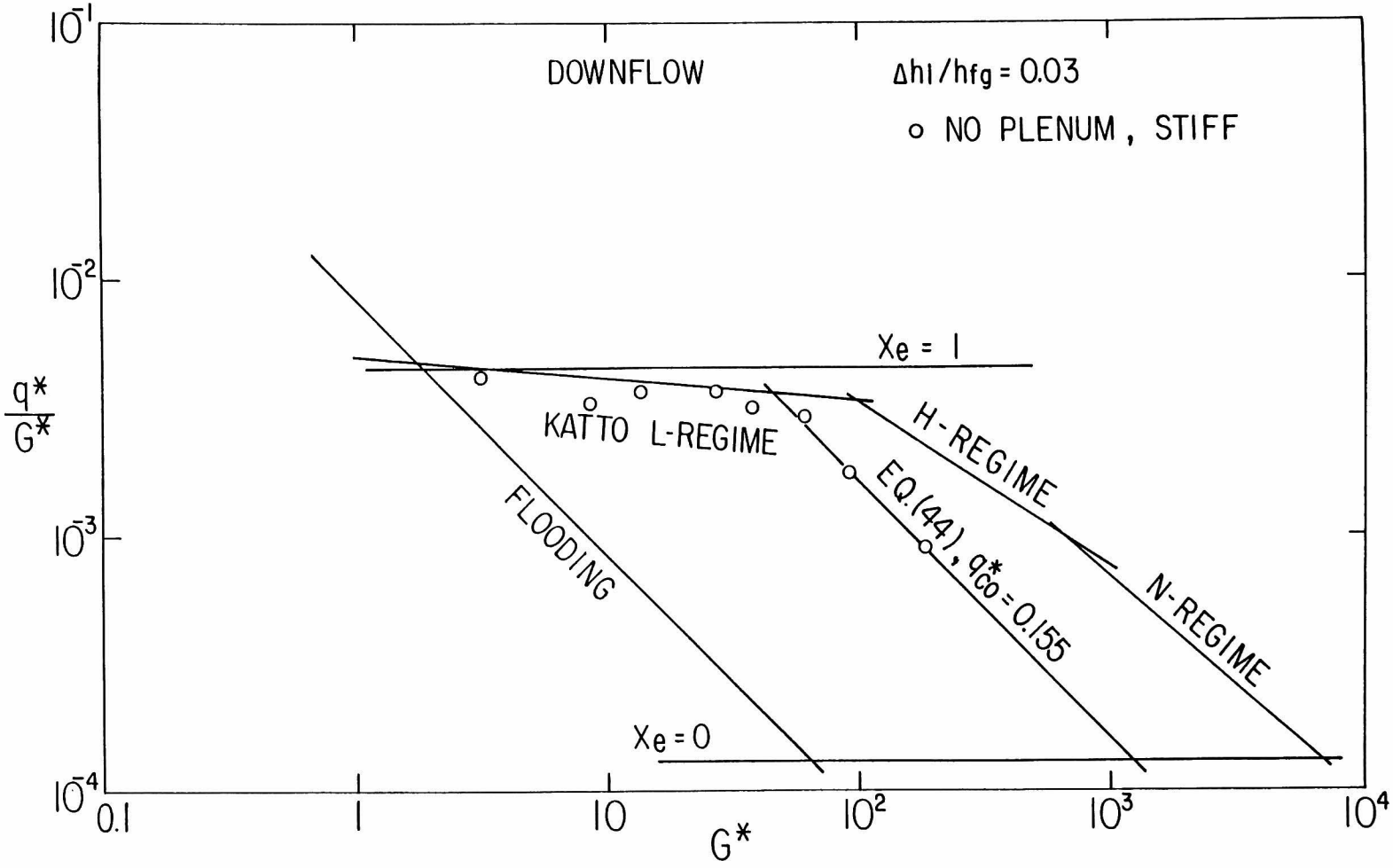


Figure 21 Correlation of downflow CHF data in terms of the boiling number and the non-dimensional mass velocity at inlet temperature 80°C.

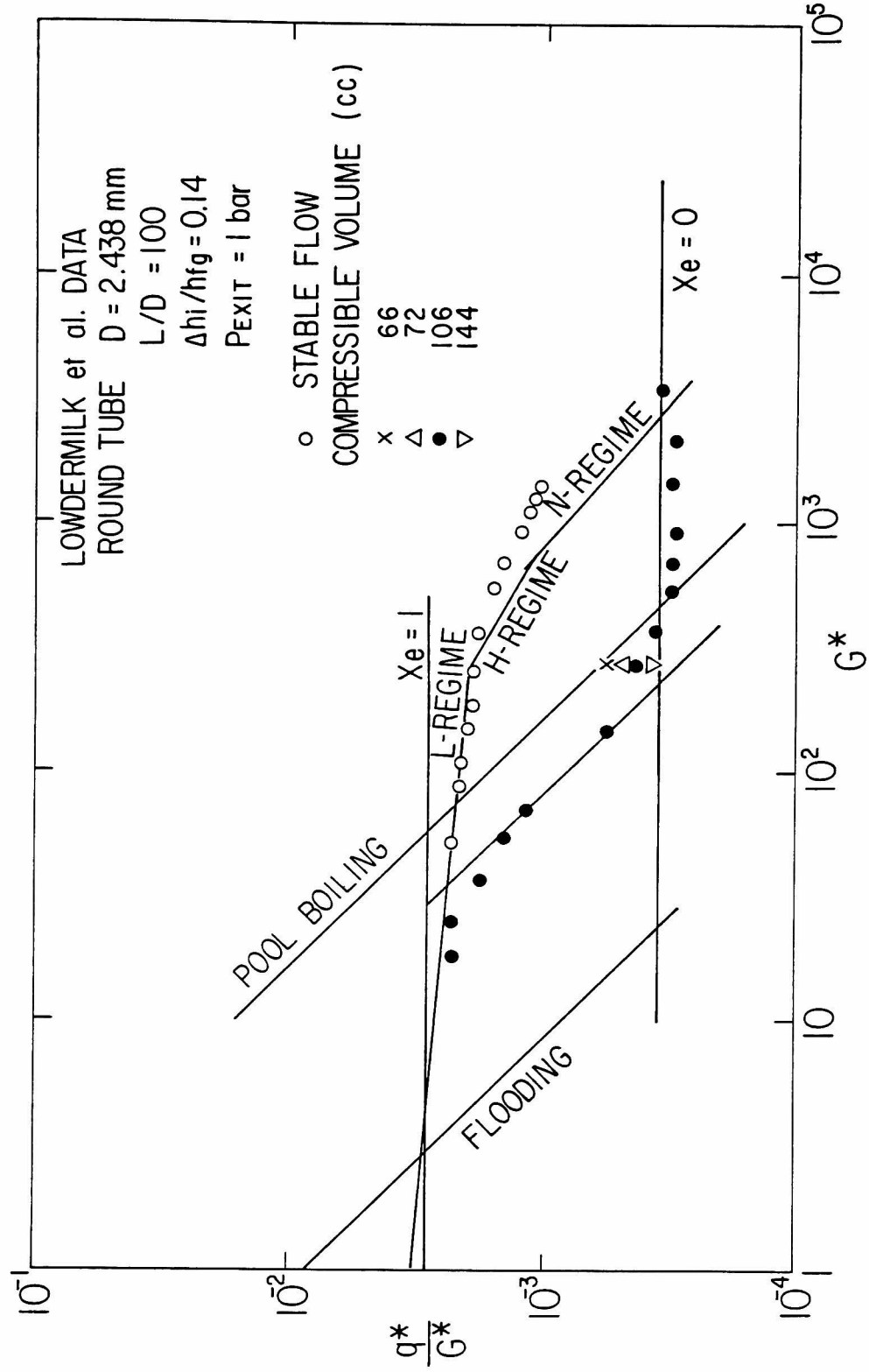


Figure 22 Lowdermilk's data plotted in terms of the boiling number and the non-dimensional mass velocity.

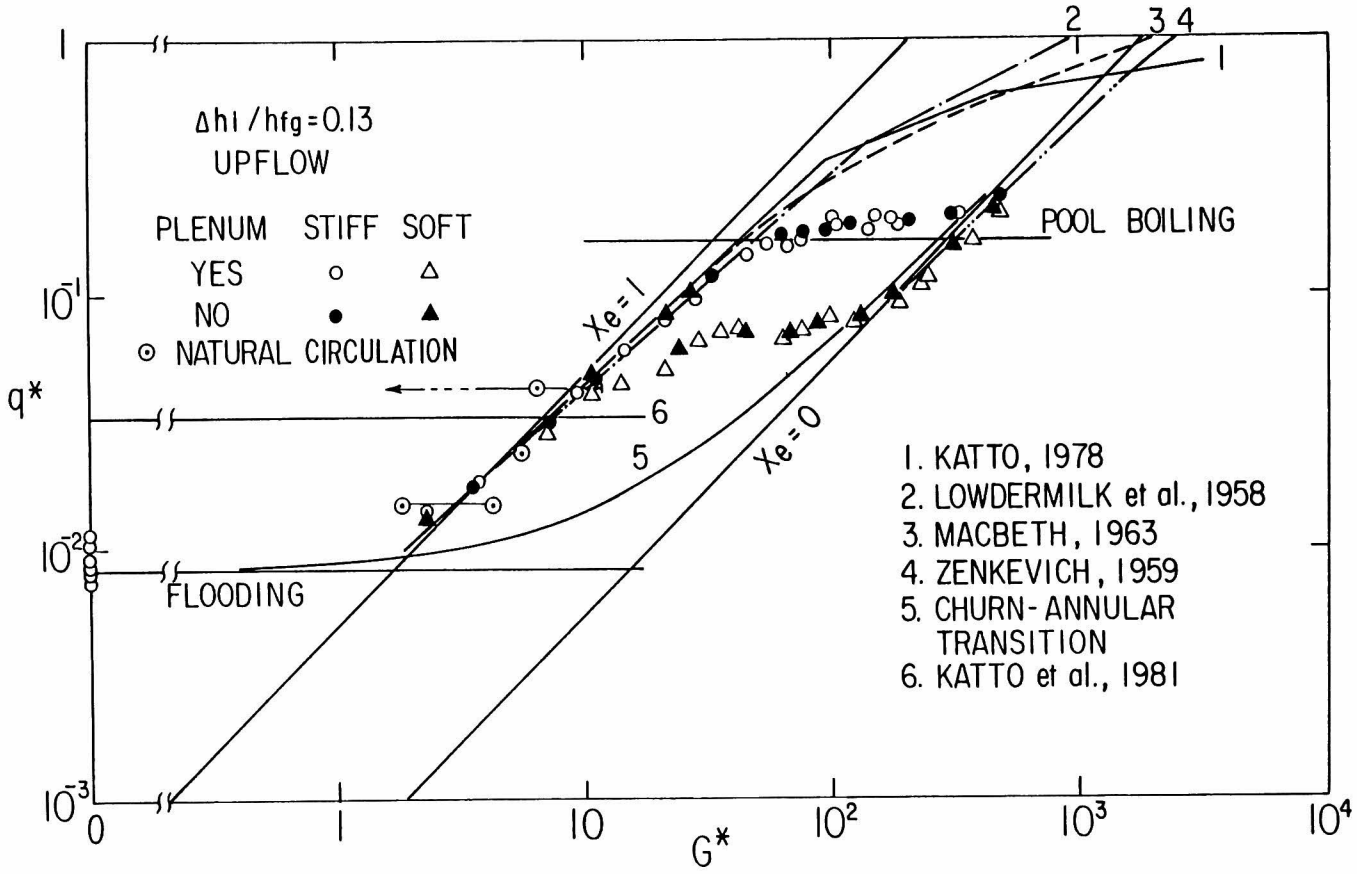


Figure 23 Comparison of CHF data for upflow at inlet water temperature 30°C with existing CHF correlations.

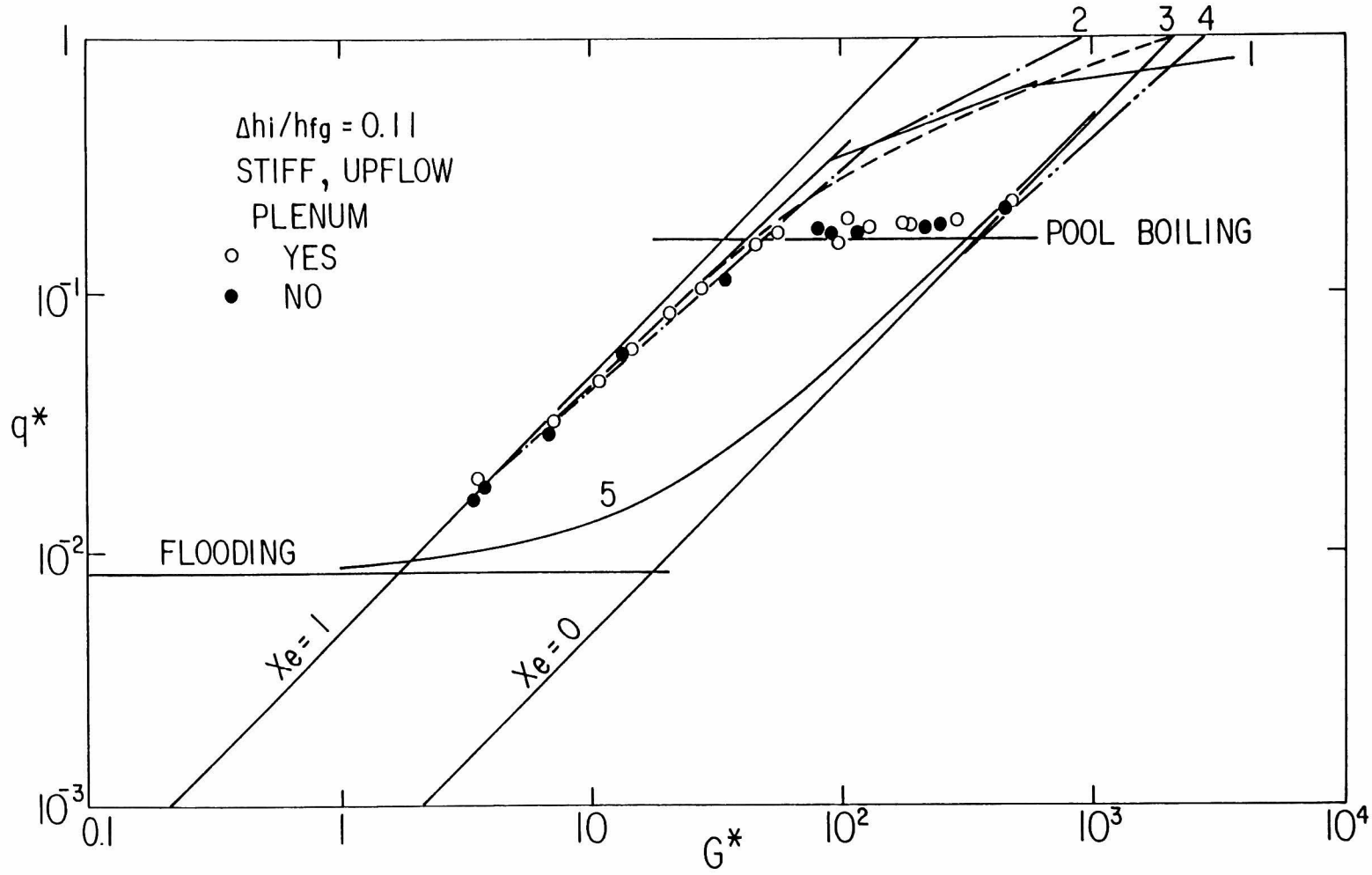


Figure 24 Comparison of CHF data for upflow at inlet water temperature 40°C with existing CHF correlations (Legend as given in Fig. 23).

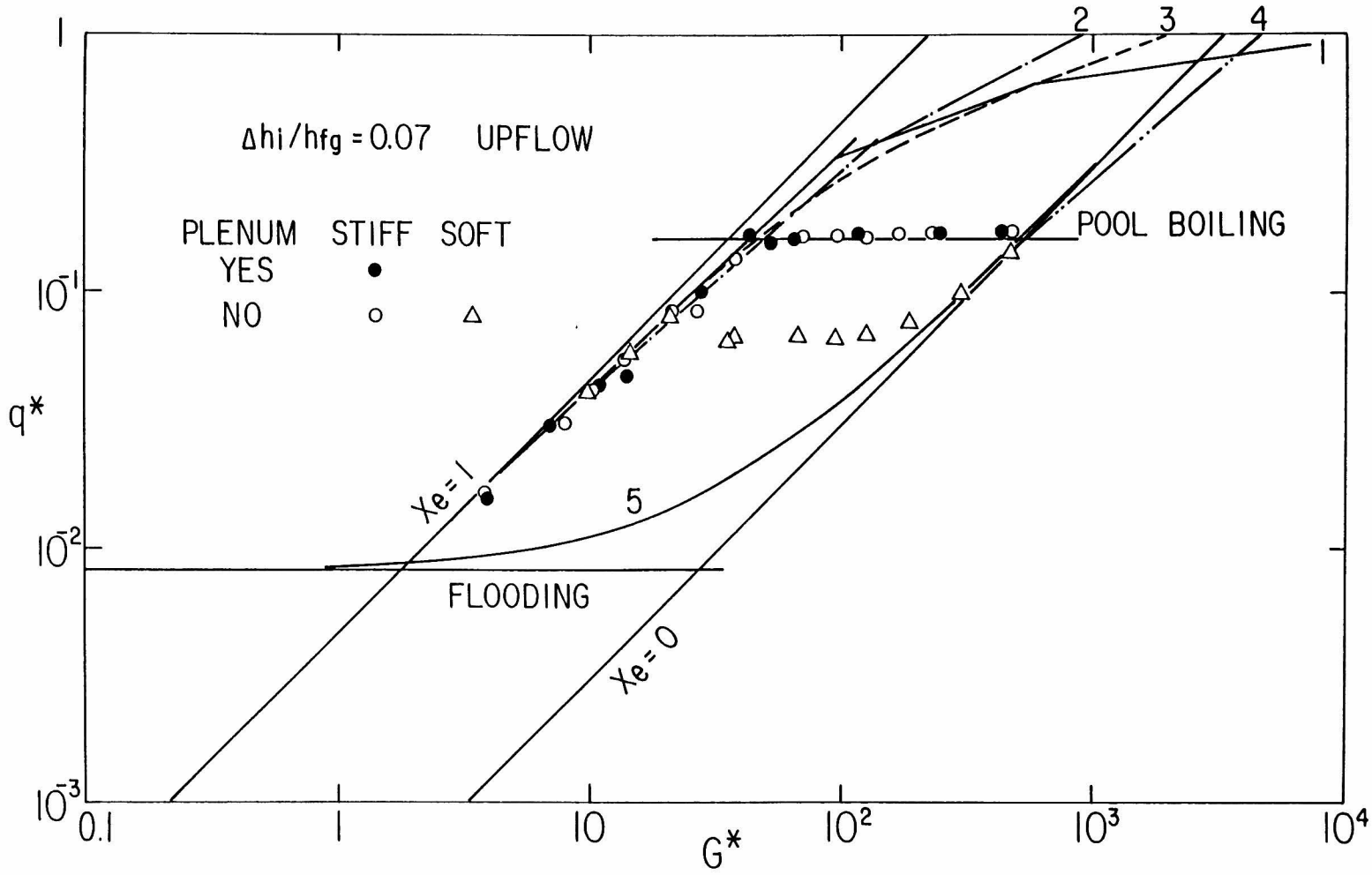


Figure 25 Comparison of CHF data for upflow at inlet water temperature 60°C with existing CHF correlations (Legend as given in Fig. 23).

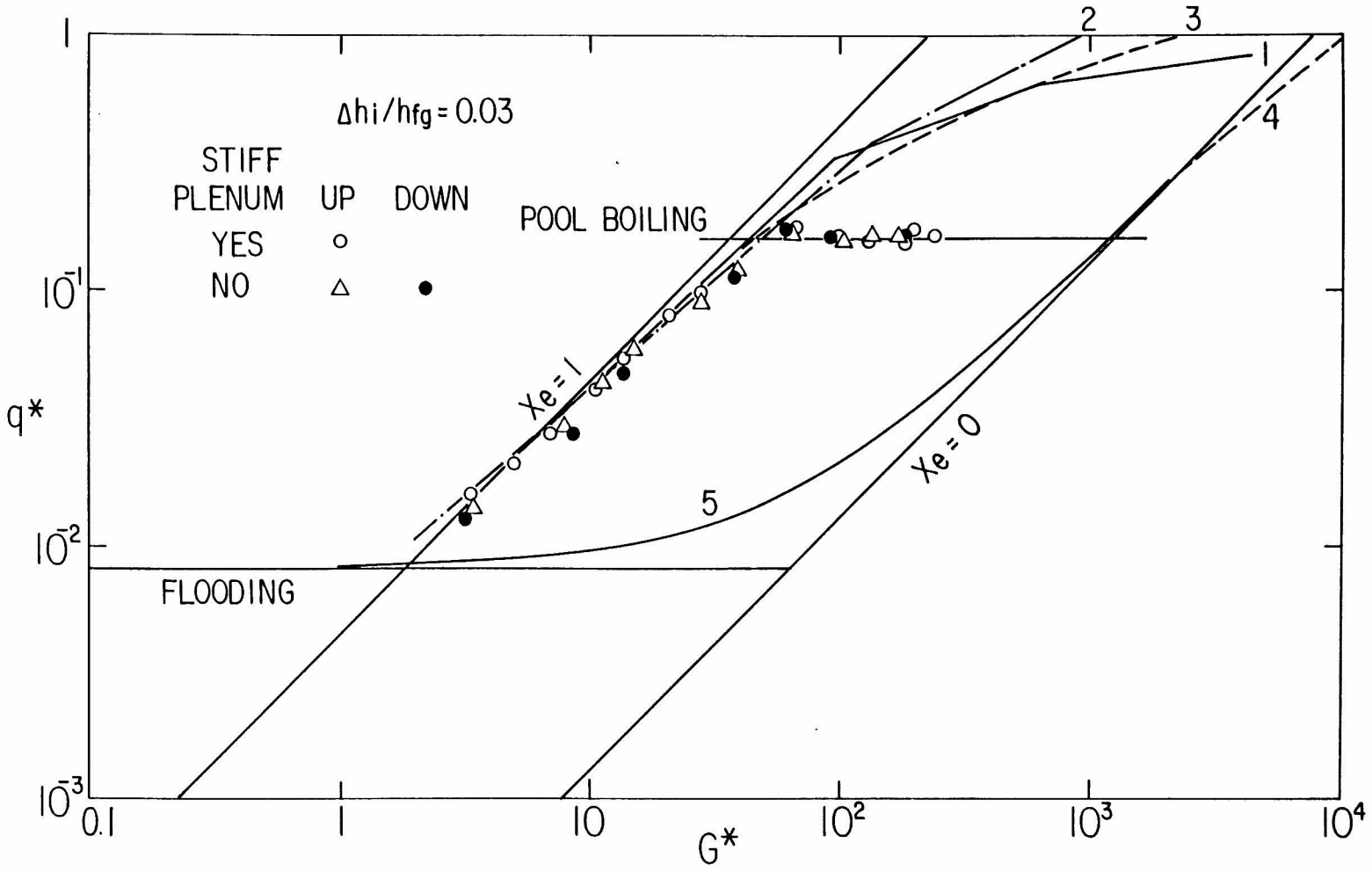


Figure 26 Comparison of CHF data for stiff conditions at inlet water temperature 85°C with existing CHF correlations (Legend as given in Fig. 23).

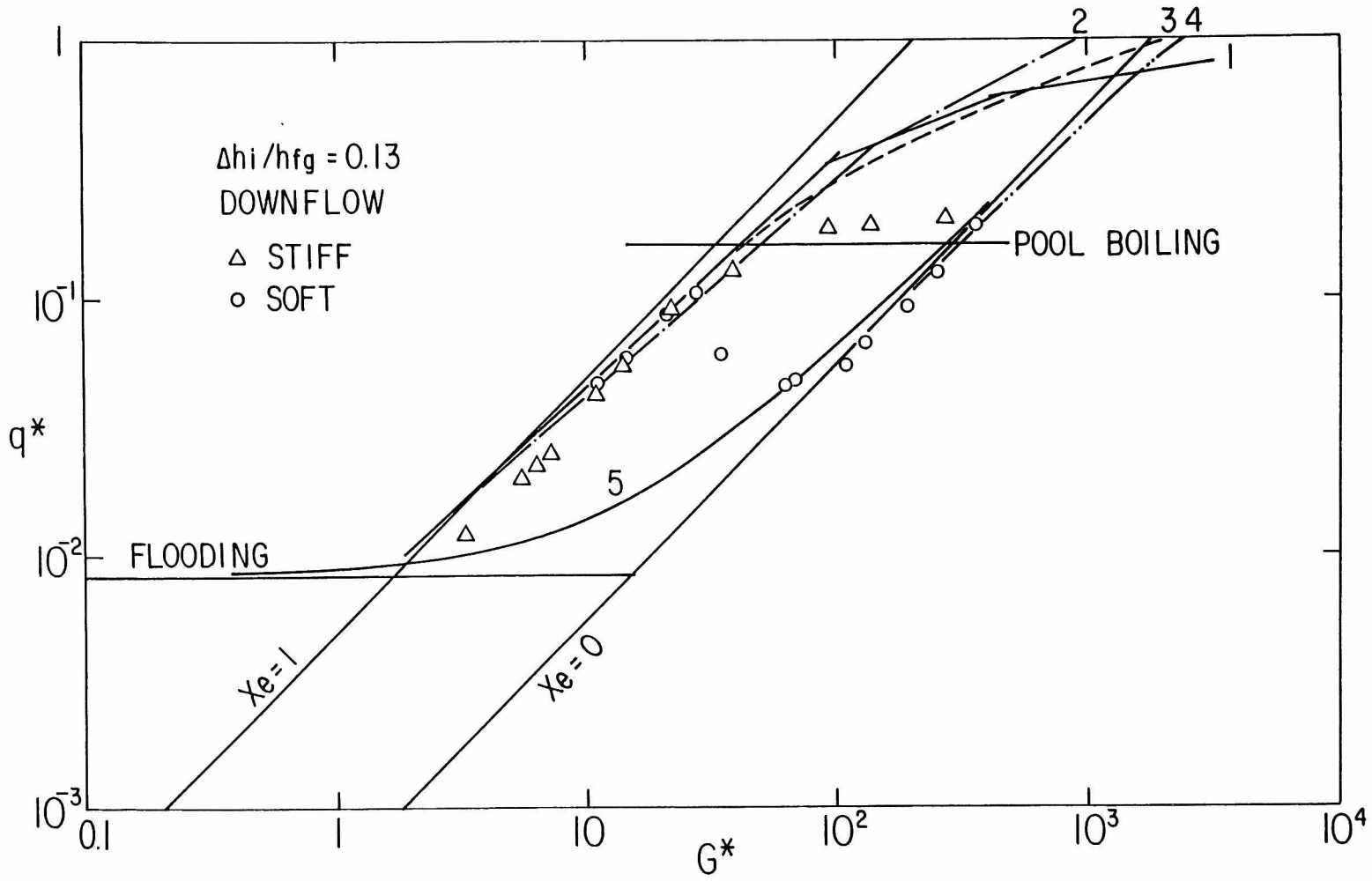


Figure 27 Comparison of CHF data for downflow at inlet water temperature 30°C with existing CHF correlations (Legend as given in Fig. 23).

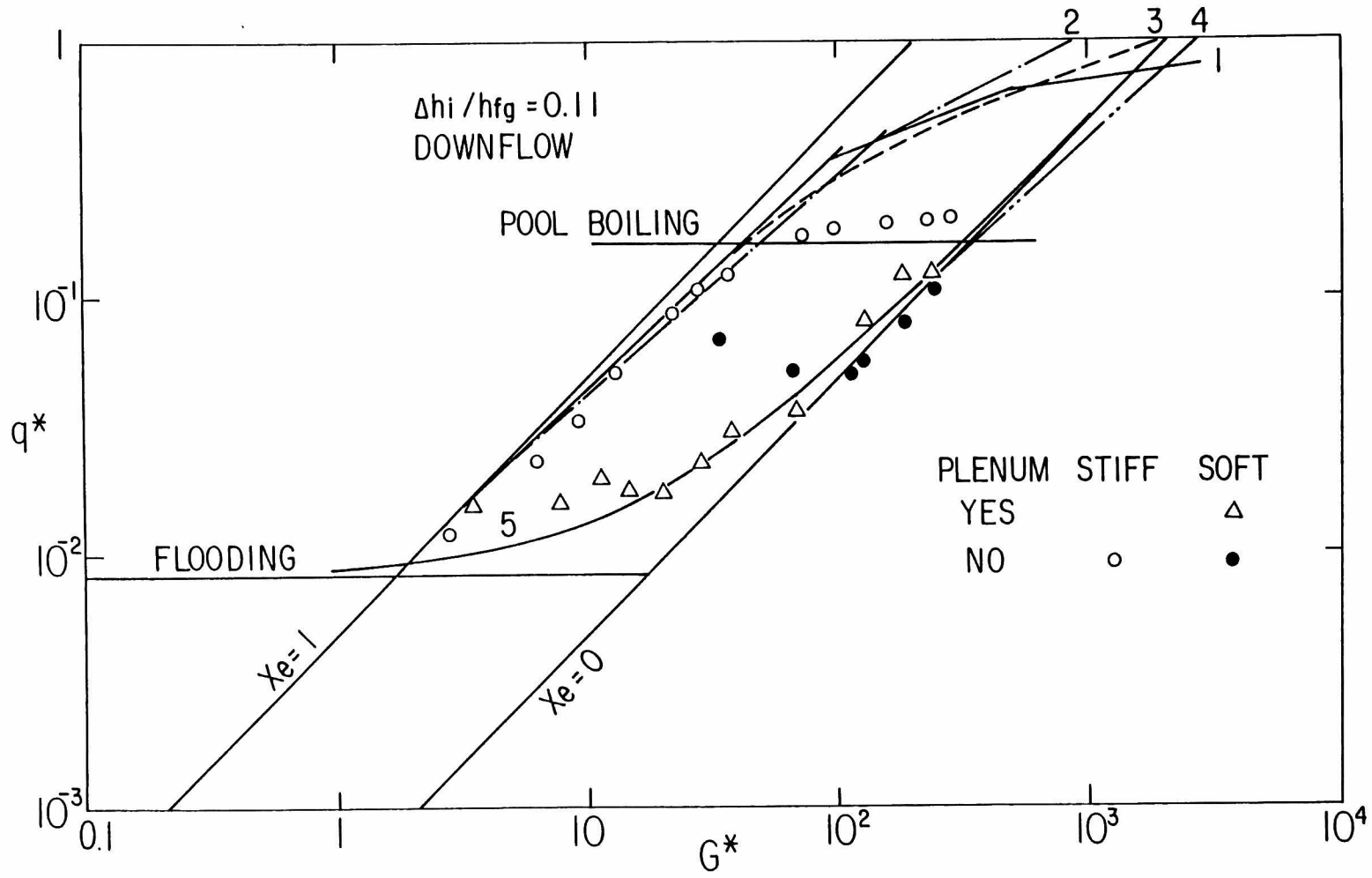


Figure 28 Comparison of CHF data for downflow at inlet water temperature 40°C with existing CHF correlations (Legend as given in Fig. 23).

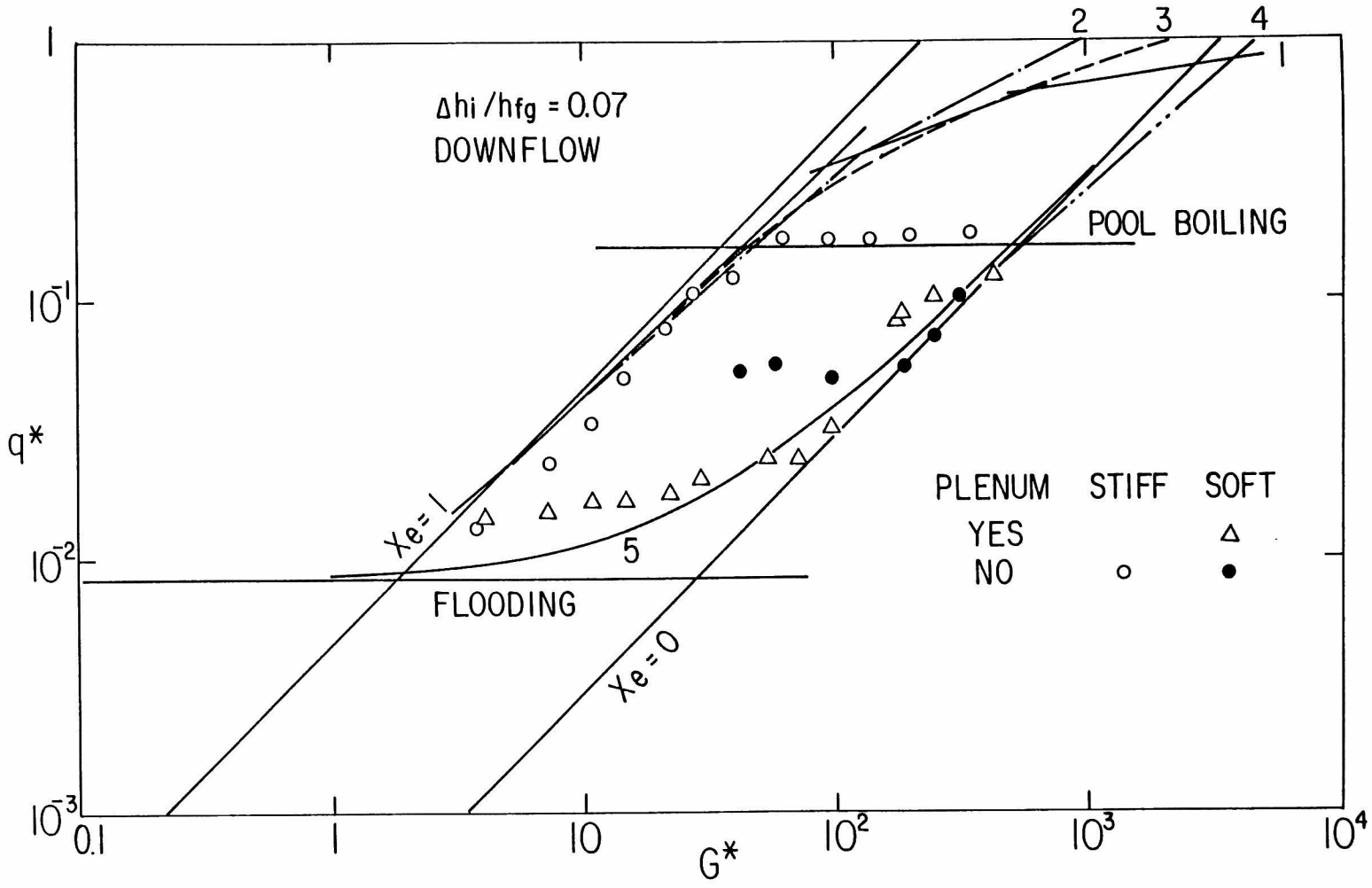


Figure 29 Comparison of CHF data for downflow at inlet water temperature 60°C with existing CHF correlations (Legend as given in Fig. 23).

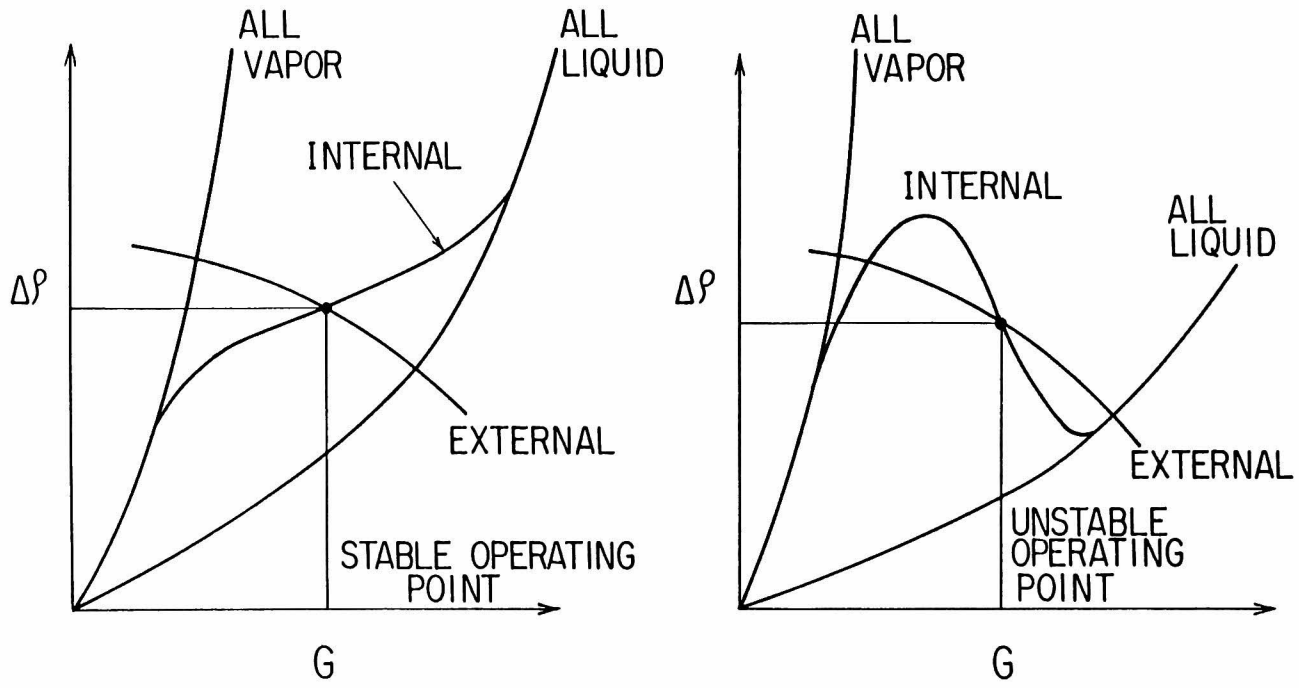


Figure 30 Stable and unstable pressure-drop characteristics.

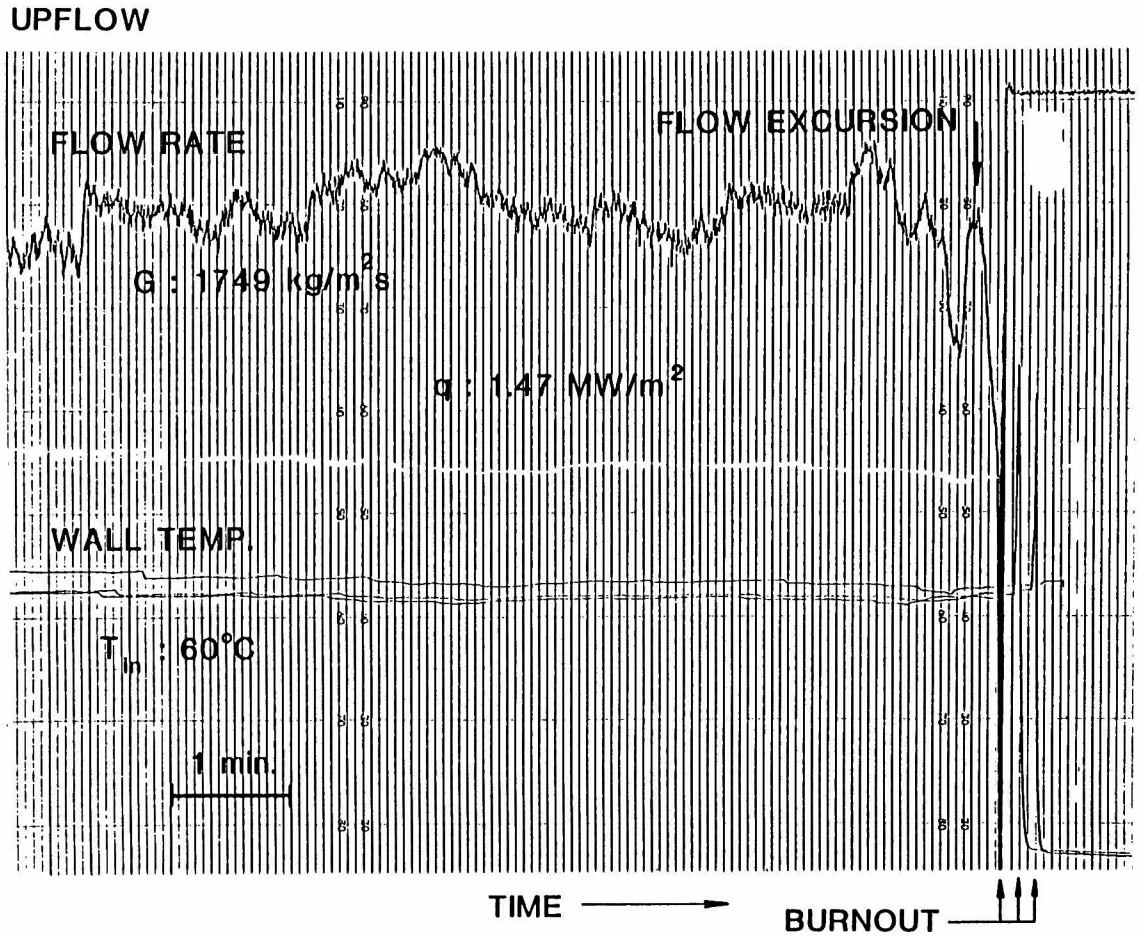


Figure 31 Example of the traces for burnout due to flow excursion.

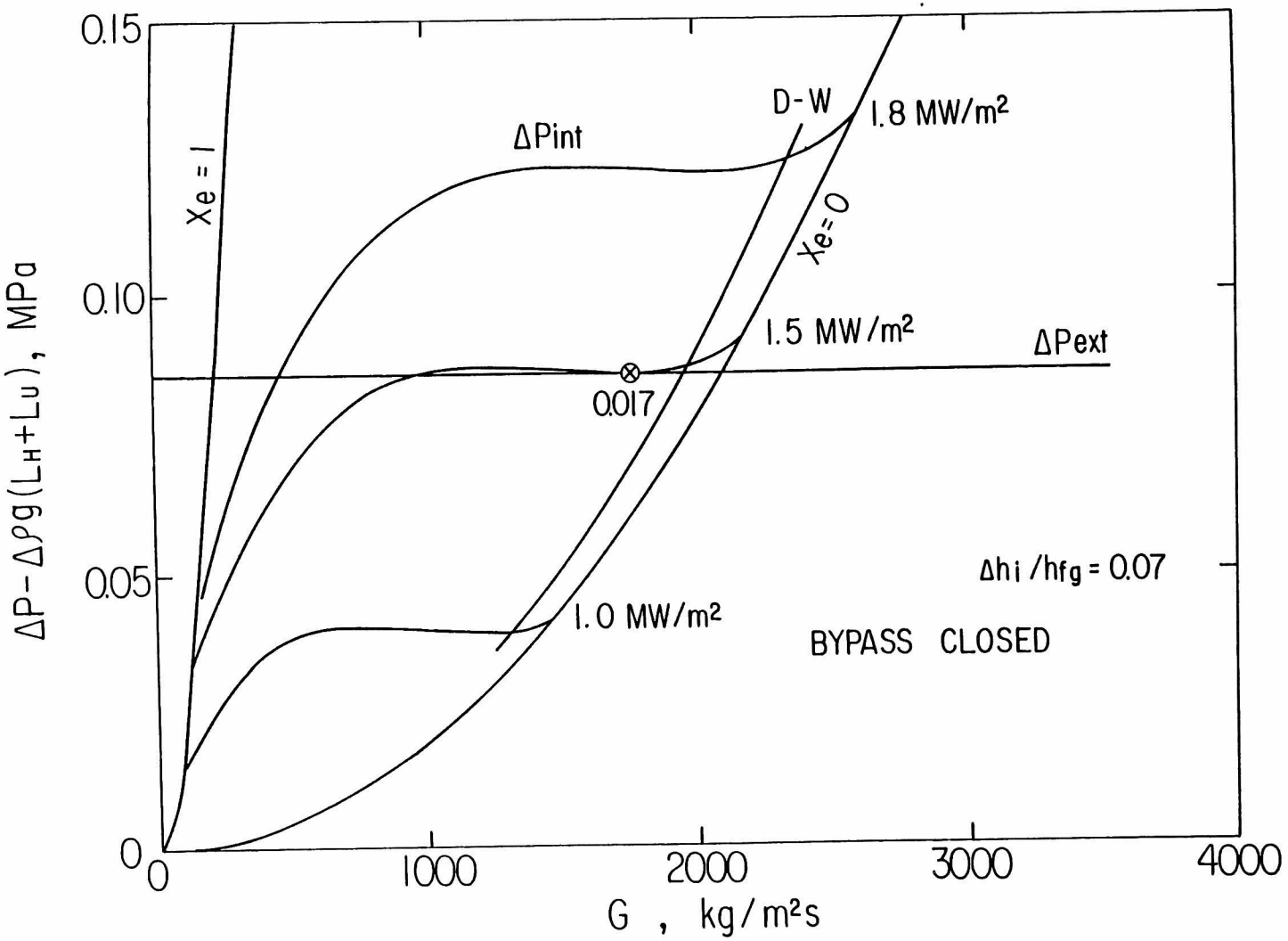


Figure 32 Example of the pressure-drop versus flow-rate curve for the case shown in Fig. 31 which resulted in a burnout due to flow excursion.

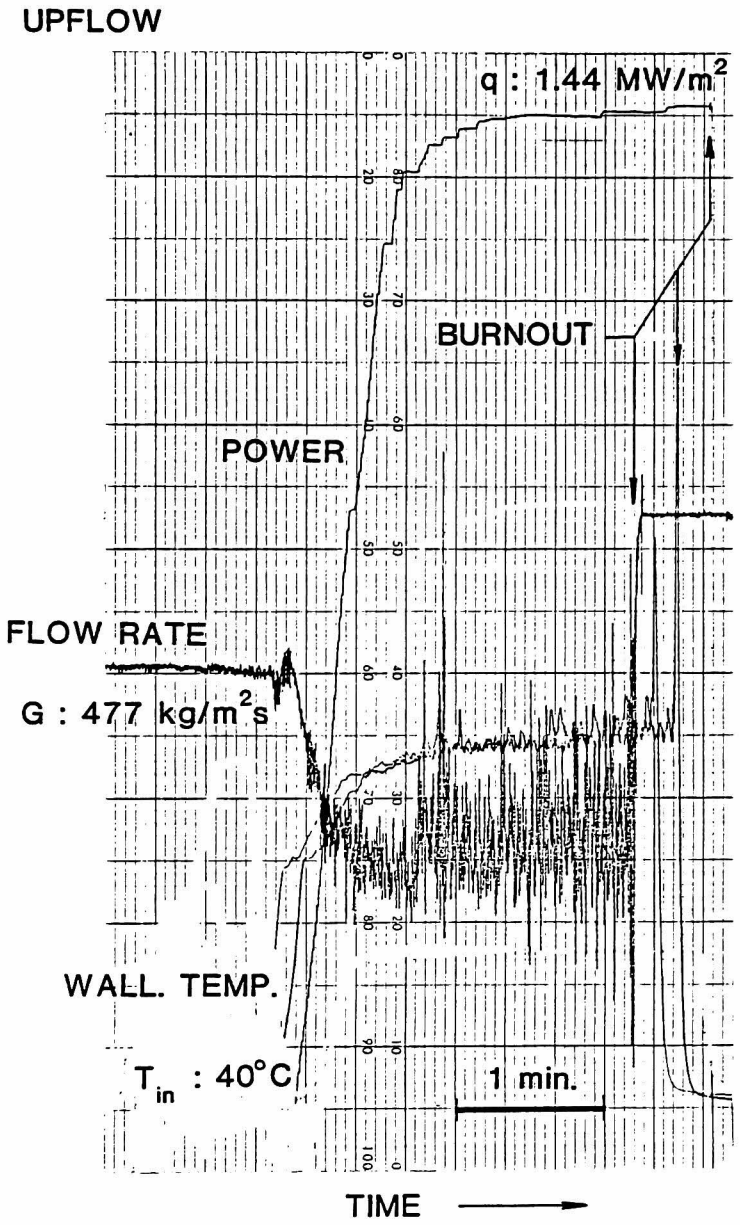


Figure 33 Example of the traces for burnout associated with the density-wave oscillations.

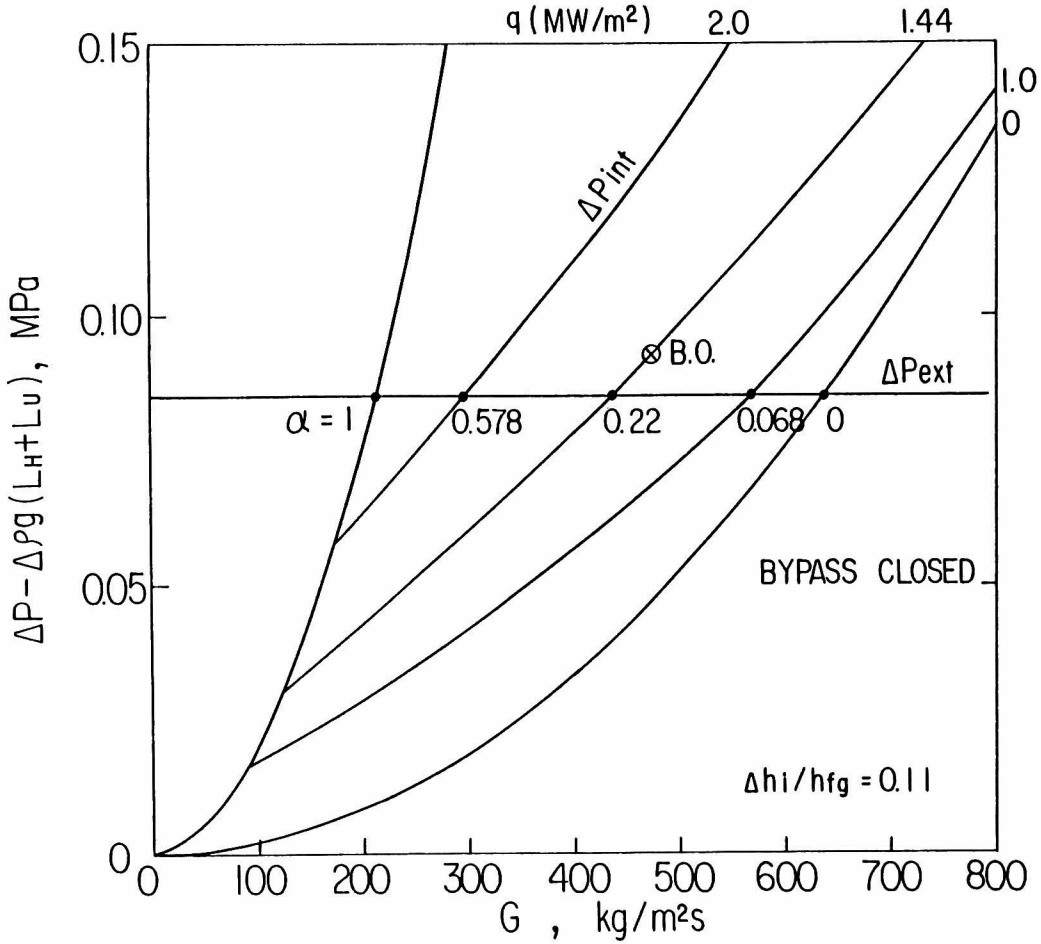


Figure 34 Example of the pressure-drop versus flow-rate curve for the case shown in Fig. 33 in which the density-wave oscillations were encountered.

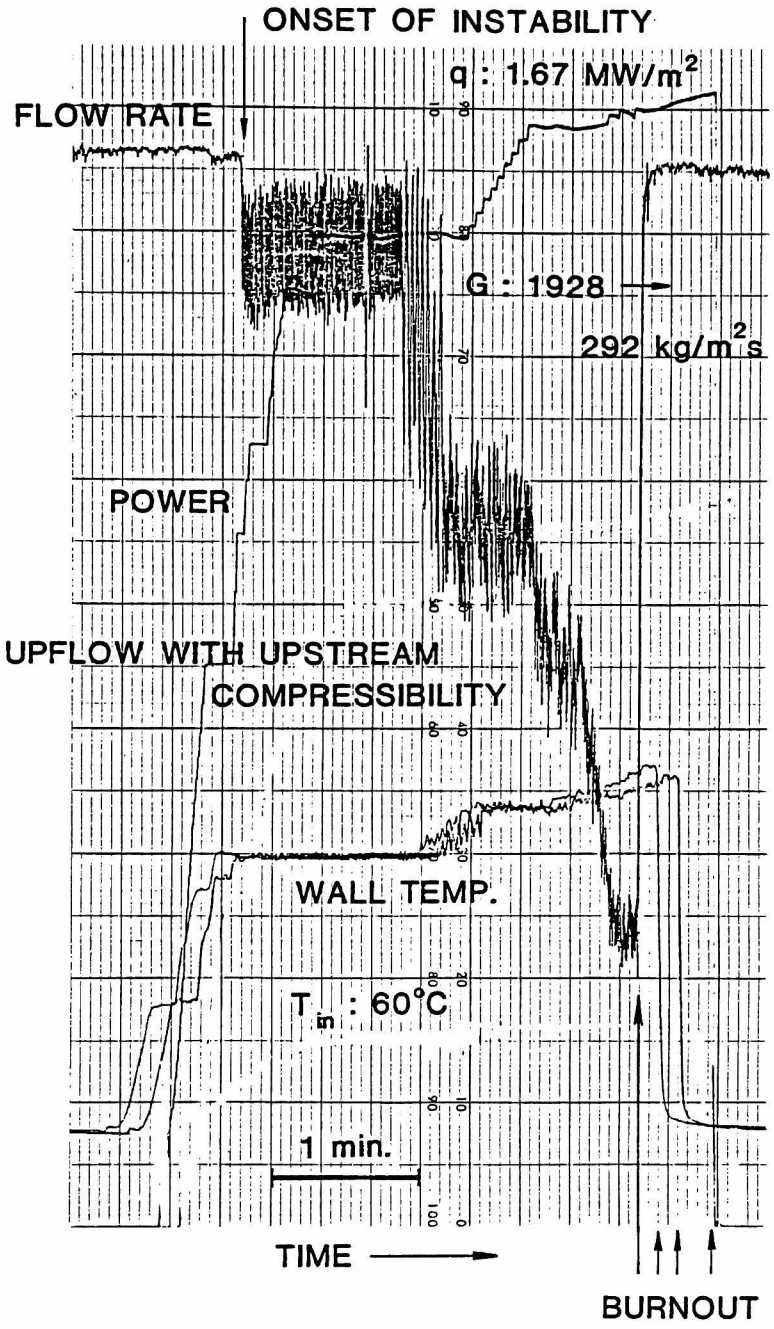


Figure 35 Example of the flow-rate traces for the pressure-drop oscillations associated with the density-wave oscillations.

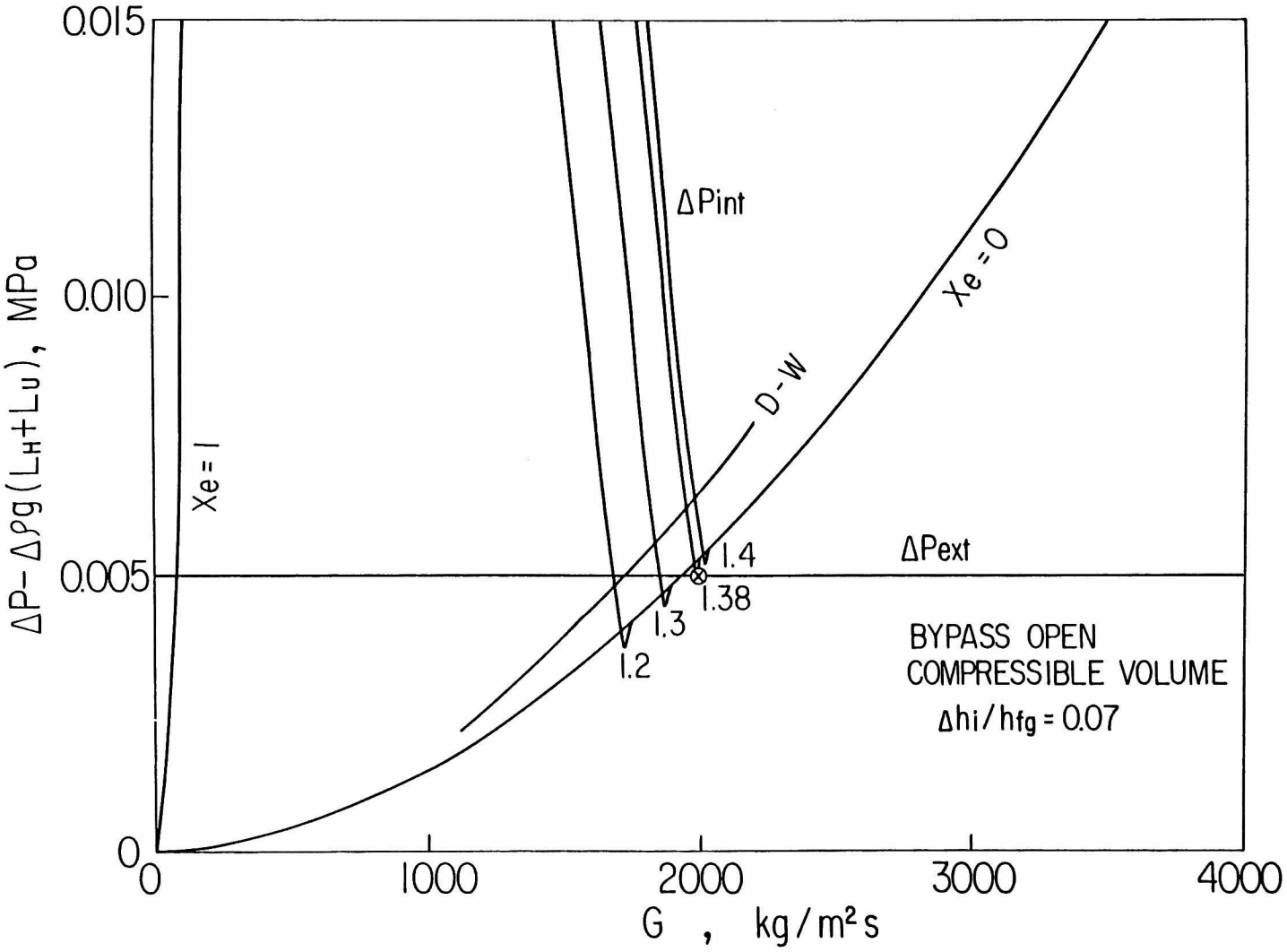


Figure 36 Example of the pressure-drop versus flow-rate curve for the case shown in Fig. 35.

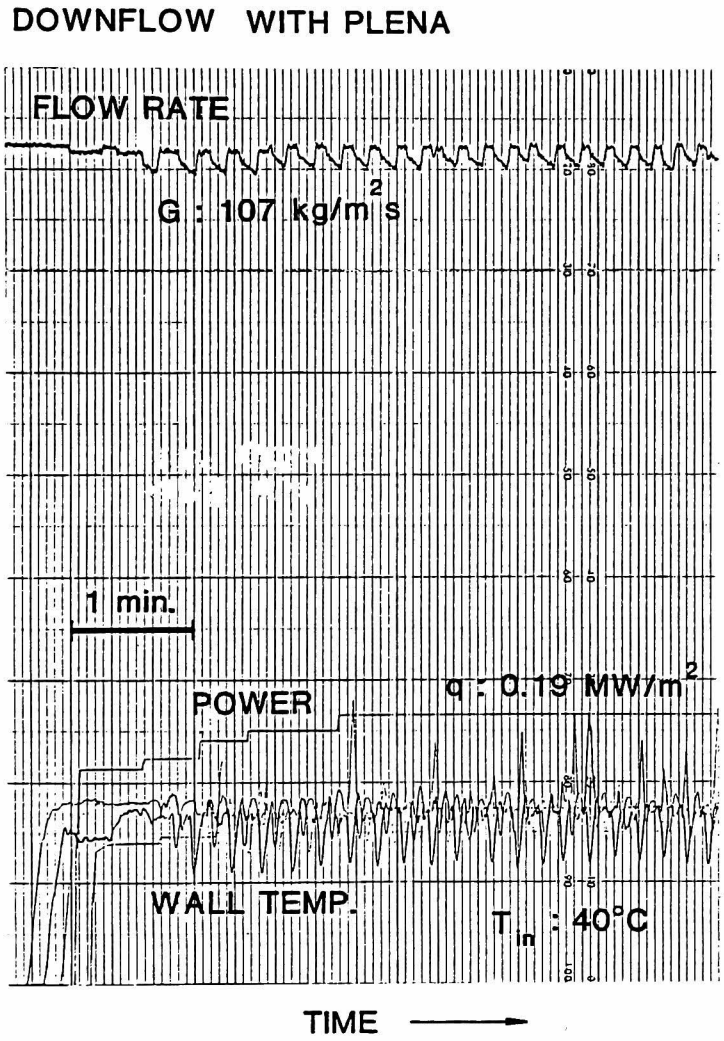


Figure 37 Periodic flow oscillations observed in downflow at low mass velocities in the test section with an upper plenum.

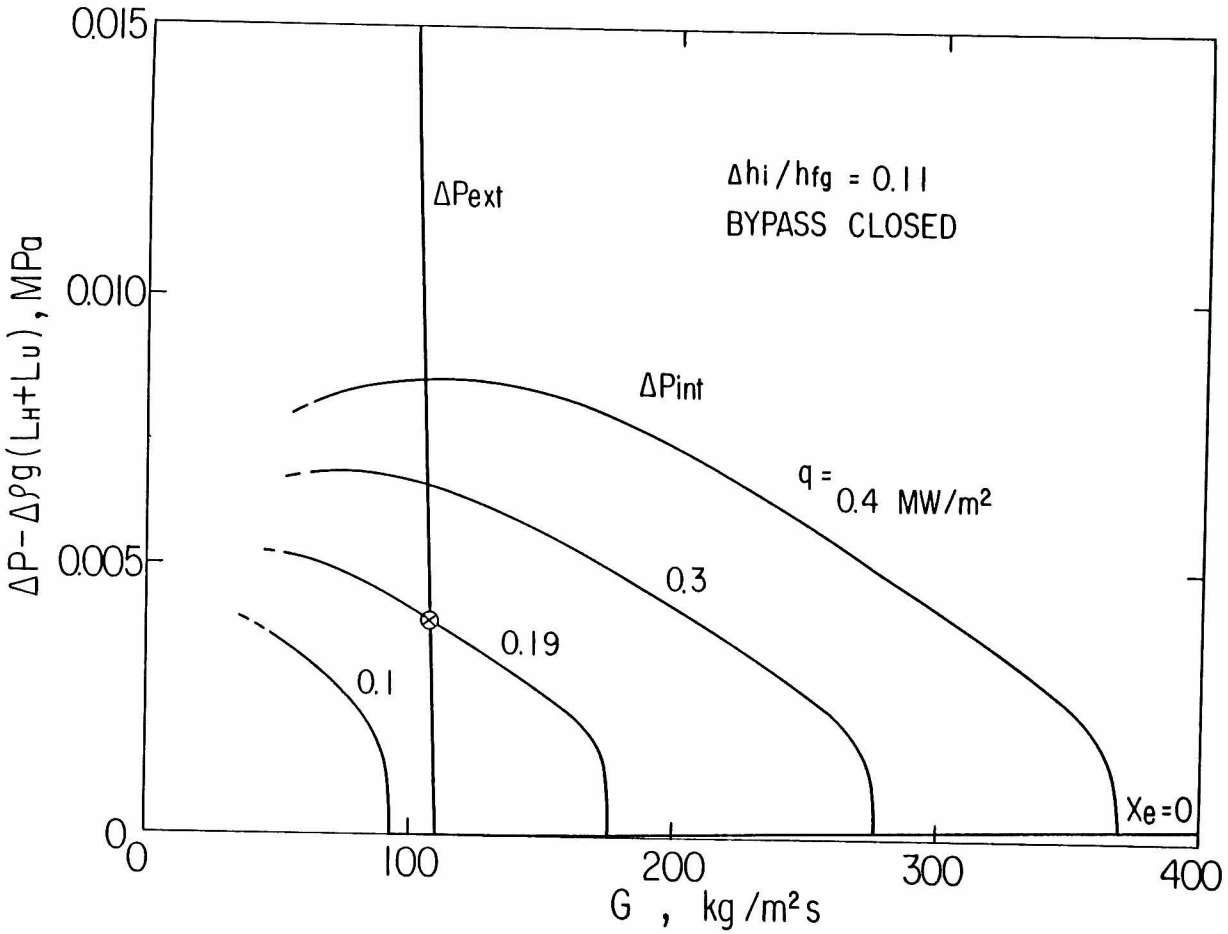


Figure 38 Pressure-drop versus flow-rate curves for the case shown in Fig. 37.

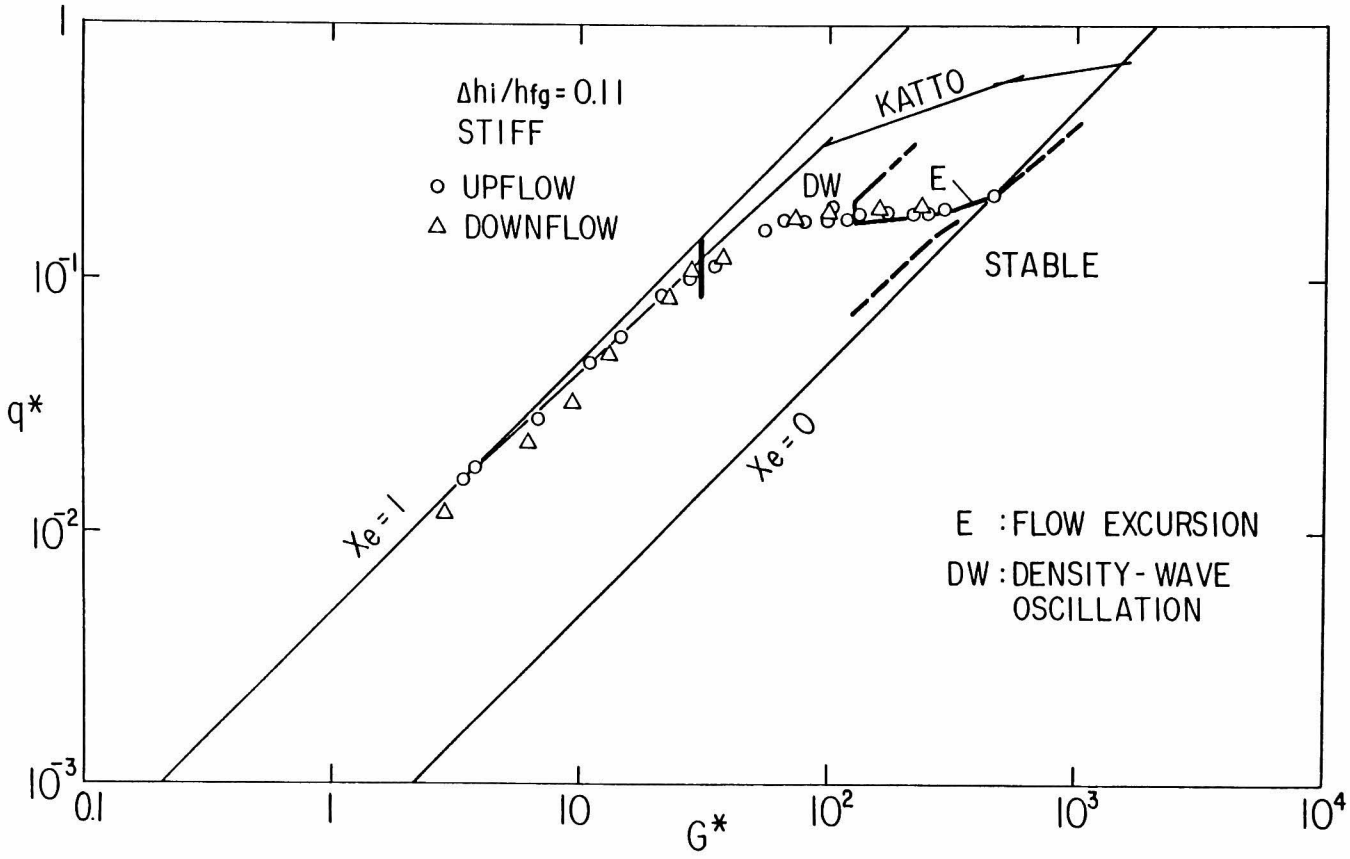


Figure 39 Stability boundaries for upflow and downflow in the stiff system at inlet water temperature 40°C.

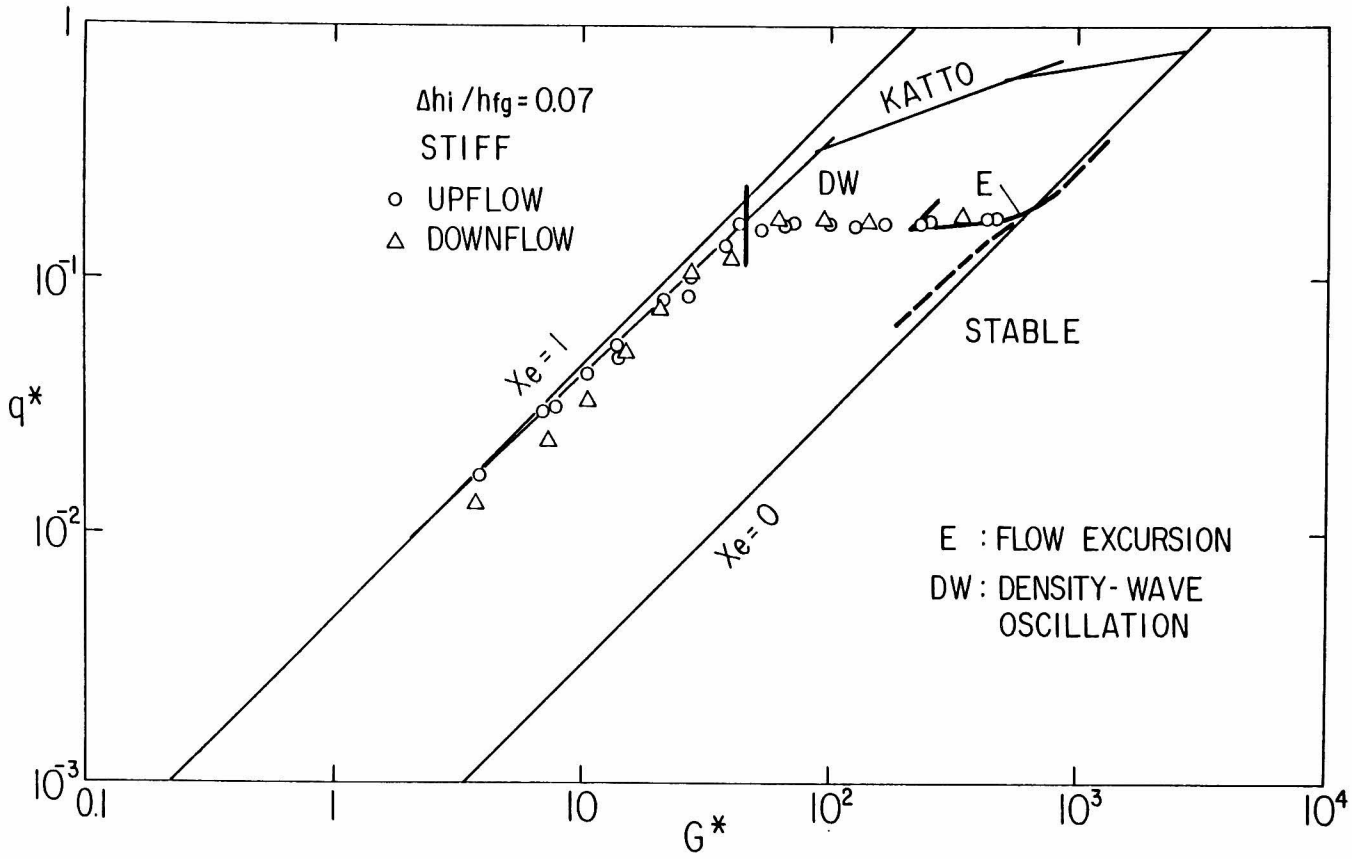


Figure 40 Stability boundaries for upflow and downflow in the stiff system at inlet water temperature 60°C.

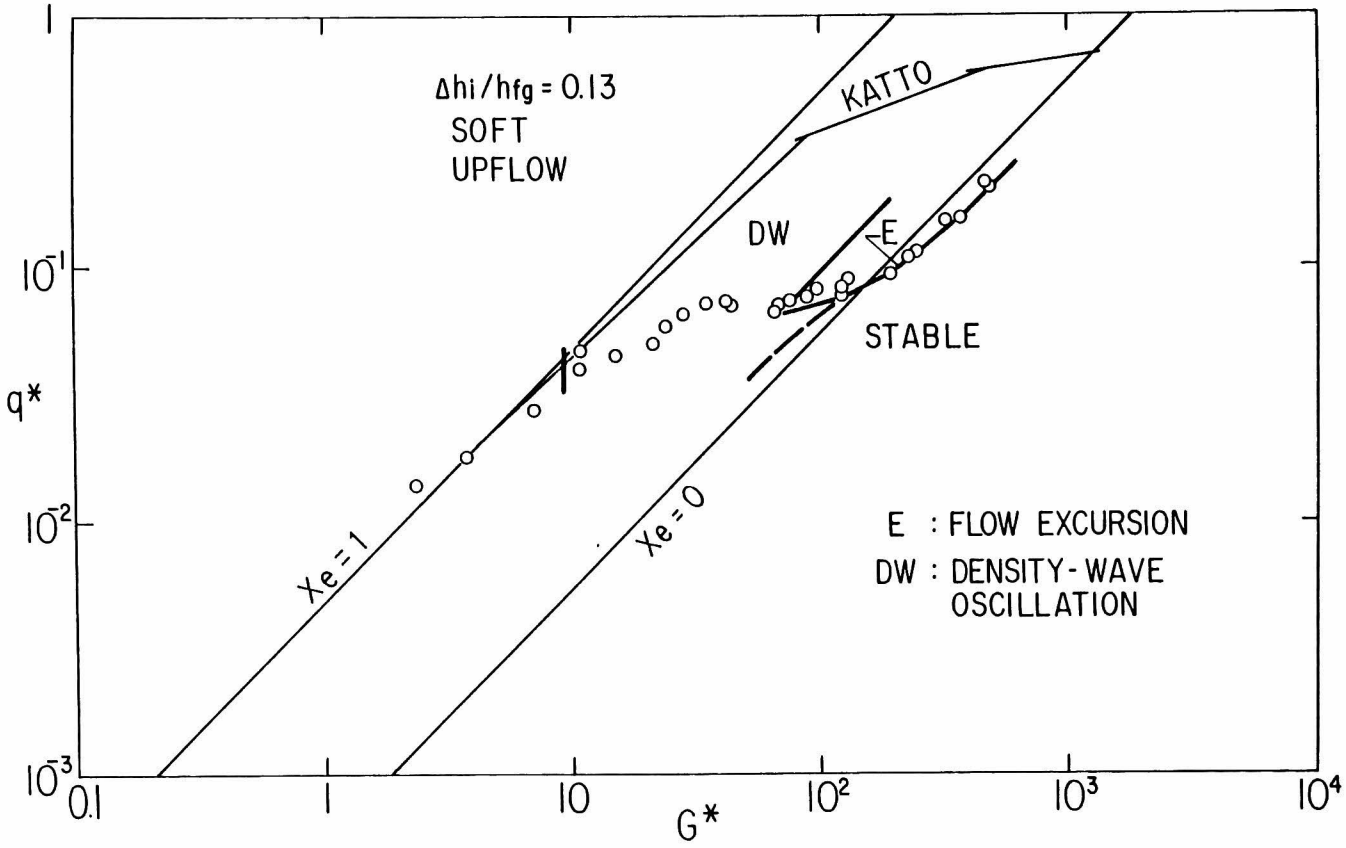


Figure 41 Stability boundaries for upflow in the soft system st inlet water temperature 30°C.

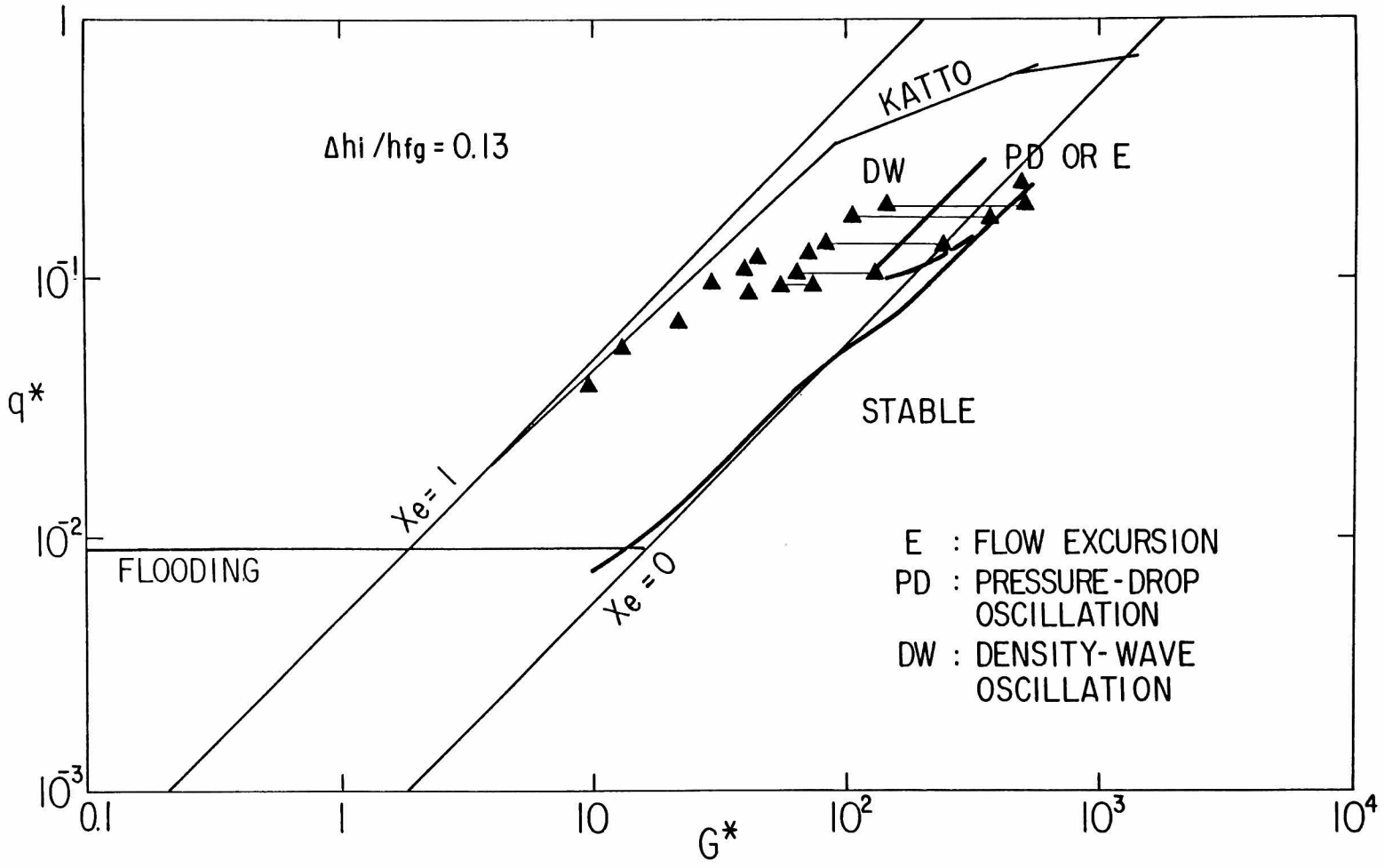


Figure 42 Stability boundaries for upflow with an upstream compressibility at inlet water temperature 30°C.

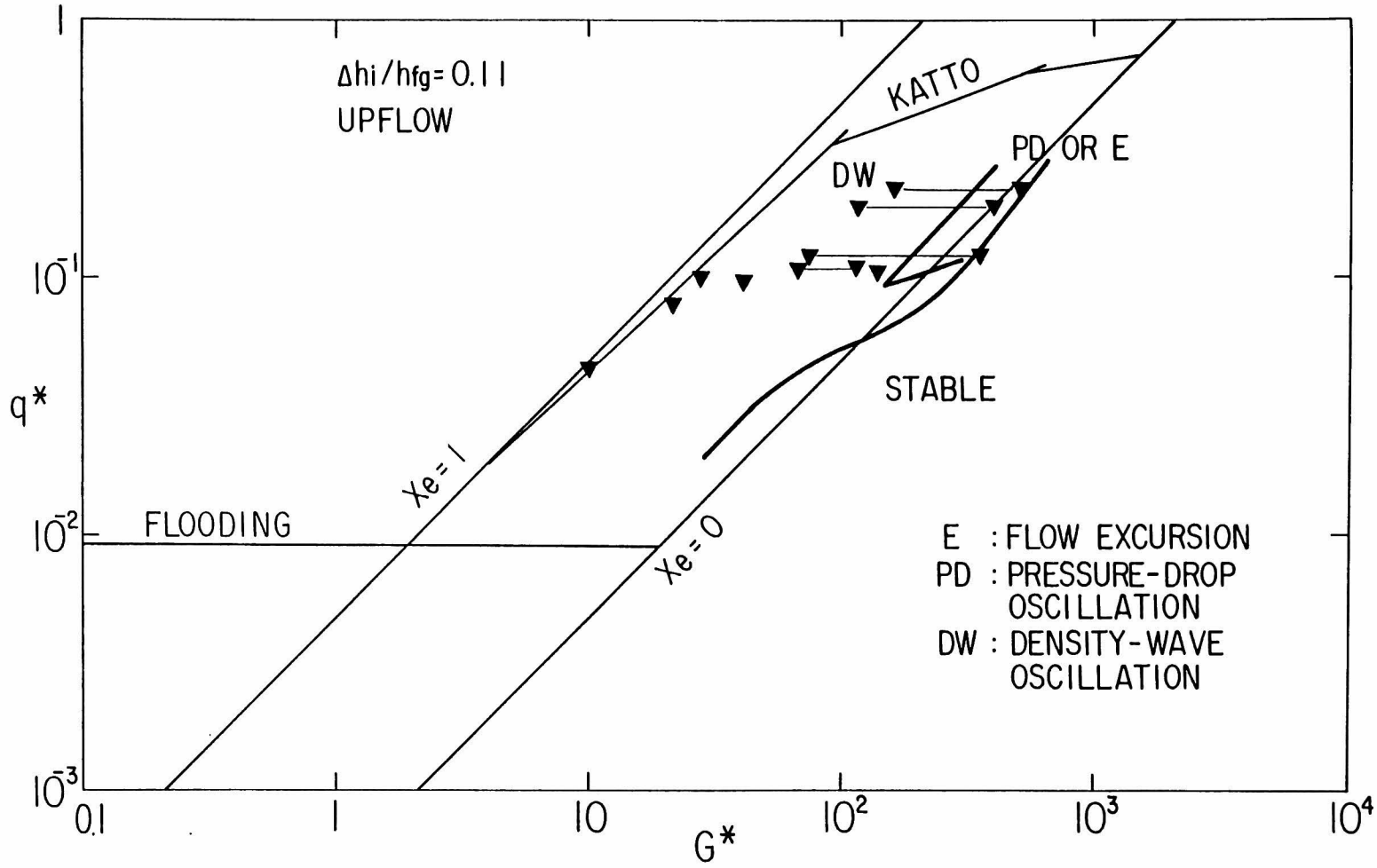


Figure 43 Stability boundaries for upflow with an upstream compressibility at inlet water temperature 40°C.

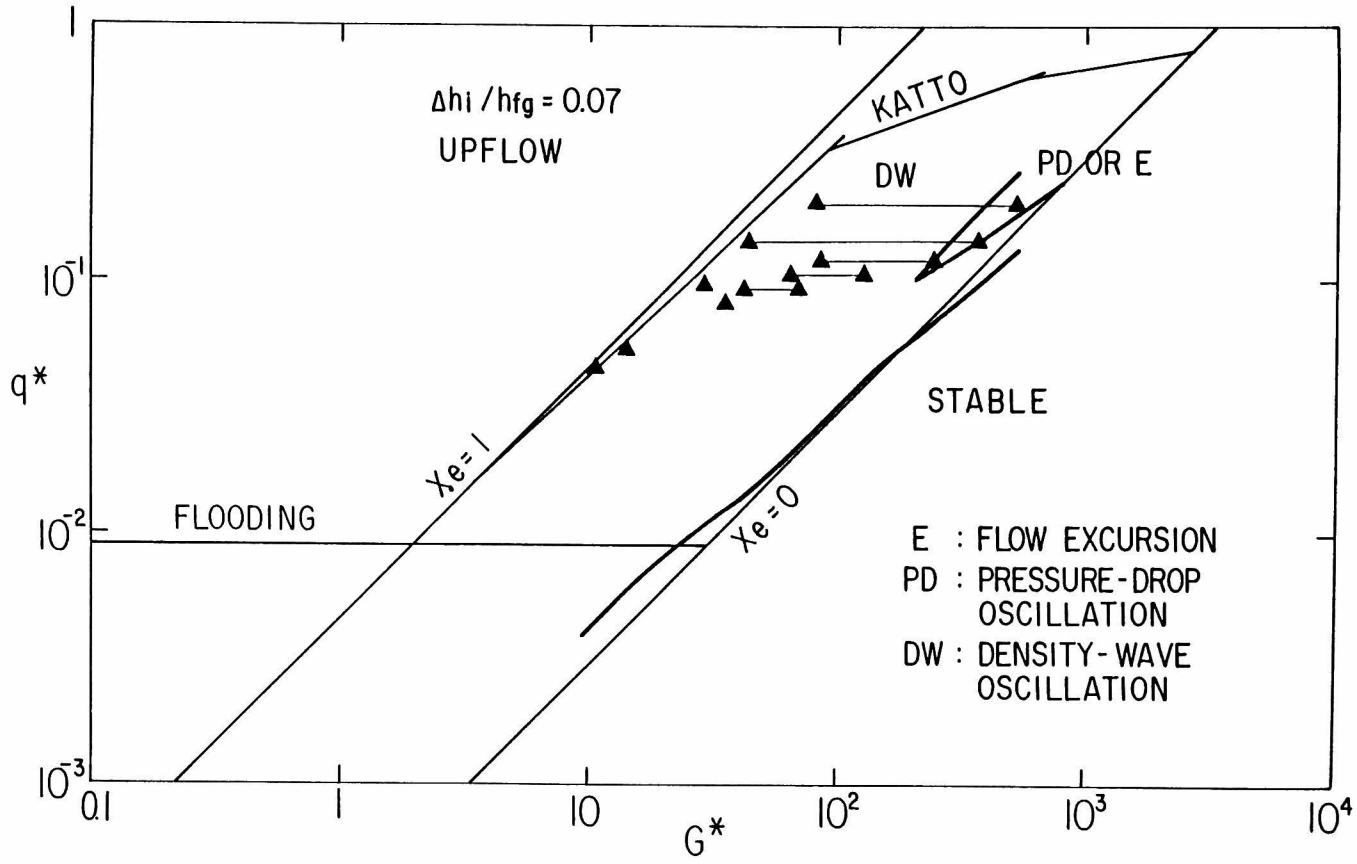


Figure 44 Stability boundaries for upflow with an upstream compressibility at inlet water temperature 60°C.

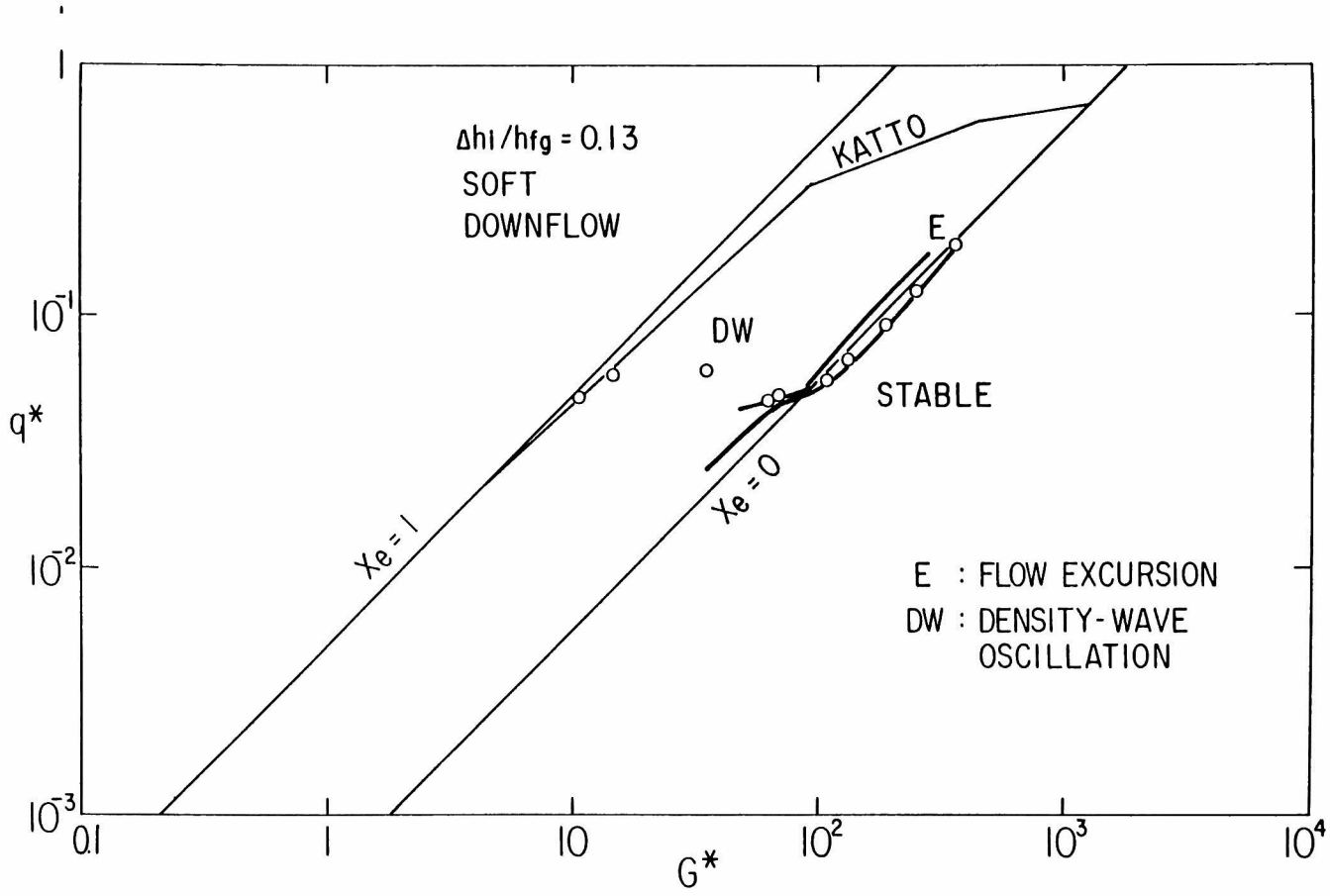


Figure 45 Stability boundaries for downflow in the soft system.

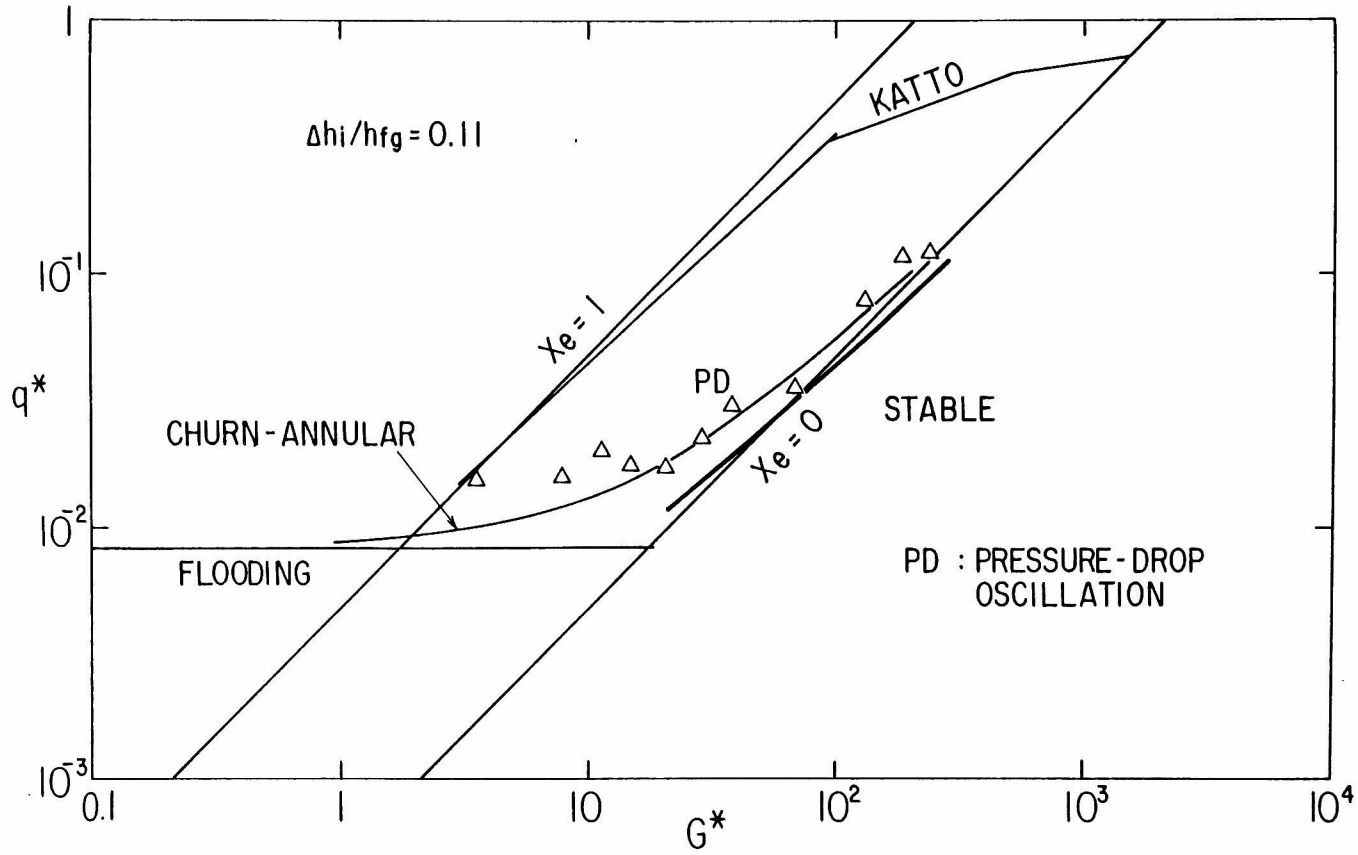


Figure 46 Stability boundaries for downflow with an upper plenum at inlet water temperature 40°C.

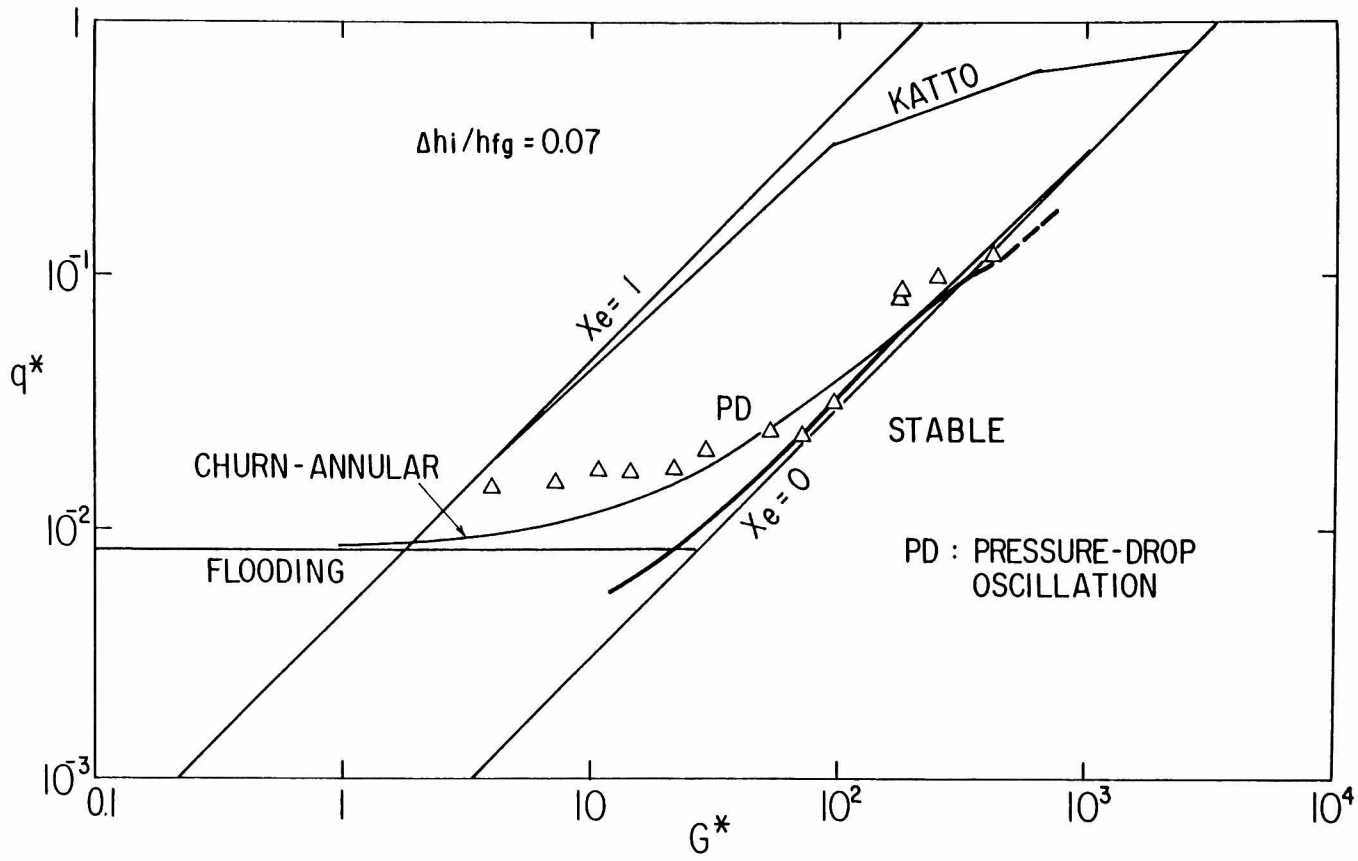


Figure 47 Stability boundaries for downflow with an upper plenum at inlet water temperature 60°C.

# CHAPTER VI.

# CRITICAL HEAT FLUX AT LOW-FLOW-RATE AND LOW-PRESSURE CONDITIONS IN THIN RECTANGULAR CHANNELS

## VI.1. INTRODUCTION

In designing a nuclear reactor system, critical heat flux (CHF) under various conditions must be known to avoid the occurrence of burnout. Critical heat flux for water flowing in a vertical rectangular channel is important in MTR-type research reactors. Most of the CHF correlations developed so far for rectangular channels [1-6] are applicable only to systems at high flow rate and positive subcooling at the burnout position as shown in Table 1. This is because the main emphasis in reactor safety has been directed to more drastic accident conditions.

However, it is noted that accidents which lead to the decay heat removal by natural convection have much higher probability of occurrence than those of severe accidents extensively studied so far. The decay heat removal by natural convection can become important under a number of accident conditions such as loss-of-heat sink (LOHS), loss-of-flow (LOF) and loss-of-coolant accidents (LOCA) in liquid cooled nuclear reactors. Regardless of the initial stages of these accidents, similar conditions, which are basically decay heat removal by natural convection boiling, can develop. Under such conditions, burnout may occur even at a low heat flux.

In addition, flow reversal occurs in many MTR-type research reactors during transient after normal shutdown, at which time the

coolant flow rate becomes so low that if it is mismatched with the decay heat removal a CHF may occur.

Among the CHF correlations for vertical rectangular channels, the Macbeth correlation [7] and the Katto correlation [8] are applicable to both high and low flow rates. They are, however, based on the experimental data at higher pressures than expected under such conditions mentioned above. The data on the CHF for low-flow-rate/low-pressure conditions are lacking, and no correlation is available at present. This is partly because various flow instabilities due to boiling may have significant effects on the CHF at low pressure [9-11], and hence the CHF may become system dependent.

In view of the above, an experimental study has been performed for water flowing in thin rectangular channels at low-flow-rate/low-pressure conditions. The effects of flow orientation, i.e. upflow and downflow, on the CHF were also observed in the experiment. This chapter provides the results obtained from the experiment and some considerations on the CHF correlations in relation to the safety of research reactors.

## VI.2. PREVIOUS WORKS

As mentioned above, the CHF correlations [1-4] widely used for research reactors are applicable when the flow rate is high and the subcooling at the burnout position is positive. They have been used equally for both upflow and downflow, because it has been assumed that the effects of flow orientation is small at very high flow rates. It is noted that under such conditions, burnout occurs due to vapor-blanketing on the heated wall, and the resulting CHF depends only on local conditions. We may call this burnout mechanism DNB-type. The guide-book [12] published by the International Atomic Energy Agency (IAEA)

in 1980, however, extrapolated the CHF at low velocities based on such high flow correlations as the Mirshak correlation [1] and the Labuntsov correlation [4] suggesting that the CHF approaches to the pool-boiling CHF at very low coolant velocities.

On the other hand, the CHF at low flow rate may be deduced also from the Macbeth correlation [7] and the Katto correlation [8], although they are applicable only to upflow and higher pressure conditions. As pointed out by Katto, their correlations at low flow rate predict the CHF caused by the permanent dryout of the liquid film on the heated wall. Therefore, the CHF occurs at high quality by this mechanism. According to these correlations, the CHF at a very low flow rate is roughly proportional to the mass velocity, contrary to the suggestion by the IAEA guidebook [12].

Recently, Monde et al.[13] obtained the CHF correlation for natural convection boiling in vertical rectangular channels submerged in saturated liquid and heated from one side:

$$q_c = \frac{0.16 h_{fg} \rho_g (\sigma g \Delta\rho / \rho_g^2)^{1/4}}{1+6.7\times10^{-4}(\rho_l/\rho_g)^{0.6}(L_H/s)} \quad . \tag{1}$$

Equation (1) suggests that the CHF at very low flow rates becomes independent of the flow rate and approaches to a certain value which is generally much smaller than the pool-boiling CHF.

For a vertical channel with a complete bottom blockage, CHF occurs due to flooding [14-19]. In this case, liquid flows down from the top and the vapor generated in the heated section flows upward. When the heat flux becomes sufficiently high, the high vapor flow remarkably reduces the liquid penetration into the heated section, thus causing a

dryout. The CHF can be calculated by using the flooding correlation of Wallis [20] given by

$$j_g^{*\frac{1}{2}} + j_l^{*\frac{1}{2}} = C \quad , \tag{2}$$

$$j_g^* = j_g\sqrt{\rho_g/(\Delta\rho g D)} \quad , \tag{3}$$

$$j_l^* = j_l\sqrt{\rho_l/(\Delta\rho g D)} \quad , \tag{4}$$

where constant C is 0.725 to 1 depending on the entrance geometry. From the heat and mass balance in the heated section and Eq.(2), one obtains

$$q_{cF} = \frac{C^2 A h_{fg}\sqrt{\rho_g g\Delta\rho D}}{A_H[1+(\rho_g/\rho_l)^{\frac{1}{4}}]^2} \quad . \tag{5}$$

In addition to these, as discussed in Chapter IV, it was observed in the experiment conducted with an annular test section that the CHF at low mass velocity occurred due to the flow regime transition from churn to annular flow. Based on the criterion for the flow regime transition, the CHF was calculated by

$$q_c = (A/A_H)h_{fg}[G\Delta h_i/h_{fg}+(1/C_0-0.11)\sqrt{\rho_g g\Delta\rho D}] \quad , \tag{6}$$

where $C_0$ is the distribution parameter [21] given by

$$C_0 = 1.2 - 0.2\sqrt{\rho_g/\rho_l} \qquad \text{for round tubes, and} \tag{7}$$

$$C_0 = 1.35 - 0.35\sqrt{\rho_g/\rho_l} \qquad \text{for rectangular channels.} \tag{8}$$

The second term in Eq.(6) is almost equal to the flooding CHF predicted by Eq.(5) at low pressures, thus Eq.(6) approaches to Eq.(5) at very low mass velocities. On the other hand, when the mass velocity and the inlet subcooling is high, the second term can be neglected. This indicates that the exit quality at burnout is very low in contrast to the high-quality CHF correlations [7,8] and that the CHF given by Eq.(6) can be much lower than predicted by those correlations.

The predictions by the above correlations are compared for the IAEA 10MW research reactor conditions [12] in Fig. 1. Here the non-dimensional critical heat flux and mass velocity, q* and G* are defined by the following equations respectively:

$$q^* = q_c/(h_{fg}\sqrt{\lambda\rho_g g\Delta\rho}) \ , \tag{9}$$

$$G^* = G/\sqrt{\lambda\rho_g g\Delta\rho} \ . \tag{10}$$

The non-dimensional group Eq.(9) was originally derived by Zuber [22] and Kutateladze [23] from the consideration of the hydraulic instability which causes the departure from nucleate boiling (DNB). The length scale $\lambda$ is the Taylor wave length scale given by the following equation,

$$\lambda = \sqrt{\sigma/(g\Delta\rho)} \ . \tag{11}$$

Using Eq.(9) the pool-boiling CHF correlation [22],[23] can be written in a simple form,

$$q^* = 0.16 \ . \tag{12}$$

It can be seen from Fig. 1 that at low pressure with typical geometrical conditions for research reactors, the flooding CHF is much lower than the pool-boiling CHF and the high-quality CHF [7],[8].

## VI.3. EXPERIMENT

### VI.3.1. Test Section

Two types of rectangular test sections were fabricated for the experiment. The cross section of the first test section is shown in Fig. 2. The nominal dimension of the flow channel are 2.4 mm in clearance and 40 mm in width. A stainless steel heater is mounted flush with a Tefron sheet on one wall, while the opposite wall consists of a transparent Pyrex plate which enables us to observe the flow regimes. The heater is 1 mm-thick, 30 mm-wide and 350 mm in effective length, and has copper electrodes silver-soldered at its upper and lower ends. These copper electrodes penetrates the upper and lower plena with electrical insulation and are connected to the cables from the power supply. Ten Chromel-Alumel thermocouples are spot-welded onto the inside wall of the heater at an interval of 35 mm along the centerline. These thermocouples are led out of the test section through the hole drilled in the copper electrodes and connected to burnout detectors which actuate a relay to switch off the power to the test section.

The flow channel of the second test section has the same nominal dimension as the first one but is heated with a pair of parallel heaters on the two opposite sides of the channel as shown in Fig. 3. The heaters are fabricated in the same manner as described above. It is noted here, however, that two parallel copper bars for two heaters run through each plenum of this test section. Thus the coolant flows through the slit between the copper bars at the inlet and outlet of the

test section. This means that the inlet and outlet restrictions are larger in the second test section than in the first one.

The power to the test section was supplied by a 20 V, 1200 A, dc power supply. The heat input to the test section was calculated from the voltage drop across the test-section heater and that across the on-line shunt rated at 15 V/1500 A.

VI.3.2. Test Loop

The test loop is basically the same as that used in the experiment with round tubes, which is shown schematically in Fig. 4. The test section was mounted vertically between the upper and lower plena in the loop. The loop was filled with ion-exchanged water, which was degassed by boiling prior to the experiment. The steam relief valve on top of the water tank was left open during the test so that the exit pressure was always near atmospheric pressure.

The flow orientation in the test section can be set either upward or downward by the valves. The inlet water flow rate was regulated with the valves just behind the flow meters and the bypass valve. The other valves were kept fully-open or fully-closed according to the flow orientation. The flow rate to the test section was measured with three turbine flowmeters.

The details have been already described in the previous chapter.

VI.3.3. Experimental Procedure

The same procedure was followed as in the experiment with round tube test section. First, the water in the loop was degassed by boiling. Then, the valves were set to obtain the desired flow orientation. The inlet water temperature was kept constant by using the cooling pipe in the downcomer and the heat input to the test section.

At each given flow rate, the power to the test section was gradually increased by small steps untill a burnout occurred. The determination of the occurrence of burnout is based on the actuation of any one of the burnout detectors, which actuate a relay to switch off the power to the test section as soon as the heater temperatures rise beyond a preset value due to the occurrence of burnout. Since the wall temperatures were recorded on a strip chart, the occurrence of burnout was observed also from the abrupt increase in the temperature traces.

The heat flux was calculated from the power to the test section and known heated area assuming a uniform heat flux. The critical heat flux is defined by the heat flux just before the occurrence of rapid temperature excursion. In some runs, a violent flow oscillation was encountered prior to the burnout. In those cases, the equilibrium (mean) flow rate read from the flow-rate trace on the strip chart was used to correlate the critical heat flux. The pattern of the flow oscillation was also observed from the flow-rate traces.

The ranges of the variables tested in the experiment are given in Table 2.

## VI.4. RESULTS AND DISCUSSIONS

### VI.4.1. Flow Regimes at Burnout

The flow regimes at low-flow-rates/low-pressure conditions are significantly affected by the large density ratio $\rho_l/\rho_g$ and the gravity. Due to these effects, various flow instabilities are encountered. Particularly the effects of gravity reveals itself in the differences of flow regimes between upflow and downflow at low flow rates. This may have significant impacts on core cooling if the difference of flow regimes causes the reduction of critical heat flux. In view of the

above, flow regimes were observed in both upflow and downflow with the test section heated from one side.

VI.4.1.1. Downflow

At the lowest mass velocities in the downflow, burnout occurs due to countercurrent-flow limitation which resembles flooding. When the heat flux is not high enough to cause burnout, the flow appears to be slug flow or churn-turbulent flow; the lower boundary of the boiling region moves up and down with a large amplitude causing the inlet flow rate and the wall temperatures to oscillate as shown in Fig. 5.

When the mass velocity is just as high (150 - 200 $kg/m^2s$, downward) as to stagnate the bubbles, the vapor accumulates in the heated section, and as a consequence dryout occurs over a wide area of the heated surface. When the inlet subcooling is small (about 15°C) in addition to the above condition, this type of burnout occurs at the lowest heat flux. It is also noted that at this range of flow rate the existence of non-condensible gas reduces the CHF as much as 20% because it accumulates in the heated section and blocks the channel.

The critical mass velocity $G_c$ which causes the bubble stagnation can be estimated from the bubble drift velocity. Assuming churn flow regime, the drift velocity can be calculated by [21]

$$V_{gj} = (C_0-1)j + \sqrt{2}(\sigma g \Delta\rho/\rho_l^2)^{1/4} . \qquad (13)$$

Using the following relations

$$V_{gj} = v_g - j , \qquad (14)$$

$$G = \rho_g j_g + \rho_l j_l \quad , \tag{15}$$

$$v_g = j_g/\alpha \quad , \tag{16}$$

and with the condition that $v_g = 0$, we obtain

$$G_c = -\sqrt{2}(\rho_l^2 \sigma g \Delta\rho)^{1/4}/C_0 \quad , \tag{17}$$

where the distribution parameter $C_0$ is given by Eq.(8) and the negative mass velocity means downflow. With Eq.(17), the critical mass velocity becomes -159kg/m$^2$s which agrees reasonably with the observation.

When the mass velocity becomes relatively high, i.e. 200 - 610 kg/m$^2$s, highly agitated steam column is formed and expels the liquid column from the heated section at heat fluxes close to the CHF. The flow appears to be in the churn or annular flow regimes. However, the upper boundary of the steam column moves rapidly with large amplitude, and the inlet flow rate oscillates violently as shown in Fig. 6. Dry patches are formed during the expulsion of the liquid column. They are, however, rewetted during the re-entry of the liquid column following the collapse of the bubble due to rapid condensation. Thus a permanent dryout occurs as soon as the exit equilibrium quality becomes zero, which retards the condensation. The flow may be characterized by the flow-regime instability and the burnout may be considered as a secondary phenomenon of the instability [9,24]. It is also noted that the compressible volume in the upper plenum may have worked as an energy storage mechanism in the flow oscillation.

VI.4.1.2. Upflow and complete bottom blockage

In the complete-bottom-blockage experiment, the (bottom) inlet valve immediately upstream of the test section was closed and the downstream valves were fully-open. Thus the condition of the test section is similar to that of a thermosiphon. In this case, burnout occurs due to flooding as mentioned before. However, the flooding phenomenon in such a thin rectangular channel as the present test section exhibits somewhat different characteristics from that in round tubes. That is, the falling liquid film is not uniform around the channel. The majority of the liquid flows down along the narrow side walls, not along the heated wall. The liquid films on the side walls are so thick (several milli-meters) that large disturbance waves are generated on the film. Sometimes the wave crests touch the liquid film on the opposite side to form liquid bridges, which are blown up and broken up into liquid droplets by the upward flow of steam. These disturbance waves, liquid bridges and droplets appear to contribute to wet the heated surface as long as the CHF is not exceeded. Dryout occurs when sufficient amount of liquid is not supplied to the heated section due to flooding.

In the upflow, the flooding burnout is also observed at very low flow rates. This means that even when all the liquid entering from the bottom is completely evaporated before it reaches the exit of the heated section, dry patches can be rewetted by the liquid falling from the top if the flooding condition is not reached.

As the flow rate is increased the contribution of the falling film gradually diminishes. The flow regime appears to be the annular flow, and hence the complete evaporation of the film on the heated surface

leads to burnout. Since in that case liquid film still remains on the unheated surface, the exit quality is rather low at the occurrence of burnout.

Flow instabilities are encountered also in the upward annular flow when the exit water temperature is below the saturation point. An example of the flow-rate trace during the instability is shown in Fig. 7. The figure indicates that the flow oscillation is damped soon after the exit water temperature reaches the saturation point. Therefore, this instability may have been caused by the rapid growth and condensation of the steam core which touches the subcooled liquid at its both ends.

Observed flow regimes at burnout for upflow are plotted in Fig. 8 in terms of the mass velocity and the exit equilibrium quality. The flow regime map denoted by solid lines is calculated by the following criteria obtained in Chapter II.

The transition criterion from the slug to churn-flow regime is given by

$$\alpha \geq 1 - 0.813 \left\{ \frac{(C_0-1)j + 0.35\sqrt{\Delta\rho gD/\rho_l}}{j+0.75\sqrt{\Delta\rho gD/\rho_l}[\Delta\rho gD^3/(\rho_l\nu_l^2)]^{1/18}} \right\}^{0.75} , \tag{18}$$

where

$$\alpha = j_g/[C_0 j+0.35\sqrt{\Delta\rho gD/\rho_l}] \quad . \tag{19}$$

The transition criterion for the churn to annular flow has been developed postulating flow reversal in the liquid film along large bubbles and is expressed as

$$j_g \geq \sqrt{\Delta\rho g D/\rho_l}(\alpha-0.11) \quad , \tag{20}$$

with the following equation for void fraction;

$$\alpha = j_g/[C_0 j+\sqrt{2}(\sigma g\Delta\rho/\rho_l^2)^{1/4}] \quad . \tag{21}$$

Figure 8 indicates that for the present test section, better agreement is obtained with the channel width w than with the hydraulic equivalent diameter D in Eq.(20). The transition criterion for the annular-mist flow is

$$j_g \geq (\sigma g\Delta\rho/\rho_g^2)^{1/4} N_{\mu l}^{-0.2} \quad , \tag{22}$$

where

$$N_{\mu l} = \mu_l/[\rho_l \sigma\sqrt{\sigma/(g\Delta\rho)}]^{1/2} \quad . \tag{23}$$

The slug-annular transition boundary derived by Jones et al.[25] for rectangular ducts is also compared in the figure. The criterion is given by

$$j_l = j_g/4 - (0.23+0.13s/w)\sqrt{\Delta\rho g w/\rho_l} \quad . \tag{24}$$

It appears that Eq.(24) corresponds to the slug-to-churn flow transition

predicted by the present criterion.

VI.4.2. Critical Heat Flux

VI.4.2.1. CHF for the test section heated from one side

The critical heat flux measured in the test section heated from one side is shown in Fig. 9. The abscissa represents the mass velocity, which is positive for upflow and negative for downflow. The figure shows that there is a minimum in the CHF at complete bottom blockage or low downflow. This minimum CHF occurred due to flooding and/or bubble stagnation, as noted previously. The minimum CHF in downflow appears at mass velocities up to the critical mass velocity (-150 to -200 $kg/m^2s$) at which the bubbles stagnate in the heated section. Beyond the critical mass velocity, the vapor bubbles are forced downward and the flow regime becomes churn or annular flow accompanied with a violent oscillation of boiling boundary. In this region, the CHF increases as the mass velocity increases (downward).

In the upflow the CHF approaches to the minimum due to flooding at the lowest mass velocities, while it increases almost linearly with increasing mass velocity. At very high mass velocities, there is some tendency that the rate of increase in CHF decreases. It is apparent that the CHF in upflow is generally higher than that in downflow. These flow characteristics described so far clearly indicate that the effects of gravity is significant at such low flow rates as tested in this experiment.

The effects of inlet subcooling on CHF also can be seen in Fig. 9. In the downflow, the CHF increases with increasing inlet subcooling while in upward flow, the effect is not obvious.

VI.4.2.2. CHF for the test section heated from two opposite sides

The CHF measured in the test section heated with two heaters is shown in Fig. 10. General tendencies of the curves are similar to those observed in the first test section, although the range of the tested flow rate is narrower. It appears that the effects of bubble stagnation are rather obscure in this case, but the minimum CHF occurs at the complete bottom blockage or at very low downflow. The effects of inlet subcooling are also the same as the test section heated from one side. With Figs. 9 and 10, it can be said that the CHF in the test section heated from two opposite sides is about a half of that in the other test section. This may be roughly explained by the factor $A/A_H$ which appears in Eqs.(5) and (6), with the conditions otherwise the same. This means that the CHF depends mainly on the total power input to the test section rather than the local heat flux at such low flow rates.

VI.4.3. Correlations

VI.4.3.1. Minimum CHF due to flooding

As has been discussed previously, there is a minimum CHF which occurs due to flooding. This minimum CHF may have a significant impact on the core cooling after the shutdown or in the post accident conditions of nuclear reactors. Based upon the observations described before, we assume that the flooding condition can be determined from the balance in the hydrodynamic forces acting on the falling films along the narrower side walls. Furthermore, we assume that the flooding condition can be expressed in the same form as Eq.(2). Then for simplicity, we consider the condition to let the liquid film hung up on the wall. This is equivalent to the condition $j_1^*=0$.

Figure 11 depicts the model of the hanging liquid film. The

relationship among the interfacial shear, wall shear and the gravity is given by

$$\tau_i + \tau_w = \Delta\rho g\delta \quad . \tag{25}$$

As the average velocity in the liquid film is very low, we may neglect the wall shear compared to the interfacial shear in Eq.(25).

The interfacial shear force can be written in terms of friction factor as

$$\tau_i = C_{fi}\rho_g v_g^2/2 \quad . \tag{26}$$

Wallis [26] obtained the friction factor for rough annular film given by the following equation;

$$C_{fi} = 0.005(1+300\delta/D) \quad . \tag{27}$$

It is assumed that Eq.(27) can be used with some modification for thin rectangular channels. As the term $\delta/D$ measures the relative roughness of the liquid film, we should replace the hydraulic diameter D by the channel width w because we consider the force balance only on the plane parallel to the channel width. Moreover, we may neglect the first term in Eq.(27) because the observed film is rather thick and the wave roughness is large. Therefore we assume the following form for the interfacial friction factor.

$$C_{fi} = k\delta/w \quad , \tag{28}$$

where k can be determined empirically, although Eq.(27) gives the value of 1.5.

Using Eqs.(25),(26) and (28) we obtain

$$v_g = \sqrt{2\Delta\rho gw/(k\rho_g)} \quad , \tag{29}$$

and the superficial vapor velocity becomes

$$j_g = \alpha v_g = \alpha\sqrt{2\Delta\rho gw/(k\rho_g)} \quad . \tag{30}$$

Here we introduce the following non-dimensional superficial vapor velocity

$$j_g^* = j_g\sqrt{\rho_g/(2\Delta\rho gw)} \quad , \tag{31}$$

which is equivalent to Eq.(3) for round tubes if D = 2w. With Eqs.(30) and (31), the condition for hanging liquid film becomes

$$j_g^* = \alpha/\sqrt{k} \quad . \tag{32}$$

From the similarity between Eq.(32) and Eq.(2) with $j_l^* = 0$ we obtain

$$C = (\alpha/\sqrt{k})^{\frac{1}{2}} \quad , \tag{33}$$

where for thin rectangular channels, the non-dimensional superficial velocities are defined by Eq.(31) and

$$j_1^* = j_1\sqrt{\rho_1/(2\Delta\rho g w)} \quad . \tag{34}$$

Therefore we finally arrive at the following equation for flooding CHF for thin rectangular channels

$$q_{cF} = \frac{C^2 A h_{fg}\sqrt{2\rho_g g\Delta\rho w}}{A_H[1+(\rho_g/\rho_1)^{1/4}]^2} \quad . \tag{35}$$

Comparing Eq.(35) to the experimental data, the value of C can be determined. Then we have

$$\begin{aligned} C &= 0.73 \text{ for the test section heated from one side and} \\ &= 0.63 \text{ for the test section heated from two opposite sides.} \end{aligned} \tag{36}$$

It is noted here that the above values are obtained based upon the measured clearances of the channel at the upper end of the heated section, i.e. 2.2 mm for the former test section and 2.15 mm for the latter. The value of C can be estimated theoretically from Eq.(33) postulating that $\alpha$ = 0.8, and thus we obtain 0.81 which is 11 to 29% higher than the empirical values.

It is also pointed out that the value of C is lower in the test section heated from two opposite sides. This may be attributed to the fact that the inlet restriction at the upper end is larger in the latter test section. In a research reactor, however, the geometrical condition at the upper end of the coolant channel is more like that in the test section heated from one side. Hence the value of C = 0.73 will be preferable.

VI.4.3.2. CHF for downflow

The minimum CHF in the downflow appears at mass velocities up to about 200kg/m$^2$s. Since the mechanism of burnout resembles flooding, the CHF may be basically correlated by Eq.(35). For a downflow, however, we need to take account of the effects of inlet subcooling as indicated in Fig. 9 and 10. In order to find the effects of inlet subcooling on the CHF, the data at those mass velocities are plotted in terms of $q_c/q_{cF}$ and the inlet subcooling as shown in Fig. 12, where $q_{cF}$ is given by Eq.(35). The figure indicates that the effects of inlet subcooling are negligible when the inlet water temperature is higher than about 70°C, while $q_c/q_{cF}$ can be correlated by the following equation at higher inlet subcooling:

$$q_c/q_{cF} = 1 + 2.9\times10^5(\Delta h_i/h_{fg})^{6.5} \quad . \tag{37}$$

At higher mass velocities, the inlet flow oscillates due to rapid evaporation and condensation, and the CHF occurs when the exit water temperature reaches saturation. Therefore, the CHF correlation can be derived from the condition $x_e = 0$ and becomes

$$q_c = A\Delta h_i G/A_H \quad . \tag{38}$$

The experimental data for downflow in the first test section are correlated in terms of the boiling number defined by $q_c/(h_{fg}G)$ or $q^*/G^*$ and non-dimensional mass velocity $G^*$ using Eq.(37) and (38) as shown in Fig. 13. The non-dimensional mass velocity for bubble stagnation is calculated from Eqs.(10) and (17). It can be seen from the figure that

the transition from the flooding to zero-exit-quality CHF is smooth at low inlet subcooling while it occurs rather abruptly at the critical mass velocity for bubble stagnation at high inlet subcooling because the intersection of Eqs.(37) and (38) appears at lower mass velocity than the critical mass velocity in the latter case.

The experimental data for the test section heated from two opposite sides can be correlated in the same manner and the result is shown in Fig. 14. The figure indicates that the data are close to the flooding line with C = 0.63 at the lowest mass velocities while they approach to the flooding line with C = 0.73 as the mass velocity increases.

VI.4.3.3. CHF for upflow

As pointed out earlier, the CHF for upflow depends little on the inlet subcooling, which is also shown in Fig. 15 for the test section heated from one side. Hence the CHF may be assumed to be a function of the mass velocity alone if the geometrical conditions remain unchanged. This function of the mass velocity should have an asymptotic value at very low flow rates which is calculated from the flooding condition. Thus the following equation is assumed for the upflow CHF;

$$q_c = q_{cF} + f(G) \ , \tag{39}$$

where $q_{cF}$ is given by Eq.(35) together with Eq.(36). Plotting the experimental data in terms of the boiling number $q^*/G^*$ against the non-dimensional mass velocity, it turned out that the CHF could be correlated by the following equation;

$$q_c = q_{cF} + 1.46\times10^{-3} h_{fg} G \ , \tag{40}$$

for the test section heated from one side and

$$q_c = q_{cF} + 1.7\times10^{-3} h_{fg} G \quad , \tag{41}$$

for the test section heated from two opposite sides.

Non-dimensional plot of the CHF data and the comparison to Eqs.(40) and (41) are shown in Fig. 16.

It should be noted here that Eqs.(40) and (41) may be valid only for the present test sections because the second term on those equations may include the geometrical parameters implicitly. Therefore further studies are needed before any general correlation is established. It is also interesting to note that the lower boundary of the general correlations may be given by

$$q_c = q_{cF} + A\Delta h_i G/A_H \quad , \tag{42}$$

which is essentially the same as Eq.(6) and thus corresponds to the churn to annular flow transition at low pressures.

VI.4.4. Discussions

The experimental results described above are compared to the conventional correlations. The comparisons are made in terms of the non-dimensional CHF and mass velocity, q* and G*, respectively. Figures 17 and 18 give the non-dimensional plots of the CHF data obtained at fixed inlet subcooling for the test section heated from one side in comparison with the conventional correlations. The Kutateladze correlation [27] for high flow CHF at low pressure is also included. The Mirshak correlation [1] and the Labuntsov correlation [4] are used

beyond their applicable ranges, postulating that when exit equilibrium quality is positive, the subcooling at the burnout position is zero. The bold lines in the figures represent the transition boundary from the churn to annular flow regime. The criterion for the transition in a rectangular channel is calculated by Eq.(42).

It can be seen from these figures that neither pool-boiling CHF correlations [23,24] nor high-quality CHF correlations [7,8] can reproduce the CHF at low mass velocity which is much lower than predicted by those correlations.

In the upflow, the CHF is close to the transition boundary from the churn to annular flow regime at high inlet subcooling, while it is between the high-quality CHF and the transition boundary at low inlet subcooling. At very low flow rate, the CHF approaches to the flooding CHF, Eq.(35). The Monde correlation [13] for natural convection boiling CHF also agrees well with the flooding CHF. At high mass velocities, the CHF curve appears to merge with the Labuntsov correlation[4]. The Mirshak correlation [1] should be properly used for downflow because it is obtained from the downflow experiment.

In the downflow, the CHF at low mass velocities can be correlated by two lines calculated by Eqs.(37) and (38), representing the flooding CHF and the condition that the exit equilibrium quality is zero, respectively. At high mass velocities, the Mirshak correlation [1] is valid.

The same discussion can be followed for the CHF with two heaters as shown in Fig. 19. The reason for the discrepancy between the experimental data and the high quality CHF correlations [7,8] is not known at present. However, it is pointed out that the CHF at low flow

rate is very sensitive to various parameters such as the system pressure, the geometry of the channel, inlet valve throttling, the pump characteristics and upstream compressibility. Particularly at low pressures, the flow easily becomes unstable due to boiling, which may result in a premature burnout. Therefore, further studies are needed to obtain the general criteria to identify which mechanism causes a burnout at a given condition.

## VI.5. SUMMARY AND CONCLUSIONS

The CHF obtained from the experiment with thin rectangular channels under low-flow-rate/low-pressure conditions appeared to be much lower than predicted by conventional correlations. The minimum CHF occurred at a complete bottom blockage and at mass velocities less than $G_c$ given by Eq.(17) in downward flow which causes a bubble stagnation in the heated section. Attention should be paid to this fact because a similar condition may develop in a research reactor prior to the flow reversal after a normal shutdown of the reactor.

Furthermore, it is noted that a complete top blockage has not been studied in this experiment, although it is more likely to occur in a research reactor and may lead to more pessimistic consequences than the bottom blockage.

Based on the above discussions, the following recommendations are made for the CHF correlations for thin rectangular channels at low pressure.

In a downflow,

(1) the Mirshak correlation [1] is relevant at high flow rate,

(2) the CHF at intermediate flow rate can be determined by the condition that the exit equilibrium quality is zero, resulting in

Eq.(38),

(3) the CHF at low mass velocities less than $G_c$ given by Eq.(17) occurs due to flooding and is correlated by Eq.(37).

In an upflow,

(1) the Labuntsov correlation [4] or the Kutateladze correlation [27] can be used at high flow rate,

(2) the CHF at low flow rate is tentatively correlated by Eqs.(40) and (41), which may be modified depending on the geometry. The lower boundary may be given by Eq.(42) corresponding to the churn-annular flow transition.

It should be noted here that these results are obtained for steady inlet-flow condition and may be valid also for a slow transient. However, under rapid transient conditions, it is more likely that a burnout will not occur even if the steady-flow CHF condition is exceeded.

## NOMENCLATURE

| | | |
|---|---|---|
| $A$ | : | Flow area |
| $A_H$ | : | Heated area |
| $C$ | : | A constant which appears in the flooding correlation |
| $C_0$ | : | Distribution parameter |
| $D$ | : | Characteristic length or hydraulic equivalent diameter |
| $D_H$ | : | Heated equivalent diameter |
| $f(G)$ | : | A function of mass velocity G |
| $f_i$ | : | Interfacial friction factor |
| $G$ | : | Mass velocity |
| $G^*$ | : | Non-dimensional mass velocity |
| $G_c$ | : | Critical mass velocity to stagnate bubbles |
| $g$ | : | Gravity |
| $h_{fg}$ | : | Latent heat of evaporation |
| $\Delta h_i$ | : | Inlet subcooling in terms of enthalpy |
| $j$ | : | Volumetric flux of two-phase mixture |
| $j_g$ | : | Volumetric flux of gas (superficial gas velocity) |
| $j_l$ | : | Volumetric flux of liquid (superficial liquid velocity) |
| $j_g^*$ | : | Non-dimensional superficial gas velocity |
| $j_l^*$ | : | Non-dimensional superficial liquid velocity |
| $k$ | : | A constant for interfacial friction factor |
| $L_H$ | : | Heated length |
| $N_{\mu l}$ | : | Viscosity number defined by Eq.(23) |
| $q$ | : | Heat flux |
| $q_c$ | : | Critical heat flux |
| $q_{cF}$ | : | Critical heat flux due to flooding |
| $q^*$ | : | Non-dimensional heat flux |
| $s$ | : | Clearance of the channel |
| $T_{in}$ | : | Inlet water temperature |
| $T_{out}$ | : | Exit water temperature |
| $V_{gj}$ | : | Drift velocity |
| $v_g$ | : | Velocity of the gas (vapor) |
| $w$ | : | Width of the channel |

Greek symbols

$\alpha$ : Void fraction

$\delta$ : Roughness of surface wave

$\Delta\rho$ : Difference of the densities of two phases

$\lambda$ : Length scale of the Taylor wave

$\mu_l$ : Viscosity of liquid

$\nu_l$ : Kinematic viscosity of liquid

$\rho_g$ : Gas (vapor) density

$\rho_l$ : Liquid density

$\sigma$ : Surface tension

$\tau_i$ : Interfacial shear stress

$\tau_w$ : Wall shear stress

Subscripts

c : Critical

F : Flooding

fg : Evaporation

g : Gas phase

H : Heated

i : Interfacial or inlet

in : Inlet

l : Liquid phase

out : Outlet or exit

## REFERENCES


[1] S. Mirshak, W.S. Durant and R.H. Towell, Heat flux at burnout, DP-355 (1959).

[2] B.A. Zenkevich and B.I. Subbotin, "Critical heat fluxes in subcooled water with forced circulation," J. Nucl. Energy, Part B, Nucl. Technology, 1[2], pp.134-136 (1959).

[3] L. Bernath, "A theory of local boiling burnout and its application to existing data," Chem. Engng. Prog. Symp. Series, 56[30], pp.95-116 (1960).

[4] D.A. Labuntsov, "Critical thermal loads in forced motion of water which is heated to a temperature below the saturation temperature," Soviet Journal of Atomic Energy (English Translation), 10, pp.516-518 (1961).

[5] W.R. Gambill and R.D. Bundy, "Heat transfer studies of water flow in thin rectangular channels," Nucl. Sci. Engng., 18, pp.69-79 (1964).

[6] D.H. Knoebel, S.D. Harris, B. Crain, Jr. and R.M. Biderman, Forced-convection subcooled critical heat flux, DP-1306 (1973).

[7] R.V. Macbeth, Burnout analysis, Part 4: Application of a local conditions hypothesis to world data for uniformly heated round tubes and rectangular channels, AEEW-R267 (1963).

[8] Y. Katto, "General features of CHF of forced convection boiling in uniformly heated rectangular channels," Int. J. Heat Mass Transfer, 24, pp.1413-1419 (1981).

[9] J.A. Bouré, A.E. Bergles and L.S. Tong, "Review of two-phase flow instability," Nucl. Engng. Des., 25, pp.165-192 (1973).

[10] D.B. Collins, M. Gacesa and C.B. Parsons, "Study of onset of premature heat transfer crisis during hydrodynamic instability in a fullscale reactor channel," ASME Paper No.71-HT-11 (1971).

[11] W.H. Lowdermilk, C.D. Lanzo and B.L. Siegel, Investigation of boiling burnout and flow instability of water flowing in tubes, NACA-TN 4382 (1958).

[12] International Atomic Energy Agency, Research reactor core conversion from the use of highly enriched uranium to the use of low enriched uranium fuels, Guidebook, IAEA-TECDOC-233 (1980) p.113.

[13] M. Monde, H. Kusuda and H. Uehara, "Critical heat flux during natural convective boiling in vertical rectangular channels submerged in saturated liquid," Trans. ASME, J. Heat Transfer, 104, pp.300-303 (1982).

[14] P. Griffith, A. Schumann and A.D. Neustal, "Flooding and burnout in closed-end vertical tubes," Two-phase Fluid Flow Symposium, Paper No.5, Inst. Mech. Eng., London, pp.21-25 (1962).

[15] W.J. Frea, "Two phase heat transfer and flooding in counter current flow," Proc. 4th. Int Heat Transfer Conf., Paper No.B5.10, Paris, (1979).

[16] H. Kusuda and H. Imura, "Stability of a liquid film in a counter-currnet annular two-phase flow," Bulletin of JSME, 17[114], pp.1613-1618 (1974).

[17] Z. Nejat, "Maximum heat flux for counter currnet two phase flow in a closed end vertical tubes," Proc. 6th. Int. Heat Transfer Conf., Paper No.FB-29, Vol.1, Toronto, Canada, pp.441-444 (1978).

[18] J.A. Block and G.B. Wallis, "Heat transfer and fluid flows limited

by flooding," AIChE Symp. Series, No.174, Vol.74, pp.73-82 (1978).

[19] P. Griffith, C.T. Avedisian and J.P. Walkush, "Counter flow critical heat flux," ibid., pp.149-155 (1978).

[20] G.B. Wallis, Flooding velocities for air and water in vertical tubes, AEEW-R123 (1971).

[21] M. Ishii, One-dimensional drift-flux model and constitutive equation for relative motion between phases in various two-phase flow regimes, ANL-77-47 (1977).

[22] N. Zuber, Hydrodynamic aspects of boiling heat transfer, AECU-4439 (1959).

[23] S.S. Kutateladze, Heat Transfer in Condensation and Boiling, AEC-tr-3770 (1959).

[24] A.E, Bergles, R.F. Lopina and M.P. Fiori, Trans. ASME, J. Heat Transfer, 89, pp.69-74 (1967).

[25] O.C. Jones, Jr. and N. Zuber, "Slug-annular transition with particular reference to narrow rectangular ducts," in Two-phase momentum, heat and mass transfer in chemical, process and energy engineering systems, Vol.1, ed. F. Durst, G.V. Tsiklauri and N.H. Afgan, Hemisphere , New York, pp.345-355 (1979).

[26] G.B. Wallis, One-dimensional two-phase flow, McGraw-Hill, New York, p.320 (1969).

[27] S.S. Kutateladze, "Critical thermal flow for the flow of a wetting liquid containing an underheated core," Energetica, 2, pp.229-239 (1959).

Table 1. Applicable ranges of critical heat flux correlations.

| Correlations | | Mirshak[1] | Zenkevich[2] | Bernath[3] | Labuntsov[4] |
|---|---|---|---|---|---|
| Hydraulic dia. | (mm) | 5.33 - 11.7 | 4.06 - 11.9 | < 30.5 | ——— |
| Heated length | (cm) | 48.3 - 61.0 | 18.5 - 160 | ——— | ——— |
| Pressure | (MPa) | 0.18 - 0.6 | 10.5 - 22 | 0.03 - 21 | 0.1 - 20 |
| Subcooling | (°C) | 5 - 75 | > 10 | 0 - 182 | 0 - 240 |
| Velocity | (m/s) | 1.52 - 13.7 | ——— | 0.09 - 47.6 | 0.7 - 45 |
| Mass Velocity | ($kg/m^2s$) | ——— | > 270 | ——— | ——— |

Table 2. Ranges of the parameters tested in the experiment

| test section heated from : | | one side | two opposite sides |
|---|---|---|---|
| mass velocity | ($kg/m^2s$) | | |
| | upward flow | 0 - 110* | 0 - 360* |
| | downward flow | 7 - 280 | 7 - 610 |
| inlet water temperature | (°C) | 12 - 100 | 20 - 100 |
| heat flux | ($MW/m^2$) | up to 0.35 | up to 1.3 |
| exit pressure | | atmospheric | atmospheric |

* Zero mass velocity means the complete bottom blockage.

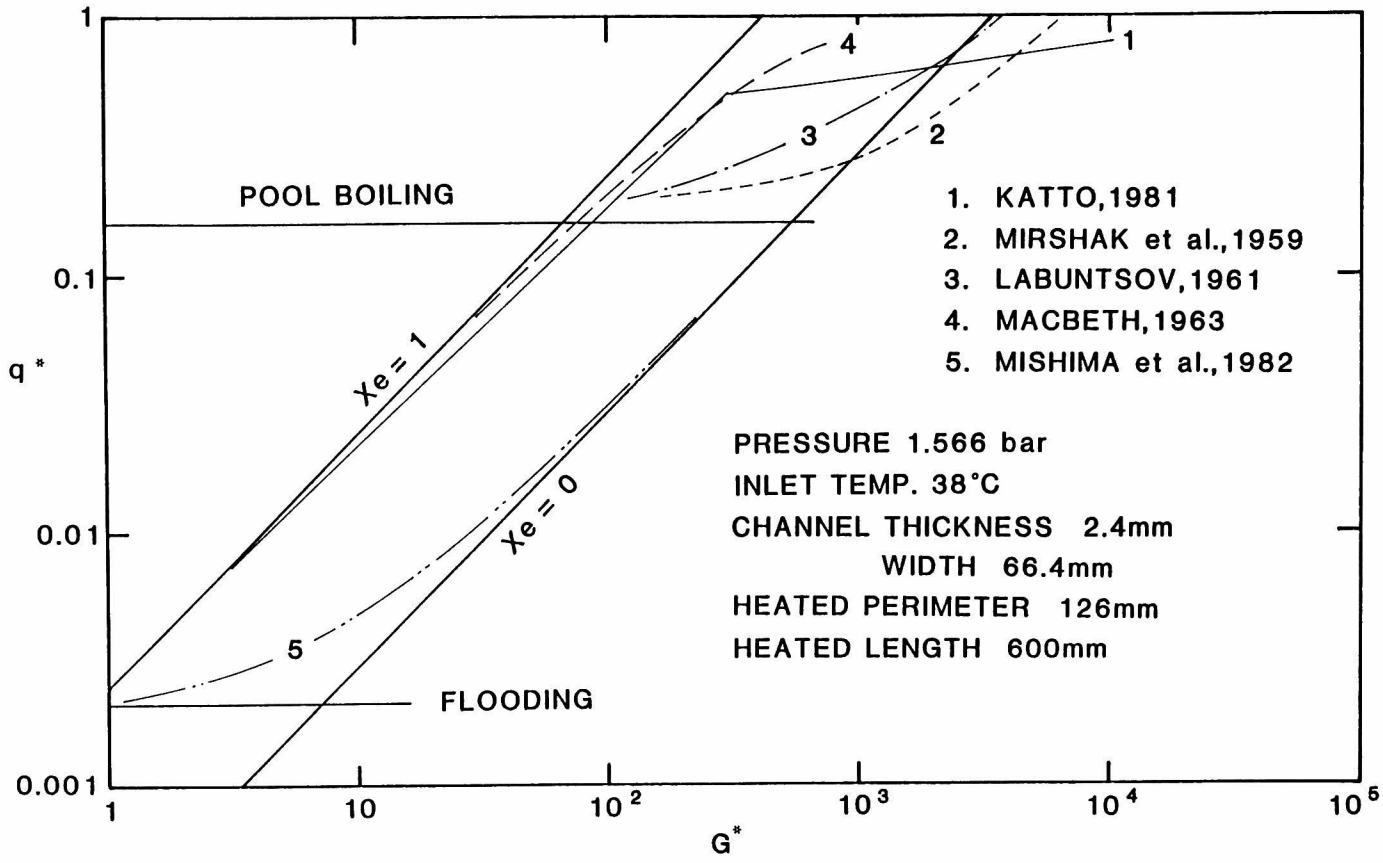


Figure 1 Critical heat flux for the IAEA 10 MW research reactor conditions [12].

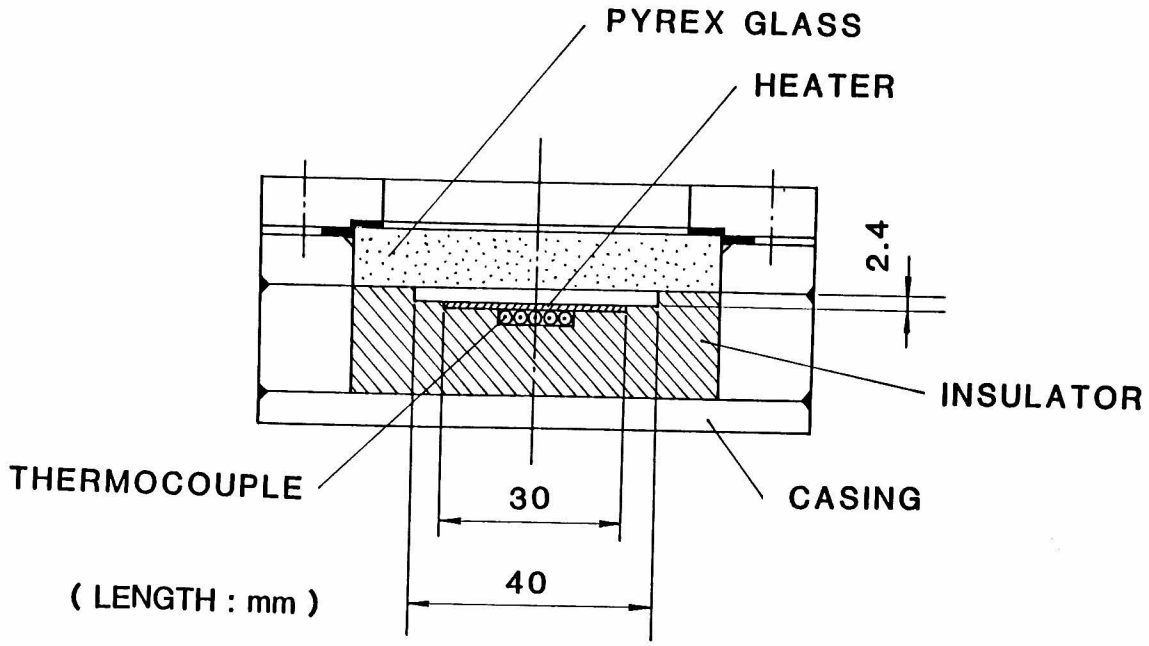


Figure 2 Cross-sectional view of the test section heated from one side.

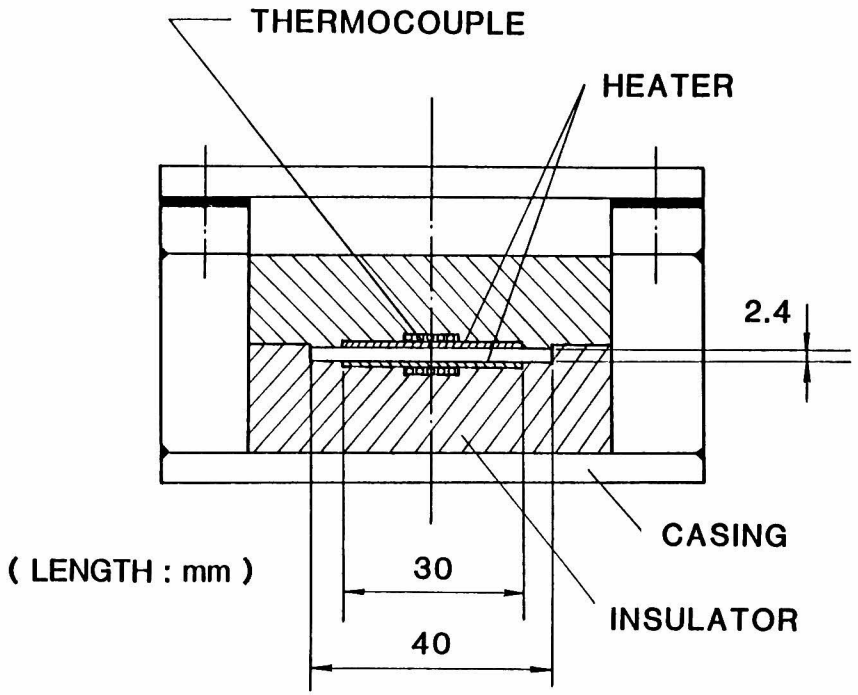


Figure 3 Cross-sectional view of the test section heated from two opposite sides.

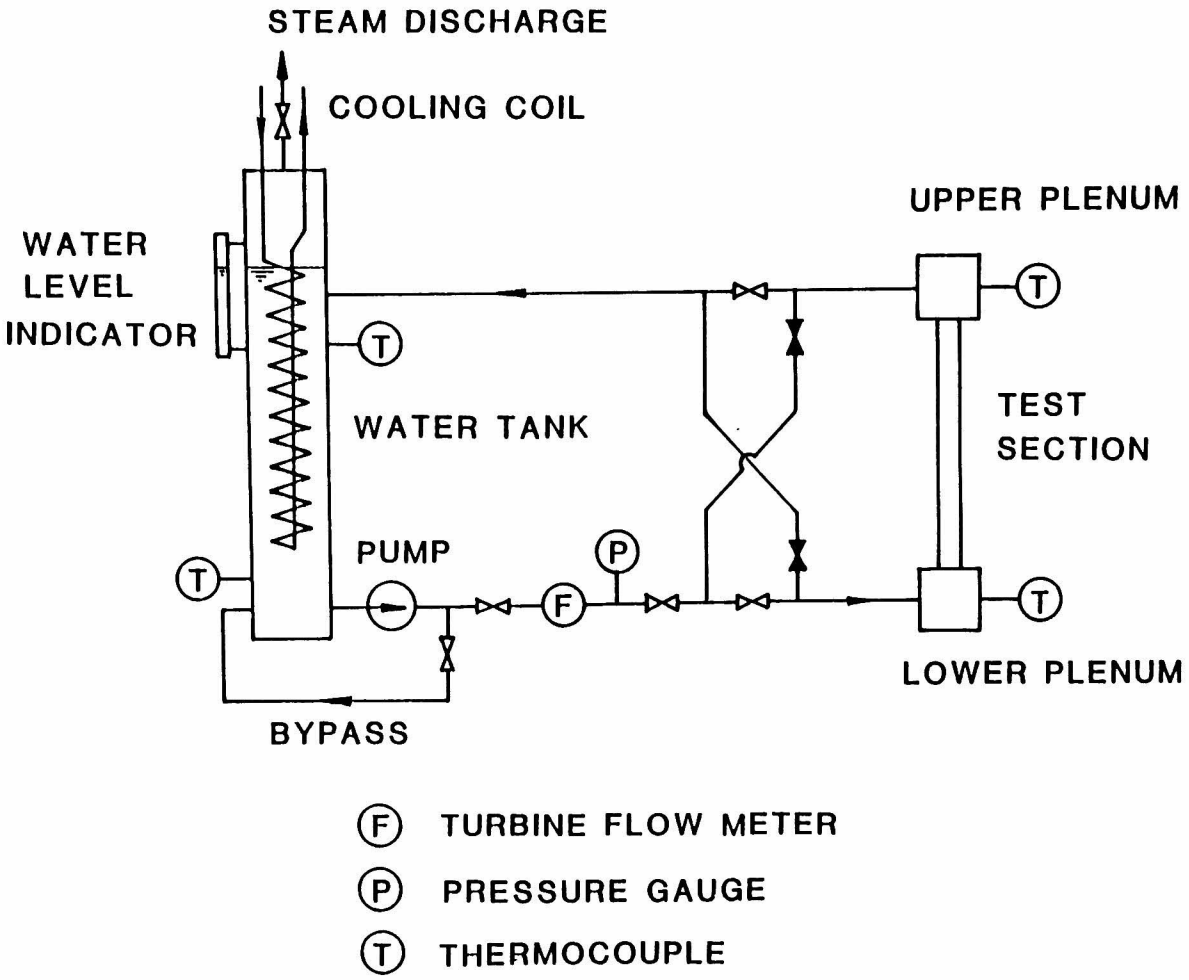


Figure 4 Schematic drawing of the test loop.

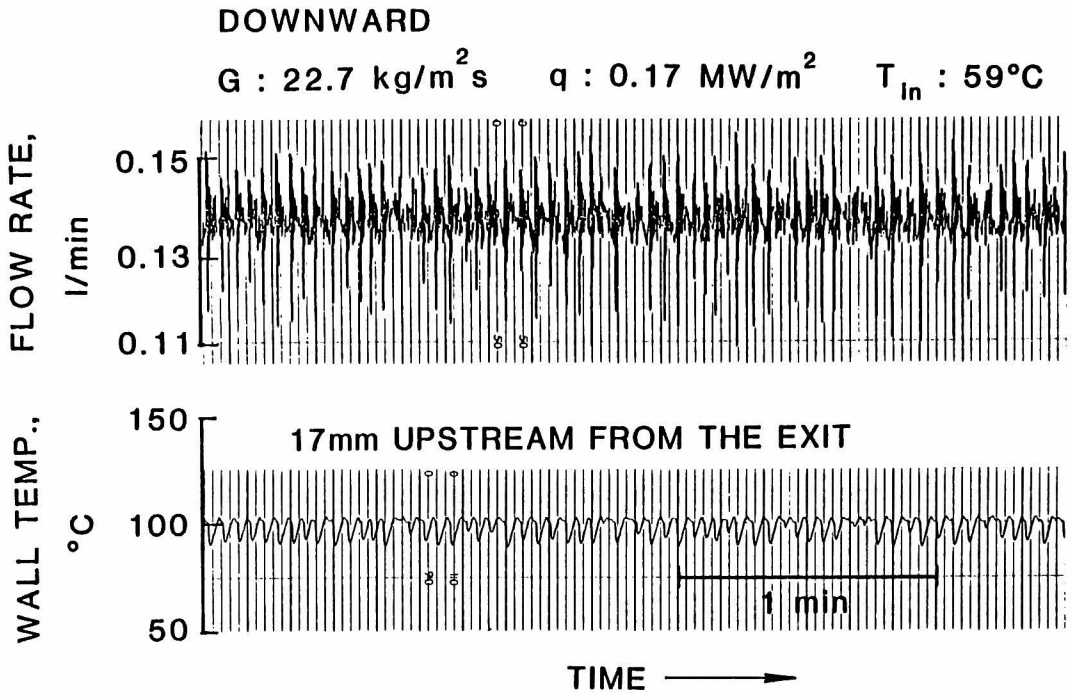


Figure 5 Flow rate and wall-temperature traces during flow instability at a mass velocity less than 100 kg/m$^2$s in downflow.

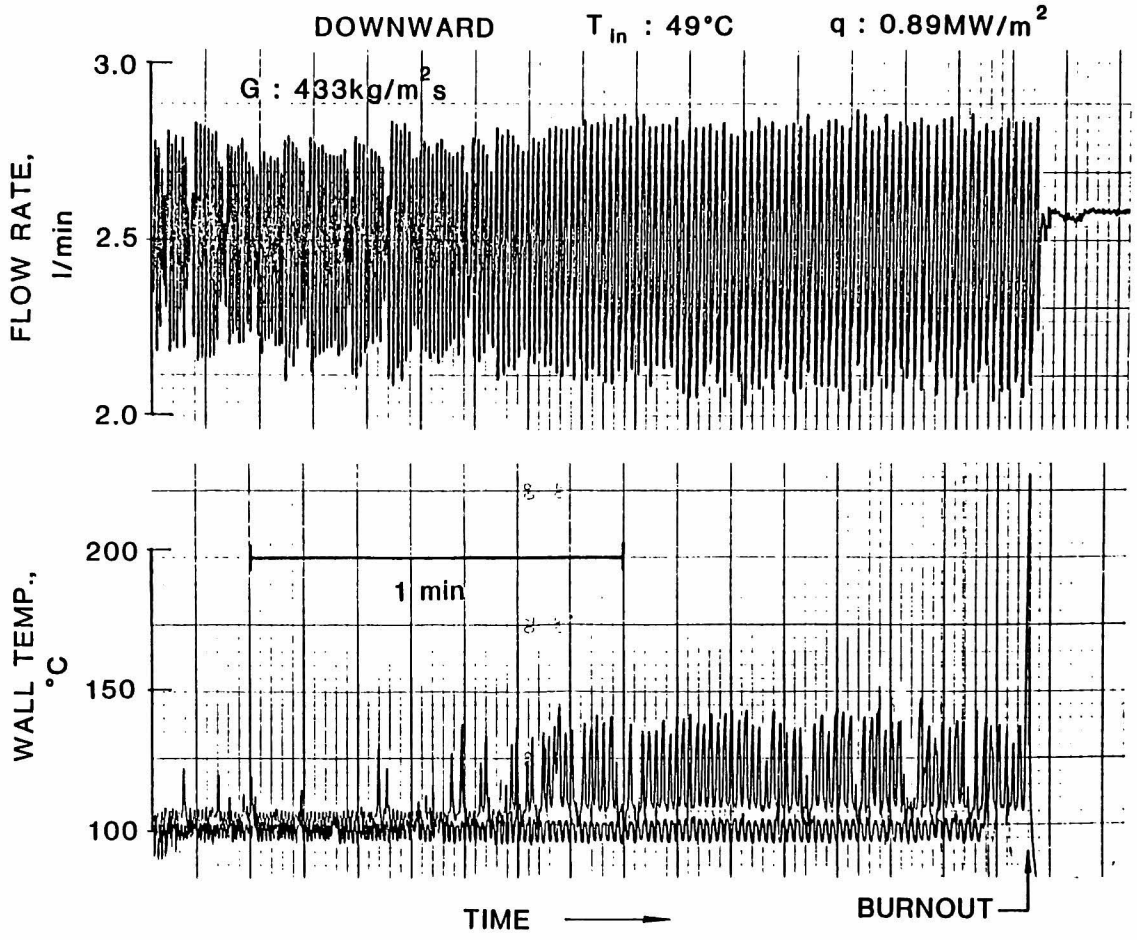


Figure 6 Flow-rate and wall-temperature traces during flow instability at a mass velocity higher than 200 kg/m$^2$s in downflow.

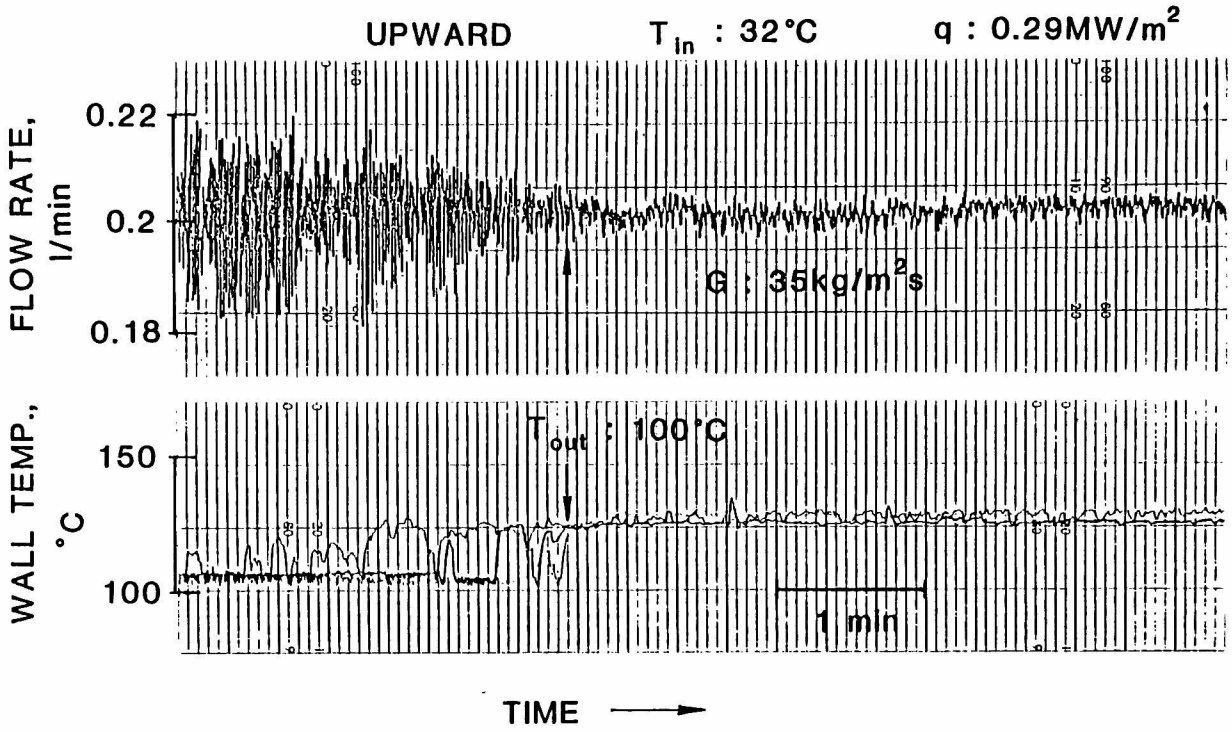


Figure 7 Flow-rate and wall-temperature traces during flow instability in upflow.

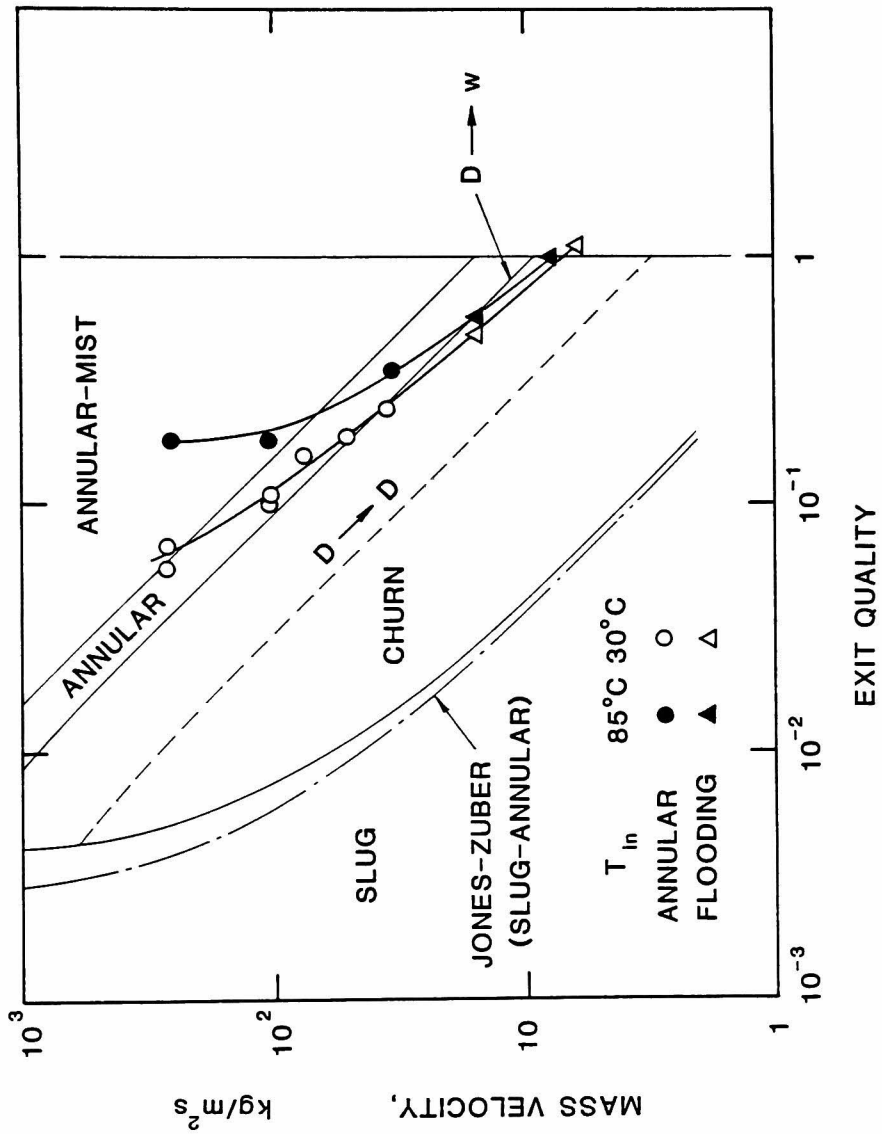


Figure 8 Flow regimes at the occurrence of burnout in upflow.

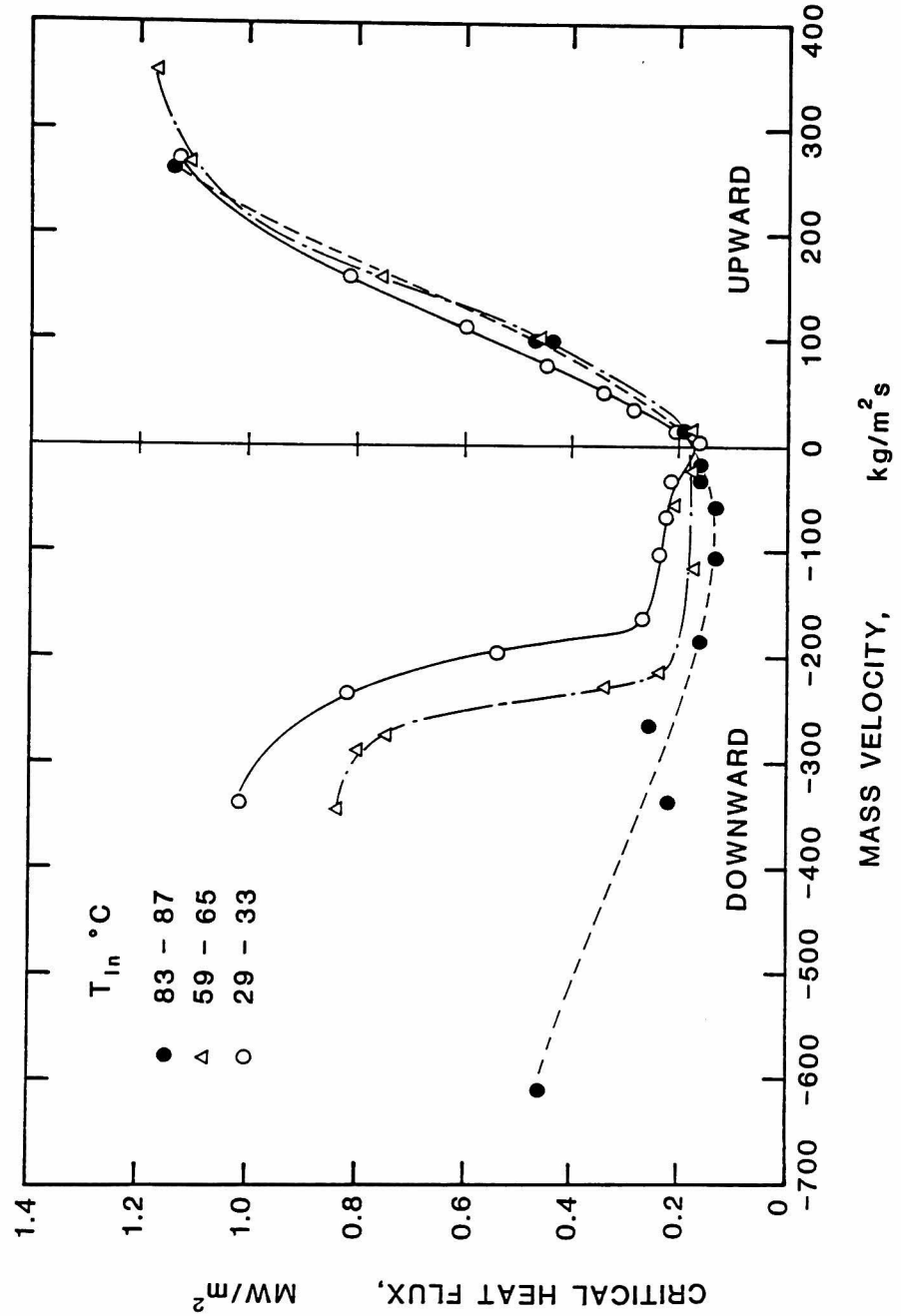


Figure 9 Critical heat flux for the test section heated from one side.

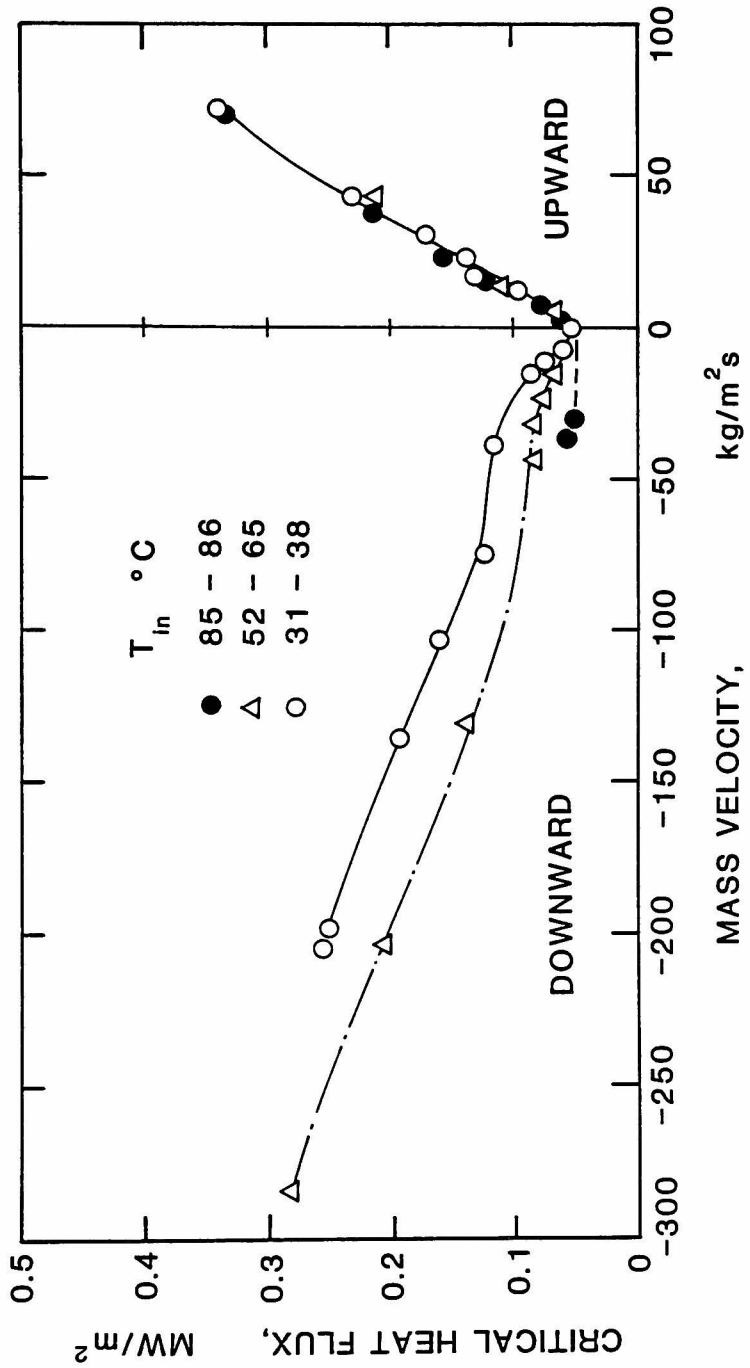


Figure 10 Critical heat flux for the test section heated from two opposite sides.

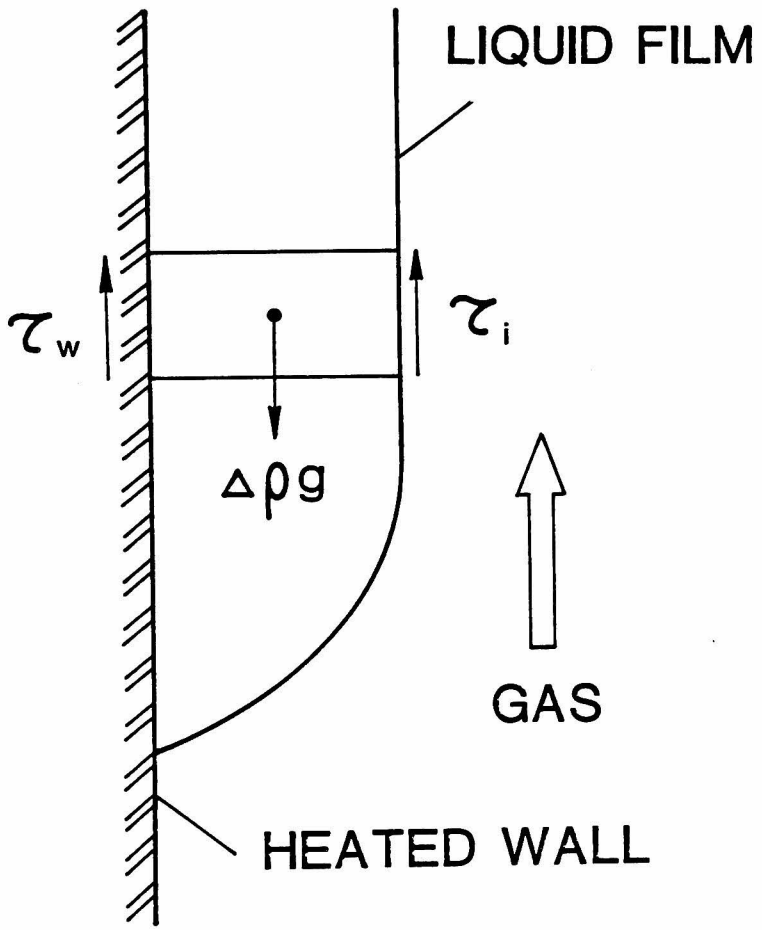


Figure 11 Model of hanging film.

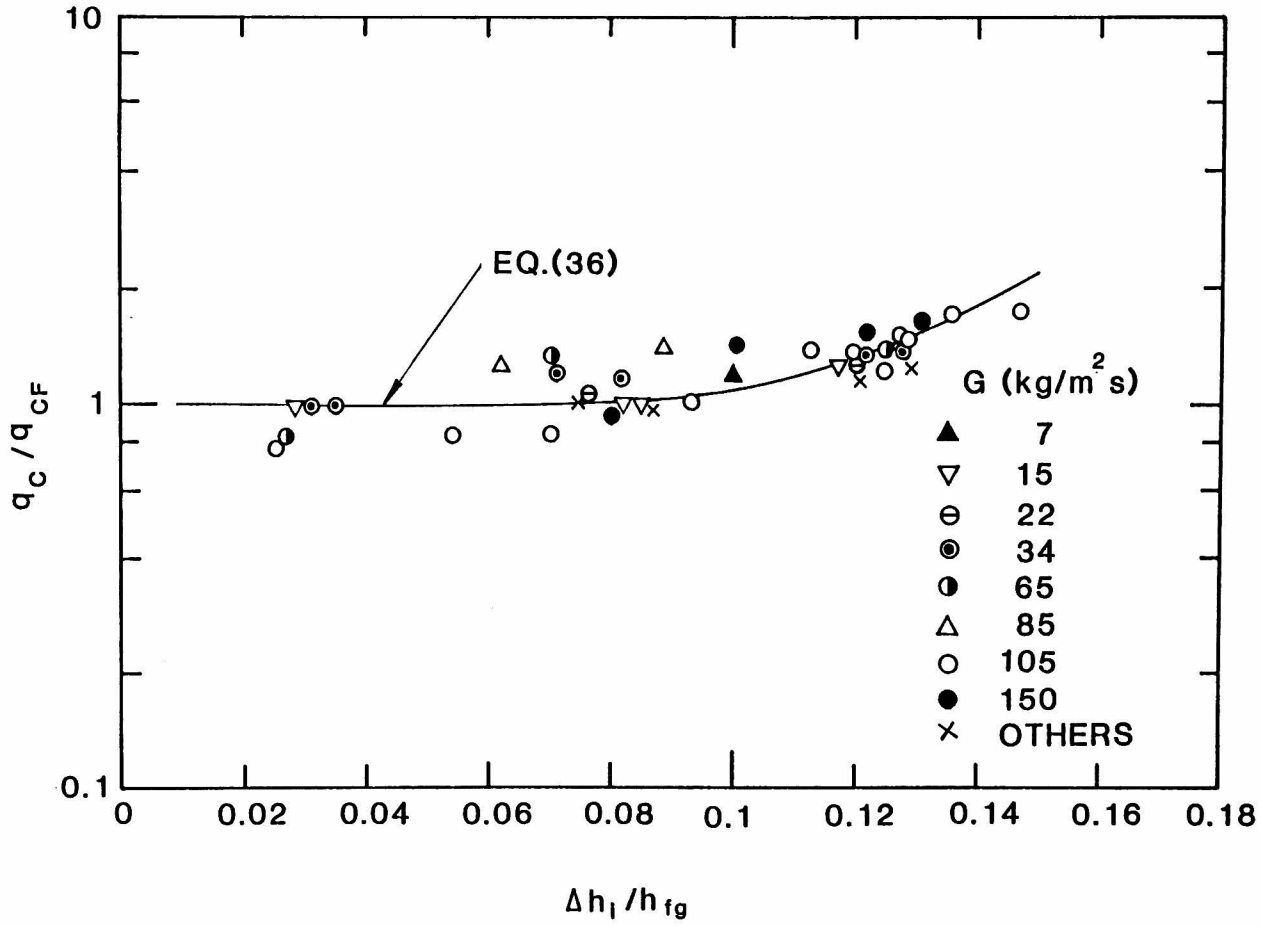


Figure 12 Effect of inlet subcooling on the CHF at mass velocities lower than the critical mass velocity in downflow.

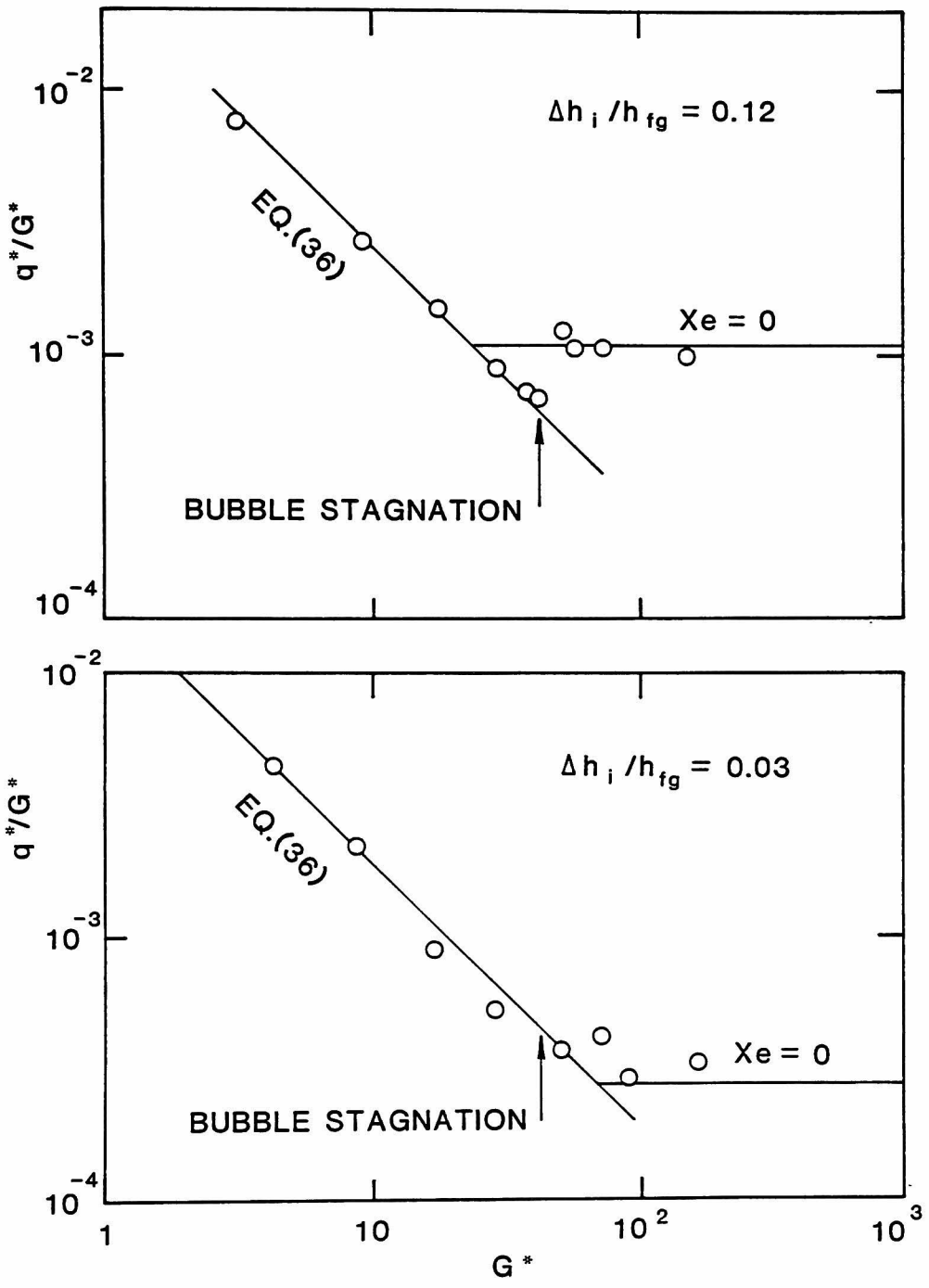


Figure 13 Non-dimensional correlation of the CHF data for downflow in the test section heated from one side.

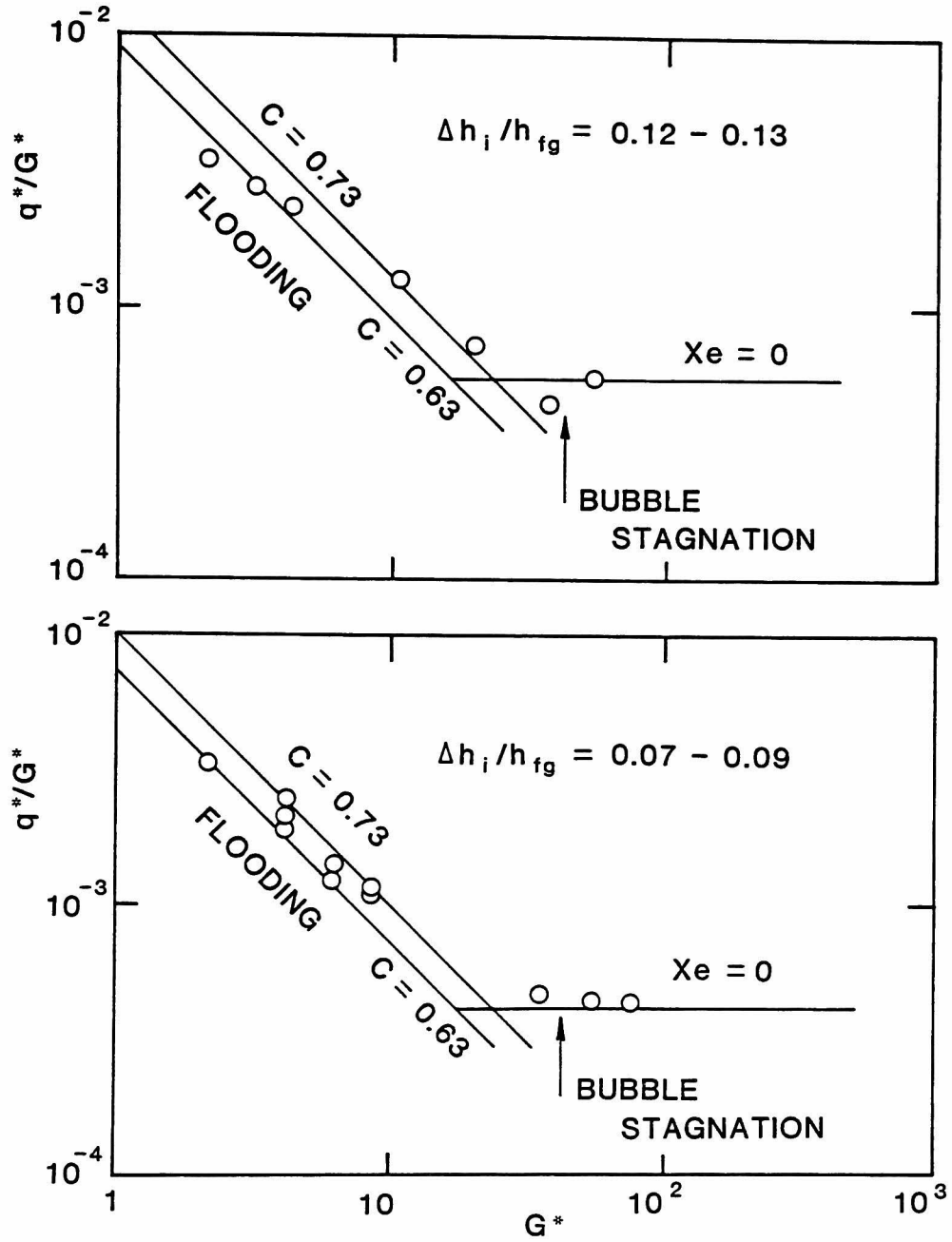


Figure 14 Non-dimensional correlation of the CHF data for downflow in the test section heated from two opposite sides.

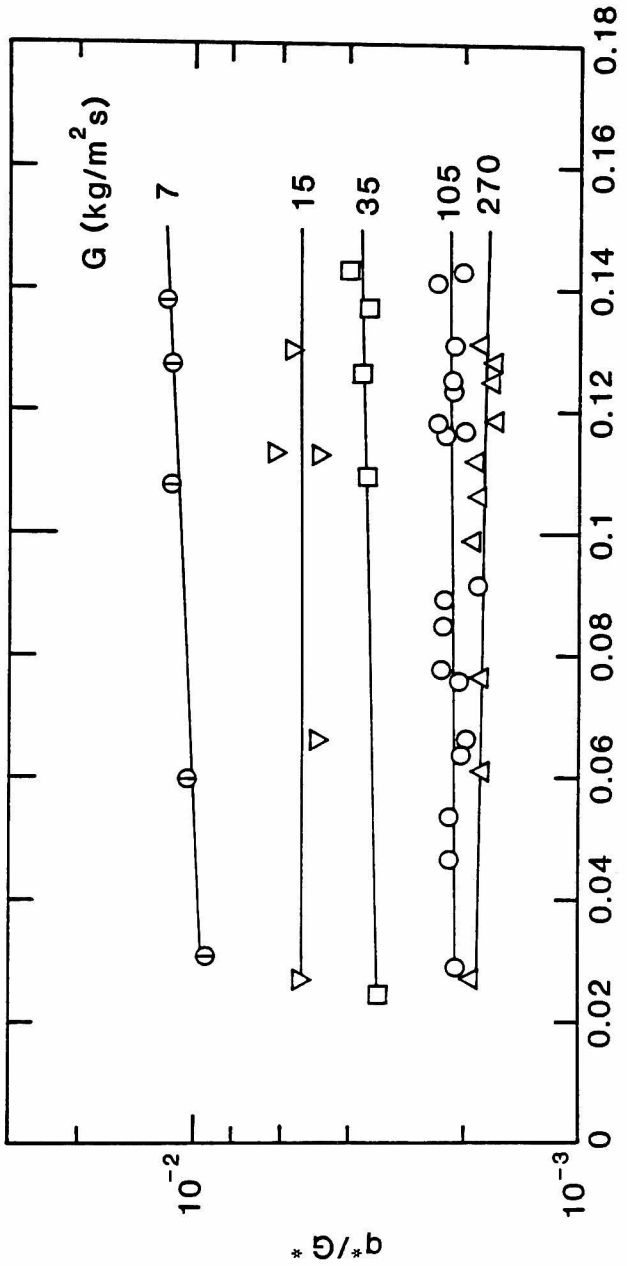


Figure 15 Effect of inlet subcooling on the CHF in upflow.

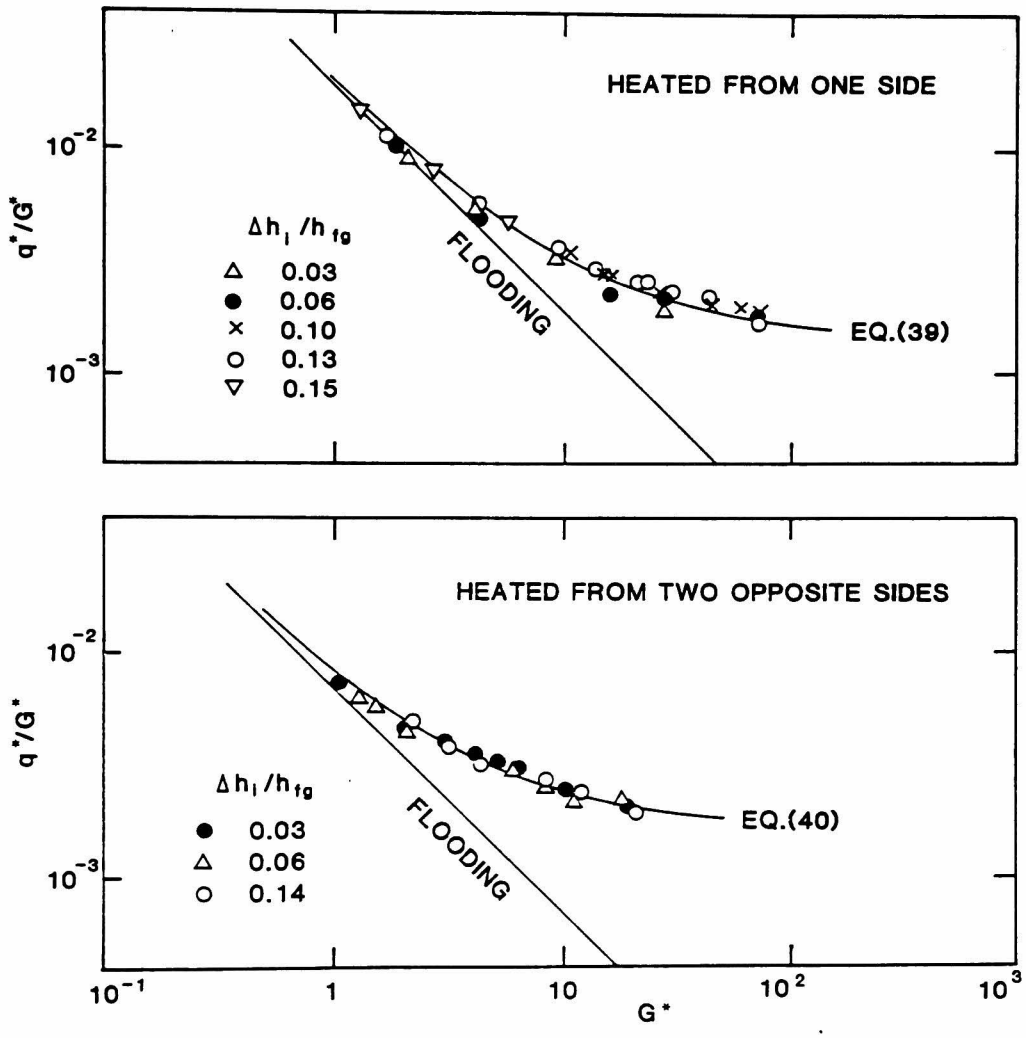


Figure 16 Non-dimensional correlation of the CHF data for upflow.

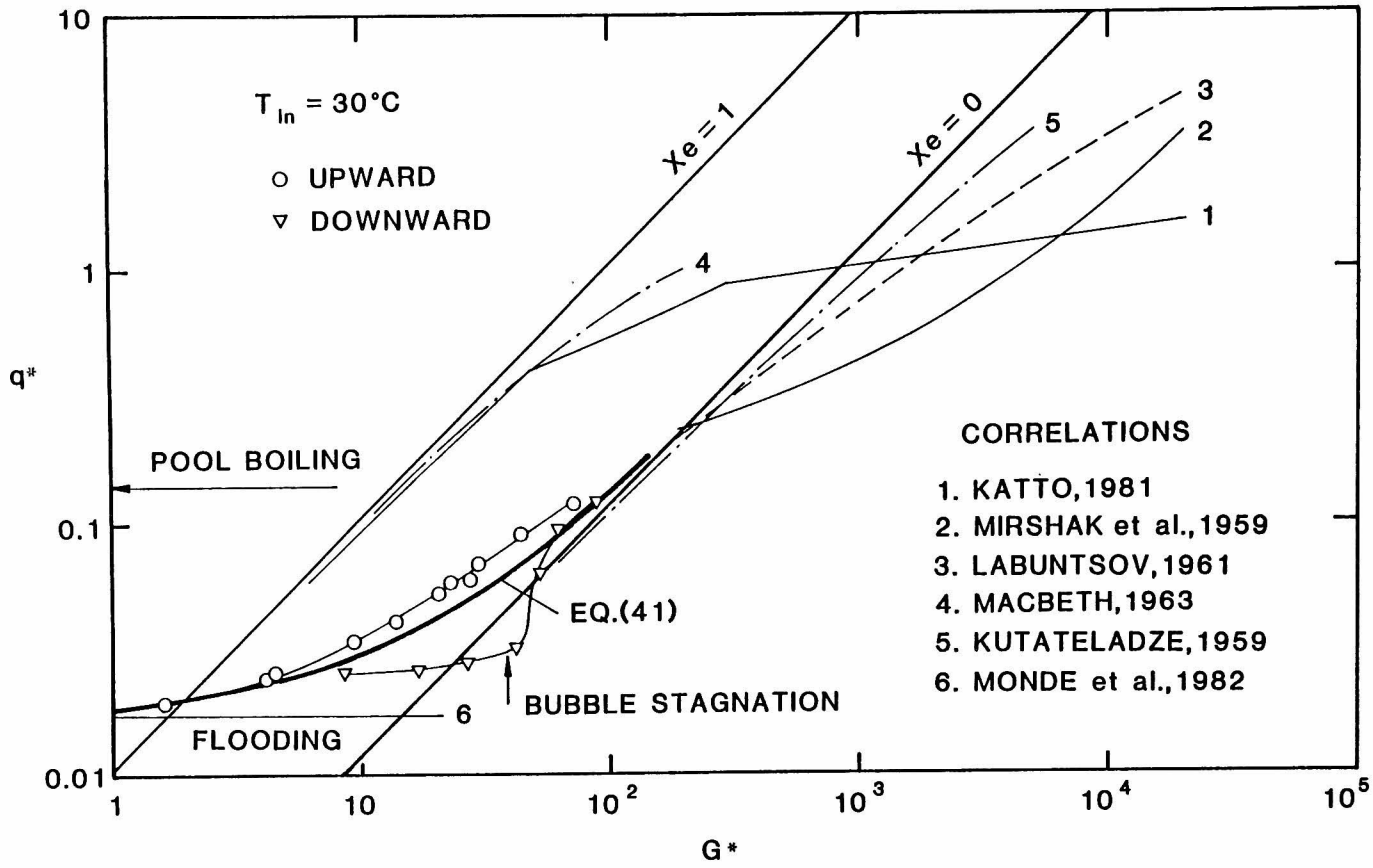


Figure 17 Non-dimensional plot of the CHF data at inlet water temperature 30°C for the test section heated from one side in comparison with several CHF correlations.

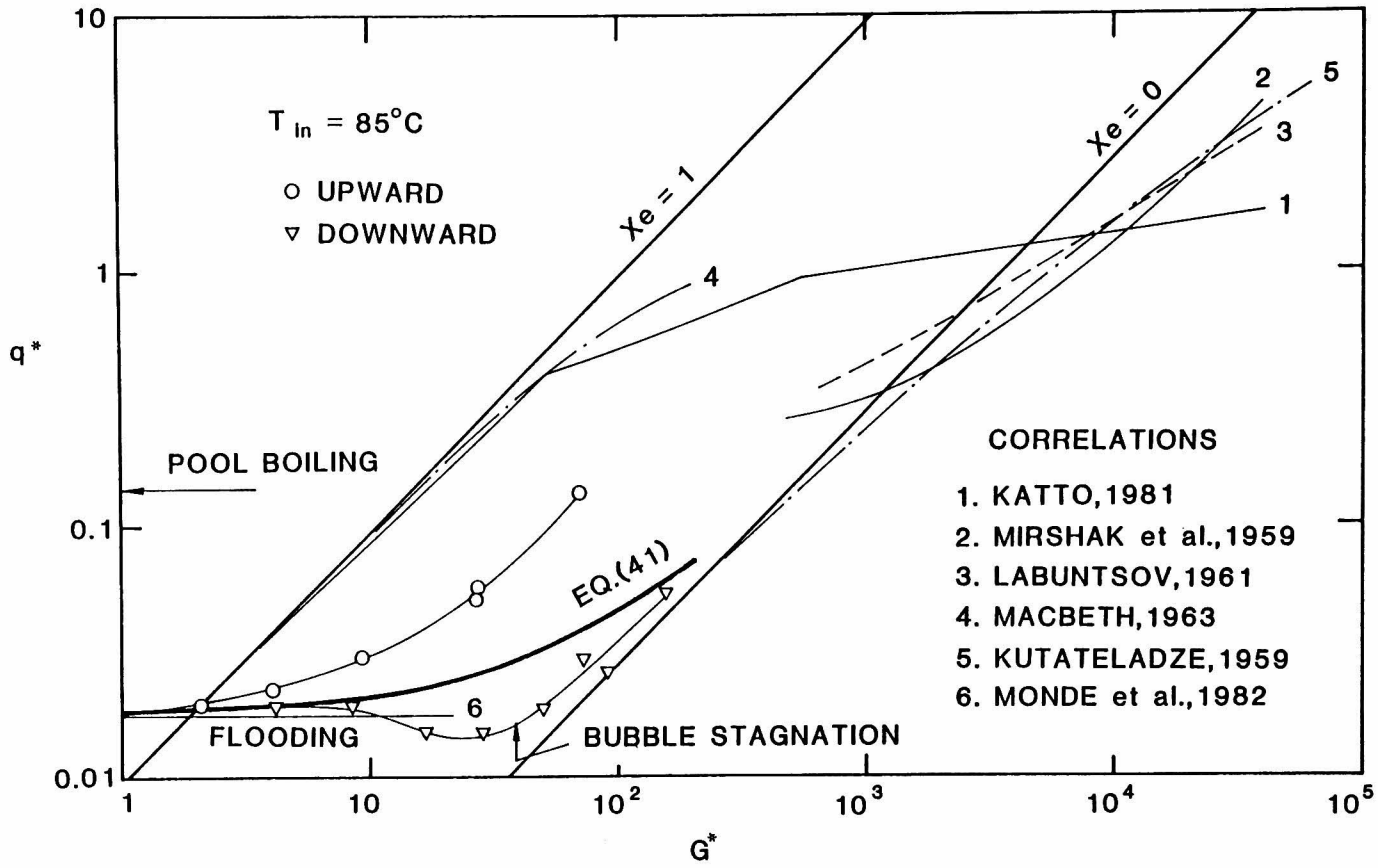


Figure 18 Non-dimensional plot of the CHF data at inlet water temperature 85°C for the test section heated from one side in comparison with several CHF correlations.

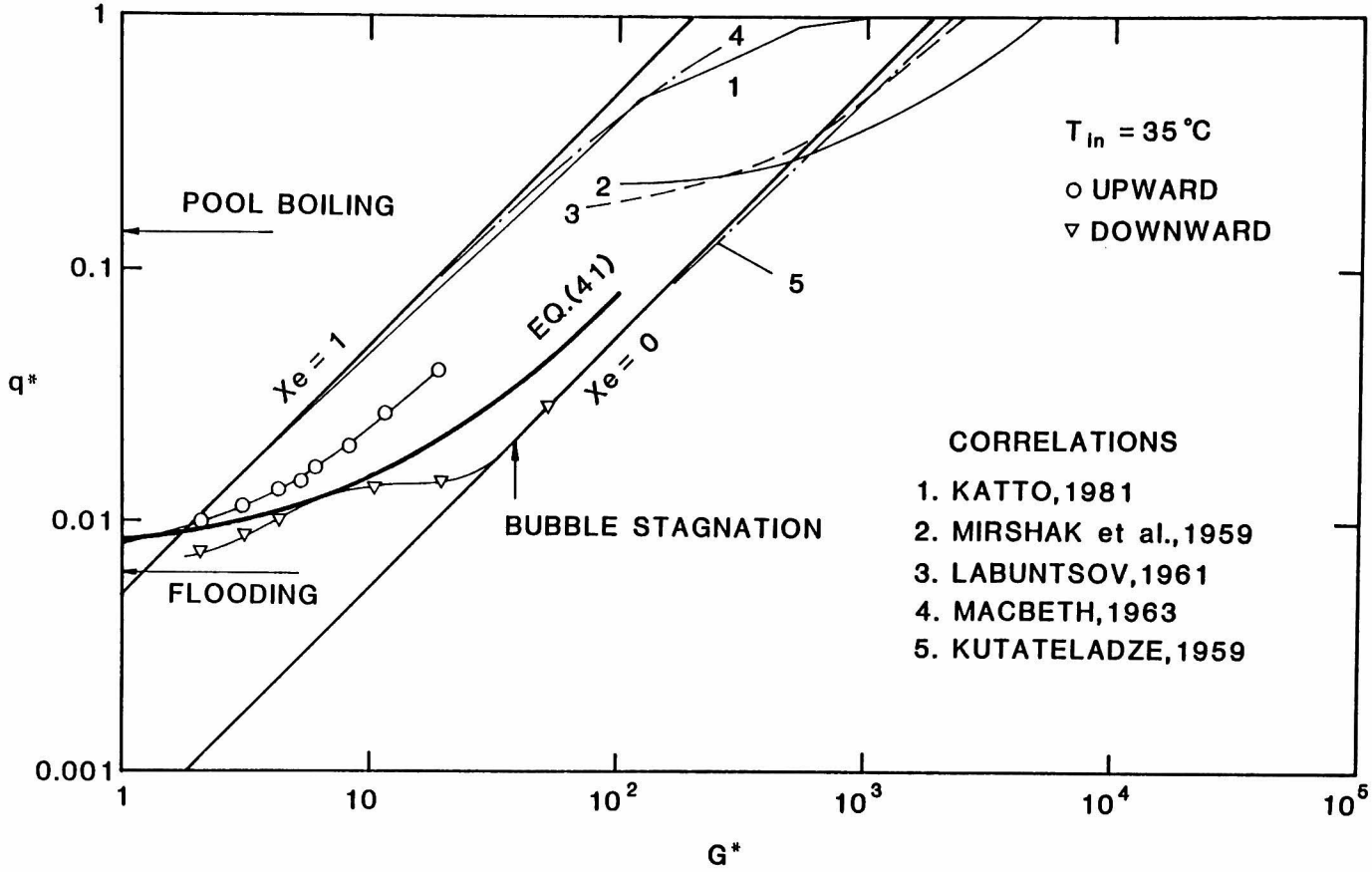


Figure 19 Non-dimensional plot of the CHF data for the test section heated from two opposite sides in comparison with several CHF correlations.

# CHAPTER VII.

# DISCUSSIONS AND RECOMMENDATIONS

## VII.1. INTRODUCTION

The purpose of this chapter is to compare the results obtained in the previous chapters with each other as well as with the results from various sources in order to provide some more generic understanding of the burnout mechanisms. In view of this, the results for each geometry of the test section, i.e. the annulus, the rectangular channels and the round tube are first compared to the existing data separately and the effects of several parameters are discussed. Then comparisons between the results for each channel geometries are made to discuss their effects on the burnout mechanisms.

## VII.2. BURNOUT IN ANNULUS

### VII.2.1. CHF at Higher Mass Velocities

The following major conclusions were extracted from the burnout experiment conducted with the annular test channel in Chapter IV:

(1) Critical heat flux at zero inlet flow (complete bottom blockage) can be predicted by flooding correlation, which gives lower CHF for larger L/D than those predicted by pool-boiling CHF correlation.

(2) Burnout at low mass velocities occurred due to liquid film dryout upon the flow regime transition from the churn to annular flow.

However, the tested range of the parameters are limited, it is necessary to see how the CHF behaves in more expanded range of parameters. For this purpose, several available data on CHF in annuli

are plotted in terms of the non-dimensional heat flux and mass velocity defined by

$$q^* = q/(h_{fg}\sqrt{\lambda \rho_g g \Delta\rho}) \quad , \tag{1}$$

$$G^* = G/\sqrt{\lambda \rho_g g \Delta\rho} \quad , \tag{2}$$

where

$$\lambda = \sqrt{\sigma/(g\Delta\rho)} \quad . \tag{3}$$

The data are compared to the following equations and some of the existing CHF correlations [1-4].

(1) Exit quality equal to unity ($x_e$ =1)

$$q^* = \frac{A}{A_H}(1 + \Delta h_i/h_{fg})\, G^* \quad . \tag{4}$$

(2) Zero exit quality ($x_e$ = 0)

$$q^* = \frac{A}{A_H}\frac{\Delta h_i}{h_{fg}}\, G^* \quad . \tag{5}$$

(3) Pool-boiling CHF [3,4]

$$q_{cP}^* = 0.16 \quad . \tag{6}$$

(4) Flooding CHF

$$q_{cF}^* = \frac{A}{A_H} \frac{C^2\sqrt{D^*}}{[1 + (\rho_g/\rho_l)^{1/4}]^2} \quad , \tag{7}$$

where

$$D^* = D/\lambda \quad . \tag{8}$$

(5) Churn-annular transition

$$q^* = \frac{A}{A_H} \left[ \frac{\Delta h_i}{h_{fg}} G^* + \left( \frac{1}{C_0} - 0.11 \right) \sqrt{D^*} \right] \quad , \tag{9}$$

where the distribution parameter $C_0$ is given by [6]

$$C_0 = 1.2 - 0.2\sqrt{\rho_g/\rho_l} \quad . \tag{10}$$

(6) The Katto correlation scheme for annulus [1]

L-regime (High-quality CHF correlation)

$$\frac{q_{cL}}{h_{fg}G} = 0.25 \frac{D_H}{L_H} \left( \frac{\sigma\rho_l}{G^2 L_H} \right)^{0.043} (1 + 1.16\ \Delta h_i/h_{fg}) \quad . \tag{11}$$

H-regime

$$\frac{q_{cH}}{h_{fg}G} = 0.12\ (\rho_g/\rho_l)^{0.133} \left( \frac{\sigma\rho_l}{G^2 L_H} \right)^{1/3} \frac{1 + K_H\ \Delta h_i/h_{fg}}{1 + 0.0081\ L_H/D_H} \quad , \tag{12}$$

where

$$K_H = 0.057 \left( \frac{69.2}{L_H/D_H} \right)^{11.0\rho_g/\rho_l} \left( \frac{\sigma\rho_l}{G^2 L_H} \right)^{-1/3} \quad . \tag{13}$$

N-regime

$$\frac{q_{cN}}{h_{fg}G} = 0.22\ (\rho_g/\rho_l)^{0.133} \left(\frac{\sigma\rho_l}{G^2 L_H}\right)^{0.433} \frac{(L_H/D_H)^{0.171}}{1 + 0.0081\ L_H/D_H} \quad . \quad (14)$$

(7) The Zenkevich correlation [2] for subcooled forced-convection CHF at low pressure.

$$q_c = h_{fg} \sqrt{\frac{\sigma g G}{\nu}}\ (2.5 + 184\ \Delta h_{sub}/h_{fg}) \times 10^{-5} \quad . \quad (15)$$

Figures 1 through 4 show the Rogers et al.[5] data for 0.156 MPa water in internally heated annuli in comparison with the above equations. It can be seen that the CHF is close to the line for the churn to annular flow transition at lower mass velocities whereas at higher mass velocities, the CHF appears to increase along the curve for subcooled boiling CHF predicted by the Zenkevich correlation [2].

Figure 4 shows the data for small $L_H/D_H$, in which case all the curves come close to each other because the flooding CHF approaches to the pool-boiling CHF. At high mass velocities, the Zenkevich correlation [2] appears to reproduce the experimental data very well. It should be noted that as most of the data are in the region below the annular-flow boundary, burnout may have occurred in the churn or slug flow region, which coincides with the observation reported in Reference [5]. On the other hand, at low mass velocities, the figures indicate that a burnout occurs at the annular flow boundary which coincides with the observation described in Chapter IV. Therefore, it is deduced that some change in the burnout mechanism may have occurred at intermediate mass velocities and the exit qualities near zero. Since rapid bubble

formation or collapse can be caused by a small change in flow rate, heat flux, subcooling, etc. at exit qualities near zero, the flow pattern (two-phase flow regimes and the stability of the flow) may be easily changed.

The other set of CHF data is available from the report on the burnout mechanisms prepared by the Japanese Society of Mechanical Engineers (JSME) [6]. Burnout experiments were performed with internally heated annuli of same design ($D_i$ = 10 mm, $D_o$ = 19 mm, L = 300 mm) independently at several universities and institutions. The data are plotted in terms of q* and G* at inlet water temperatures 95, 85 and 70°C in Figs. 5, 6 and 7, respectively. Figure 5 shows the CHF data in intermediate region between low flow CHF and high-flow subcooled-boiling CHF. In this case, the annular flow boundary defined by three curves, namely the churn-to-annular, slug-to-annular and slug-to-annular-mist flow transitions which are predicted by the criteria previously obtained. In the preceding chapters, the last two transition boundaries were omitted because the annular flow boundary was important only at low mass velocities where the boundary was defined only by the churn-annular transition. The churn-annular transition is given by Eq.(9). The second and the third transitions are given by the following criteria:

(1) Slug-to-annular flow transition

$$\alpha \geq 1 - 0.813 \left[ \frac{(C_0-1)j + 0.35 \sqrt{\Delta\rho g D/\rho_1}}{j + 0.75 \sqrt{\frac{\Delta\rho g D}{\rho_1}} \left( \frac{\Delta\rho g D^3}{\rho_1 \nu_1^2} \right)^{1/18}} \right]^{0.75} , \qquad (16)$$

and

$$\alpha = \frac{j_g}{C_0 j + 0.35\sqrt{\Delta\rho g D/\rho_l}} \quad . \tag{17}$$

(2) Annular-mist flow transition

$$j_g \geq \left(\frac{\sigma g \Delta\rho}{\rho_g^2}\right)^{1/4} N_{\mu l}^{-0.2} \quad , \tag{18}$$

where

$$N_{\mu l} = \frac{\mu_l}{(\rho_l \sigma \sqrt{\sigma/g\Delta\rho})^{1/2}} \quad , \tag{19}$$

and

$$\alpha = \frac{j_g}{C_0 j + \sqrt{2}\left(\frac{\sigma g \Delta\rho}{\rho_l^2}\right)^{1/4}} \quad . \tag{20}$$

These criteria can be expressed in terms of q* and G* using the following relations:

$$G = \rho_g j_g + \rho_l j_l \quad , \tag{21}$$

$$q = \frac{A}{A_H} h_{fg} G (x_e + \Delta h_i / h_{fg}) \quad , \tag{22}$$

$$x_e = \rho_g j_g / G \quad . \tag{23}$$

The data were obtained under apparently the same conditions, nevertheless, they are divided into two groups, i.e. higher CHF data and lower CHF data at a given range of flow rate. It was pointed out [6]

that some flow instability had been probably involved in the lower CHF data. The figure indicates, however, that these data are fairly along the annular-flow boundary, that is the CHF may have occurred due to the annular-flow transition. The other group of data are in the annular-mist flow regime. The discrepancy between these two groups was not completely interpreted but it should be noted here that the loop characteristics may be changed, for example, by inlet throttling even in a given test loop, as has been observed in Chapter V.

Figure 6 shows the CHF data in the intermediate region between the regime of CHF due to annular flow transition and the subcooled-boiling CHF regime. Figure 7 shows the CHF data in the subcooled-boiling regime, which are well reproduced by the Zenkevich correlation [2].

VII.2.2. CHF at Higher Pressures

It was pointed out in Chapter IV (Fig.13) that the region where the annular flow regime appears shrinks toward higher quality as the pressure increases, thus the CHF due to the transition to annular flow approaches to high-quality CHF. Since the flow becomes more stable at higher pressures, it can be said that the CHF at high pressure and low flow rate is well correlated by such high-quality CHF correlations as the Katto correlation [1].

The CHF data at high flow rates and high pressure conditions reported by JSME [6] are shown in Figs. 8 and 9. The same test sections as used in the low pressure experiment were employed for this case, too. It can be seen that the boundary of the annular flow regime moves toward higher quality and approaches to the Katto CHF curve at high pressure. The CHF data appear to be correlated by the high-quality CHF correlation satisfactorily. It is also noted that since the data are below the

annular-flow boundary, burnout may have occurred in the slug or bubbly flow regime at high flow rate. Moreover, as the CHF is above the pool-boiling CHF, the DNB-type burnout may have occurred in this region.

## VII.3. BURNOUT IN ROUND TUBES

### VII.3.1. Upflow

In chapter V, the following conclusions were made for the CHF for upflow in round tubes:

(1) There is a minimum in CHF at the complete bottom blockage condition, at which burnout occurs due to countercurrent flow limitation.

(2) Low flow CHF is well correlated by the conventional high-quality CHF correlations [7]-[9] which indicates that the mechanism of burnout is the liquid-film dryout. As the mass velocity increases, the critical quality at burnout decreases because the liquid entrainment increases and in turn the flow rate in the liquid film decreases.

(3) At higher flow rates, the flow appears to be largely affected by the density wave oscillations which cause premature burnout. The premature burnout may be a result of the liquid deficiency caused by the temporary reduction of the flow rate during the instability.

(4) At sufficiently high flow rate and heat flux, and at exit quality near zero, burnout occurs immediately after the onset of flow excursion. In that case, the total liquid starvation in the heated section causes the dryout over wide area of the heated surface.

In view of the flow-regime map obtained in Chapter II, the flow regime at burnout appears to be mostly the annular or annular-mist flow.

The predicted annular flow boundaries at high pressures are shown in Figs. 12 through 17, together with the CHF data for a round tube (10 mm ID, $L_H$ = 800 mm) taken from Reference [10]. It can be seen that the annular-flow boundary gradually moves toward higher quality as the pressure increases. The churn-to-annular flow boundary disappears at very high pressure and instead, the slug-to-annular and the slug-to-annular-mist flow boundaries become dominant.

Since the density ratio $\rho_l/\rho_g$ is smaller at higher pressures, the void fraction decreases at a given quality and thus the two-phase friction factor is reduced. For this reason, the flow is generally more stable at higher pressures. Therefore, it is expected that the stable-flow CHF will be more likely to occur in a high pressure system, and hence the CHF could be correlated well by the conventional high-quality CHF correlations [7]-[9].

VII.3.2. Downflow

The conclusions for the CHF in downflow are as follows:

(1) The downflow CHF is as much as 30% lower than the upflow CHF which is well reproduced by the conventional high-quality CHF correlations [7]-[9] at very low flow rates in a stiff system. This may be attributed to the effects of buoyancy which becomes more important at lower flow rates. The mechanism of burnout at low flow rates will be the liquid-film dryout.

(2) In a stiff system at high flow rates, the downflow CHF is as high as the upflow CHF. The density-wave oscillations appear to predominate in this region.

(3) Such destabilizing effects as reducing inlet restriction and providing upstream compressibility appear to be enlarged by the

buoyancy effects which decreases the CHF substantially.

(4) At sufficiently high mass velocity and heat flux, and exit quality near zero, burnout occurs due to flow excursion, as is the case in upflow. When the test section has a plenum at the top, the pressure drop oscillations are encountered before burnout occurs.

These observations were made at the exit pressure near atmospheric. Since the flow becomes more stable at higher pressures, it is expected that the difference in CHF between the soft system and the stiff system becomes smaller. However, further studies are needed to draw definite conclusions for higher pressure systems.

## VII.4. BURNOUT IN RECTANGULAR CHANNELS

### VII.4.1. Upflow

From the experiment conducted for upflow in rectangular channels, the following results are obtained for burnout mechanisms and the CHF.

(1) The minimum CHF is obtained at complete bottom blockage (zero inlet flow) condition, where burnout occurred due to countercurrent flow limitation.

(2) The CHF at intermediate flow rates increases along the line for approximately constant exit quality. This critical exit quality lies somewhere between the high-quality CHF curve and the annular-flow boundary which limit the lower boundary of the CHF. Both visual observation and the CHF data indicate that burnout occurs in the annular flow regime at intermediate mass velocities.

(3) It is known that subcooled-boiling CHF such as the Labuntsov correlation [11], the Kutateladze correlation [12] and the Zenkevich correlation [2] can be used at high mass velocities,

where DNB-type burnout occurs. From this fact and the results obtained for low mass velocities, it is deduced that the CHF curve at intermediate mass velocity merge with those curves at higher mass velocities.

(4) It is known that the conventional high-quality CHF correlations [7,13] have been obtained mainly based on high pressure data. The behavior of the CHF at high pressures for rectangular channels will be the same as for annuli.

VII.4.2. Downflow

As regards to the mechanisms of burnout and the CHF for downflow in rectangular channels, the results are summarized again as follows:

(1) Burnout occurs due to countercurrent flow limitation at low mass velocities less than the critical value to stagnate steam bubbles in the heated channel. The resultant CHF is the minimum and much lower than the pool-boiling CHF.

(2) At intermediate mass velocities beyond the critical mass velocity for bubble stagnation, burnout occurs at about zero exit quality. In this region, vigorous flow oscillations arise, which amplitude increases with increasing mass velocity and heat flux. Due to this instability, the CHF is decreased substantially.

(3) It is known that at high mass velocities, subcooled-boiling CHF correlations such as the Mirshak correlation [14] are relevant. In this region, DNB-type burnout will take place.

Visual observation revealed that the flow regime at burnout was basically the churn or slug flow at intermediate and high mass velocities. However, it appears to be flow regime instability, because

the flow regime varies between the slug or churn flow and the annular flow during a cycle of large bubble formation and collapse. The flow rate traces are very similar to those observed for the pressure-drop oscillations in the round tube experiment. The upper plenum may have worked as an energy storage mechanism to excite flow oscillations in this case, too. Therefore, the flow-regime instability may be considered as an secondary phenomenon of the pressure drop oscillations.

VII.4.3. Flow Instabilities

The observation of flow rate traces indicated that the flow is largely affected by the flow instabilities both in upflow and downflow and that the downflow is generally less stable than the upflow. This may be because of the buoyancy effects. The significance of flow instabilities in a boiling system has been pinted out earlier by many investigators in relation to the core cooling of MTR-type research reactors [15-18] in which the coolant channels are rectangular.

Redpath and Whittle [18] conducted an experiment with single rectangular channel, in which the flow rate was gradually reduced until the onset of flow instability keeping the heat flux constant (constant-power experiment). They found that parallel-channel flow instabilities would occur at a reactor power larger than the normal maximum of 15 MWt (at that time), at a level (∿32 MWt) which exceeds that accepted for subcooled burnout.

Waters [15] performed heat transfer experiments with rectangular channels for the Advanced Test Reactor (ATR) in order to investigate the upper-limit heat flux for the ATR. A chopped cosine axial heat flux pattern was used in the tests and in one test section a lateral flux peaking factor of 1.36 peak/average was also used. Both constant-power

experiment (stiff system) and constant-head experiment (soft system) were conducted. In the latter, the heat flux was gradually increased until the onset of flow instability keeping the valve throttling constant. It was found that flow instabilities, not boiling burnout, would limit heat fluxes in the ATR. The flow instabilities occurred at the minimum in the internal (system-demand) pressure-drop versus flow-rate curve, corresponding with beginning of bulk boiling.

A simple criterion for estimating the locus of the minima in the internal pressure-drop versus flow-rate curves for rectangular ducts and round tubes was proposed by Forgan and Whittle [16]. The criterion is expressed as

$$\frac{\Delta T_c}{\Delta T_i} = \frac{1}{1 + \eta/(L_H/D_H)} \quad , \tag{24}$$

where $\Delta T_c$ is the bulk water temperature rise at the condition of minimum pressure drop and $\Delta T_i$ is the difference between the exit saturation temperature and the inlet water temperature. The value of the parameter $\eta$ was determined empirically to be 25. It was pointed out that the minimum pressure drop correspond to detachment of steam bubbles from the heater surface.

Equation (24) is applicable to the present rectangular channels. Predicted stability boundary is shown in Figs. 10 and 11, together with the present CHF data. The subcooled-boiling CHF curves [2, 12] appear to be close to the predicted stability boundary. Therefore, it is probable that some instabilities have been involved in obtaining the CHF data on which those correlations are based. However, this speculation needs to be verified. On the other hand, the Mirshak correlation [14]

predicts lower CHF than the stability boundary. This agrees with the observation by Redpath and Whittle [18].

Since the CHF data fall above the minima in the internal pressure-drop versus flow-rate curves, as given in Figs. 10 and 11, and in addition to this, because of the existence of upstream compressibility (upper plenum), the instability observed in the downflow may be pressure-drop oscillations. On the other hand, neither flow excursion nor pressure-drop oscillations were observed in the upflow. Instead, the flow rate traces indicated that the density-wave type oscillations were encountered at high flow rate and high heat flux conditions. In those cases, the flow appeared to be in the annular flow or annular-mist flow regime in which the boiling boundary oscillated violently.

## VII.5. EFFECT OF GEOMETRY ON BURNOUT MECHANISMS

### VII.5.1. Burnout due to Countercurrent Flow Limitation

At complete bottom blockage or very low flow conditions, burnout due to countercurrent flow limitation (CCFL) appears to be common to all the basic geometries. This type of burnout is important because it results in the minimum CHF which can be much lower than the pool-boiling CHF in ordinary systems.

The relation between the CHF due to CCFL and the pool-boiling CHF was discussed in Chapter IV. It was pointed out there that the CHF due to flooding increases with increasing diameter and decreasing heated length until it reaches the pool-boiling CHF. In other words, the pool-boiling burnout can be considered as an extreme case of burnout due to CCFL.

Observed mechanisms of burnout due to CCFL are somewhat different

between channel geometries. In the annulus, falling film is formed on both the heated and unheated walls almost equally, and burnout occurs when the liquid film on the heated surface dries out due to CCFL. The CHF is well reproduced by Eq.(7) with C = 1 and by using the hydraulic equivalent diameter, i.e. 2s as the characteristic length. As regards to the characteristic length, there is some inconsistency among investigators. Richter [19] used the average circumference of the annulus, i.e. $(D_i + D_o)/2$, whereas Ueda and Suzuki [20] used the hydraulic equivalent diameter. Theoretically, the hydraulic equivalent diameter is derived as the characteristic length if we assume uniform liquid film equally on the inner and the outer walls. However, further studies are needed on this point.

In rectangular channels, the falling film is not uniform around the channel. The majority of the liquid flows down along the narrow side walls, not along the heated wall. This may be due to large aspect ratio of the channel. The wider walls (one of which is heated) easily dry out but are drenched by the passage of large disturbance waves and liquid bridges generated from the liquid film on the narrow side walls. Permanent dryout of the heated surface occurs when sufficient amount of liquid is not supplied to the heated section due to CCFL. The CHF in this case is correlated by Eq.(7), using 2w (two times of the channel width) as the characteristic length, with c = 0.73 and 0.63 for the test section heated from one side and that heated from two opposite sides, respectively.

In round tubes, the flow was not observed visually but the CHF due to CCFL is correlated by the following equation:

$$q_{cF}^* = \frac{A}{A_H} j_g^* \sqrt{D^*} \quad , \tag{25}$$

where the non-dimensional superficial velocity of the vapor is approximated at the CCFL condition by

$$j_g^* \simeq 8 \, (\rho_g/\rho_l)^{1/4} \quad . \tag{26}$$

when the liquid film is thin and can be considered smooth. For a tube with a large diameter, the CHF due to CCFL can be given by

$$q_{cF}^* = 3.2 \frac{A}{A_H} \quad . \tag{27}$$

Equations (25) and (27) are compared with some existing data [21,22] plotted in terms of $q^*_{cF}$ and the parameter $\zeta$ given by

$$\zeta = \frac{A\sqrt{D^*}}{A_H[1 + (\rho_g/\rho_l)^{1/4}]^2} \quad . \tag{28}$$

Using Eq.(28), Equation (7) can be rewritten as

$$q_{cF}^* = C^2\zeta \quad . \tag{29}$$

The results are shown in Fig. 18 in comparison with several existing data [21-23]. Equation (26) appears to give rather high CHF. This will be attributed to the simplification in deriving Eq.(26) based on the assumption that the liquid film can be considered smooth and the wall shear stress neglected in comparison with the interfacial shear

stress. However, the predicted CHF is still within the scatter of the experimental data. As for the other geometries, the data of Kusuda et al.[22] for externally heated annuli and those from the present experiment also shown in Fig. 18. It appears that the CHF is lower in annuli and rectangular channels than in round tubes at given $\zeta$.

VII.5.2. Burnout at Low Mass Velocities

It turned out that the behavior of the CHF at low and intermediate mass velocities was different between round tubes and the other geometries. In round tubes, the boiling number behaves as a function of G* as shown in Fig. 19, whereas the curve becomes concave for annulus and rectangular channels as shown in Figs. 20 and 21, respectively. In round tubes, burnout occurs due to almost complete evaporation of the liquid entering the heated section, thus the critical quality being close to unity when the liquid entrainment is not much. On the other hand, in the annulus and the rectangular channels, substantial amount of liquid remains on the unheated surface at the occurrence of burnout, thus the critical quality being low. It should be noted, however, that the mechanism of burnout itself was the same for all the channel geometries, i.e. burnout occurred when the liquid film on the heated surface dried out completely.

Therefore it may be assumed that the critical quality is , as stated by Ishii et al.[24], approximately equal to

$$x_{ec} = x_{eR}\, \xi_h/\xi \quad , \tag{30}$$

if the liquid film is uniform in circumference. Here $x_{eR}$ is the critical quality in round tubes and can be calculated from the Katto

L-regime correlations [1,9,13], as given by

$$x_{eR} = \left( \frac{\sigma \rho_l}{G^2 L_H} \right)^{0.043} \quad . \tag{31}$$

If we use the critical quality, the Katto L-regime correlations can be rewritten as

$$q_{cL}^* = \frac{A}{A_H} (x_{ec} + \Delta h_i / h_{fg}) \, G^* \quad . \tag{32}$$

There are some data [25] for annulus which agree reasonably well with Eq.(32), as presented in Fig. 22.

From the above discussions, it is deduced that the CHF for annulus lies somewhere between the curve given by the reduced critical quality and the annular-flow boundary. However, this should be limited to a low pressure system, because at high pressures, it is recognized that the Katto L-regime correlation [1] reproduced the CHF data well. These results do not appear to be fully consistent at present. In order to solve the problem, a burnout experiment at intermediate pressures must be performed, which is out of the scope of this investigation.

The same argument can be followed for rectangular channels. Comparisons between the CHF data for rectangular channels and Eq.(30) are given in Figs. 23 and 24. In that case, however, the reduction of the critical quality may not be given only by the geometrical consideration because the liquid film on the unheated walls (narrower side walls) is much thicker than that on the heated wall. Therefore, a certain parameter would be needed to take account of the effect of non-uniform distribution of film flow rate, if one would calculate the

critical quality more accurately.

From the above discussions, it may be concluded that the difference in the behavior of the CHF curve between the different geometries is attributed to the amount of liquid flowing along the unheated wall at the occurrence of burnout. However, in any case at low mass velocities, the mechanism of burnout appears to be the dryout or breakdown of the liquid film on the heated surface. Therefore, if the film flow rate and the criteria for the dryout or breakdown of liquid film are known in detail, the CHF can be predicted theoretically. For example, the entrainment-limited burnout has been already explained by the entrainment and deposition rate by several authors. However, it is also probable that those criteria are met consequently if such hydrodynamical phenomena as countercurrent flow limitation, flow-regime transition and flow excursion cause the liquid deficiency in the heated channel. Therefore, in such cases, the CHF can be calculated by using the criteria for such hydrodynamical phenomena.

VII.5.3. Burnout at High Mass Velocities

At high mass velocities, burnout occurs when the exit quality is near zero or slightly negative. The flow is more or less unstable in this region because a small variation in heat flux or flow rate yields a large change in void fraction, particularly at low pressures. Under such conditions, the difference in the channel geometry itself may not have a significant effect on the mechanisms of burnout but such factor as the hydraulic characteristics of the channel, inlet throttling, upstream compressibility, the pump characteristic, the bypass and the flow orientation may have.

The mechanisms of burnout in this region will be two fold, namely

the total liquid starvation and the DNB-type burnout. When the heat flux is not so high as to cause DNB-type burnout, burnout occurs due to the temporary reduction of the flow rate caused by the flow instability. Particularly the flow excursion directly leads to burnout due to total liquid starvation, in which case the CHF can be obtained from the criterion for the flow excursion. When the heat flux is sufficiently high, the DNB-type burnout may occur due to the vapor-blanketing over the heated surface even if the hydrodynamical condition is such that sufficient amount of liquid can be supplied to the heated section.

## VII.6. CONCLUSIONS

The results from this chapter are summarized as follows:

(1) There is a minimum in CHF which occurs due to countercurrent flow limitation at the complete bottom blockage condition. The CHF due to CCFL in a round tube appears to be a little higher than that in an annulus and a rectangular channel. The CHF can be calculated from an appropriate model for the CCFL.

(2) The behavior of CHF as a function of mass velocity differs between round tubes and the other channel geometries with unheated wall at low and intermediate mass velocities. The overall trends of CHF are illustrated in Figs. 25 and 26. In a round tube, the region where the CHF curve appears is bounded by the following four curves: the high-quality CHF curve, the annular-flow boundary, subcooled-boiling CHF curve and the flooding (or CCFL) line. On the other hand, in an annulus and a rectangular channel, the high-quality CHF curve should be replaced by the curve determined by the reduced critical quality due to the remaining liquid film on the unheated wall. This argument may be valid only for low

pressure systems, because there are some evidents that the high-quality CHF correlation reproduces the CHF data well at high pressures.

(3) The effect of buoyancy (or flow orientation) is such that moves the CHF curve to more unstable region in downflow.

(4) The effect of pressure on the CHF curve is depicted in Figs. 27 for a round tube. The annular-flow boundary moves toward higher quality as the pressure increases. In addition to this, the flow becomes more stable at higher pressures. This will be the reason why the CHF at high pressures are well correlated by the stable-flow high-quality CHF correlations. In an annulus and a rectangular channel, the annular-flow boundary moves to the region above the curve for reduced critical quality. Therefore, it may be deduced that the region where the CHF curves appear is the same as in a round tube at high pressures. However, it is still subject to further studies on this point.

(5) In any case at low mass velocities, the mechanism of burnout appears to be the dryout or breakdown of the liquid film on the heated surface. Therefore, if the film flow rate and the criteria for the dryout or breakdown of liquid film are known in detail, the CHF can be predicted theoretically. However, it is also probable that those criteria are met consequently if such hydrodynamical phenomena as countercurrent flow limitation, flow-regime transition and flow excursion cause the liquid deficiency in the heated channel. Therefore, in such cases, the CHF can be calculated by using the criteria for such hydrodynamical phenomena.

(6) In the subcooled-boiling CHF region at high mass velocities, the

CHF may be correlated well by the conventional CHF correlations. The CHF in this region appears to be more or less affected by the flow instabilities. In a round tube, the data clearly indicated that burnout occurred due to flow excursion at high mass velocity and heat flux, in which case the wide area of the heated surface dried out due to total liquid starvation. When the heat flux is sufficiently high, DNB-type burnout will occur due to vapor-blanketing over the heated surface.

## NOMENCLATURE

$A$ : Flow area

$A_H$ : Heated area

$C$ : Constant in the Wallis correlation for flooding

$C_0$ : Distribution parameter

$D$ : Tube diameter or characteristic length

$D^*$ : Non-dimensional tube diameter

$D_i$ : Diameter of the inner wall

$D_o$ : Diameter of the outer wall

$D_H$ : Heated equivalent diameter

$G$ : Mass velocity

$G^*$ : Non-dimensional mass velocity

$g$ : Gravity

$h_{fg}$ : Latent heat of vaporization

$\Delta h_i$ : Inlet subcooling

$\Delta h_{sub}$ : Subcooling at the burnout location

$j$ : Volumetric flux of the two-phase mixture

$j_k$ : Superficial velocity (volumetric flux) of k phase (k = g or l)

$K_H$ : Parameter for the effect of inlet subcooling in the Katto H-regime CHF correlation

$L$ : Length

$L_H$ : Heated length

$N_{\mu l}$ : Viscosity number

$q$ : Heat flux

$q^*$ : Non-dimensional heat flux

$q_c$ : Critical heat flux

$q_{cF}$ : CHF due to flooding

$q_{cH}$ : CHF in the Katto H-regime

$q_{cL}$ : CHF in the Katto L-regime

$q_{cP}$ : Pool-boiling CHF

$s$ : Gap of annulus or rectangular channel

$\Delta T_c$ : Temperature rise in the heated section

$\Delta T_i$ : Inlet temperature subcooling

$x_e$ : Exit equilibrium quality

$x_{ec}$ : Critical quality

$x_{eR}$ : Critical quality obtained from the Katto L-regime correlation

Greek symbols

$\alpha$ : Void fraction

$\Delta\rho$ : Difference of the density between two phases

$\zeta$ : Parameter for flooding CHF correlation

$\eta$ : Parameter used in the Forgan and Whittle equation

$\lambda$ : Length scale of the Taylor wave

$\mu_k$ : Viscosity of k phase (k = g or l)

$\nu_k$ : Kinematic viscosity of k phase (k = g or l)

$\xi$ : Wetted perimeter

$\xi_H$ : Heated perimeter

$\rho_k$ : Density of k phase (k = g or l)

$\sigma$ : Surface tension

Subscripts

c : Critical or coolant

e : Exit

F : Flooding

fg : Difference between the two phases

g : Gas phase

H : Heated region or the Katto H-regime

i : Inlet or inner

L : The Katto L-regime

l : Liquid phase

o : Outer

P : Pool-boiling

R : Round tube

## REFERENCES


[1] Y. Katto, "Generalized correlation of critical heat flux for the forced convection boiling in vertical uniformly heated annuli," Int. J. Heat Mass Transfer, 22, pp.575-584 (1979).

[2] B.A. Zenkevich, "The generalization of experimental data on critical heat fluxes in forced convection of sub-cooled water," J. Nucl. Energy, Part B : Reactor Technology, 1, pp.130-133 (1959).

[3] S.S. Kutateladze, Heat transfer in condensation and boiling, AEC-tr-3770 (1959).

[4] N. Zuber, Hydrodynamic aspects of boiling heat transfer, AECU-4439 (1959).

[5] J.T. Rogers, M. Salcudean and A.E. Tahir, "Flow boiling critical heat fluxes for water in a vertical annulus at low pressure and velocities," Proc. 7th. Int. Heat Transfer Conference, Munich, 4, Paper No.FB-28, p.339 (1982).

[6] F. Tachibana et al., ed., Report on burnout mechanisms : 1965 Research for peacefull use of atomic energy, JSME Report (June 15, 1967) in Japanese.

[7] R.V. Macbeth, Burnout analysis, Part 4 : Application of a local conditions hypothesis to world data for uniformly heated round tubes and rectangular channels, AEEW-R267 (1963).

[8] W.H Lowdermilk, C.D. Lanzo and B.L. Siegel, Investigation of boiling burnout and flow stability for water flowing in tubes, NACA-TN-4382 (1958).

[9] Y. Katto, "A generalized correlation of critical heat flux for the forced convection boiling in vertical uniformly heated round

tubes," Int. J. Heat Mass Transfer, 21[12], pp.1527-1542 (1978).

[10] T. Kuroyanagi and T. Iwamura, Flow reduction transient burnout in a vertical tube, 1, JAERI-M8774 (1980).

[11] D.A. Labuntsov, "Critical thermal loads in forced motion of water which is heated to a temperature below the saturation temperature," Soviet Journal of Atomic Energy (English Translation), 10, pp.516-518 (1961).

[12] S.S. Kutateladze, "Critical thermal flow for the flow of a wetting liquid containing an underheated core," Energetica, 2, pp.229-239 (1959).

[13] Y. Katto,"General features of CHF of forced convection boiling in uniformly heated rectangular channels," Int. J. Heat Mass Transfer, 24, pp.1413-1419 (1981).

[14] S. Mirshak, W.S. Durant and R.H. Towell, Heat flux at burnout, DP-355 (1959).

[15] E.D. Waters, Heat transfer experiments for the Advanced Test Reactor, BNWL-216 (1966).

[16] R. Forgan and R.H. Whittle, "A correlation for the minima in the pressure drop versus flow-rate curves for sub-cooled water flowing in narrow heated channels," Nucl. Engng. Design, 6, pp.89-99 (1967).

[17] P.J. Kreyger and W.A. Essler, "Flow-instability-induced burnout of non-uniformly heated channels with a constant pressure drop," Nucl. Engng. Design, 12, pp.148-152 (1970).

[18] W. Redpath and R.H. Whittle, The coolant flow stability in DIDO under subcooled nucleate-boiling conditions, AERE-R-4731 (1964).

[19] H.J. Richter, "Flooding in tubes and annuli," Int J. Multiphase

Flow, 7[6], pp.647-658 (1981).

[20] T. Ueda and S. Suzuki, "Behavior of liquid films and flooding in counter-current two-phase flow. Part 2. Flow in annuli and rod bundles," Int. J. Multiphase Flow, 4, pp.157-170 (1978).

[21] P. Griffith, W.A. Schumann and A.D. Neustal, "Flooding and burnout in closed-end vertical tubes," Two-phase Fluid Flow Symposium, Paper No.5, Inst. Mech. Engrs., London (1962).

[22] H. Kusuda and H. Imura, "Stability of a liquid film in a counter-current annular two-phase flow," Bull. JSME, 17[114], p.1613 (1974).

[23] W.J. Frea, "Two-phase heat transfer and flooding in counter current flow," 4th. Int. Heat Transfer Conference, Paris, Paper No.B5.10 (1970).

[24] M. Ishii and H.K. Fauske, "Boiling and dryout behavior in a liquid-metal fast breeder reactor subassembly bundle under low heat flux and low flow conditions," Nucl. Sci. Engng., 84, pp.131-146 (1983).

[25] T. Kuroyanagi and T. Iwamura, Flow reduction transient burnout in an annular test section, JAERI-M8047 (1979).

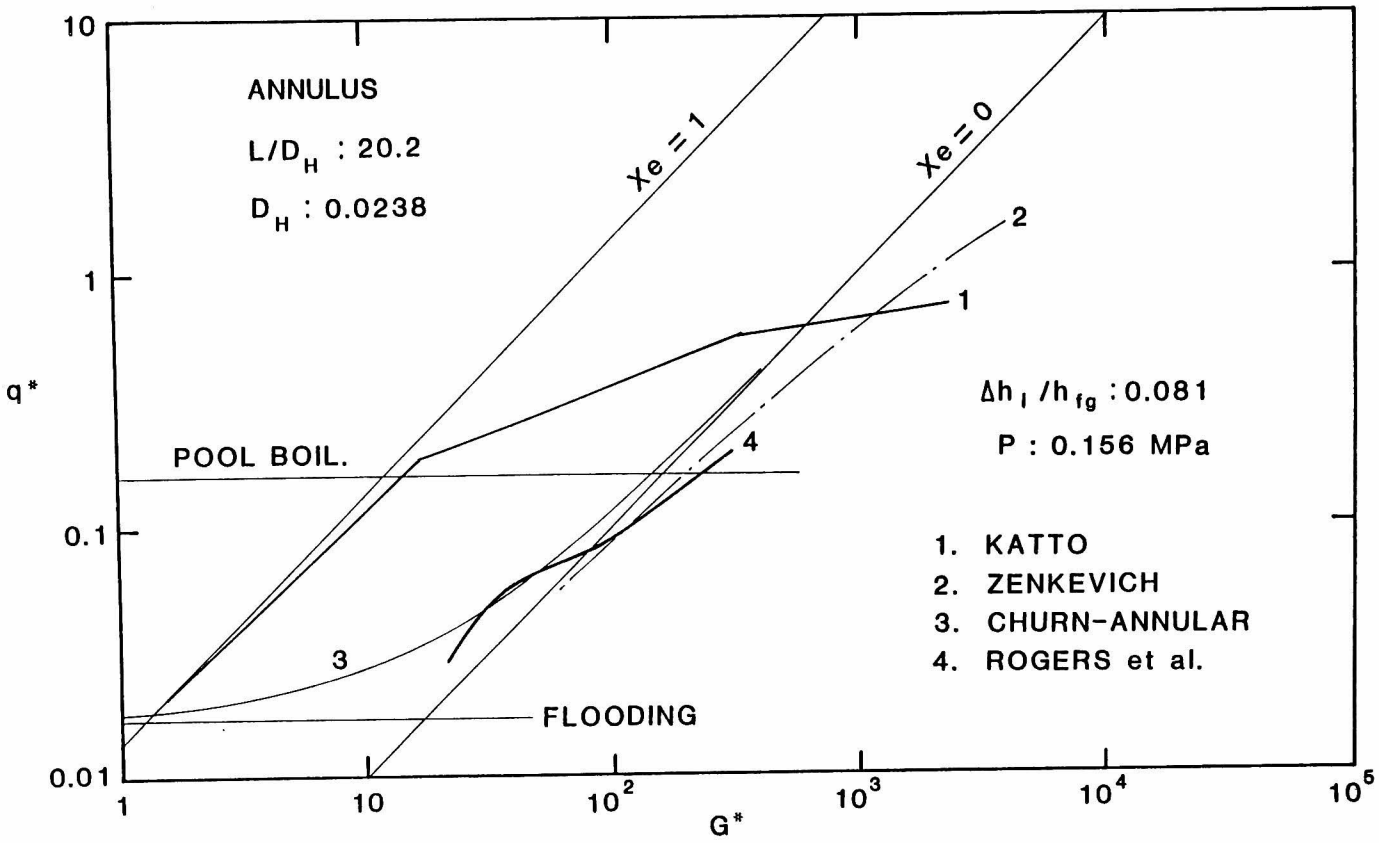


Figure 1 Rogers et al. [5] data for annulus at $\Delta h_i/h_{fg}$ = 0.081.

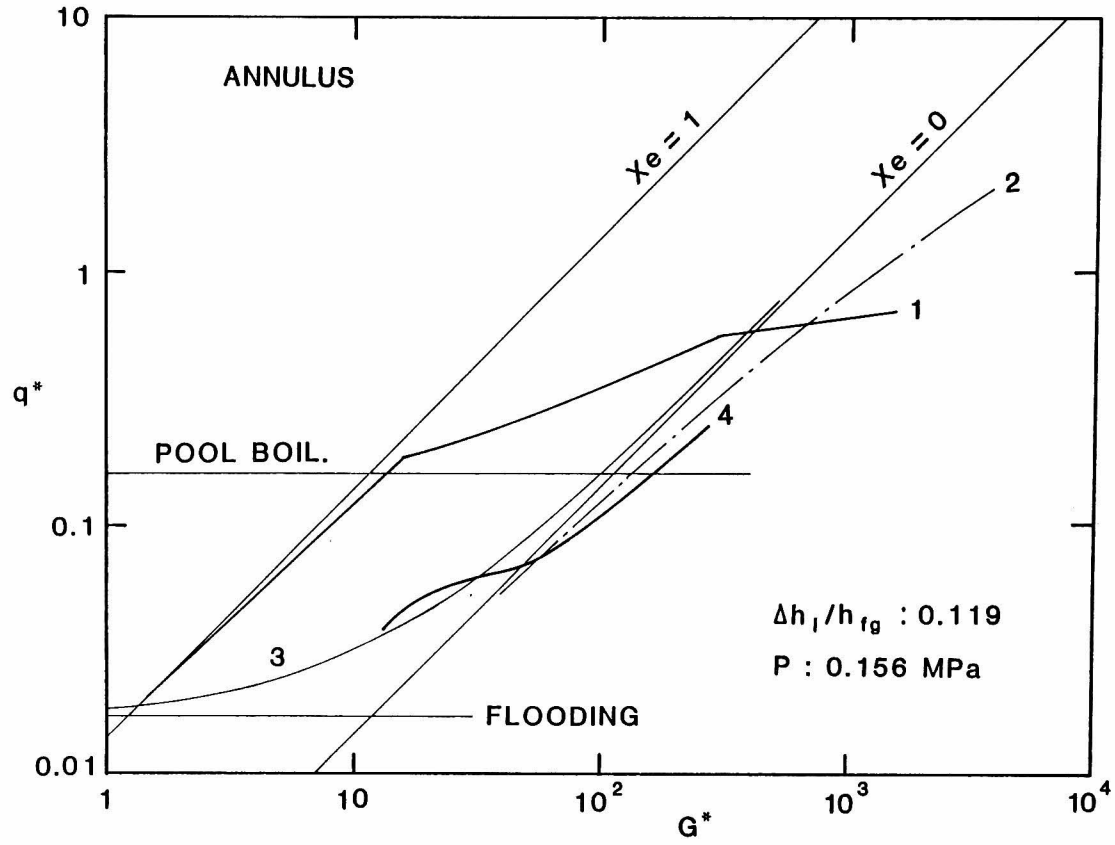


Figure 2 Rogers et al. [5] data for annulus at $\Delta h_i/h_{fg}$ = 0.119 (Legend as given in Fig. 1).

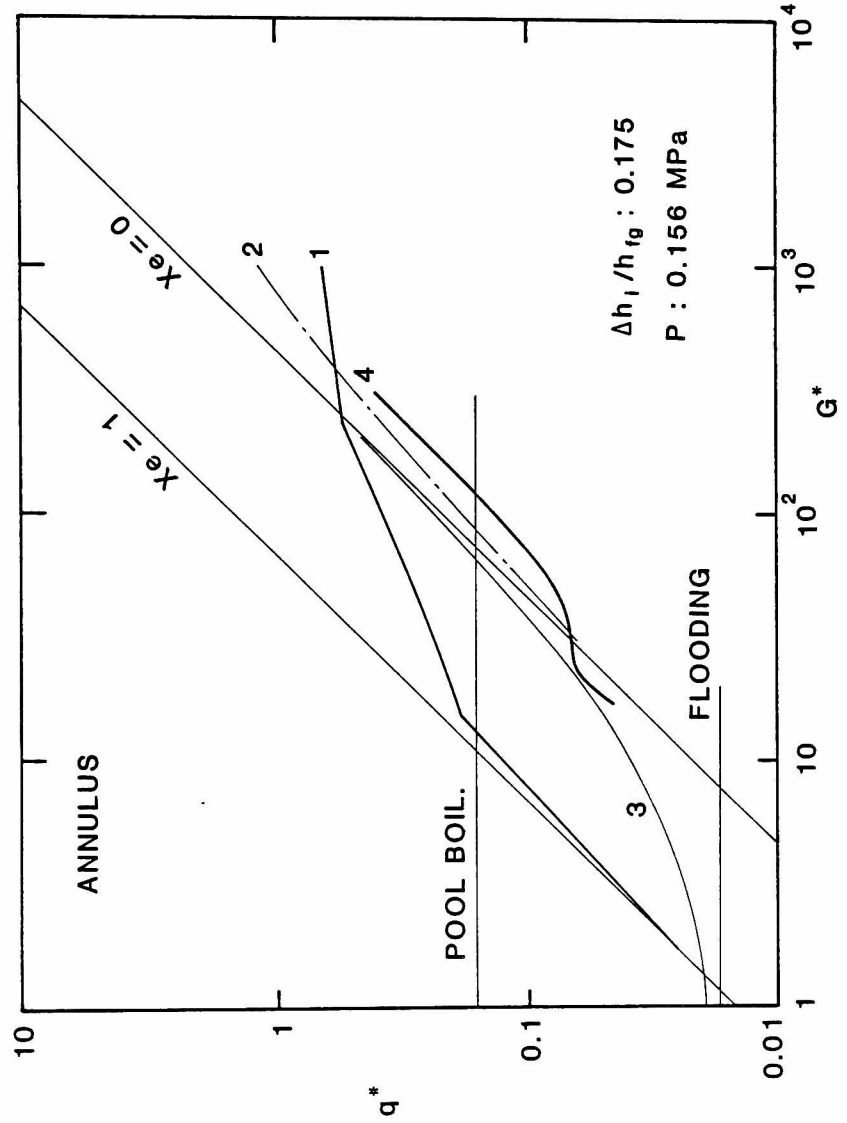


Figure 3 Rogers et al. [5] data for annulus at $\Delta h_i/h_{fg}$ = 0.175 (Legend as given in Fig. 1).

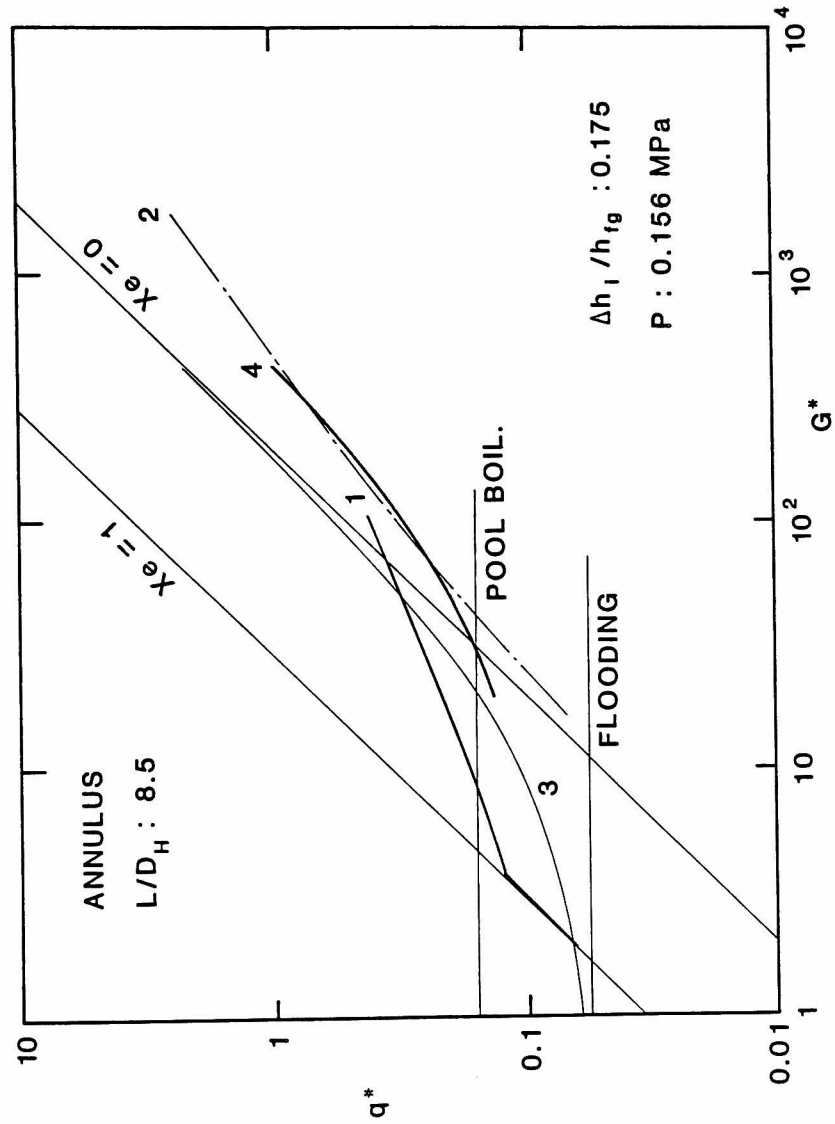


Figure 4 Rogers et al. [5] data for annulus with small $L_H/D_H$ (Legend as given in Fig. 1).

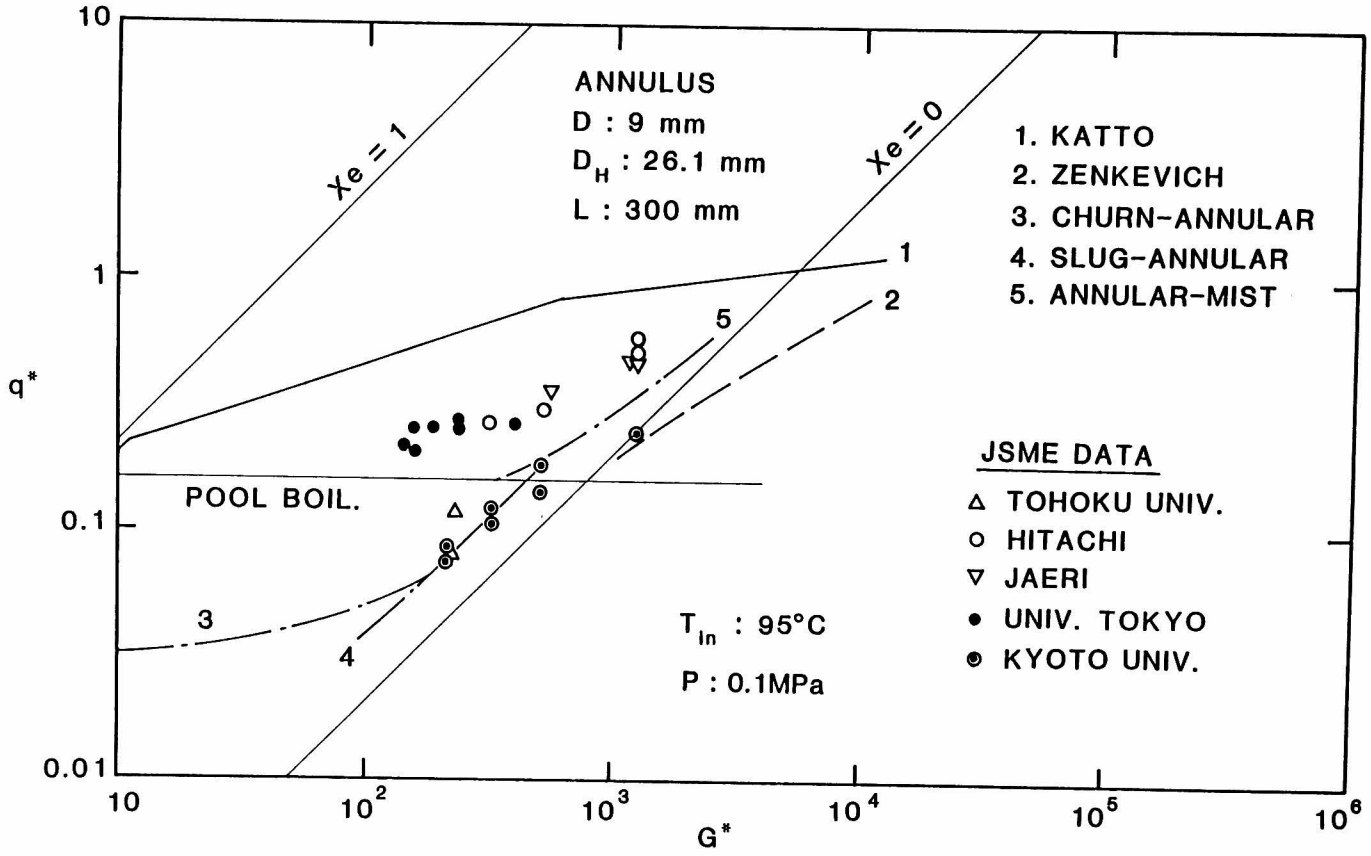


Figure 5 JSME data [6] for atmospheric pressure water in an annulus at inlet water temperature 95°C.

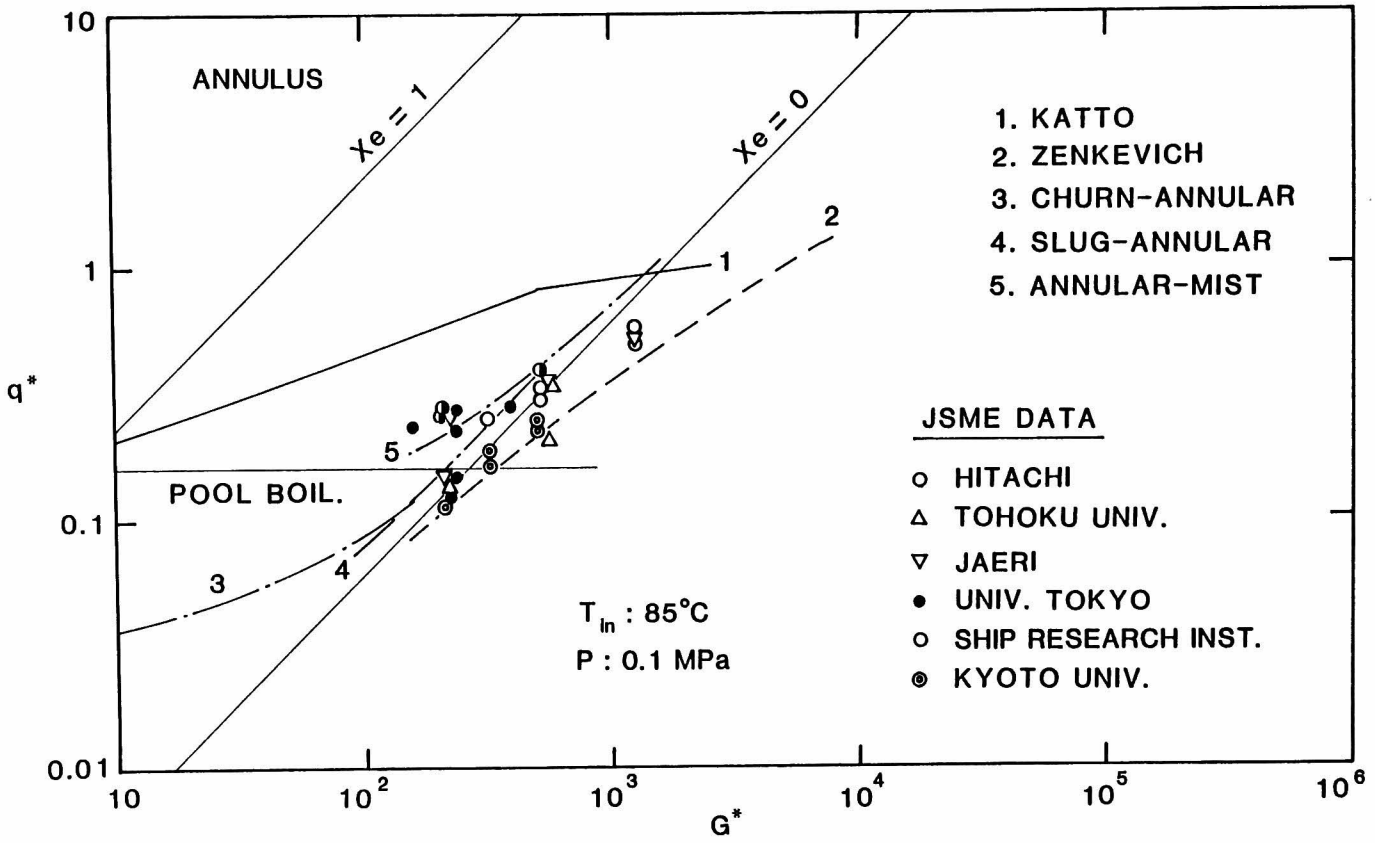


Figure 6 JSME data [6] for atmospheric pressure water in an annulus at inlet water temperature 85°C.

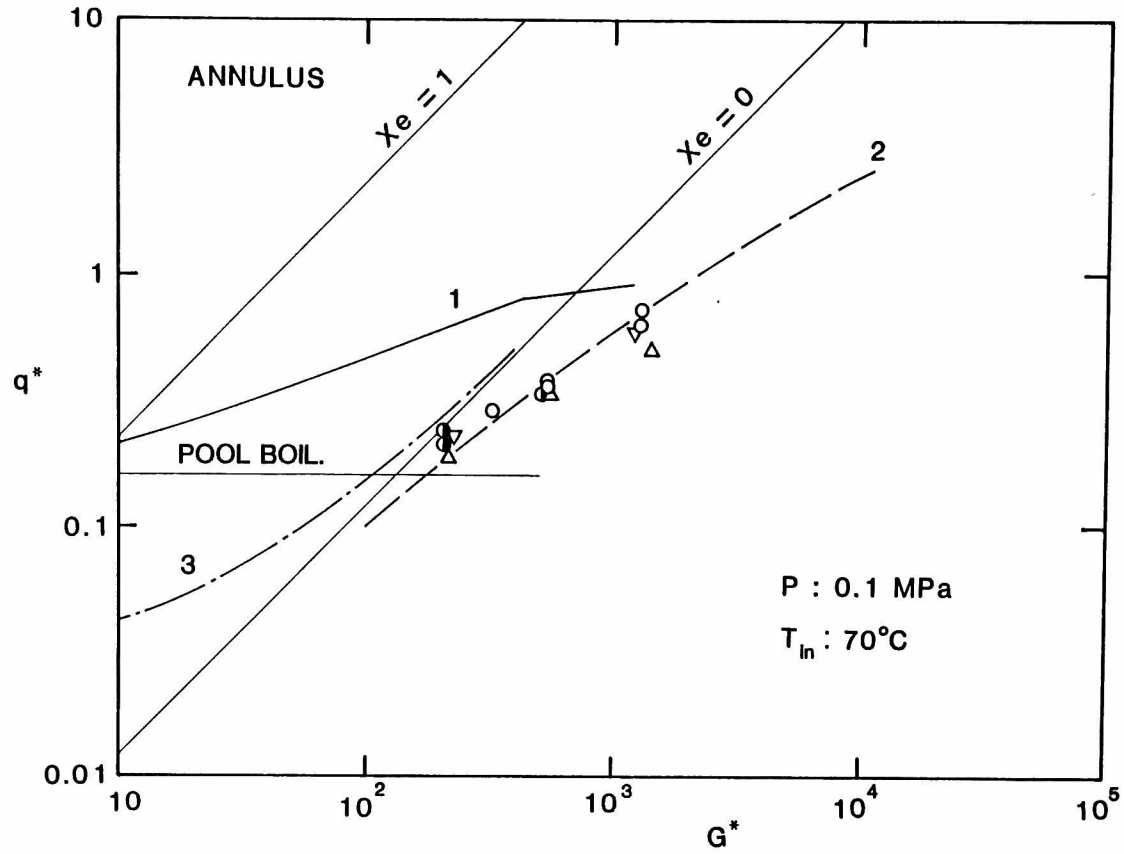


Figure 7 JSME data [6] for atmospheric pressure water in an annulus at inlet water temperature 70°C (Legend as given in Fig. 6).

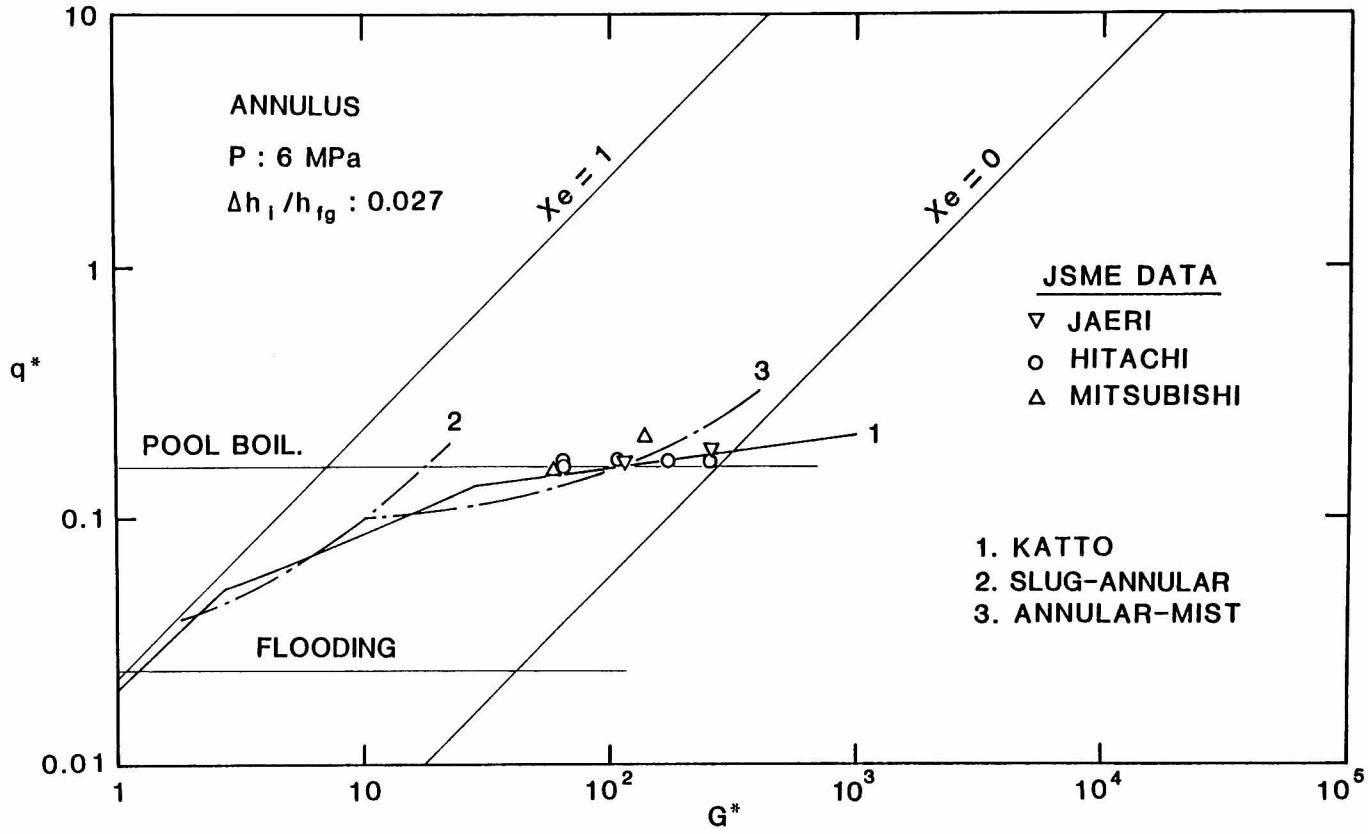


Figure 8 JSME data [6] for 6 MPa water in an annulus at $\Delta h_i/h_{fg}$ = 0.027.

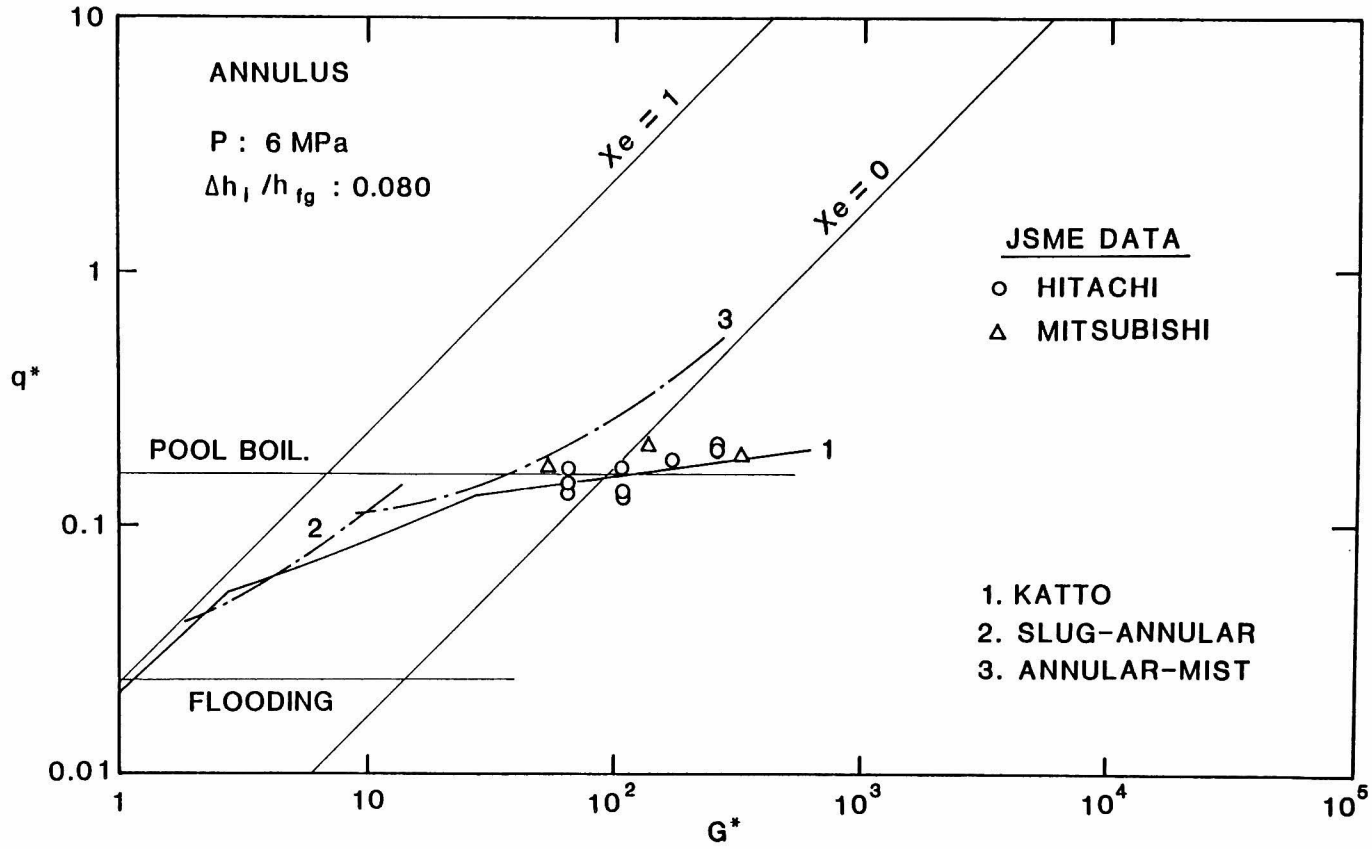


Figure 9 JSME data [6] for 6 MPa water in an annulus at $\Delta h_i/h_{fg} = 0.080$.

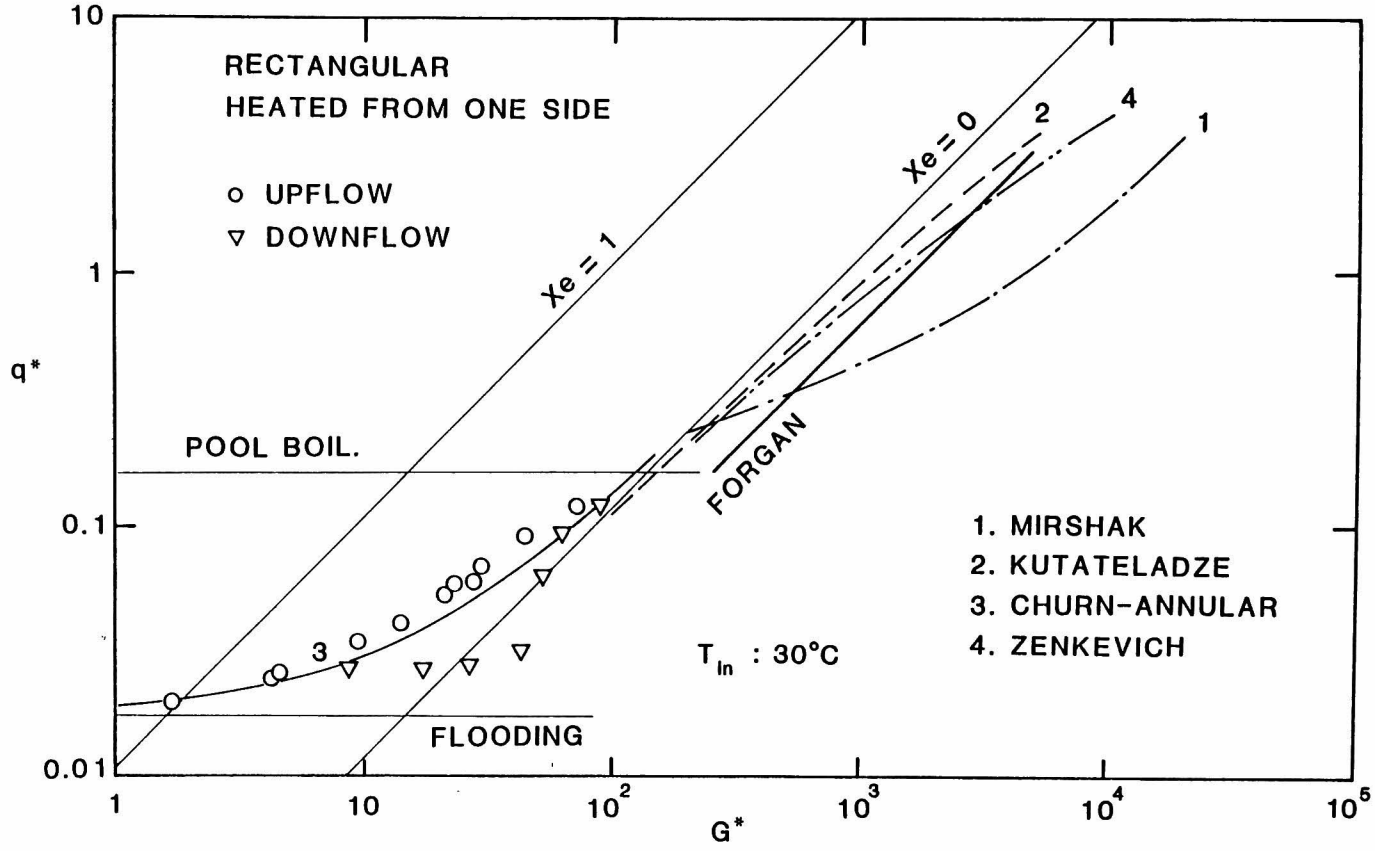


Figure 10 Minimum in the pressure-drop versus flow-rate curve for the test section heated from one side.

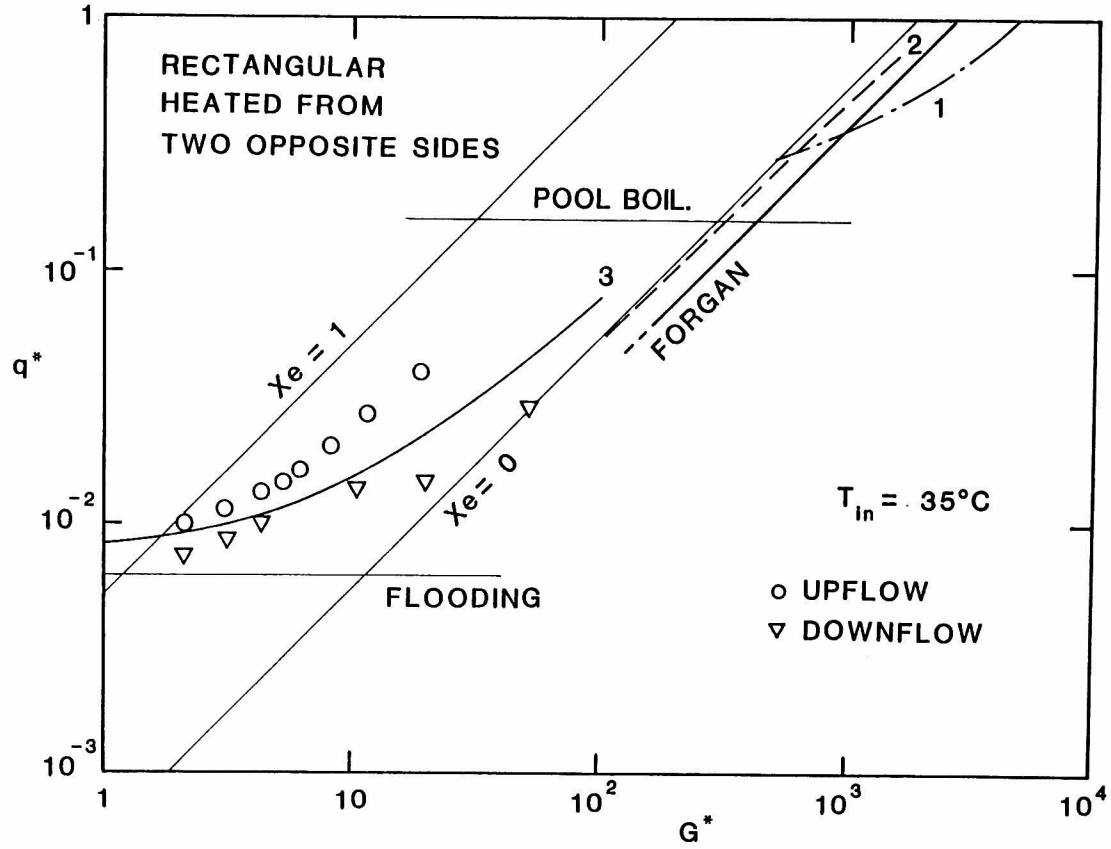


Figure 11 Minimum in the pressure-drop versus flow-rate curve for the test section heated from two opposite sides (Legend as given in Fig. 10).

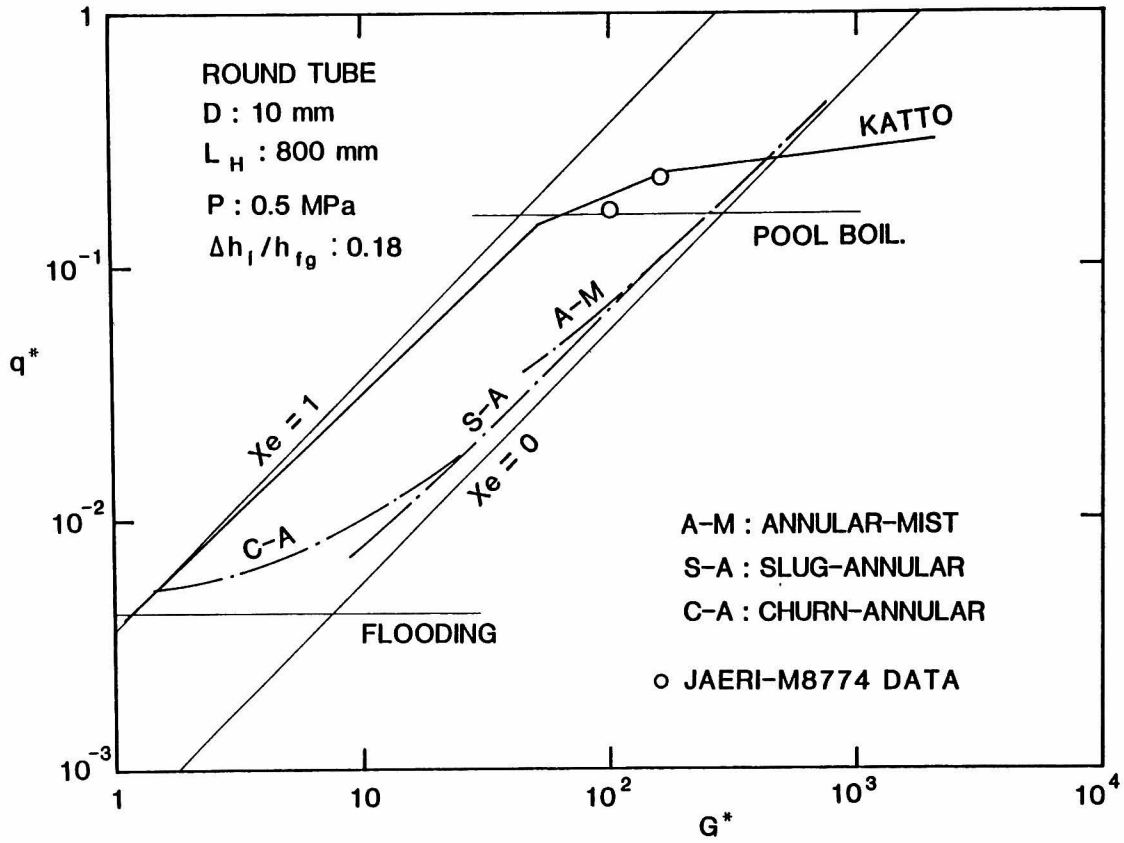


Figure 12 Annular-flow boundary and CHF data [18] at system pressure 0.5 MPa and $\Delta h_i/h_{fg}$ = 0.18.

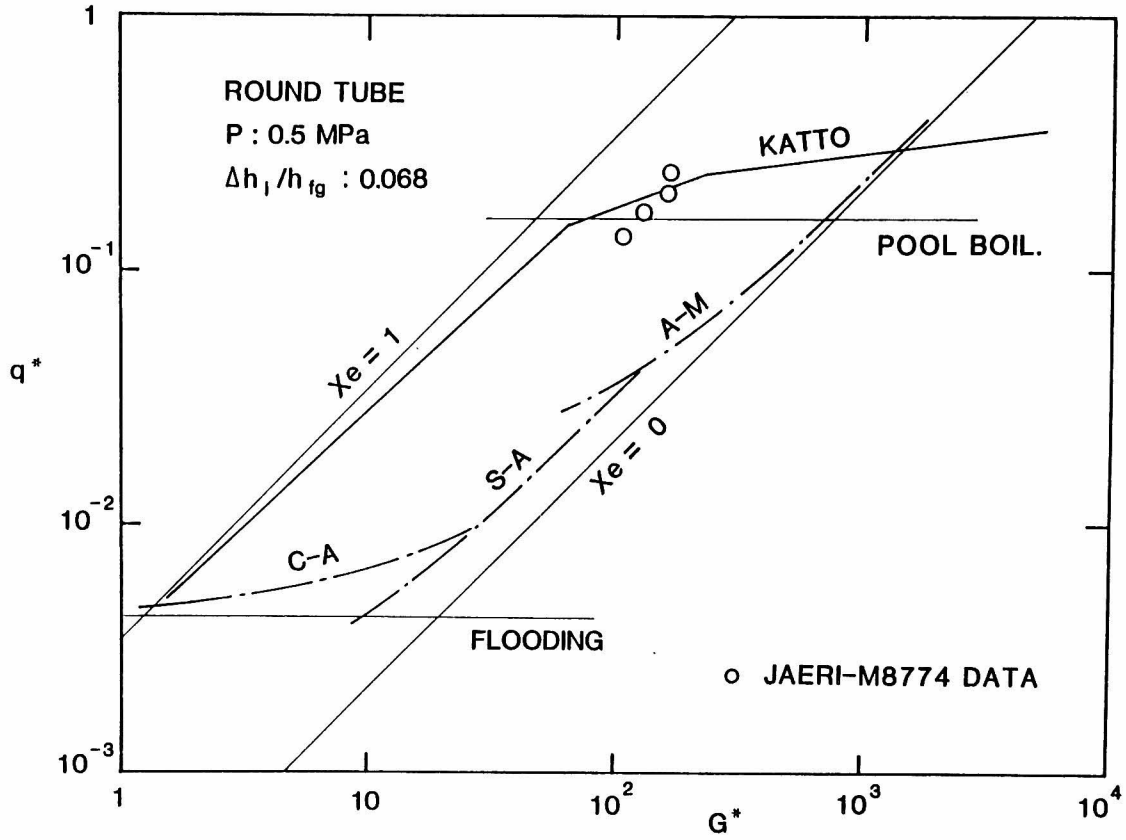


Figure 13 Annular-flow boundary and CHF data [18] at system pressure 0.5 MPa and $\Delta h_i/h_{fg}$ = 0.068 (Legend as given in Fig. 12).

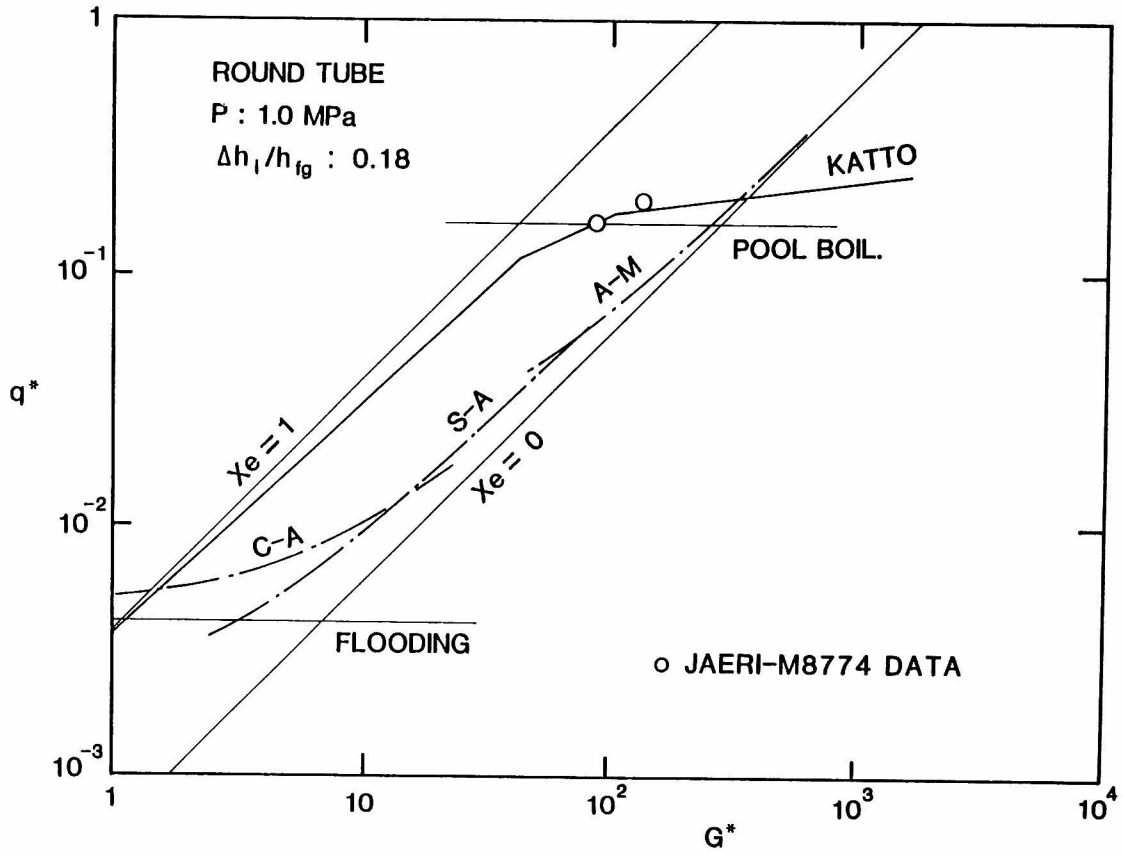


Figure 14 Annular-flow boundary and CHF data [18] at system pressure 1.0 MPa and $\Delta h_i/h_{fg}$ = 0.18 (Legend as given in Fig. 12).

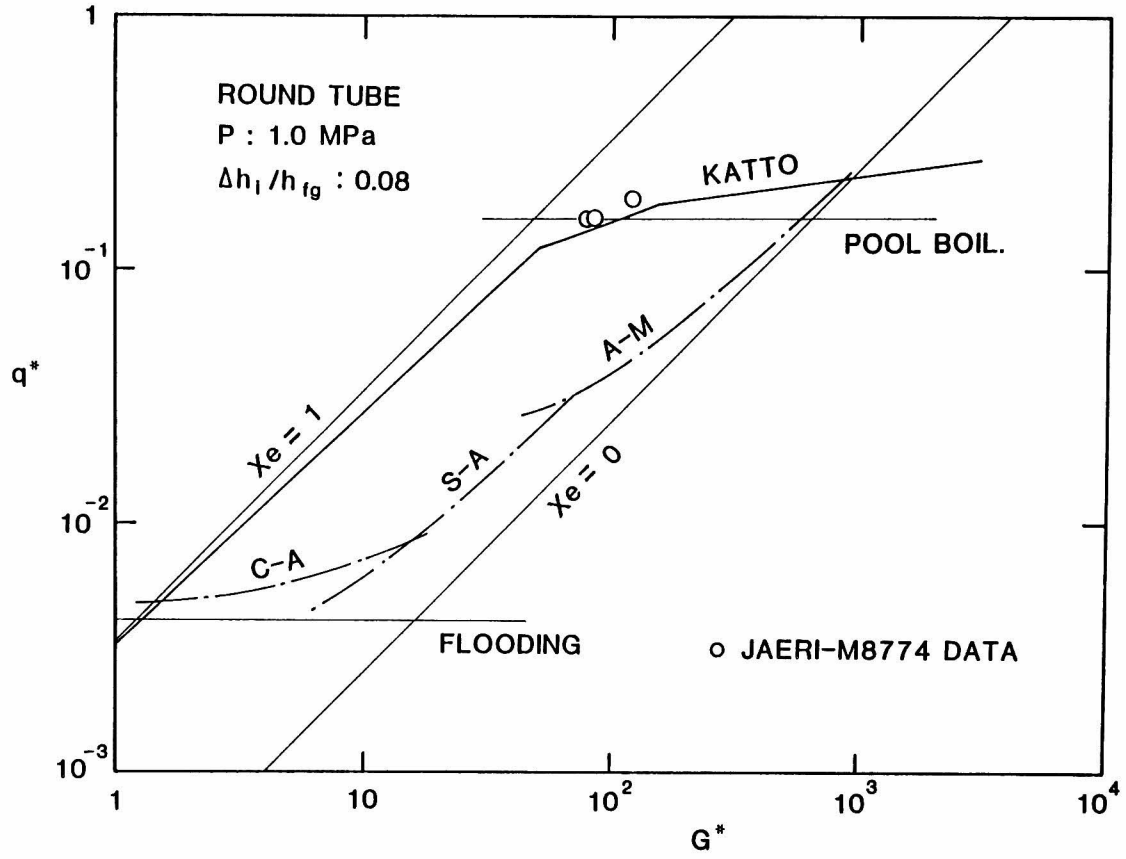


Figure 15 Annular-flow boundary and CHF data [18] at system pressure 1.0 MPa and $\Delta h_i/h_{fg}$ = 0.08 (Legend as given in Fig. 12).

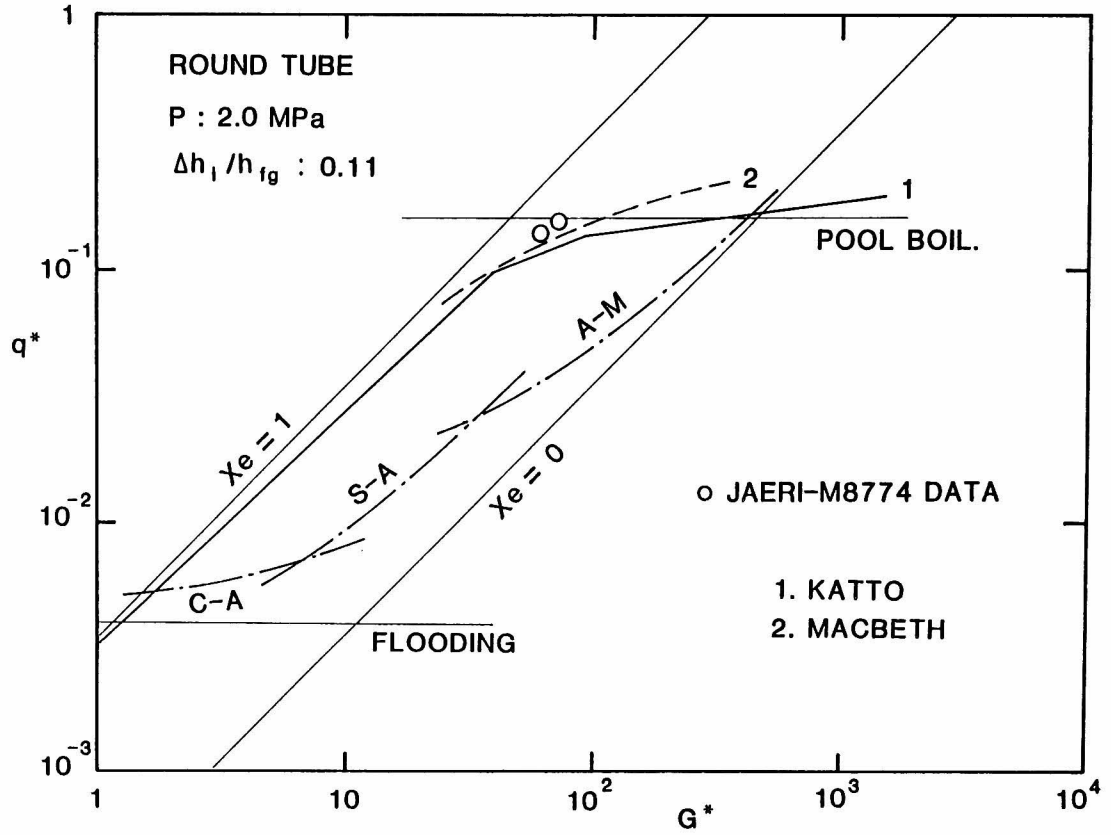


Figure 16 Annular-flow boundary and CHF data [18] at system pressure 2.0 MPa and $\Delta h_i/h_{fg}$ = 0.11 (Legend as given in Fig. 12).

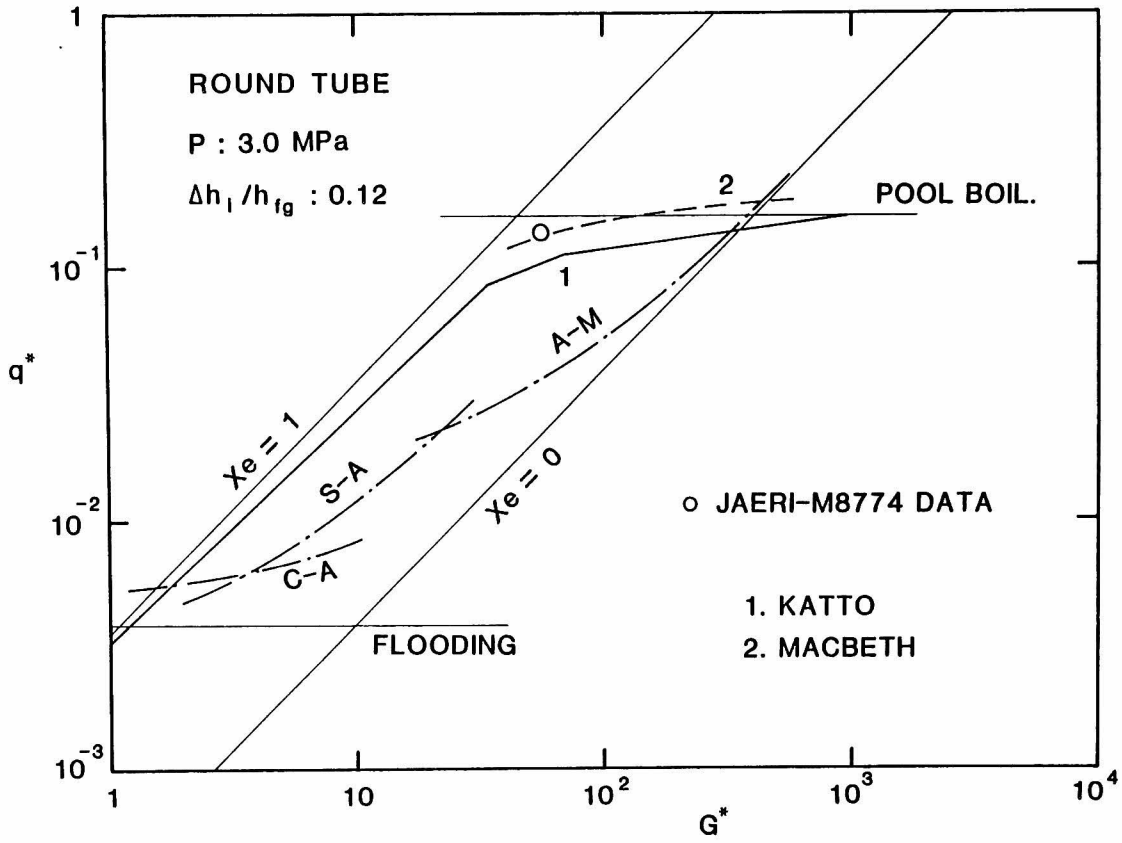


Figure 17 Annular-flow boundary and CHF data [18] at system pressure 3.0 MPa and $\Delta h_i/h_{fg}$ = 0.12 (Legend as given in Fig. 12).

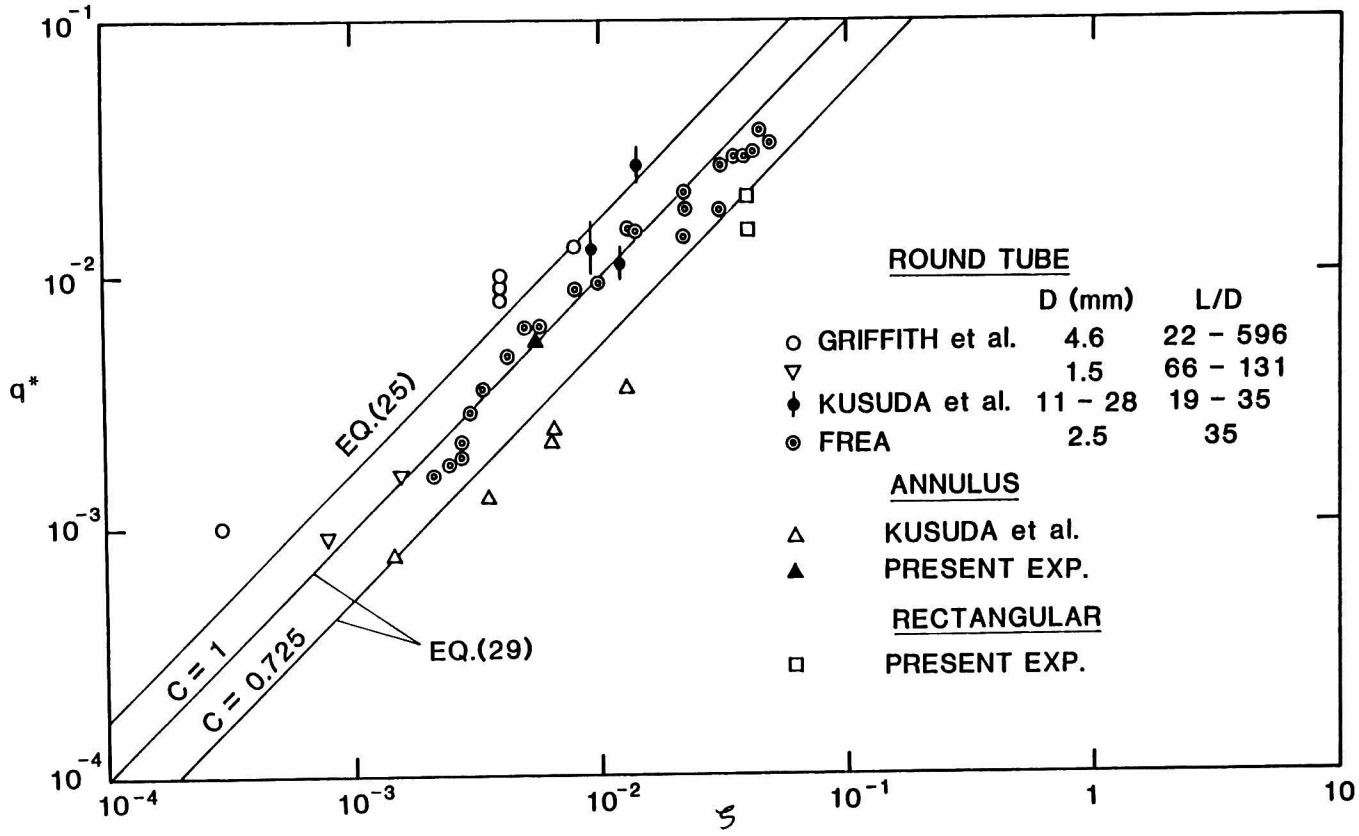


Figure 18 Comparison between the correlations and the experimental data on flooding CHF for water at 0.1 MPa.

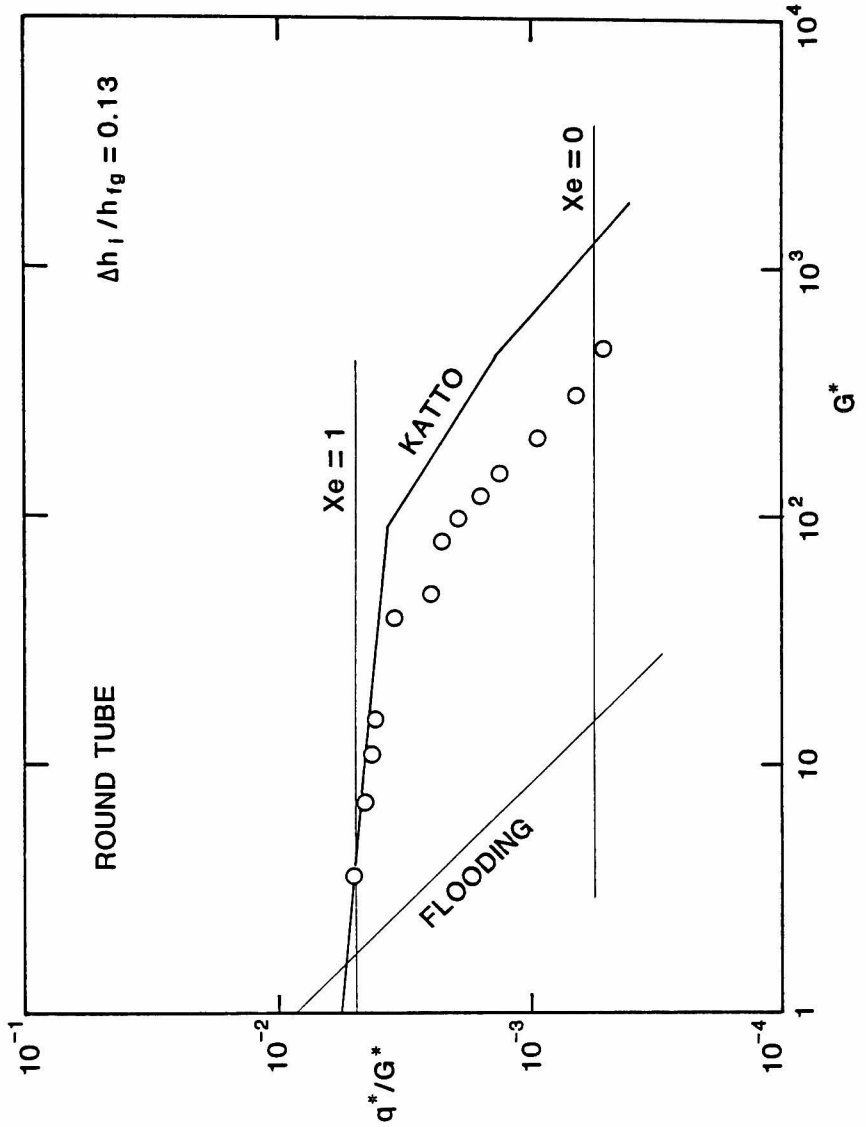


Figure 19 Boiling number as a function of non-dimensional mass velocity for CHF in the round tube.

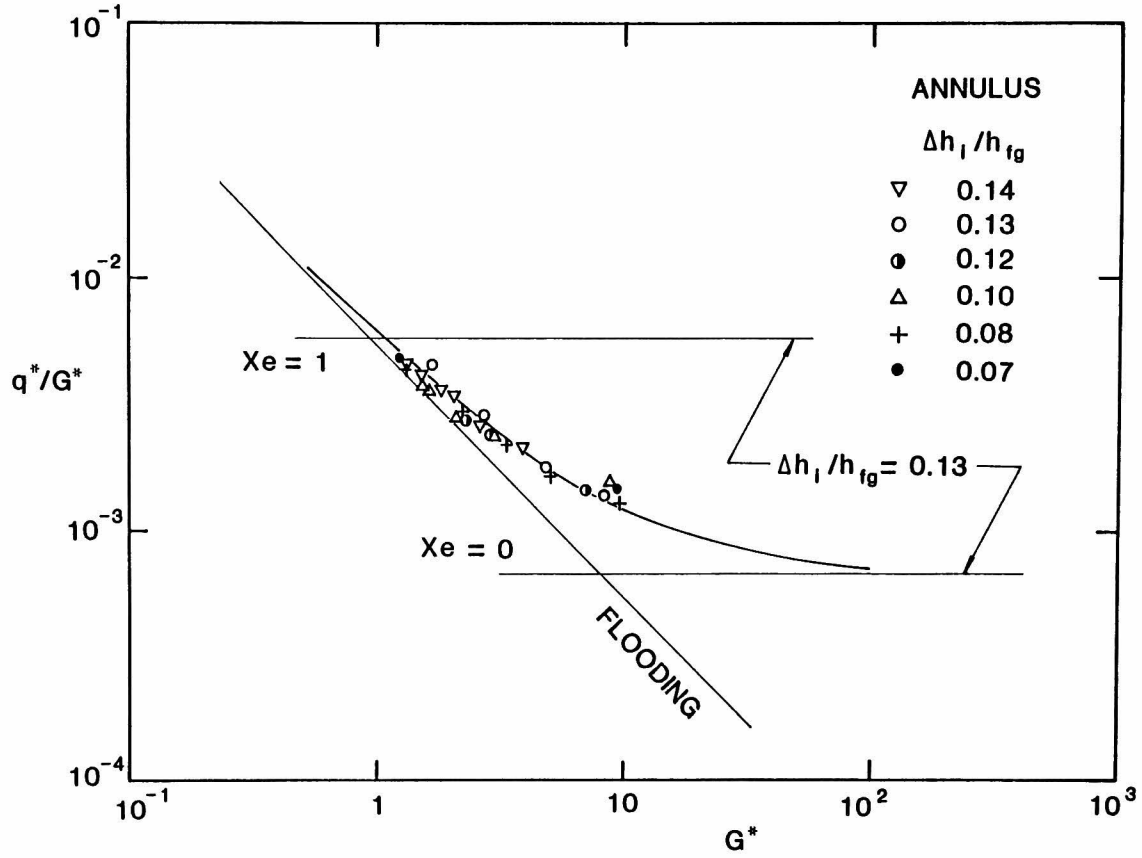


Figure 20 Boiling number as a function of non-dimensional mass velocity for CHF in the annulus.

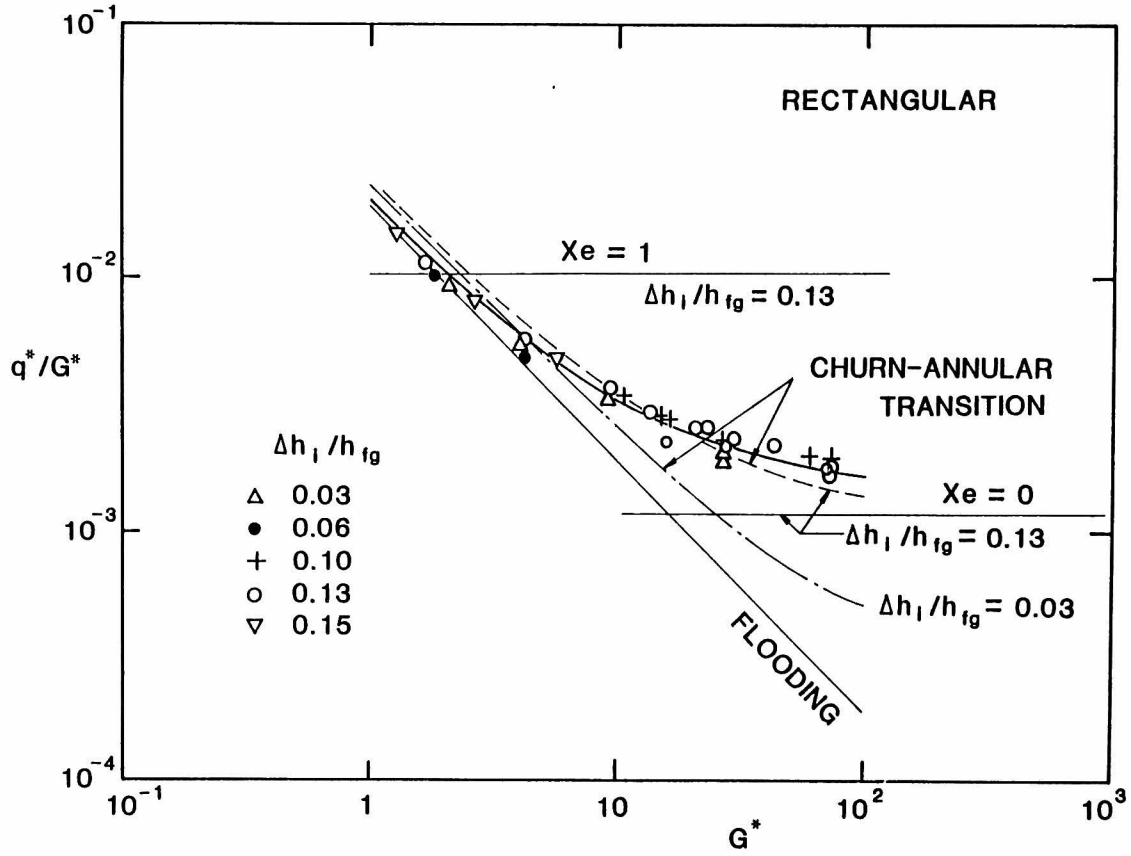


Figure 21 Boiling number as a function of non-dimensional mass velocity for CHF in the rectangular channel heated from one side.

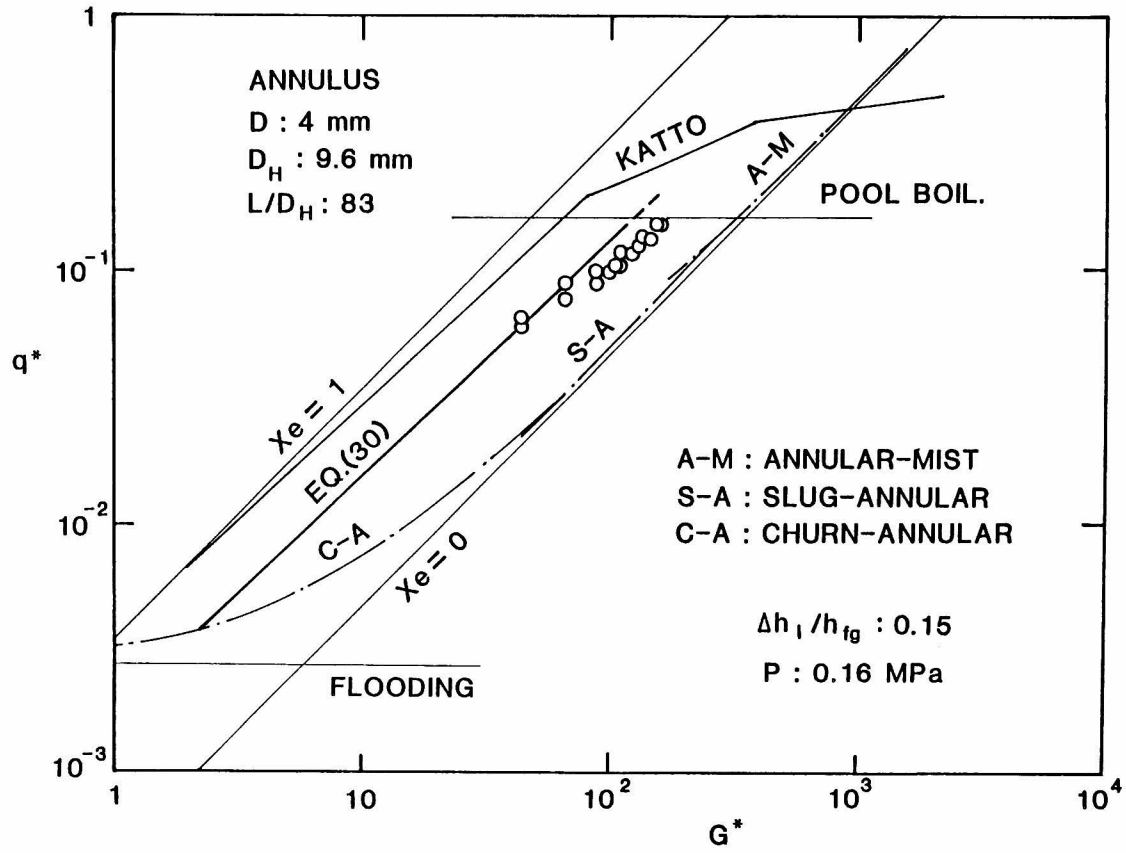


Figure 22 Predicted CHF based on the reduced critical quality in comparison with existing data [25] for annulus.

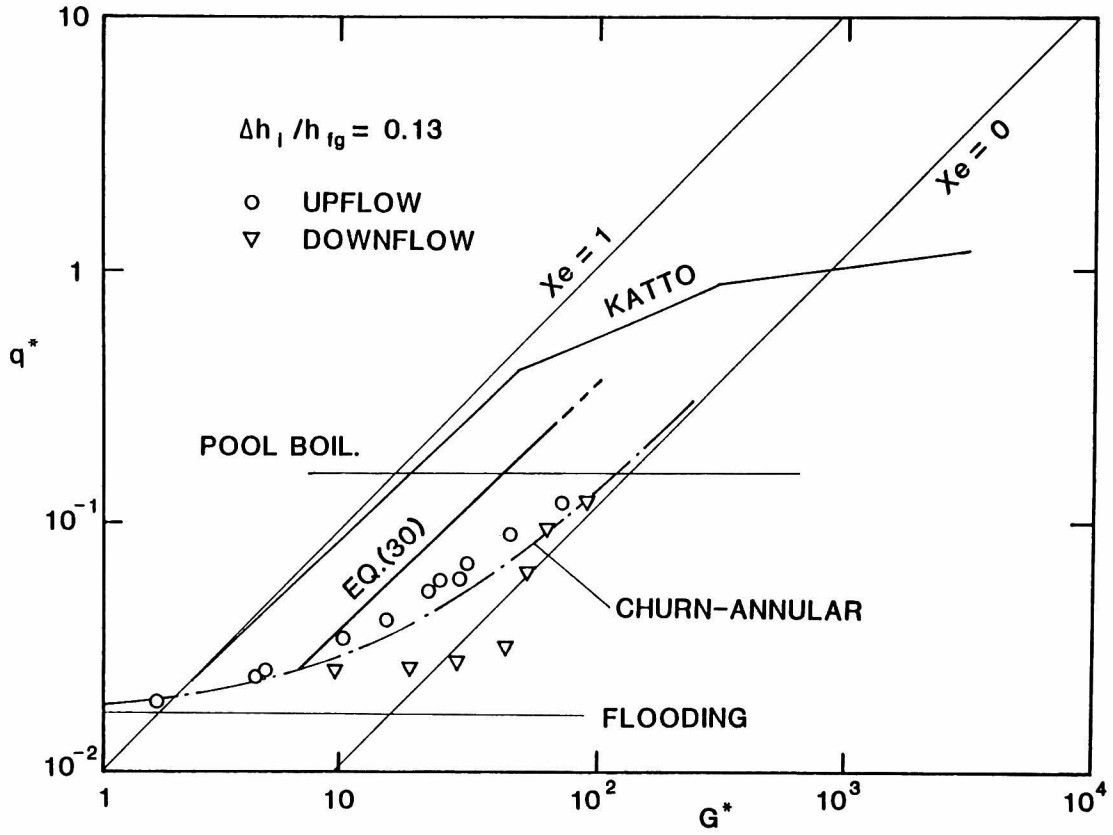


Figure 23 Comparison between the predicted CHF based on the reduced critical quality and the data for the rectangular channel heated from one side.

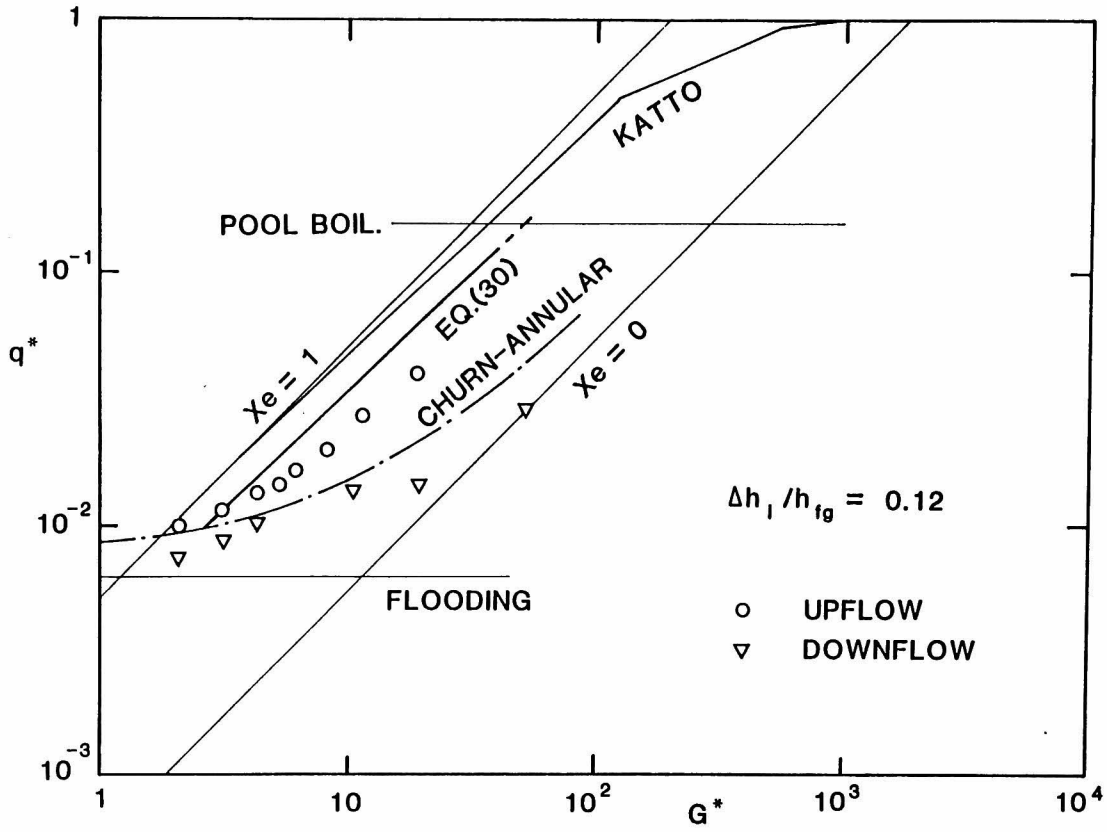


Figure 24 Comparison between the predicted CHF based on the reduced critical quality and the data for the rectangular channel heated from two opposite sides (Legend as given in Fig. 23).

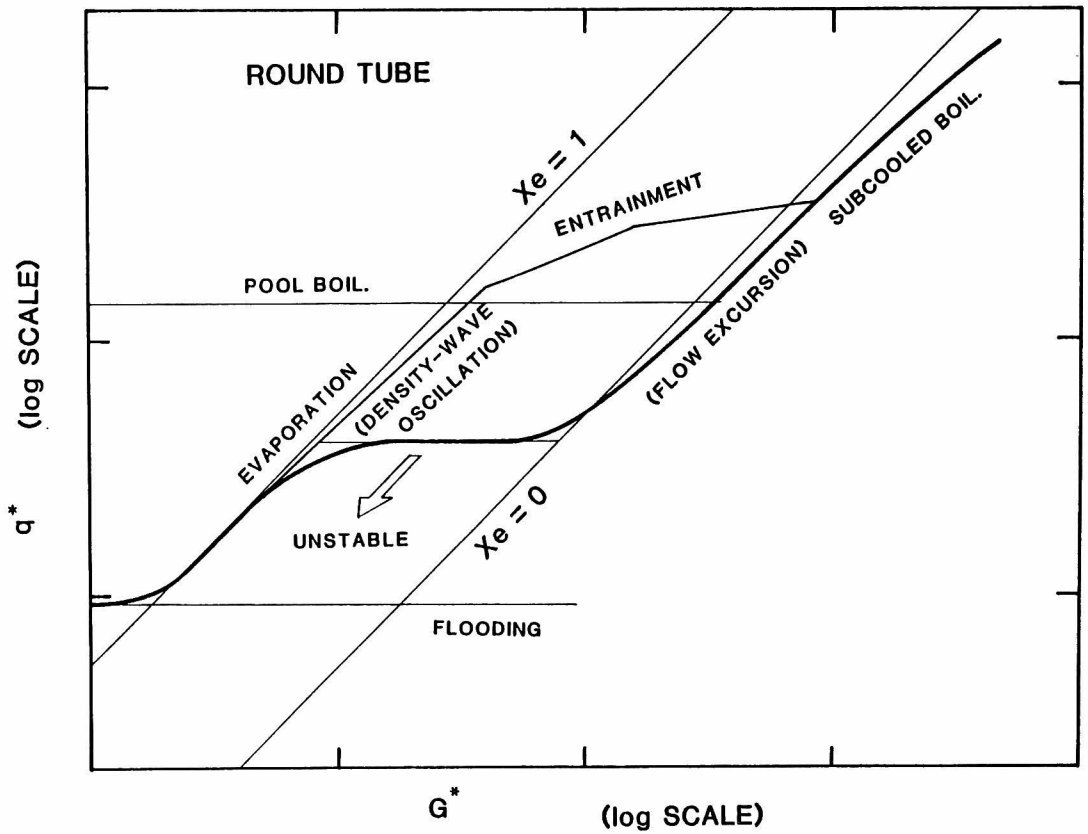


Figure 25 General trends of CHF in a round tube as a function of non-dimensional mass velocity at a given inlet subcooling and a low pressure.

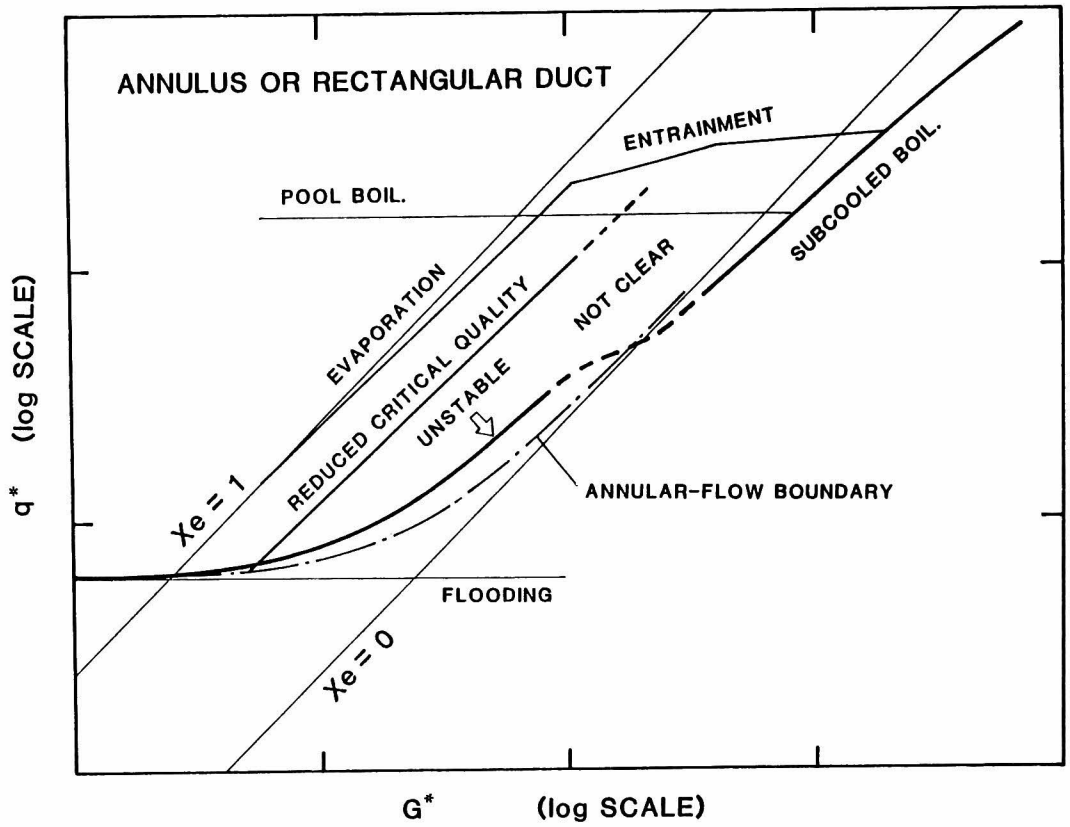


Figure 26 General trends of CHF in an annulus and a rectangular channel as a function of non-dimensional mass velocity at a given inlet subcooling and a low pressure.

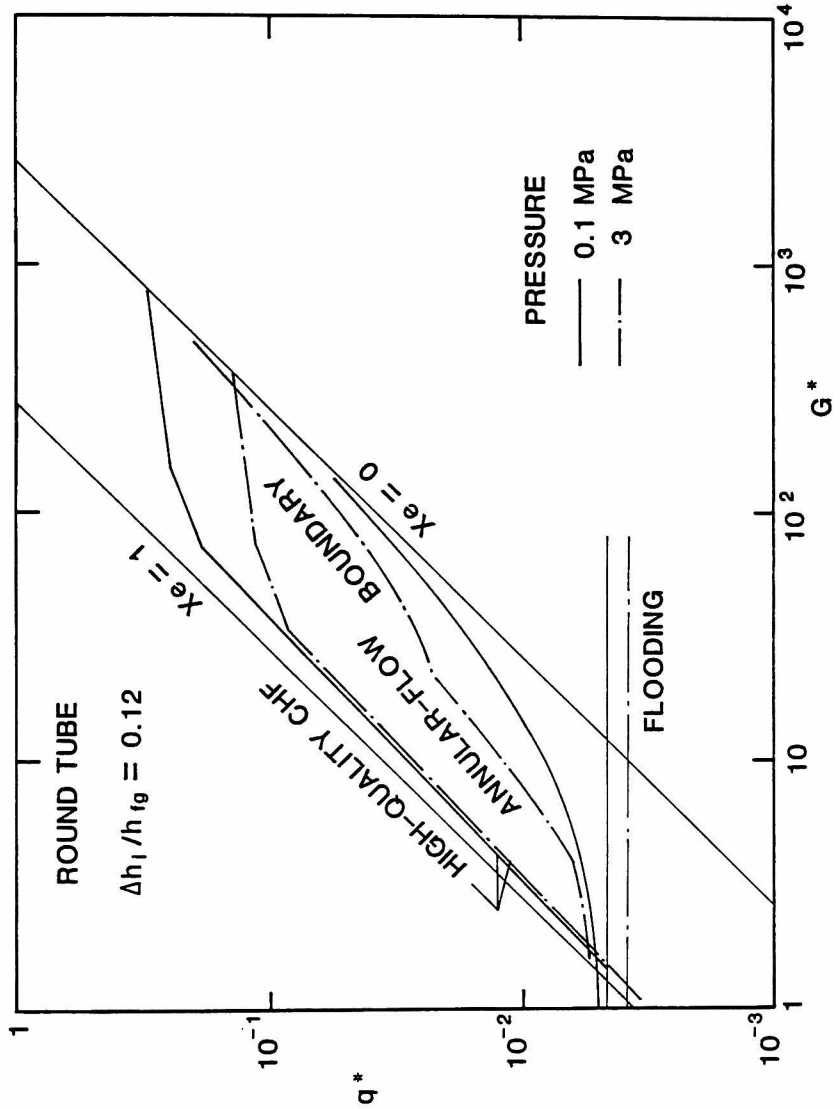


Figure 27 Effect of pressure on the boundaries of CHF curves for a round tube.

Chapter VIII

# SUMMARY AND CONCLUSIONS

## VIII.1. FLOW REGIME TRANSITIONS

New flow regime transition criteria for upward gas-liquid flow in vertical tubes have been developed considering the mechanisms of flow regime transitions. These new criteria can be compared to existing criteria and experimental data under steady-state and fully developed flow conditions by using relative velocity correlations.

The criteria showed reasonable agreements with the existing data for atmospheric air-water flows. Further comparisons with data for steam-water in round tubes and a rectangular channel at relatively high system pressures have been made. The results confirmed that the present flow regime transition criteria could be applied over wide ranges of parameters as well as to boiling flow.

## VIII.2. FLOODING AND FLOW REVERSAL

Basic equations which describe the film flow in round tubes, rectangular ducts and annuli have been derived from the balance of forces acting on the liquid film and the gas core. Those equations are essentially the same as the previously obtained equations.

Using the basic equations and with appropriate friction factors, the countercurrent flow limit has been calculated. However, it turned out that the theoretical limit were much higher than the observed flooding velocities obtained from the experiment with thin rectangular channels. The discrepancy was explained by the observation that the flooding velocities were controlled by the onset of large disturbance

waves at the top, not by the film flow in the channel. The majority of the liquid appeared to flow down along the narrow side walls, which flow pattern was peculiar to thin rectangular channels.

The observed flooding velocities were compared to the existing flooding theories for round tubes by using two-fold of the width (wider span) as the characteristic length. The predictions appeared to be much higher than the data, which were instead tentatively correlated empirically.

### VIII.3. BURNOUT IN ANNULI

An experimental study has been performed on the critical heat flux at low flow rates typical of natural-convection conditions, with an annular test section. The data indicated that a premature burnout occurred due to flow-regime transition from the churn to annular flow. It has been shown that the burnout observed in the experiment is similar to a flooding-limited burnout, although the loop circulation has been maintained at low flow rates. The data can well be correlated by the newly developed CHF criterion derived from the churn-to-annular flow transition criterion.

Since the outer tube of the test section was a Pyrex glass tube, a detailed visual observation on the dryout and rewetting processes have been made. Dry patches appeared on the surface of the heated wall in the churn flow regime. However, they were repeatedly rewetted mainly by the passages of liquid slugs or bridges. In this experiment, permanent dryout of the heated wall occurred when these liquid bridges disappeared at the churn to annular flow transition. Falling liquid as well as climbing film was observed at this point, however, those liquid film did not appear to be thick enough to quench dry patches.

Due to the above mechanism of burnout, the observed CHF are much smaller than the standard pool-boiling or high-quality CHF criteria. There are some indications that the presently observed premature burnout may be limited to a low pressure system. However, at present, the boundaries between different CHF mechanisms are not well established. Further studies are needed on this point particularly at intermediate pressures.

VIII.4. BURNOUT IN ROUND TUBES

An experiment has been conducted with a round tube test section in order to investigate the relation between burnout phenomenon and flow instabilities at atmospheric pressure.

There was observed a minimum in the CHF at the complete bottom blockage in which burnout occurred due to flooding. The CHF at low mass velocities appeared to be well correlated by the high-quality CHF correlations, although in downflow the CHF was as much as 30% lower than the prediction at very low mass velocities due to the effect of buoyancy. The CHF at intermediate mass velocities appeared to be significantly affected by the density wave oscillations. The less stable was the system, the more reduction of CHF encountered.

In downflow, the effect of buoyancy enlarged such destabilizing effects as small inlet throttling and upstream compressibility. Particularly at very low downflow, the CHF reduced as low as close to the flooding CHF. Under such conditions, the pressure-drop oscillations were observed.

At high mass velocities, burnout occurred near zero exit quality. When the heat flux is sufficiently high, the flow excursion was observed which directly lead to a burnout.

The above observations were made at atmospheric pressures. There are some indications that at high pressures, the flow is generally stable, which may be the reason why the most of the CHF data at high pressures are well correlated by the conventional CHF correlations. However. in order to establish the boundary of the occurrence of stable-flow CHF, further studies will be necessary.

## VIII.5. BURNOUT IN RECTANGULAR CHANNELS

The critical heat flux at low-flow-rate and low-pressure conditions has been studied for water flowing in thin rectangular channels in relation to the core cooling of MTR-type research reactors. The experiment has been performed with two types of rectangular channels, i.e. the one heated from one side and the other heated from two opposite sides. Critical heat flux was measured both in upflow and downflow. The CHF at complete bottom blockage was also studied.

The results indicated that the burnout could occur at much lower heat flux than pool-boiling CHF or than the conventional high-quality CHF correlations. There was observed a minimum CHF at complete bottom blockage and at very low downflow. The low values of CHF at very low downflow appeared to be due to the stagnation of the bubble in the heated section. This fact indicates that a special care should be taken in analyzing the boiling phenomenon which occurs when the coolant flow is very low in a low pressure system.

Visual observation revealed that the burnout in upflow mainly occurred in annular flow regime, while that in downflow occurred due to countercurrent flow limitation and/or flow instability. The instability appeared to be the pressure-drop oscillations, in which the upper plenum worked as an energy storage mechanism to excite the oscillations.

## VIII.6. CONCLUSIONS

Experimental study has been conducted with three basic channel geometries, i.e. annulus, rectangular duct and round tube, in order to investigate the burnout mechanism focussed on low-flow-rate and low-pressure conditions. The following conclusions are extracted from the results of the experiment:

(1) In any case at low mass velocities, burnout appears to occur due to the dryout or breakdown of the liquid film on the heated surface as has been recognized by many investigators. Therefore, if the film flow rate and the criteria for the dryout or breakdown of liquid film are known in detail, the CHF can be predicted theoretically. On the other hand, it is also probable that those criteria are met consequently if such hydrodynamical phenomena as countercurrent flow limitation, flow regime transition and flow excursion cause the liquid deficiency in the heated channel. Therefore, in such cases, the CHF can be calculated by using the criteria for such hydrodynamical phenomena.

(2) There is a minimum in CHF which occurs due to countercurrent flow limitation at the complete bottom blockage. Thus the minimum CHF can be calculated from an appropriate CCFL criterion.

(3) In a boiling system at low pressures, the flow is more or less unstable. Large amplitude flow instability may cause the total liquid deficiency in the heated channel due to temporary flow reduction, thus reducing the CHF substantially. The effects of buoyancy on the flow appeared to be destabilizing in downflow. The destabilizing effects of less inlet throttling, upstream compressibility and bypassing have been also observed.

ACKNOWLEDGEMENTS

The author gratefully acknowledges the assistance of his thesis advisor, Dr. Hideaki Nishihara, Professor of Kyoto University, who provided constant guidance, interest and encouragement. He also would like to express his sincere gratitude to Dr. Itaru Michiyoshi, Professor of Kyoto University, for his continuous interest and valuable discussions on this study. He also would like to express his thanks to Dr. Akira Sakurai, Professor of Kyoto University, for reviewing this work.

Thanks are also due to Dr. Toshikazu Shibata, Dr. Itsuro Kimura, Professors of Kyoto University, and Dr. Keiji Kanda, Associate Professor of Kyoto University, for the opportunity and support of this work.

Special thanks are extended to Dr. Mamoru Ishii of Argonne National Laboratory, who introduced the author into this research and provided many useful suggestions on the subject.

The author is indebted to Messrs. Hiroshi Nakamura, Yasusuke Araki, Ryusho Ikegawa, Kaoru Minami at Research Reactor Institute of Kyoto University, and Mr. Nobuyuki Yagoro of Kinki University for their assistance in the experiment.

The author also would like to thank all of the staff members of Nuclear Reactor Division at Research Reactor Institute of Kyoto University for the opportunity for this work.

Finally, the author would like to express deep appreciation to his wife, Makiko, for her continued encouragement and patience. Without her devotion, this work could never have been accomplished.

(4) It turned out that the critical exit quality at burnout considerably reduced in annuli and rectangular channels because of remaining liquid film on the unheated surface. On the other hand, there are some indications that at high pressures, the critical quality is near unity even in the other channel geometries than round tubes. It may be explained by the location of the annular-flow boundary which moves toward higher quality at high pressures. However, this needs to be verified in future studies.